Modeling and Robust Adaptive Tracking Control of a Planar Precision Positioning System

Dissertation
zur Erlangung des akademischen Grades
Doktoringenieur (Dr.-Ing.)

vorgelegt der Fakultät für Informatik und Automatisierung

der Technischen Universität Ilmenau

von

M.Sc. Kai Treichel

vorgelegt am 17. Oktober 2016
verteidigt am 01. August 2017

1. Gutachter: Prof. Dr.-Ing. Johann Reger
2. Gutachter: Prof. Dr.-Ing. Florian Holzapfel
3. Gutachter: Prof. Dr. Naira Hovakimyan

urn:nbn:de:gbv:ilm1-2017000665

"Said the straight man to the late man, where have you been? I've been here and I've been there and I've been in between..."

King Crimson

Zusammenfassung

Präzisionspositioniersysteme bilden eine wesentliche Grundvoraussetzung für moderne Produktionsprozesse in den vielschichtigen Anwendungen der Mikro- und Nanotechnologie. An die Regelung dieser Systeme werden hohe Anforderungen bzgl. Bandbreite, Genauigkeit, Robustheit und Stabilität gestellt. Die wichtigste Anforderung jedoch, bildet die dynamische Verfolgung komplexer Referenztrajektorien mit höchster Präzision.

Zur Erreichung dieser Ziele ist zumeist eine möglichst genaue Kenntnis der wesentlichen Systemparameter erforderlich, deren Identifikation in der Regel aufwändig und teuer ist. Zudem können sich je nach Produktionsprozess oder Anlage Parameter mit der Zeit verändern, was die Erreichung dieser Ziele gefährdet.

Aus betriebswirtschaftlicher Sicht ist es daher erstrebenswert, die Parameteridentifikation während des Betriebs innerhalb der Regelung durchzuführen. Dies reduziert den Aufwand bei der Systemidentifikation und stellt zudem sicher, dass die Regelung sich auch gegenüber Veränderungen anpassen kann.

Aus dieser Motivation heraus beschäftigt sich die vorliegende Dissertation mit der Entwicklung eines adaptiven Folgeregelungskonzepts für das planare Präzisionspositioniersystem PPS1405 der Firma Tetra. Die Grundlage hierfür bildet die Entwicklung sowie die Identifikation detaillierter Systemmodelle der wesentlichen Komponenten des PPS1405. Das entwickelte Modell dient zum einen als Grundlage für modellbasierte Regelungsentwürfe und zum anderen als realistische Simulationsumgebung zur Erprobung und Bewertung dieser Verfahren. Ferner gibt es Einblicke über die potentielle Anwendbarkeit von adaptiven Regelungen und bestätigt diese.

Aufbauend darauf, basiert der angestrebte Folgeregelungsentwurf auf der Idee eines zweistufigen Ansatzes, bestehend aus einem nominellen Folgeregler und einer adaptiven Erweiterung mittels $\mathcal{L}_1$ adaptiver Regelung. Letztere erscheint im Hinblick auf herausragenden Performance- und Robustheitseigenschaften vielversprechend. Für die adaptive Folgeregelung werden sowohl Ansätze für Zustands- als auch Ausgangsrückführungen entwickelt, wobei aufgrund der zur Verfügung stehenden Messsignale nur letztere am Versuchsstand implementiert werden. Experimentelle Ergebnisse bestätigen die Leistungsfähigkeit der entwickelten Regelung. Diese erfüllt alle gestellten Anforderungen hinsichtlich der Positionsabweichung und erzielt Regelgüten, die mit existierenden Reglern bisher nicht erreicht wurden.

Abstract

Precision positioning systems constitute an essential prerequisite for modern production processes in the diverse applications of micro- and nanotechnology. Associated with the control of these systems there are high demands with respect to bandwidth, accuracy, robustness and stability. The most important requirement, however, is dynamic tracking of complex reference trajectories with highest precision.

To achieve these objectives, usually a good knowledge of system parameters is necessary, whereby their identification is mostly laborious and expensive. In addition, depending on the production process or plant, parameters may change with time which may endanger the achievement of these goals.

From an economic perspective, it is therefore desirable that parameter identification is carried out during operation, within the control scheme. This reduces the effort for system identification and also ensures that the controller may also adapt to parametric changes.

Based on this motivation, the present thesis deals with the development of an adaptive tracking control concept for the planar precision positioning system PPS1405 build by the motor manufacturer Tetra. The development and identification of detailed system models of the most important components of the PPS1405 is the foundation for this. The developed model serves firstly as a basis for model-based control design and secondly as a realistic simulation environment for testing and evaluation of the controllers designed. Furthermore, the model gives insights about the potential applicability of adaptive control which is confirmed throughout the analysis.

Following this, the aspired tracking control design is based on the idea of a two-stage approach, comprising a nominal tracking controller and an adaptive augmentation exploiting ideas from $\mathcal{L}_1$ adaptive control. The latter seems promising in view of remarkable performance and robustness properties. For the adaptive tracking controller, both, state and output feedback schemes are developed, whereas in view of the available measurement signals only the output feedback scheme is implemented at the test rig.

Experimental results confirm the efficiency of the proposed control scheme. It meets all specifications with regard to tracking errors and yields tracking performance that has not been obtained by any of the existing controllers so far.

Danksagung

Die vorliegende Dissertation entstand während meiner Tätigkeit als wissenschaftlicher Mitarbeiter am Fachgebiet Regelungstechnik der Technischen Universität Ilmenau.

Am Gelingen dieser Arbeit waren viele mir nahestehende Personen beteiligt, denen ich an dieser Stelle meinen persönlichen Dank aussprechen möchte.

An erster Stelle möchte ich mich bei meinem Doktorvater Prof. Dr.-Ing. Johann Reger für die hervorragende wissenschaftliche Betreuung dieser Arbeit bedanken. Vor allem danke ich ihm dafür, dass er auch über Ländergrenzen und Zeitzonen hinweg stets die Zeit gefunden hat mich bei fachlichen Fragen mit seinem Wissen und seiner Erfahrung zu unterstützen.

Ich bedanke mich bei allen aktuellen und ehemaligen Kollegen des Fachgebiets Regelungstechnik für die tolle Zusammenarbeit in einem kollegialen und sehr humorvollen Klima. Insbesondere bedanke ich mich bei Remon Al Azrak für die vielen interessanten Gespräche und anregenden fachlichen Diskussionen, bei Dr. Kai Wulff, Steffen Mauch, Bernd Schmidt, Alexander Barth und Christoph Weise, deren Türen immer für Fragen offen standen. Darüber hinaus bedanke ich mich bei Nora Dempwolf, Nadja Kühling, und Jessica Wizowsky.

Ich danke allen meinen Bachelor- und Masterstudenten, die im Rahmen ihrer Abschlußarbeiten einen wichtigen Beitrag zum Gelingen dieser Arbeit leisteten.

Die letzten drei Jahre meiner Tätigkeit waren geprägt durch ein nahezu tägliches Pendeln zwischen Jena und Ilmenau. Zur Reduktion der Fahrtzeiten und -kosten unterstützten mich Freunde und Kollegen mit regelmäßigen Übernachtungmöglichkeiten. Hierfür möchte ich mich vom ganzen Herzen bei Remon Al Azrak, Alexander Barth, Jan Deters und Marc-Anthony Brunsch bedanken. Besonders hervorheben möchte ich an dieser Stelle Lorenz Esch, der mich darüber hinaus stetig in meinem Promotionsvorhaben bestärkt und motiviert hat.

Ferner danke ich allen Korrekturlesern für ihre wertvollen Hinweise und ihre Geduld.

Ohne den Rückhalt und die Liebe in der eigenen Familie wäre diese Arbeit nicht einmal ansatzweise möglich gewesen. Meiner Verlobten Julia möchte ich dafür danken, dass sie mir in all den Jahren den Rücken freigehalten und mich stetig unterstützt hat, obwohl sie meinetwegen viele Entbehrungen hinnehmen musste.

Meinen Kindern Jakob und Aaron danke ich dafür, dass sie mir mit ihrer Unbekümmertheit auch in schwierigen Zeiten immer ein Lächeln auf die Lippen zaubern.

Meinen Schwiegereltern in spe, Carmen und Frank Müller, möchte ich für ihre unermüdliche und tatkräftige Unterstützung bei der Betreuung meiner beiden Söhne und sonstigen Belangen danken.

Meinen Eltern Natalja und Holger Treichel danke ich für die moralische und seelische Unterstützung sowie die Unterstützung während meiner gesamten schulischen und akademischen Ausbildung.

Ein Dankeschön soll auch an meine besten Freunde und Bandmitglieder Florian Jogwick und Eugen Rolnik gehen.

Kai Treichel Ruttersdorf, den 16.10.2016

Contents

To Julia, Jakob, Aaron and my Parents

Chapter 1

Introduction

The ongoing scientific and technological development is characterized by the tendency to explore smaller and smaller areas of matter. The foundation of microtechnology in the 60s of the last century followed by nanotechnology in the 80s has not only enriched numerous fields in science and technology but also daily life. It is not an exaggeration to state that the development of microelectronics was the foundation for the information-technology revolution and all the movements resulting out of this. For a long period of time Moore's law, stating that the number of transistors in a dense integrated circuit doubles approximately every two years, was considered as a common and valid rule within the art. Increasing complexity of integrated circuits remaining or decreasing the foot print imply a significant improvement of the related machines and facilities for the production processes of micro and nano equipment. This concerns especially the requirements for the accuracy of measurements as well as for the positioning of machine elements.

Precision positioning and precision motion control are therefore fundamental prerequisites of all modern production processes in the fields of micro- and nanotechnology. These processes are manifold and encompass numerous areas of science including physics, biology, materials science and chemistry [34]. The most prominent examples include photolithographic processes in semiconductor manufacturing [13], stereolithographic microfabrication of tissue engineering scaffolds [46], micro- and nanofabrication/assembly of micro/nano-electromechanical systems (MEMS/NEMS) [28, 116], cell tracking and DNA analysis in molecular biology [34].

1.1 State of the Art

1.1.1 Planar Precision Positioning Systems

Precision positioning systems are highly complex mechatronic devices used for measuring and manipulating matter on a small scale of length.

For the manipulation and measurement of microscopic objects on a displacement range of several hundreds of micrometers, state-of-the-art precision positioning systems resort to actuation principles based on smart materials (piezoelectric, magnetostrictive, piezomagnetic) or micro-electromechanical systems (MEMS) [34]. For instance, piezoelectric positioning stages are ubiquitous in nanopositioning applications such as scanning probe microscopy (SPM) [39], cell tracking and DNA analysis in molecular biology [33].

For precise positioning over long displacement ranges of several hundreds of millimeters, since the 1960s, there has been considerable research effort for the development of so-called planar positioning stages, based on electromagnetic actuation principles. This effort was mainly driven by the need of the semiconductor industry for a

precision high-speed positioning device that was capable of travel over long displacements in a plane and providing a small yawing motion, thus managing 2+1 degrees-of-freedom (DOF) [11, 122]. Since then, the ever increasing requirements of the diverse applications in the field of micro- and nanotechnology, such as photolithography [13, 105], micro-stereolithography, precision laser cutting as well as micro- and nanofabrication of MEMS/NEMS [28, 116], led to positioning stages whose positioning accuracy is only limited by sensors and electronics. Thus, depending on the choice of sensors, state-of-the-art positioning stages, exploiting electromagnetic actuation principles, may even provide accuracy in the nanometer to subnanometer range [151], while allowing for long range displacements of several of hundreds of millimeters.

Essentially, such a planar positioning device is based on the concept of planar motor. Roughly speaking, a planar motor may be considered as an unrolled version of a rotatory machine [136]. Likewise, it consists of a stationary part, the stator, and a moving part, the mover. Exploiting the different principles of rotatory machines for the creation of planar motors, according [57] a planar motor may be classified into three types:

- reluctance planar motor
- induction planar motor
- permanent magnet planar motor

A famous example for a reluctance planar motor is the Sawyer stepper motor invented by B. A. Sawyer in 1968 [122]. It is the first planar motor used in semiconductor industry [11]. Due to its working principle this motor may be operated in open loop which renders superfluous the need of position feedback. This, as a major advantage, allows cost effective design. However, due to the incremental principle, positioning accuracy is limited by an economically viable production and accuracy of the tooth pitch of stator and mover/forcer [123]. Due to the open loop operation, these motors are prone to external disturbances. However, using additional sensors and feedback control as in [112], this draw back may be overcome at the expense of cost efficiency with respect to the original design.

Induction motors are AC machines (see e.g. [37, 88]). Their mover typically consists of three-phase coil units, while the stator resembles a conductive (reaction) plate with a massive back-iron [37]. Energizing the coils with currents creates a traveling magnetic field which induces voltages in the stator part, as described in [37, 88]. This gives rise to thrust forces (Lorentz forces) as a consequence of interaction between induced currents inside the reaction plate and the changing magnetic field. Due to the absence of permanent magnets no cogging effects are encountered [11]. However, the absence of permanent magnets results in a higher energy consumption [82] and lower force density as compared to reluctance and permanent magnet motors [37]. The fact that coils are moved, necessitates the use of trailing cables for supplying the mover which is detrimental to positioning accuracy. Swapping the roles of stator and mover is possible, but according to [11] of less advantage, because this leads to an increase of mover inertia, worsening the dynamic response.

Permanent magnet planar motors may be considered as the unrolled counterpart of rotatory DC-machines. Therefore, these motors are also referred to as planar Lorentz motors or brushless DC-motors, respectively [11]. Functioning on the principle of Lorentz' Law, these motors feature a relatively simple mechanical structure, comprising permanent magnet arrays in combination with properly oriented coils [57, 123,

136]. Thereby, magnets and coils may be integrated either in the stator or the mover, respectively [123].

Realizing the motor in a moving magnet formation, has the advantage that there are no moving cables [57, 123]. The driving coils, on the other hand, may be arranged either in a two-phase [35, 81] or a three-phase [22] formation, while the former one represents a minimal configuration [123]. Due to the presence of permanent magnets, these motors exhibit high force densities which allows for fast, dynamic positioning.

By virtue of the simple mechanical design of planar motors, in general, no mechanical transmission mechanisms such as gearboxes or belts are needed [135]. Moreover, for enabling a smooth, non-contacting guidance of the mover with respect to the transversal plane, most planar motors are equipped with air bearings [26, 35, 138]. All these measures provide near zero friction, no wear, high speed and high precision capabilities. Additionally, due to the non-contacting principle, the use of lubricants is rendered superfluous [136].

However, some applications, e.g. photolithographic processes in semiconductor manufacturing, require precise positioning in vacuum. In these cases, where air bearings are obviously not applicable, precision roller guide ways [151, 152] or magnetic levitation [22, 57, 87] is applied for guiding the mover. A major drawback of precision guide ways or roller bearings, respectively, is friction [152].

Since there is no mechanical transmission or guidance along the directions of motion, both, the induction motor and the permanent magnet motor must be operated in closed loop. For this purpose, position feedback must be provided by appropriate position sensors capable of providing very fine resolution. For long range motion of several meters and position resolutions in the submicrometer range, usually, high-grade analog optical encoders in conjunction with efficient interpolation schemes are applied [39, 135, 146]. For ultra precise measurements down to the subnanometer scale, the use of laser interferometers is inevitable [39]. Additionally, permanent magnet planar motors as presented in [35, 57, 81, 138] require a motor commutation law for feedback control.

The simple mechanical structure of planar motors enables the complete integration of sensors and actuators. This contributes to a compact and cost effective design. The high level of integration feature and the remarkable properties of these motors render them highly attractive for precision positioning applications of all kinds.

The recent trend in the development of planar precision positioning stages is towards designing lightweight systems. This trend is driven by the need of the semiconductor industry for faster and faster positioning stages for achieving an increase of throughput [60, 104, 105]. In the following, the present thesis focuses on permanent magnet planar motors.

1.1.2 Control of Planar Precision Positioning Systems

Although the absence of mechanical transmission and guiding systems is absolutely necessary for achieving precise and smooth positioning, this measure prevents self-locking mechanisms of the motor. This in fact renders the motor sensitive to disturbances and load changes and makes it inevitable to apply constant servo-control.

Disturbances are diverse and often arise from force ripples [135] originating from different sources. For instance, force ripple may occur as a consequence of modeling uncertainty in the commutation scheme of the motor [117], [57], asymmetries and offsets in power amplifiers [117], or magnetization effects of ferrous components in the traversing range, i.e. cogging/reluctance forces [135]. Moreover, positioning accuracy is challenged by high frequency current ripples due to PWM-power-amplifiers

[135], eddy current damping effects [123], spring force effects of air supply hoses and downhill-slope forces due to an inaccurate stator adjustment.

Other limiting factors include structural vibration [60, 114, 135], undesired coupling effects between motion axes as well as parameter variations caused by load changes and different ambient temperatures.

All these effects pose high challenges with regard to achieving the main requirement in the diverse applications of micro- and nanotechnology. That is, fast and precise tracking of complex path geometries and complex reference trajectories.

To cope with these problems many control approaches have been reported in the literature. For meeting the requirement on tracking, 2-DOF control architectures are widely used [27, 34]. These methods employ inversion based feedforward and feedback control. They have the advantage that feedforward and feedback may be designed independently of each other. For a detailed overview of the state-of-the-art on feedforward and tracking controller design we would like to refer to Section 4.1. Therefore, this section rather focuses on feedback schemes.

In this respect, a widely used standard in motion control is the P-PI controller implementing a PI controller for the inner velocity loop and a P controller for the outer position loop [149]. Although in practice these controllers show unsatisfactory steady state errors (see [149]), they are still used due to their simplicity.

PID controllers are ubiquitous in all kinds of motion control applications (see [13, 133, 136]), also in the context of planar permanent magnet motors (see e.g. [35, 136, 138]). For enhancing the disturbance rejection capabilities of PID controlled feedback loops, disturbance observers are applied. For instance, in [32] the authors use a linear disturbance observer, while in [35] a sliding mode observer is applied. In [135] a very complex composite control architecture with adaptive ripple compensation and other features is developed around a PID feedback loop.

Other popular approaches include $\mathcal{H}_\infty$ control [60, 105, 133] and iterative learning control (ILC) [99].

Viewed from an economic standpoint, concepts form adaptive control such as the famous *model reference adaptive control* (MRAC)[5, 71, 102] approach represent interesting alternatives to the controllers presented above. This is because these concepts are designed for identifying unknown parameters of a system during operation, while using these estimates for the parameterization of a controller to achieve desired closed loop performance. The desired dynamics of the closed loop system is thereby specified in terms of a reference model defined by the control engineer. The error between reference model and plant output is supplied to an adaptation law which adjusts the controller parameters, minimizing this error.

At best this reduces the effort of parameter identification of the system in question and also diminishes the expense of controller tuning.

The basic requirement for the application of these controllers is the knowledge of the fundamental structure of the system as well as the property that unknown parameters can be represented as linear combinations of known variables such as states or known nonlinearities.

For the fulfillment of the first requirement only once a detailed model is needed to ensure that the synthesis of an adaptive controller may be feasible. In general, the latter requirement is true for mechanical systems [131] and thus also applies to planar motors.

Despite this fact, it seems that MRAC based controllers are very rare in motion control applications. A recent, promising concept in this direction is $\mathcal{L}_1$ adaptive control [68]. $\mathcal{L}_1$ adaptive control basically originated as a modification from standard MRAC

(see e.g. [69]) and offers remarkable features. According to [68] this includes decoupling of the adaptation from the control loop and therefore arbitrarily fast adaptation with guaranteed transient performance. Moreover, a priori transient and steady state performance bounds may be computed, e.g. based on parameter intervals of uncertain parameters. Furthermore, the philosophy of $\mathcal{L}_1$ adaptive control is based on the understanding that uncertainties may only be compensated for in the achievable bandwidth of the control channel in order to avoid excitation of unmodeled high frequency dynamics [68]. This in fact poses a realistic control goal because any system exhibits unmodeled dynamics. For these reasons the approach seems ideal for motion control applications.

To the best of our knowledge the concept of $\mathcal{L}_1$ adaptive control has not yet arrived in the field of motion control. Moreover, only few papers employ $\mathcal{L}_1$ adaptive control for solving tracking tasks [15, 30, 96]. In [30] a backstepping approach for tracking the position of a quadrotor is combined with an $\mathcal{L}_1$ adaptive architecture. The authors in [96] extend an $\mathcal{L}_1$ adaptive set-point tracking controller by a nonlinear controller for reducing a time-lag between measured output and reference trajectory. Although the considered system appears to be flat, however, the authors do not use a feedforward for decreasing the time-lag.

In [15] a nonlinear dynamic inversion $\mathcal{L}_1$ controller is developed for a flight control system.

However, to the best of our knowledge the application of $\mathcal{L}_1$ adaptive control for solving tracking control problems for planar precision positioning systems has not been reported in the literature until now. Against this background, this thesis aims at filling this gap. For a more detailed overview on MRAC and $\mathcal{L}_1$ adaptive control schemes we would like to refer to Section 4.2.

1.2 Goals and Contributions of the Thesis

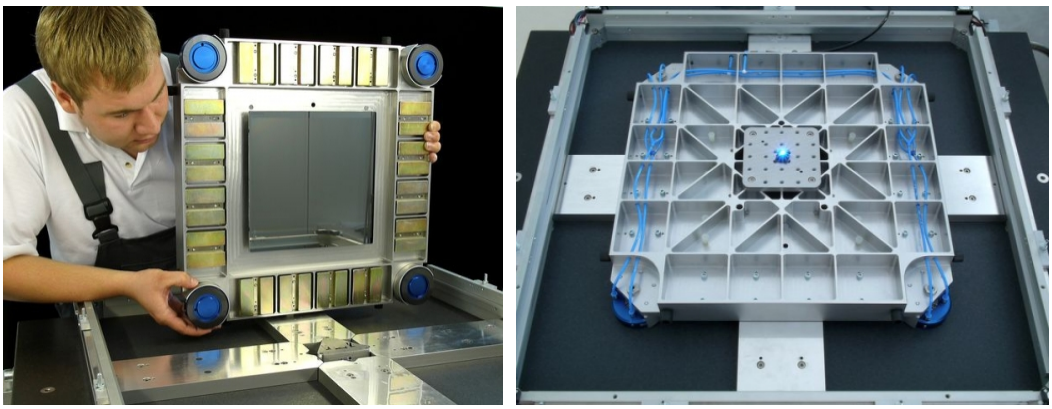

FIGURE 1.1: PPS2020 planar positioning system. Photos courtesy of Tetra, Germany.

This thesis is the outcome of an industrial research collaboration of Control Engineering Group TU-Ilmenau with the planar motor manufacturer Tetra GmbH Ilmenau.

The primarily goal of this collaboration is the design of an advanced motion control strategy for Tetra's commercial positioning system PPS2020. The PPS2020, shown in Figure 1.1, is a state-of-the-art, high precision, non-contact planar motor with 3 DOF.

It is used for precision machining applications such as laser cutting and serves as a microfabrication tool for the fabrication of tissue engineering scaffolds and other three-dimensional structures $\geq 400\,\mathrm{nm}$, based on the technology of micro-stereolithography.

These applications require fast and precise tracking of complex path geometries and complex reference trajectories with positioning errors below $1\,\mu\mathrm{m}$. However, positioning accuracy is highly challenged by external disturbances and structural vibration as exposed above.

The manufacturer recognized that existing industrial standard motion controllers that have been used up to now, are not able to track reference trajectories with sufficient precision.

Therefore, the manufacturer is interested in a new motion control architecture that provides tracking with highest precision and a fair amount of disturbance rejection qualities. For economic reasons it is desired that the effort of controller tuning is reduced. This imposes the requirement that the majority of controller parameters may be parameterized by means of a priori known plant parameters and tuning of the remaining controller gains follow certain systematics. By virtue of the fact that a priori known parameters may be uncertain to some extend, it is desired that the controller possesses a learning component and adapts to parametric uncertainties during operation without sacrificing performance.

For meeting these challenging requirements, we consider a two-stage model-based control design approach. Namely, for addressing the requirement of a priori parameterization and systematic design, in the first stage, a nominal LQR/LQG type tracking controller is derived, showing perfect tracking under ideal conditions. For the rejection of parametric uncertainty and recovery of nominal performance, in the second stage, an adaptive augmentation of the nominal design is applied. In particular, for the adaptive part, the recent methodology of $\mathcal{L}_1$ adaptive control is applied in view of its outstanding performance and robustness properties. The two step approach has the advantage that better plant knowledge, that may be available at a later time, may straightforwardly be incorporated within the nominal design for improving performance.

Since the foundation of any model-based control design approach is represented by an adequate model, the first contribution of this thesis is the development of a detailed model including the relevant components of planar positioning systems. Owing to the fact that the literature on $\mathcal{L}_1$ adaptive control mainly focuses on regulation rather then tracking problems, this work contributes to a systematic extension of $\mathcal{L}_1$ regulation schemes to also solve tracking problems. Finally, we contribute to a transition of $\mathcal{L}_1$ adaptive control into motion control practice and evaluate the suitability of the proposed approach by experimental results.

1.3 Organization of the Thesis

This thesis is organized in six Chapters. Following the introduction, Chapter 2 introduces the experimental motion stage system. Here, all the relevant components such as mechanical construction, sensors, actuators and real-time environment are described in detail.

Chapter 3 is dedicated to modeling the stage. Using a physical modeling approach, we derive and identify models for the actuator dynamics and the mechanical part of the stage. We further investigate possible sources of disturbances and propose phenomenological models for their description. The model derived serves well as a realistic simulation environment for the design and the assessment of advanced control

strategies. Based on the analysis of these models, we address fundamental performance limitations attributed to these machines and deduce specifications for controller design.

In Chapter 4, model based tracking controller design is presented. Thereby, following the aspired two step approach, we address the design of full-state and output feedback based nominal and $\mathcal{L}_1$ adaptive tracking controllers. Finally, for achieving a successful transition into practice, implementation issues such as windup modifications, controller order reduction and numerical problems are addressed.

In Chapter 5, the effectiveness of the proposed schemes is verified by measurements conducted at the test rig. Moreover, the achieved performance is compared to existing controllers and the results are discussed.

Finally, Chapter 6 concludes this thesis and lists recommendations for future research.

Chapter 2

Introduction of Planar Motion Stage

The main focus of this thesis lies on the design of sophisticated, robust and adaptive motion controllers for high precision, planar positioning systems. In order to test and evaluate the derived control algorithms under realistic conditions we use TETRA's electrodynamic, planar positioning system PPS1405 [137] as an experimentation and validation/verification platform. A sketch of the platform is shown in Figure 2.1.

The following chapter is dedicated to providing a brief introduction to the basic design and operation principles of the PPS1405 planar motion stage. First, we will give a general description of the mechanical design and the actuation principles. Following the definition of a typical control task, we provide general such as technical details concerning the sensors and actuators applied and finally present a description of the real-time environment, respectively.

2.1 General System Description & Operation Principle

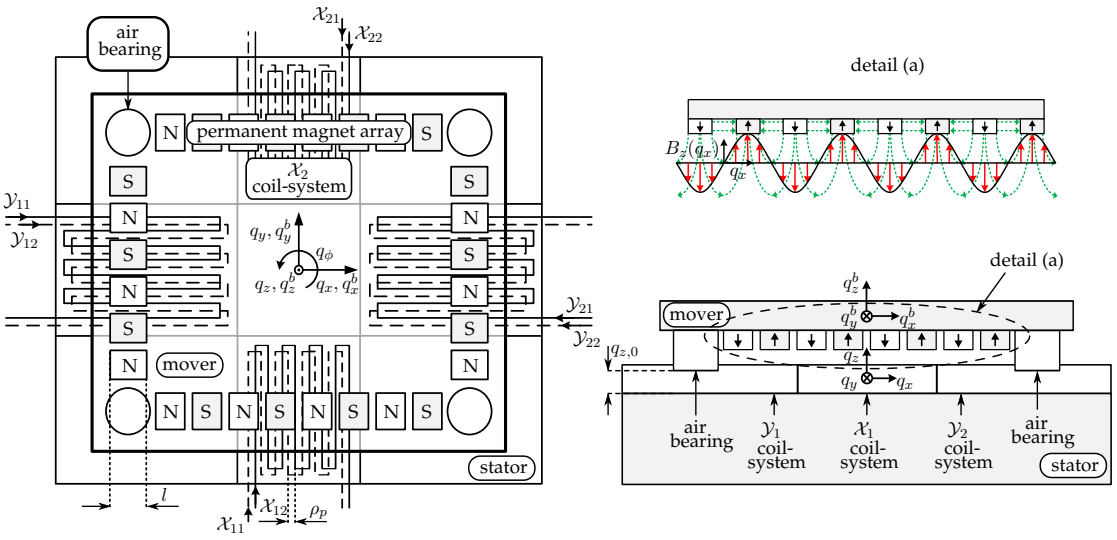

FIGURE 2.1: Top view of motion stage (left), side view of $\mathcal{X}_1$-permanent magnet array (PMA) (top right) with magnetic field lines (green), vertical vector components of the flux density (red) and sinusoidal magnitude of the vertical vector components (black). Side view of motion stage (bottom right).

The PPS1405 positioning system is a small scale prototype of the PPS2020 [137] a commercially available motion system built by the motor manufacturer TETRA (see Figure 1.1). It is a directly driven Lorentz motor of linear, non-contact, DC brushless type and

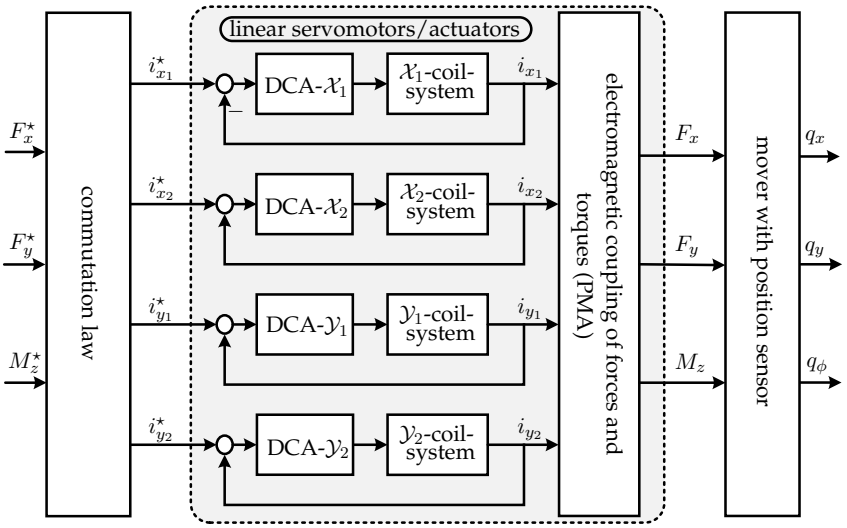

FIGURE 2.2: Signal flow diagram of the motion stage.

similar to those presented in [26, 32, 35, 45, 138]. A sketch of the motion stage is illustrated in Figure 2.1. The stage essentially consists of a passive moving element, the so-called mover, and an active non moving part, the stator.

Roughly speaking, a rigid aluminum plate constitutes the mover that may be positioned in 3 DOF in the plane: two translational q_x, q_y and one rotational q_ϕ (cf. Figure 2.1). It is equipped with permanent magnet arrays, hence passive, and guided by pressurized air employing aerostatic suspension bearings. The advantages of using an aerostatic guiding system have been discussed in detail in Section 1.1.1.

The stator part of the machine is a massive base unit made of granite. It comprises four permanently fixed two-phase-coil-systems arranged in a crosswise manner.

If current is applied to the coils due to the special construction the current flows perpendicular with respect to the magnetic field of the permanent magnets. Consequently and in accordance with Lorentz' law the forces and torques (F_x, F_y, M_z) are exerted on the mover accelerating it along its motion-axes (q_x, q_y, q_ϕ) (see Figure 2.2). The forces and torques are proportional to the current applied and act perpendicular with respect to the direction of current flow as well as perpendicular to the magnetic field direction.

In order to control the phase currents considered as control inputs four PWM two-phase digital current amplifiers (DCAs) are employed as servo-amplifiers for the corresponding two-phase-coil-systems (cf. Figure 2.2). Intuitively a combination of a permanent magnet array and a coil can be regarded as a linear motor. Combining the latter with a current amplifier resembles a linear servomotor.

The mover's motion is described in an inertial coordinate frame (i-frame) (q_x, q_y, q_z) located at the center of the stator surface and a body-fixed frame (b-frame) (q_x^b, q_y^b, q_z^b) coincident with the center of gravity (CG) and the principle axes of rotation (Figure 2.1). The position coordinates q_x and q_y of the mover's center of gravity and its yaw angle q_ϕ are measured with an integrated optical, incremental sensor underneath the mover (see Section 2.2 for a detailed description).

Please note that the architecture described above is widely used and similar to other motors reported in the literature (see e.g. [26, 32, 35, 45, 81, 138]).

For clarity of presentation, we denote the elements of the four linear servomotors that produce thrust forces in the q_x- and q_y-directions by $\mathcal{X}_i$ and $\mathcal{Y}_i$, respectively, where $i = 1, 2$ serves as system index (c.f. Figures 2.1 and 2.2). Note that the motors $(\mathcal{X}_1, \mathcal{X}_2)$

such as $(\mathcal{Y}_1, \mathcal{Y}_2)$ oppose each other. Usually the linear servomotor pair $(\mathcal{X}_1, \mathcal{X}_2)$ is driven simultaneously in order to achieve symmetric movement in the direction of q_x. The same applies to the servomotors $(\mathcal{Y}_1, \mathcal{Y}_2)$. The index $j = 1, 2$ in $\mathcal{X}_{ij}$ and $\mathcal{Y}_{ij}$ is to represent the j-th phase of the i-th servomotor, coil-system or DCA. Accordingly, the eight real-valued scalar coil phase currents are expressed by $i_{x_{ij}}(t)$ and $i_{y_{ij}}(t)$. They are measured and driven to the desired references $i^\star_{x_{ij}}(t)$ and $i^\star_{y_{ij}}(t)$ by the DCAs (cf. Figure 2.2). For a more compact notation we introduce the vectors

$$i_{x_1}(t) = \begin{pmatrix} i_{x_{11}}(t) \\ i_{x_{12}}(t) \end{pmatrix} \quad i_{x_2}(t) = \begin{pmatrix} i_{x_{21}}(t) \\ i_{x_{22}}(t) \end{pmatrix} \quad i_{y_1}(t) = \begin{pmatrix} i_{y_{11}}(t) \\ i_{y_{12}}(t) \end{pmatrix} \quad i_{y_2}(t) = \begin{pmatrix} i_{y_{21}}(t) \\ i_{y_{22}}(t) \end{pmatrix}$$
$$i^\star_{x_1}(t) = \begin{pmatrix} i^\star_{x_{11}}(t) \\ i^\star_{x_{12}}(t) \end{pmatrix} \quad i^\star_{x_2}(t) = \begin{pmatrix} i^\star_{x_{21}}(t) \\ i^\star_{x_{22}}(t) \end{pmatrix} \quad i^\star_{y_1}(t) = \begin{pmatrix} i^\star_{y_{11}}(t) \\ i^\star_{y_{12}}(t) \end{pmatrix} \quad i^\star_{y_2}(t) = \begin{pmatrix} i^\star_{y_{21}}(t) \\ i^\star_{y_{22}}(t) \end{pmatrix}$$

for the measured and reference currents of the four coil/DCA-systems such as the vectors for the total currents given by

$$i^\star(t) = \begin{pmatrix} {i^\star_{x_1}}^{\mathrm{T}}(t) & {i^\star_{x_2}}^{\mathrm{T}}(t) & {i^\star_{y_1}}^{\mathrm{T}}(t) & {i^\star_{y_2}}^{\mathrm{T}}(t) \end{pmatrix}^{\mathrm{T}} \in \mathbb{R}^8 \tag{2.1}$$
$$i(t) = \begin{pmatrix} {i_{x_1}}^{\mathrm{T}}(t) & {i_{x_2}}^{\mathrm{T}}(t) & {i_{y_1}}^{\mathrm{T}}(t) & {i_{y_2}}^{\mathrm{T}}(t) \end{pmatrix}^{\mathrm{T}} \in \mathbb{R}^8. \tag{2.2}$$

The forces caused by the dedicated currents $i_{x_{ij}}(t)$ and $i_{y_{ij}}(t)$ are denoted by $F_{x_{ij}}(t)$ und $F_{y_{ij}}(t)$. Further, let

$$q(t) = \begin{pmatrix} q_x(t) \\ q_y(t) \\ q_\phi(t) \end{pmatrix} \in \mathbb{R}^3 \quad q^\star(t) = \begin{pmatrix} q^\star_x(t) \\ q^\star_y(t) \\ q^\star_\phi(t) \end{pmatrix} \in \mathbb{R}^3 \tag{2.3}$$

be the generalized state coordinates and

$$\tau(t) = \begin{pmatrix} F_x(t) \\ F_y(t) \\ M_z(t) \end{pmatrix} \in \mathbb{R}^3 \quad \tau^\star(t) = \begin{pmatrix} F^\star_x(t) \\ F^\star_y(t) \\ M^\star_z(t) \end{pmatrix} \in \mathbb{R}^3$$

the generalized forces and torques. Quantities with superscript $\star$ represent desired references.

Figure 2.2 illustrates a typical control task. Here usually the aim is to specify/devise a suitable input $\tau^\star(t)$ for the generalized forces $\tau(t)$ on the mover such that its position $q(t)$ tracks a desired reference trajectory $q^\star(t)$ as best as possible. A motor commutation law as illustrated in the leftmost block of Figure 2.2 maps the desired reference $\tau^\star(t)$ to the corresponding phase current reference $i^\star(t)$. The subsequent current control loop of the DCAs aims at driving $i(t)$ to the reference $i^\star(t)$. Through the electromagnetic coupling of forces and from $i(t) \to i^\star(t)$ we have $\tau(t) \to \tau^\star(t)$, thus $q(t) \to q^\star(t)$, as desired. The problem of finding such an input $\tau^\star(t)$ is referred to as a (trajectory) tracking control problem or servo problem.

Remark 2.1.1. Before we go on with the subsequent sections, we shall briefly digress for commenting on the notation used throughout the thesis. By virtue of the fact that the established standard notation for electromagnetic field theory and systems theory share some important symbols, we will use the following notation for an appropriate distinction between the respective variables. For the field theoretic part of the thesis, we will indicate vectors and vector valued functions by the standard $\vec{(\cdot)}$-notation. On

the other hand, as common, in the systems theoretic parts of the thesis we will drop the $\vec{(\cdot)}$-notation and state explicitly the dimensions of vectors and matrices, as already done above.

2.2 Sensor System

For measuring the positions q_x, q_y and yaw angle q_ϕ with sufficient precision, the LIK-2D [50], a two dimensional, linear optical encoder from Numerik Jena is used. It operates on the non-contacting principle of photoelectric [146] or imaging scanning [49] and is of incremental type. Thus, loosely speaking, a relative position measurement is obtained by simply counting position increments.

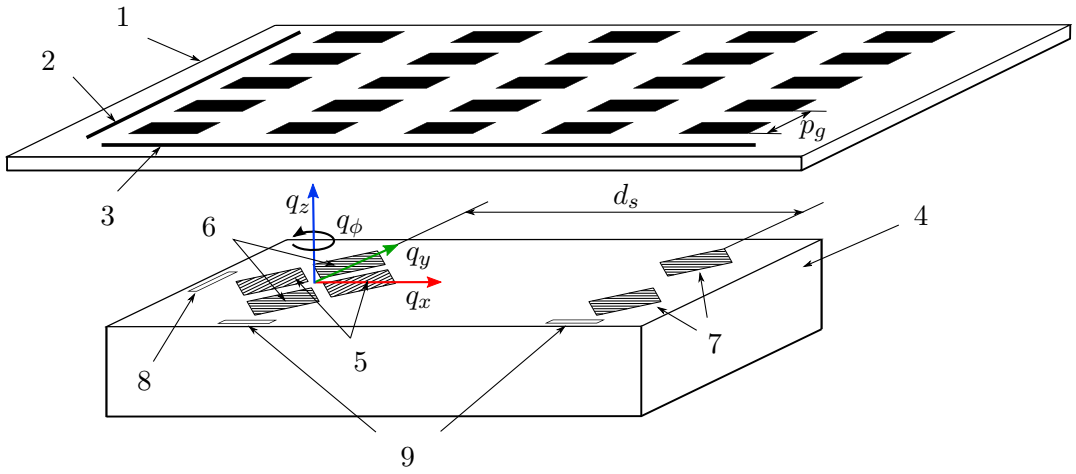

1 reference scale	4 scanning head	7 scanning unit q_y-axis (y_2)
2 reference mark q_x-axis	5 scanning unit q_x-axis	8 reference sensor q_x-axis
3 reference mark q_y-axis	6 scanning unit q_y-axis (y_1)	9 reference sensors q_y-axis

FIGURE 2.3: Scheme of the linear, optical encoder LIK-2D.

2.2.1 Sensor Construction

Essentially, the sensor system comprises a photoelectric scanning head and a reference scale. An illustration of the measurement system is shown in Figure 2.3. The reference scale (1) is a glass grid plate with reflective and non-reflective zones. A particular grating pitch p_g and the size of the scale determine the nominal resolution of the sensor and its measuring range, respectively.

Due to the incremental measuring principle, the sensor can only provide relative position information (counts) with respect to an arbitrarily chosen zero position. In order to obtain an absolute position coordinate, as required in most applications, the scale is equipped with additional reference marks $(2, 3)$ with known absolute position. In the case of the LIK-2D, the reference marks indicate the beginning of the measuring range [50]. Hence, based on the detection and the respective values of these marks, we can calculate an arbitrary zero position from which absolute positioning is possible. To do so, an initial reference movement to the respective reference marks is required. This is known as the so-called homing procedure.

Furthermore, the scanning head (4) may be subdivided into six sensor elements. That is, three reference sensors $(8, 9)$ dedicated to detecting the previously mentioned reference marks and three scanning units $(5, 6, 7)$ for measuring the positions in the q_x and q_y directions. For the detection of yawing motion, along the q_y axis, two positions, i.e. y_1 (6) and y_2 (7), are measured. The yaw angle q_ϕ is simply computed as per

$$q_\phi = \arctan\left(\frac{y_1 - y_2}{d_s}\right). \tag{2.4}$$

Therein, variable d_s denotes the distance between the y_1 and the y_2 sensor elements (c.f. Figure 2.3).

Each of the three scanning units $(5, 6, 7)$ consists of an LED light source, an array of photovoltaic cells (photodetector) and a light shutter—the so-called scanning reticle. The scanning reticle basically constitutes a plate with multiple and equally spaced, translucent slits that have the same or a similar pitch as the reference scale [49]. For gaining higher accuracy, in some cases, the Moiré effect is exploited [39, 97] by performing a slight rotation of the scanning reticle with respect to the reference scale [97].

2.2.2 Measurement Principle

According to references [39, 49, 146], the basic operation of an optical encoder in one dimension is as follows. The light source of the scanning unit emits light that is transmitted through the scanning reticle. Due to reflective and non-reflective patterns on the scale, the light is selectively reflected back onto the photocells. If the scale moves relative to the scanning head, the photocells receive light with modulated intensity and convert it into electrical signals. These output signals are approximately sinusoidal.

Additional, external signal conditioning electronics convert these signals into analog, DC-free sine and cosine waves providing both position and directional information. The traveled distance of the scale relative to the reticle is hence, the product of the grating pitch and the number of passed intensity peaks of the sinusoidal output signal. Consequently, the resolution of the position increment is equal to the grating pitch.

For obtaining even higher position resolution, i.e. smaller position increments, in addition to the exploitation of the Moiré effect, sophisticated digital interpolation methods are used (see e.g. [146]). The position increment received from the interpolation circuit is an integer multiple of the grating pitch and typically of a factor up to 1024 [146]. Eventually, the desired displacement information is obtained by counting these increments.

2.2.3 Technical Details and Remarks

In the design of the PPS1405 the location of the scanning head and the scale is selected such that unnecessary cabling of the moving element is avoided. Therefore, the reference scale is placed underneath the mover, while the sensor head is embedded within the center of the stator plate. Asides the advantages of the non-contacting measurement principle, i.e. frictionless motion and no wear, this particular design prevents adverse effects on the mover dynamics related to external wiring of the mover e.g. via trailing cables as exposed in [57, 97, 123]. Moreover, due to the special sensor placement, the distance between the measured position and the actual workpiece is very small. All these measures turn out advantageous with respect to position accuracy.

Eventually, Table 2.1 summarizes the most significant technical parameters of the applied sensor system that we briefly comment in the following lines: The reference

reference scale	material	glass, thickness $1.1\,\mathrm{mm}$
	grating pitch	$20\,\mu\mathrm{m}$
	measuring range (linear)	$140\,\mathrm{mm} \times 50\,\mathrm{mm}$
	measuring range (angular)	$\pm 0.25^\circ$
	position of reference marks	beginning of measuring range
scanning head	max scanning freq. (bandwidth)	$500\,\mathrm{kHz}$
	freq. of evaluation circuit	$10\,\mathrm{MHz}$
	interpolation factor	8192
	resolution after interpolation	$2.44\,\mathrm{nm}$
	max traversing speed	$10\,\mathrm{m\,s^{-1}}$
	communication interface	EtherCAT slave

TABLE 2.1: Technical data of the position sensor, partially adopted from [50].

scale is custom built by Compugrafics (Jena/Maua). It exhibits a grating pitch of $20\,\mu\mathrm{m}$ and a measuring rang of $140\,\mathrm{mm} \times 50\,\mathrm{mm}$.

A crucial parameter, especially in an automatic control related context, is the maximum scanning frequency of the sensor head. In fact, this parameter is related to the frequency response of the sensor and corresponds to the maximum attainable bandwidth at which it can provide reliable measurements. Typically, the bandwidth is limited by the frequency response of the photodetectors. According to [50] the maximum scanning frequency of the LIK-2D is given by $500\,\mathrm{kHz}$. Since the internal interpolation schemes of the LIK-2D limit the attainable bandwidth of the position signal, the bare LIK-2D encoder head is used without internal interpolation. Instead, its analog sine/cosine outputs are used directly and combined with a custom-designed evaluation/interpolation circuit. The latter runs on an FPGA with a sample rate of $10\,\mathrm{MHz}$ and provides a position increment of $2.44\,\mathrm{nm}$, i.e. an interpolation of factor 8192. It outputs a 32 bit position value at the same sampling rate. Therewith, the entire bandwidth of $500\,\mathrm{kHz}$ is exploited enabling the perception of maximum traversing speeds up to $10\,\mathrm{m\,s^{-1}}$. Additionally, the sensor is endowed with an EtherCAT slave interface providing real-time communication with the controller hardware (see 2.4).

2.3 Actuator System

The actuation of the motion stage is achieved by means of four linear permanent magnet servomotors. As exposed in Section 2.1, the individual motors are directly integrated within the mechanical structure of the PPS1405. It is this high level of integration feature and a fair amount of other remarkable properties (see Section 1.1.1) that make these motors attractive to high performance motion control applications.

2.3.1 Actuator Construction

Intuitively, the stage as a whole or similarly each of the linear motors can be seen as an electromechanical transducer, converting electrical into mechanical energy and vice versa. Such devices generally consist of the following basic construction elements: [44]

- electrical drive circuitry

- electromechanical coupling mechanism
- mechanical subsystem

For the sake of simplicity, let us consider an individual $\mathcal{X}_1$ linear servomotor element as depicted in Figure 2.4. The Figure presents a simplified representation of the $\mathcal{X}_1$ linear motor, in side view (a), and top view (b).

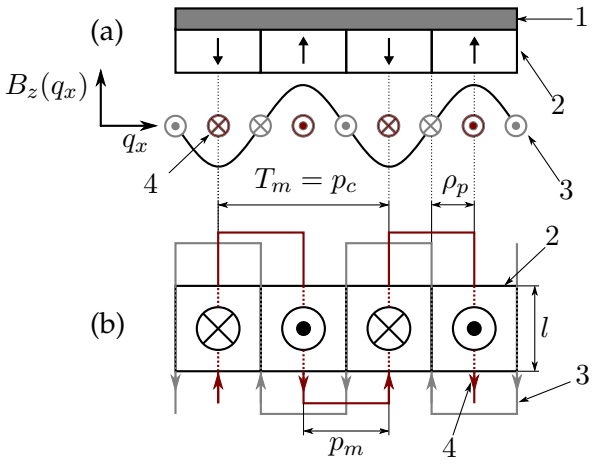

1 back-iron plate	3 $\mathcal{X}_{11}$ phase of $\mathcal{X}_1$-coil
2 permanent magnet array	4 $\mathcal{X}_{12}$ phase of $\mathcal{X}_1$-coil

FIGURE 2.4: Simplified representation of the $\mathcal{X}_1$ linear motor. (a) side view of the construction and (b) top view.

Therein, a two-phase coil system $(3, 4)$ together with a dedicated two-phase current amplifier (not shown), forms the electrical drive circuitry. This circuit supplies the electromechanical system with currents, representing the control inputs.

As a special feature of the PPS1405 such a coil system is built in a planar, printed circuit board (PCB) construction, similar to the coils presented in [82]. This special formation of coils can be imagined as a stack of multiple, alternating circuit board layers, where each layer carries (in alternate sequence) through plated, meandering copper traces, representing the respective inductances of the phases, shaping the coil. For the correct functioning of the motor, the two phases are shifted with respect to each other by an amount ρ_p. This is referred to as phase pitch (cf. Figure 2.4). Owing to that shift, the individual phases of the coil overlap, why this construction of coils is also referred to as *overlapped two-phase planar coil formation* [82].

The advantages of planar PCB coils can be summarized as follows. Due to the simple construction, these coils are easily fabricated. This in turn results in greater flexibility regarding the geometry and shapes of the coils. Due to the absence of a core, planar coils exhibit reduced overall geometric dimensions and thus allow for better miniaturization [82]. Hence, they enable a cost-effective and compact motor design with fewer components and faster assembly.

However, a downside of the planar coil formation is the overall reduction of electromagnetic forces that can be attributed to the absence of a core. Moreover, as a consequence of the overlapping of phases, there is crosstalk between the phases. This effect is based on the mutual induction that takes place when a current is applied to either phases. We elaborate more on these effects and its mathematical description in Sections A and 3.1.2.

individual magnet geometry	width	6.6 mm
	depth	50 mm
	height	8 mm
array	distance of adjacent magnets	4.1 mm
back-iron	depth	50 mm
	height/thickness	10 mm

TABLE 2.2: Geometrical dimensions of the permanent magnet array.

The second element of the electrical drive circuitry is the switched power amplifier (Tetra's TEAM AC1) operating in current mode [10]. For achieving efficient bipolar operation of the linear motor, the amplifier is realized in an H-bridge configuration. Thereby, the coil is placed inside the H-bridge circuit, while the latter is directly driven by a digital PWM circuit/module. Due to the rapidly switching voltage, with frequencies up to 200 kHz, at the input of the coil, an average current flow through the coil can be accomplished. Thereby, the amplitude of the current depends on the duty cycle (pulse width) of the PWM signal. The latter is controlled by the pulse width modulated output of a discrete time proportional integral current controller. For a better smoothing of the PWM signal, a reduction of current ripple such as an enhanced electromagnetic compatibility (EMC), before and after the driving coil, chokes with additional snubber circuits are installed. The current measurement needed for control is measured via the voltage drop over a shunt or so-called sensing resistor [10].

The functional counterpart to the electrical driving circuit constitutes the electromechanical coupling mechanism. In particular, the coupling mechanism is represented by the permanent magnet array located above the driving coil as shown in Figure 2.4.

Due to the long traversing range of these motors, the permanent magnet arrays are designed for exhibiting a distinct sinusoidal magnetic field distribution (see Figure 2.4 (a)). The reason for this is the ease of electronic commutation and control of the motor.

In order to accomplish a periodicity of $T_m = 2p_m$ of the magnetic field, the permanent magnet array is constructed of independent, parallel aligned, rectangular magnets exhibiting a magnet pitch of p_m (see Figure 2.4). Furthermore, the magnets have all the same geometrical dimension (see Table 2.2) but an alternating polarity, optimized for meeting the sinusoidal relationship. That means that the magnetization of two adjacent magnets are equal in magnitude, but opposite in direction [57]. This fact is indicated by the arrows in Figure 2.4 (a). This particular arrangement is known as north-south (NS) configuration which is the one encountered in the PPS1405. Another popular approach for the layout of permanent magnet arrays is the famous approach by Halbach [56, 57, 82]. However, according to reference [82] such an Halbach array is much more complicated to manufacture compared to the simple NS configuration.

Additionally, the magnets are attached to a back-iron plate. This measure provides an increase in magnetic field strength and thus results in higher force densities. Since the back-iron is magnetized by the magnets inside the array, its thickness must be dimensioned such that magnetic saturation effects are prevented. For a reduction of the weight of the mobile part however, the back-iron should be as thin as possible.

Due to the challenging problems encountered in the design of such an array, the design process is usually accompanied with finite element methods.

Finally, the mechanical subsystem is the permanent magnet array itself, or the mover, in the case of the complete motion stage system. This completes the construction of the motor.

2.3.2 Working Principle

The electromechanical coupling mechanism is based on the fact that current carrying wires exposed to an external magnetic field experience forces, known as Lorentz forces. As exposed in Appendix A in much more detail, these forces are proportional to the current I applied and proportional to the length l of the wire inside the magnetic field $\vec{B}$. Moreover, they act perpendicular with respect to the direction of current flow as well as perpendicular to the magnetic field direction, that is

$$\vec{F} = I\vec{l} \times \vec{B}. \tag{2.5}$$

To explain the operation principle of linear or planar actuators, consider Figure 2.5 illustrating a simple example on how a translational motion of such actuators might be achieved.

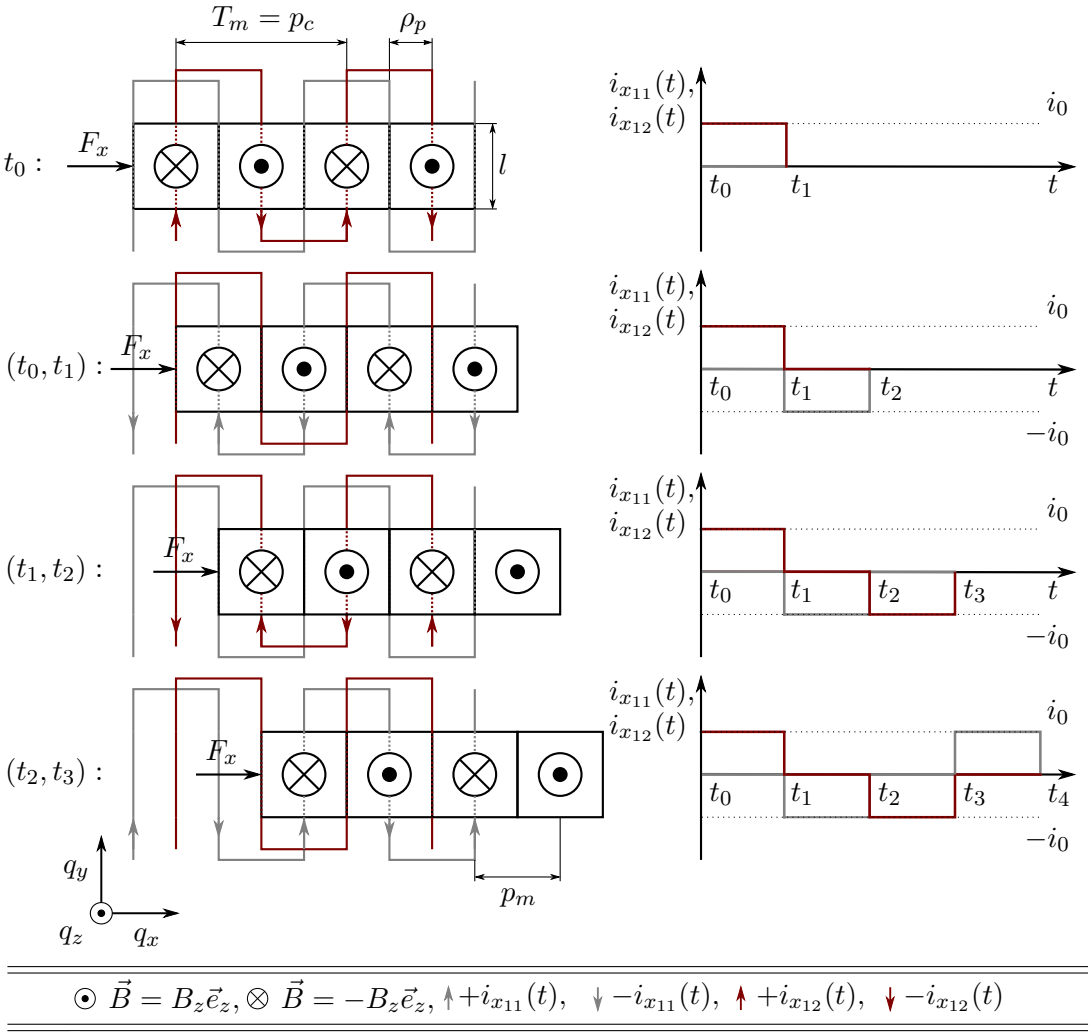

FIGURE 2.5: Working principle of a linear or planar motor and the role of current commutation.

In the spirit of Figure 2.4 (b), Figure 2.5 presents the $\mathcal{X}_1$ linear motor in top view. Also, the individual phases, i.e. $\mathcal{X}_{11}$ and $\mathcal{X}_{12}$, are indicated in gray and red, respectively. For the correct operation over long traversing ranges it is essential that the coil pitch p_c is equal to the magnet period T_m. This ensures the alignment of the peak current amplitude with the peak magnetic flux density [82]. Additionally, the phases must encounter a relative phase shift ρ_p with respect to the magnet period, that is $\rho_p = T_m/4$. In the case of a sinusoidal flux density distribution this corresponds to a relative phase shift of $\pi/2$.

The left hand side of Figure 2.5 illustrates a discrete motion of the magnetic circuit as a result of Lorentz forces. The motion is depicted at different instances in time, taking place when the respective current profiles (shown on the right) are applied.

For the sake of exposition, let us naively apply constant currents to either phase and observe the resulting motion. To this end, let us first consider the current profile $(i_{x_{11}}(t), i_{x_{12}}(t)) = (0, i_0)$ for $t \in [t_0, t_1)$ and let us start at an initial position of $q_x = 0$. Taking further the fact into account that each magnet has its one force contribution, the total Lorentz force acting on the coil is given by

$$\vec{F}_L = -4i_0 l B_z (\vec{e}_y \times \vec{e}_z) = -4i_0 l B_z \vec{e}_x. \tag{2.6}$$

By virtue of the fact that the coil is rigidly attached to a massive stator base, a reaction force of opposite sign, i.e.

$$F_x = 4i_0 l B_z, \tag{2.7}$$

is imparted on the permanent magnet array. The latter is thus accelerated along the positive q_x direction which, obviously, results in a displacement of the array, with the array settling at a position of $q_x = \rho_p$. Then, at the near end of the time interval (t_0, t_1) phase $\mathcal{X}_{11}$ of the driving coil will be perfectly aligned with the centerlines of the individual magnets. Please note that for $(i_{x_{11}}, i_{x_{12}}) = (0, i_0)$ on the considered time interval position $q_x = \rho_p$ constitutes an equilibrium point because it represents a zero crossing of the flux density distribution resulting in a zero net force at that point (see Figure 2.4 (a)). The changes in sign of the flux density distribution before and after the zero lead to corresponding forces that attract the mobile part exactly to that zero.

Starting now from position $q_x = \rho_p$, at time t_1 we must set $(i_{x_{11}}, i_{x_{12}}) = (-i_0, 0)$ in order to achieve the same force/motion as in the first case. Then, on $t \in (t_1, t_2)$ the array is consequently driven to $q_x = 2\rho_p$.

This can analogously be extended for the intervals (t_2, t_3) and (t_3, t_4) (not shown on the left), where respectively the currents $(i_{x_{11}}, i_{x_{12}}) = (0, -i_0)$ and $(i_{x_{11}}, i_{x_{12}}) = (i_0, 0)$ must be applied for achieving a translational motion in the same direction. The only difference for these cases is the fact that $F_x = 3i_0 B_z$ due to a less number of wires exposed to the magnetic field. From this we can conclude that for obtaining a uniform force distribution over long traversing ranges, magnet arrays must be sufficiently long, such that the coil is completely exposed to the magnetic field. Similarly, the coils should be long enough such that end effects can be neglected.

Another important conclusion that can be drawn from this example is the fact that continuous translational motion is only possible if and only if the currents alternate in (coil) phases and in sign. And this, in dependence of the actual position of the mobile part. This underlines the need for an appropriate allocation strategy for the proper distribution of currents to the respective coil phases. Such a strategy is known as commutation law. Indeed, it is easy to see that without a commutation of currents the

motor will get stuck at the zero crossings of the flux density distribution. That is exactly the point in the middle of two neighboring magnets. In fact, this is the reason why a minimum of two phases per coil are necessary for achieving a proper motion.

Please note that the current profiles from Figure 2.5 were chosen for the purpose of illustration only. They do not represent the correct commutation for the motor. Actually, with these current profiles the motor „jumps“ between the zero crossings of the field distribution of the individual magnets. However, once the magnetic field distribution along the translational axes is known a commutation law can be derived that provides a homogeneous force distribution and thus enables smooth, continuous motion. This will be treated in Section 3.1.3.

Moreover, we find that due to the special construction, it is the vertical magnetic field component that is crucial for the generation of translational forces. Thus, the geometrical dimensions of the magnet arrays are mainly optimized for shaping the vertical component to a pure sinusoid. Note, however, that also other field components result in forces. This is evident from the vector product of the Lorentz force equation.

For instance, consider a component of the magnetic field $B_x\vec{e}_x$ along q_x. Obviously, for currents flowing in the direction of q_y this component gives rise to a vertical (levitation) force. As long as coils are sufficiently long with respect to the magnet width l, a component $B_y\vec{e}_y$ of the field would exhibit zero force contribution since it is in parallel with the current flow.

Integrating a set of four linear actuators in a mechanical structure as shown in Figure 2.1, results in a planar actuator, providing motion in the (q_x, q_y)-plane including a small yawing motion q_ϕ.

2.3.3 Technical Details and Remarks

Table 2.3 summarizes the most important technical parameters of the planar actuator.

Note that an important advantage of planar actuators is their integrated design allowing the placement of sensors and actuators close to the center of gravity of the moving mass. According to reference [114], this helps minimizing guiding system flexibilities (rocking modes) which is beneficial for control and the positioning precision of the drive. Also, following the same reference, due to the fact that coils are rigidly attached to the massive stator base, this increases the inertia of the actuator with respect to the mover, such that actuator flexibilities are minimized equally. Additionally, the placement of the sensor head on the same side as the driving coils as in the PPS1405 results in a so-called colocated sensor-actuator configuration. This particular arrangement is preferable from a control theoretic point of view because it is easy to stabilize and easy to robustify [114]. In particular, a colocated system is always minimum phase which is also favorable in view of tracking control and feedforward design. On the other hand, non-colocated sensor-actuator pairs, where sensors and actuators are placed on different locations, can result in non-minimum phase systems complicating robust tracking controller design.

2.4 Real-Time Environment

The basic architecture of the real-time environment is illustrated in the block diagram in Figure 2.6. For compliance with international automation standards and for the sake of scalability such as modular expandability of the drive, sensors and actuators of the

permanent magnet arrays (PMAs)	material	NdFeB
	remanence	1.2 T-1.5 T
	magnet period	$21.4\,\mathrm{mm}$
	number of periods q_x	11
	number of periods q_y	7
	flux density distribution	harmonic/sinusoidal
coil-systems	construction	planar (PCB)
	number of phases per coil	2
digital current amplifiers (DCAs)	operation principle	PWM
	PWM carrier frequency	$200\,\mathrm{kHz}$
	PWM-voltage	$24\,\mathrm{V}$
	reference current input	16 bit int ($\pm 2^{15}$ digit)
	output current range	$\pm 3\,\mathrm{A}$
	communication interface	EtherCAT
linear servomotor	force constant per coil	$1.6\,\mathrm{N\,A^{-1}}$
	maximum force per coil	$4.8\,\mathrm{N}$
	positioning range q_x	$\pm 70\,\mathrm{mm}$
	positioning range q_y	$\pm 25\,\mathrm{mm}$
	maximum velocity	$50\,\mathrm{mm\,s^{-1}}$

TABLE 2.3: Technical data of the actuator system.

PPS1405 are conceived as EtherCAT slave devices. EtherCAT (*Ethernet for Control Automation Technology*) is an Ethernet-based fieldbus technology initiated by the Beckhoff Automation company. The fieldbus is especially designed for hard and soft real-time requirements with short cycle times ($\leq 100\,\mu\mathrm{s}$) and precise synchronization ($\leq 1\,\mu\mathrm{s}$), essential for motion control applications. The EtherCAT technology basically works on the master/slave communication principle.

The master device, in this respect, is typically constituted by an embedded-PC or a PLC. In particular, on the motion stage platform a CX2040 embedded-PC from Beckhoff Automation is applied (see Figure 2.6). It runs the entire motion control software at a sampling time of $125\,\mu\mathrm{s}$ and communicates with the slave devices, i.e. the sensors and actuators, via EtherCAT. As a special feature of the EtherCAT technology, the entire communication network can be addressed within one frame. This is possible because the slave devices read the data and processes it on the fly as the telegram passes through the device. This crucially minimizes communication delays.

Programming and hardware configuration of the embedded-PC is done on a host-PC in TwinCAT 3 as shown in Figure 2.6. TwinCAT 3 represents the development environment provided by Beckhoff. It supports programming according to the IEC 61131-3 standard and also provides interfaces for C/C++ and Matlab®/Simulink®. The latter is used for the implementation of advanced motion control algorithms in a *rapid control prototyping* kind of manner. For this purpose Beckhoff provides a TwinCAT target for an automatic code generation (cg) in Simulink®. This generates a so-called TcCOM object that might directly be implemented in the TwinCAT 3 environment with final deployment on the CX2040.

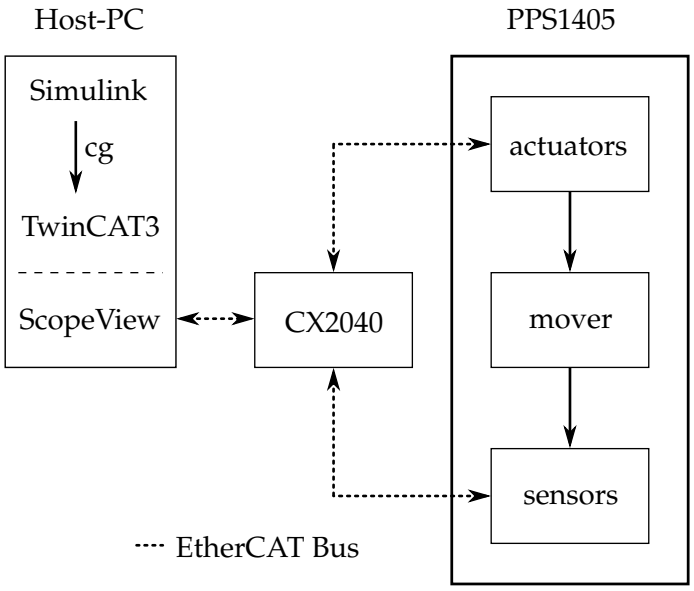

FIGURE 2.6: Beckhoff real-time environment of the PPS1405 motion stage. Dotted lines indicate the directions of EtherCAT Bus communication while the abbreviation cg represents the process of automatic code generation.

For the real-time visualization and logging of process and measurement data, we use a further Beckhoff tool called ScopeView (cf. Figure 2.6).

Chapter 3

Modeling

Modern control and systems theory is a vast field with a wide variety of methods and tools to choose from. However, whether or not the selection of a definite control method is feasible in a certain application is mainly determined by the underlying nature and the fundamental properties of the system to be dealt with. Hence, for the design and evaluation of advanced and model based control techniques, it is indispensable to have an adequate mathematical representation of the considered dynamic system at hand.

To this end, the following chapter is dedicated to deriving a general mathematical model description for planar positioning systems of the presented type (see Chapter 2). The primary goal we pursue here, is to gain insights into the constitutive properties and challenges that may be attributed to the considered class of motion control systems. This includes, for instance, answering the following related questions:

1. What is the essential class of system, i.e. is the system linear, nonlinear, time varying or time invariant?

2. What are the prominent dynamics relevant for control? Are there couplings or any dynamics limiting control?

3. What are the main sources of uncertainties and disturbances and how are they characterized?

4. What is the nature (matched/unmatched) of these disturbances, i.e. at which point in the control loop are they injected?

In order to answer the questions 1. to 4., in Section 3.1, we firstly carry out a physical modeling procedure, where we consider fundamental physical laws such as conservation principles and balance equations. Doing so, we focus on the most prominent dynamics and uncertainties, while striving for the lowest model complexity possible. Indeed, driven by the idea of adaptive control we attempt to gain a model for which the synthesis of adaptive control algorithms turns out feasible.

The result is a set of ordinary differential and difference equations that help analyzing the aforementioned attributes. Measurements taken from the test rig serve for validation and verification purposes and a possible refinement of the derived models. Thus, the developed model obtained, reflects the overall characteristics and challenges of the system in an adequate and realistic manner. Hence, it serves well for the design and the assessment of advanced control techniques.

Section 3.2 is dedicated to an analysis of the model with respect to its fundamental systems theoretic properties. Especially an analysis of the uncertainty structure reveals possible points of contact for adaptive control.

Finally, deduced from the analysis presented, we address fundamental performance limitations of such machines in Section 3.3 and formulate specifications for controller design in Section 3.4.

3.1 Physical Modeling

In this section we present a complete physical model of the PPS1405 planar motion stage, derived on the basis of the fundamental principles governed by this system. This model is mainly based on our previous work published in [139, 141]. The model is validated with measurement results, to illustrate its ability in reflecting the reality in an adequate manner.

We begin with the analytical modeling approach by splitting up the motion stage into the most significant sub-elements. Referring to Figure 2.2 we divide the motion stage system into the following subsystems:

- sensor
- actuator/linear servomotors
- commutation law
- mover

What follows next, is a one-by-one modeling treatment of the elements listed above.

3.1.1 Sensor Dynamics

Note that due to its working principle the sensor has a remarkably high bandwidth. It is therefore by far the fastest element within the whole signal chain (see Section 2.2). This leads us to the following assumption that shall hold for the reminder of this text.

Assumption 3.1.1. *The Sensor is without any dynamics. It measures the actual position coordinates q_x, q_y, q_ϕ exactly modulo measurement noise.*

3.1.2 Actuator Dynamics

As elaborated in 2.3 four linear servomotors form the actuating elements of the planar motor. Each of these comprises

- a two-phase coil-system
- a two-phase DCA and
- a permanent magnet array.

For the purpose of modeling let us proceed in the same logical order as given above. To this end, we begin with modeling the electrical driving circuit, i.e. the driving coils.

Derivation of a Coupled Two-Phase Driving-Coil Model

Using Faraday's law of electromagnetic induction (see Appendix A), we next derive the voltage equations for the two-phase driving-coil systems of the PPS1405 motion stage.

Due to the special coil formation (see Section 2.3.1) and the movement of the permanent magnets relative to the coils, it is expected that both transformer-EMF and motion-EMF effects will be encountered. The flux linkage as a key parameter of electromechanical coupling will capture both of these effects.

Following the lines of thought of [44] the application of Faraday's law yields

$$u_{x_{1j}}(t) = R_{x_{1j}}\, i_{x_{1j}}(t) + \dot{\Psi}_{x_{1j}}(i_{x_{11}}, i_{x_{12}}, q_x) \tag{3.1}$$

for the voltage equation of the entire $\mathcal{X}_1$ driving-coil system. For $j = 1, 2$, voltage $u_{x_{1j}}(t) \in \mathbb{R}$ denotes the source or input voltage, $R_{x_{1j}} \in \mathbb{R}_+$ is the respective phase winding resistance and $\Psi_{x_{1j}}(i_{x_{11}}, i_{x_{12}}, q_x) \in \mathbb{R}$ represents the magnetic flux linkage linking the circuits $\mathcal{X}_{11}$ and $\mathcal{X}_{12}$.

As discussed in one of the previous sections, the flux linkage term depends on phase currents $i_{x_{1j}}(t) \in \mathbb{R}$ as well as on position $q_x(t)$.

Since the B-field of the permanent magnets permeates through air which is a linear medium, this implies that the flux, i.e. the flux linkage, is linear in the currents (cf. equations (A.26) and (A.26)). Computing the rate of change of $\Psi_{x_{1j}}(i_{x_{11}}, i_{x_{12}}, q_x)$ equation (3.1) turns to

$$u_{x_{11}}(t) = R_{x_{11}}\, i_{x_{11}}(t) + L_{x_{11}} \frac{di_{x_{11}}(t)}{dt} + M_{21}^{x_1} \frac{di_{x_{12}}(t)}{dt} + \frac{\partial \Psi_{x_{11}}}{\partial q_x}\, \dot{q}_x(t) \tag{3.2}$$

$$u_{x_{12}}(t) = R_{x_{12}}\, i_{x_{12}}(t) + L_{x_{12}} \frac{di_{x_{12}}(t)}{dt} + M_{12}^{x_1} \frac{di_{x_{11}}(t)}{dt} + \frac{\partial \Psi_{x_{12}}}{\partial q_x}\, \dot{q}_x(t), \tag{3.3}$$

where $L_{x_{1j}} \in \mathbb{R}_+$ denotes self inductances and $M_{21}^{x_1}, M_{12}^{x_1} \in \mathbb{R}_+$ the mutual inductances of either phase of the $\mathcal{X}_1$-coil.

Thereby the first terms account for ohmic losses, whereas the second and the third represent self and mutual induction of the coil. The last terms model the back-EMF that arises due to a mechanical displacement of the permanent magnet array/magnetic circuit relative to the coils.

Apparently, the back-EMF voltage in the last two equations is expressed in terms of the partial derivative of the flux linkages.

Next, let us define $B_{x_{ij}}(q_x)$ as the vertical/normal flux density component above the dedicated driving-coil system $\mathcal{X}_{ij}$ and let $\bar{l}_{x_{ij}}$ denote the effective wire length of the coils inside the magnetic field. Using further the result of Example A.1.1, the partial derivatives of the last summands of equations (3.2) and (3.3) may be rewritten as

$$\frac{\partial \Psi_{x_{1j}}(q_x)}{\partial q_x} = \bar{l}_{x_{1j}} B_{x_{1j}}(q_x) = K_{x_{1j}}(q_x). \tag{3.4}$$

For a compact notation we use the vectors $i_{x_1} = (i_{x_{11}}, i_{x_{12}})^{\mathrm{T}}$ and $u_{x_1} = (u_{x_{11}}, u_{x_{12}})^{\mathrm{T}}$ as introduced in Section 2.1 and rewrite (3.2) and (3.3) in the form

$$\tilde{L}_{x_1} \frac{di_{x_1}(t)}{dt} = u_{x_1}(t) - R_{x_1}\, i_{x_1}(t) - K_{x_1}(q_x)\, \dot{q}_x(t) \tag{3.5}$$

with

$$R_{x_1} = \begin{pmatrix} R_{x_{11}} & 0 \\ 0 & R_{x_{12}} \end{pmatrix}, \quad \tilde{L}_{x_1} = \begin{pmatrix} L_{x_{11}} & M_{21}^{x_1} \\ M_{12}^{x_1} & L_{x_{12}} \end{pmatrix}, \quad K_{x_1} = \begin{pmatrix} K_{x_{11}}(q_x) \\ K_{x_{12}}(q_x) \end{pmatrix} \tag{3.6}$$

representing the resistance matrix, the generalized inductance matrix and the back-EMF vector for a complete $\mathcal{X}_1$ coil.

Doing so for $\mathcal{X}_2, \mathcal{Y}_1$ and $\mathcal{Y}_2$ and combining the results yields

$$\tilde{L}\frac{di(t)}{dt} = u_s(t) - R\,i(t) - K(q)\,\dot{q}(t), \tag{3.7}$$

where we introduced the supply or input voltage vector

$$u_s = (u_{x_{11}}, u_{x_{12}}, \ldots, u_{y_{21}}, u_{y_{22}})^{\mathrm{T}} \in \mathbb{R}^8, \tag{3.8}$$

the block diagonal matrices

$$R = \mathrm{diag}(R_{x_1}, \ldots, R_{y_2}) \in \mathbb{R}_+^{8\times 8} \tag{3.9}$$

$$\tilde{L} = \mathrm{diag}(\tilde{L}_{x_1}, \ldots, \tilde{L}_{y_2}) \in \mathbb{R}_+^{8\times 8} \tag{3.10}$$

and finally

$$K(q) = \begin{pmatrix} K_{x_1}(q_x) & 0 & 0 \\ K_{x_2}(q_x) & 0 & 0 \\ 0 & K_{y_1}(q_y) & 0 \\ 0 & K_{y_2}(q_y) & 0 \end{pmatrix} \in \mathbb{R}^{8\times 3}. \tag{3.11}$$

Parameter values for these matrices are given in Table C.1 in Appendix C.

The phase currents of the respective coil-systems are controlled by means of switched DCAs with a fixed current control architecture. For gaining insights in the transient behavior, we model the closed loop consisting of the DCAs and coils in the next section.

Remark 3.1.1. To be precise, for motion along the translational axes (q_x, q_y) one could also model the back-EMF voltages

$$u_{x,z_{ij}}(t) = \frac{\partial \Psi_{x_{ij}}(q_z)}{\partial q_z}\dot{q}_z(t), \quad u_{y,z_{ij}}(t) = \frac{\partial \Psi_{y_{ij}}(q_z)}{\partial q_z}\dot{q}_z(t)$$

resulting from the fluctuation of the flight height $q_z(t)$, i.e. vertical motion, and

$$u_{x,\phi_{ij}}(t) = \frac{\partial \Psi_{x_{ij}}(q_\phi)}{\partial q_\phi}\dot{q}_\phi(t), \quad u_{y,\phi_{ij}}(t) = \frac{\partial \Psi_{y_{ij}}(q_\phi)}{\partial q_\phi}\dot{q}_\phi(t)$$

as a consequence of rotational motion around the vertical axis. To account for these effects in the coil model, one would simply add these terms to the right hand side of equations (3.2) and (3.3).

However, in contrast to the back-EMF expected from translational motion, these effects are negligible due to comparably small positions and rates of q_z and q_ϕ respectively (cf. Assumption 3.1.9).

Derivation of a two-phase Digital Current Amplifier Model

The DCAs' current control loop (see simplified scheme in Figure 3.1) consists of a multivariable moving average filter of order $N = 8$ located in the feedback path and a multivariable discrete PI-controller (velocity algorithm) in ISA-form. The filter aims to

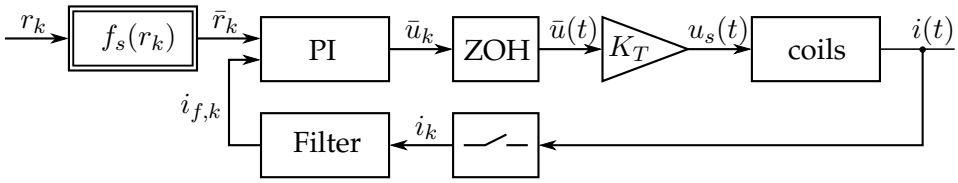

FIGURE 3.1: Assumed, simplified Hammerstein model of the closed current loop of the entire motion system modeling the average time behavior.

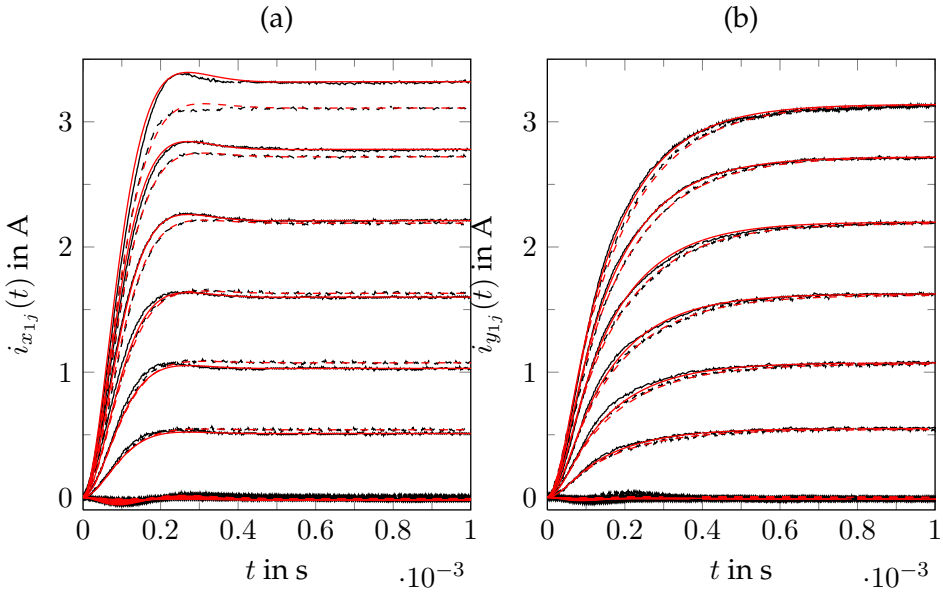

FIGURE 3.2: Comparison of model (red) with measured (black) current transient response of phases 1 (solid) and 2 (dashed) of linear motors $\mathcal{X}_1$ (a) and $\mathcal{Y}_1$ (b).

remove PWM induced current ripple from the measured A/D converted phase currents $i_k = i(kT_s) \in \mathbb{R}^8$ (neglecting quantization) so as to improve the current signals $i_{f,k} \in \mathbb{R}^8$ for the control. Note that T_s denotes the sampling time. The filter and controller are given by the discrete-time system

$$i_{f,k} = \tfrac{1}{N+1}\left(i_k + i_{k-1} + \cdots + i_{k-N}\right) \tag{3.12}$$

$$\bar{u}_k = \bar{u}_{k-1} - K_p\left(i_{f,k} - i_{f,k-1}\right) + K_i T_s\left(\bar{r}_k - i_{f,k}\right), \tag{3.13}$$

where $r_k = i^\star(kT_s) \in \mathbb{R}^8$ is the reference current, $\bar{u}_k \in \mathbb{R}^8$ the control signal, and $K_p \in \mathbb{R}^{8\times 8}$ as well as $K_i \in \mathbb{R}^{8\times 8}$ are the (diagonal) controller gain matrices. Note that $\bar{r}_k = f_s(r_k)$ is a modification of r_k by some function $f_s : \mathbb{R}^8 \to \mathbb{R}^8$ for casting nonlinear steady state behavior into a Hammerstein model with static input nonlinearity and LTI dynamics.

Since the amplifiers are PWM-switched with 200 kHz the current ripple is moderate. Focusing on the average transient behavior, we model them as ideal continuous voltage amplifiers with gain $K_T \in \mathbb{R}^{8\times 8}$ (cf. Figure 3.1). Thus, we have the continuous coil input voltage $u_s(t) = K_T\,\bar{u}(t)$, where $\bar{u}(t) \in \mathbb{R}^8$ is the average continuous time signal of the PWM control $\bar{u}_k$.

Figure 3.2 compares simulations with experiments on the linear motors $\mathcal{X}_1$ and $\mathcal{Y}_1$

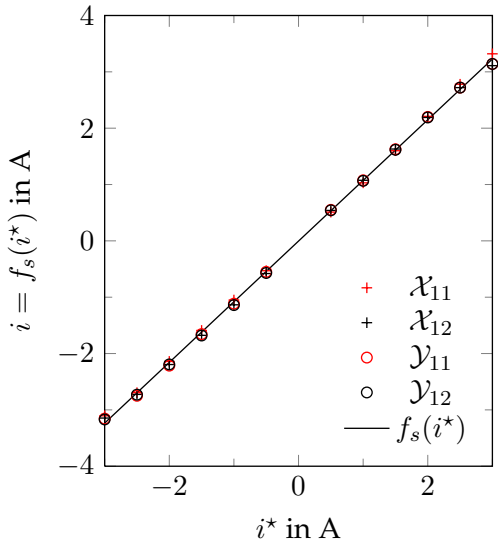

FIGURE 3.3: Identified static I/O characteristics of current control loop with regression line $i = f_s(i^\star) = 1.0769\, i^\star - 0.0039792$ as a scalar single fit valid for all linear motors.

via measured transient current responses on reference current steps from $0.5\,\mathrm{A}$ to $3\,\mathrm{A}$ (in $0.5\,\mathrm{A}$ steps over the current range of the DCAs). The model matches the transient behavior well. Notice the effect of mutual induction (small undershoots) which is suppressed quit well by the current controller.

The quantity $f_s(r_k)$ obtained from measurement data shown in Figure 3.3, serves to adjust the DC-gain. Note that the result from Figure 3.2 was obtained by putting the dedicated measurement points of the corresponding phases (see Figure 3.3) into dedicated look-up-tables (see Table C.3 in Appendix C). However, since the relationship between reference current input $i_k^\star$ and output i_k is first and foremost of linear affine nature, the stationary relationship of all phases together can be approximated by

$$\bar{r}_k = f_s(r_k) = p_1\, r_k + p_0 \tag{3.14}$$

where $p_1 \in \mathbb{R}$ and $p_0 \in \mathbb{R}^8$ result from linear regression (cf. Figure 3.3). Although the offset vector p_0 is negligible small, we keep it for analyzing the effects of offsets and asymmetries in current amplifiers on the mover dynamics in Section 3.1.5.
The observed differences and asymmetries in the DC-gain of the respective phases (especially $\mathcal{X}_1$) can be traced back to temperature drifts and inaccurate current measurements. Note, however, that for an accurate set point regulation of the position of the mover, the DC-gain of the current loop is not critical because the plant shows integral behavior. In similar cascade control settings, e.g. for the position or the angular velocity control of DC-motors, even simpler proportional controllers are used for the current loop (see [25]) as the main purposes of the current controller are: speeding up the response by forcing the current to flow in the right direction, decoupling the phases from each other, i.e. rejecting the mutual induction, and suppressing the effects of output disturbances (back-emf). These requirements are met by the DCAs' current control loop. For trajectory tracking control, however, the DC-gain (p_1) has to be known for an appropriate inversion. The affine term p_0 causes undesired force ripples and torques, respectively. These effects will be discussed in Section 3.1.5.

A frequency response analysis of the closed current loop revealed a closed loop

bandwidth of $>2\,\mathrm{kHz}$, if the bandwidth is defined as the frequency ω_b at which the magnitude of the bodeplot is greater than $-3\,\mathrm{dB}$. Therefore, and in view of the step responses, it can be concluded that the closed-loop dynamics of the DCAs and coils is very fast compared to the mover. Finally, the requirements of decoupling and back-emf suppression are met such that we neglect the current loop dynamics and just consider the static relationship

$$\lim_{k\to\infty} i_k = \bar{r}_k = p_1\, r_k + p_0 \;\Leftrightarrow\; i(kT_s) = p_1\, i^\star(kT_s) + p_0 \tag{3.15}$$

instead.

Due to the small sampling time, $T_s = 5\,\mu\mathrm{s}$, of the DCAs the static DCA-coil-model is treated as continuous, i.e.

$$i(t) = p_1\, i^\star(t) + p_0. \tag{3.16}$$

The parameter values of the complete DCA model are provided in Appendix C.

Modeling of Magnetic Flux Density, Lorentz Forces & Torques

The magnetic field of a permanent magnet array is governed by the flux density $\vec{B}$. Generally, $\vec{B}$ is a vector-valued function of positions (q_x, q_y, q_z) in the three dimensional space. It may be decomposed as per

$$\vec{B}(q_x, q_y, q_z) = B_x(q_x, q_y, q_z)\,\vec{e}_x + B_y(q_x, q_y, q_z)\,\vec{e}_y + B_z(q_x, q_y, q_z)\,\vec{e}_z \tag{3.17}$$

into its respective vector components (B_x, B_y, B_z) and the unit vectors $(\vec{e}_x, \vec{e}_y, \vec{e}_z)$ of the standard basis of $\mathbb{R}^3$. The flux density distribution of such an array heavily depends on its geometrical dimensions as well as on the considered observation point in space. Thus, a model of the magnetic field distribution essentially involves the computation of a functional dependency of the B-field with respect to the spatial coordinates as well as the dimensional parameters. Once known, this model will be utilized for the computation of Lorentz forces and torques and the derivation of an appropriate commutation law for the control of the motor. As discussed earlier (see Section 2.3.1), the permanent magnet arrays are designed for a sinusoidal distribution along the translational axes. This will be verified next, by modeling and measurements conducted at the test rig.

For modeling permanent magnetic structures in the three dimensional space, essentially two popular methods exist. That is, the method of equivalent current and the method of equivalent charge [24, 44, 57, 103]. These models are based on the central idea or observation that there exist equivalent mechanisms that produce exactly the same field as a permanent magnet. For the purpose of modeling, the actual field of the magnetic structure might thus be replaced by its equivalent counterpart in free space, in which there are no magnetic materials. Then, standard methods may be applied to the magnetic equivalent, for obtaining a field solution.

In this respect the equivalent current model basically stems from the observation that a (tightly wound one layer) solenoid with current density $\vec{J}$ gives rise to exactly the same magnetic field as a permanent magnet with equal shape and proper magnetization. Thus, the magnetization inside the magnet may be modeled by a distribution of equivalent surface or volume currents. That is governed by

$$\nabla \times \vec{M} = \vec{J}_m \tag{3.18}$$

$$\vec{M} \times \vec{n} = \vec{J}_{ms}, \tag{3.19}$$

where $\vec{M}$, $\vec{J}_m$, $\vec{J}_{ms}$ and $\vec{n}$ denote respectively, the magnetization of the material, the equivalent magnetic volume current density, the equivalent magnetic surface current density and the surface normal containing $\vec{J}_{ms}$ [24, 44, 57].

On the other hand, the equivalent charge model is rather a phenomenological model considering the fact that fictitious isolated magnetic charges, i.e. magnetic monopoles, (although not existent) placed at the top and bottom faces of the magnet also produce exactly the same field as the permanent magnet itself [24]. Indeed, this abstraction comes close to our natural intuition of magnetic north and south poles. Analogously, the field of the permanent magnet might be reduced to a distribution of equivalent charge given by [44, 57, 103]

$$\nabla \cdot \vec{M} = \rho_m \tag{3.20}$$

$$\vec{M} \cdot \vec{n} = \rho_{ms}. \tag{3.21}$$

Therein ρ_m is the equivalent magnetic volume charge density, ρ_{ms} is the equivalent magnetic surface charge density and $\vec{n}$ is the surface normal containing ρ_{ms}.

For the computation of $\vec{B}$, the equivalent currents or charges are inserted into Maxwell's magnetic field equations as equivalent source terms for which then standard methods can be applied [44]. Please note, that the volume densities are not existent, if the magnetization $\vec{M}$ inside the permanent magnet is uniform because the spatial derivatives of a constant $\vec{M}$ vanish.

For obtaining the field solutions for rectangular or cuboidal magnets, as encountered in the magnet array of the PPS1405, in the literature mostly the equivalent charge model is adopted (see e.g. [1, 44, 81] among others). Following the lines of thought of [24, 44, 57, 103] we next present a sketch of the derivation of the field solution for the permanent magnet array of the PPS1405. To this end, let us recall Maxwell's magnetic field equations (see Appendix A) given by

$$\nabla \times \vec{H} = \vec{J} + \frac{\partial \vec{D}}{\partial t} \tag{3.22}$$

$$\nabla \cdot \vec{B} = 0. \tag{3.23}$$

For the simplification of the problem at hand it is convenient to impose reasonable field conditions. Therefore, consider the following assumptions:

Assumption 3.1.2. *It is unlikely that the magnetic field of a permanent magnet will change over time. Hence, we assume that the magnetic field produced by the permanent magnets is independent of time, i.e. it is static.*

Assumption 3.1.3. *Owing to the fact that there is no electric current inside the permanent magnets producing the magnetic field, we assume that the permanent magnet is located in a current free region in free space and thus assume the absence of current densities $\vec{J}$.*

With these assumptions we find that the magnetic field of an isolated permanent magnet is governed by

$$\nabla \times \vec{H} = 0 \tag{3.24}$$

$$\nabla \cdot \vec{B} = 0. \tag{3.25}$$

According to Definitions B.2.1 and B.2.2 its vector field may be classified as irrotational and solenoidal. This means that there are no magnetic sources and sinks. As a consequence of Helmholtz' Theorem (see Theorem B.2.1 and corollary B.2.1) an irrotational vector field can be derived from the gradient of a scalar potential. Thus, introducing the magnetic scalar potential ϕ_m yields

$$\vec{H} = -\nabla\phi_m. \tag{3.26}$$

Now, substituting the constitutive relation (A.7) into (3.25) we obtain

$$\nabla \cdot \vec{B} = \mu_0 \nabla \cdot (\vec{H} + \vec{M}) = 0. \tag{3.27}$$

By virtue of the last equation, it can be seen that ϕ_m satisfies Poisson's equation, that is

$$\nabla^2\phi_m = \nabla \cdot \vec{M}, \tag{3.28}$$

where $\nabla \cdot \vec{M} = \rho_m$ defines a magnetic volume charge density (cf. (3.20)). Assuming the knowledge of $\rho_m = \rho_m(\vec{r})$, in accordance to [44], solutions for ϕ_m may be found using the Green's function $G(\vec{r}, \vec{r}')$ for the Laplacian. The solution for the scalar potential is then given by [44],

$$\phi_m(\vec{r}) = \int_V G(\vec{r}, \vec{r}')\rho_m(\vec{r}')\, dV', \tag{3.29}$$

where $\vec{r}$ is a position vector to an observation point, while $\vec{r}'$ denotes the vector to a source point. For problems in the three dimensional space it is well known [44] that

$$G(\vec{r}, \vec{r}') = -\frac{1}{4\pi}\frac{1}{|\vec{r} - \vec{r}'|} \tag{3.30}$$

such that

$$\phi_m(\vec{r}) = -\frac{1}{4\pi}\int_V \frac{\rho_m(\vec{r}')}{|\vec{r} - \vec{r}'|}\, dV'. \tag{3.31}$$

Following [44, 103] this can be rewritten as per

$$\phi_m(\vec{r}) = -\frac{1}{4\pi}\int_V \frac{\nabla' \cdot \vec{M}(\vec{r}')}{|\vec{r} - \vec{r}'|}\, dV' + \frac{1}{4\pi}\int_S \frac{\vec{M}(\vec{r}') \cdot \vec{n}}{|\vec{r} - \vec{r}'|}\, dS', \tag{3.32}$$

where $\vec{M} \cdot \vec{n} = \rho_{ms}$ defines the magnetic surface charge also assumed to be known (cf. (3.21)). Please note that ∇' and ∇ operate only on the primed and unprimed coordinates, respectively. Due to

$$\vec{B}(\vec{r}) = \mu_0\vec{H}(\vec{r}) = -\mu_0\nabla\phi_m(\vec{r}) \tag{3.33}$$

and relation

$$\nabla\frac{1}{|\vec{r} - \vec{r}'|} = -\frac{(\vec{r} - \vec{r}')}{|\vec{r} - \vec{r}'|^3} \tag{3.34}$$

it follows that

$$\vec{B}(\vec{r}) = -\frac{\mu_0}{4\pi}\int_V \frac{\rho_m(\vec{r}\,')\,(\vec{r}-\vec{r}\,')}{|\vec{r}-\vec{r}\,'|^3}\,dV' + \frac{\mu_0}{4\pi}\int_S \frac{\rho_{ms}(\vec{r}\,')\,(\vec{r}-\vec{r}\,')}{|\vec{r}-\vec{r}\,'|^3}\,dS'. \tag{3.35}$$

That is the flux density distribution outside an isolated permanent magnet in free space.

On the basis of the last equation the authors of reference [44] derive an analytical relationship for the field components (B_x, B_y, B_z) of a rectangular permanent magnet as a function of space and geometrical dimensions. This includes the following assumption:

Assumption 3.1.4. *It is assumed that the magnetization inside the permanent magnet is uniform and directed along q_z, i.e.*

$$\vec{M} = M_s\vec{e}_z. \tag{3.36}$$

From that, one can conclude that there is no volume charge density but a surface charge density $\rho_{ms} = +M_s$ on the top face of the magnet and $\rho_{ms} = -M_s$ on the bottom face of the magnet. Since the derivation of the analytical expression is quite tedious we resort to the solution of [44] given by

$$B_x(q_x,q_y,q_z) = \frac{\mu M_s}{4\pi}\sum_{k=1}^{2}\sum_{m=1}^{2}(-1)^{k+m}\ln(\mathcal{R}) \tag{3.37}$$

$$B_y(q_x,q_y,q_z) = \frac{\mu M_s}{4\pi}\sum_{k=1}^{2}\sum_{m=1}^{2}(-1)^{k+m}\ln(\mathcal{S}) \tag{3.38}$$

$$B_z(q_x,q_y,q_z) = \frac{\mu M_s}{4\pi}\sum_{k=1}^{2}\sum_{n=1}^{2}\sum_{m=1}^{2}(-1)^{k+n+m}\arctan(\mathcal{T}), \tag{3.39}$$

where $\mathcal{R}$, $\mathcal{S}$, $\mathcal{T}$ are given by

$$\mathcal{R} = \frac{(q_y-q_{y,1})+\sqrt{(q_x-q_{x,m})^2+(q_y-q_{y,1})^2+(q_z-q_{z,k})^2}}{(q_y-q_{y,2})+\sqrt{(q_x-q_{x,m})^2+(q_y-q_{y,2})^2+(q_z-q_{z,k})^2}} \tag{3.40}$$

$$\mathcal{S} = \frac{(q_x-q_{x,1})+\sqrt{(q_x-q_{x,1})^2+(q_y-q_{y,m})^2+(q_z-q_{z,k})^2}}{(q_x-q_{x,2})+\sqrt{(q_x-q_{x,2})^2+(q_y-q_{y,m})^2+(q_z-q_{z,k})^2}} \tag{3.41}$$

$$\mathcal{T} = \frac{(q_x-q_{x,n})(q_y-q_{y,m})}{(q_z-q_{z,k})\sqrt{(q_x-q_{x,n})^2+(q_y-q_{y,m})^2+(q_z-q_{z,k})^2}}. \tag{3.42}$$

Therein, $(q_{x,1}, q_{x,2})$, $(q_{y,1}, q_{y,2})$ and $(q_{z,1}, q_{z,2})$ denote the positions of the edges of the permanent magnet. The assumptions imposed by [44] are also valid for our case. So, we adopt this model for the spatial description of the permanent magnet arrays of the PPS1405 motion stage. Note, however, that the model given above is only valid for an individual magnet. For computing the field distribution of a complete array with N_m magnets we must calculate the solutions for every individual magnet placed at its respective position inside the array and finally perform a superposition of the individual field solutions[1]. Taking into account the alternating polarity of the adjacent magnets within the array, the superposition of the N_m field solutions may be expressed

[1] Note that the principle of superposition holds due to the linearity of Maxwell's equations.

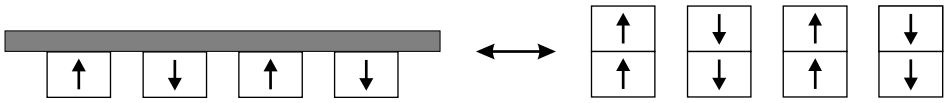

FIGURE 3.4: Magnet mirroring for back-iron plate (image adopted from [57]).

as [44, 82]

$$\vec{B}(q_x, q_y, q_z) = \sum_{i=1}^{N_m} (-1)^i \, \vec{B}_i(q_x, q_y, q_z). \tag{3.43}$$

Note, that a similar model is given in [1].

Although this is not required by the model, for the sake of simplicity we introduce a further assumption, i.e.

Assumption 3.1.5. *It is assumed that the individual permanent magnets inside the magnet array have the same physical characteristics in terms of magnetization, except their alternating polarity, and are equal in their geometric dimension and shape.*

The presence of a back-iron plate As discussed in Section 2.3.1, the individual permanent magnets are attached to a back-iron plate (see Figure 3.4). In view of the derived magnet model, this issue deserves some special attention. Interestingly, with the so-called method of images (see [44] Section 3.7), it can be shown [44, 57] that the combination of a back-iron plate and a permanent magnet results in a magnetic field that is equivalent to the field produced by a magnet that has doubled height. This effect is illustrated in Figure 3.4. On the left, four magnets attached to a back-iron plate are shown. The magnets form an (NS) array with alternating magnetization/polarity. This is indicated by means of arrows. The right hand side of Figure 3.4 represents the magnets together with their images (mirrored at the boundary surface). Both representations give rise to exactly the same field. This result shows that a back-iron may increase the magnetic field strength and thus, the force density of the planar motor. As a consequence of the result discussed above, it can be concluded that the model as given in equations (3.37)-(3.43) may be applied even in the presence of iron. For the accommodation of back-iron effects in a consistent manner, we simply have to (virtually) double the height of the magnets.

Doing so, and taking also into account the magnetization and constant air gap $q_{z,0}$ as given in Table 3.1, the three dimensional field distribution of the vector components $B_x(q_x, q_y)$, $B_y(q_x, q_y)$ and $B_z(q_x, q_y)$ may be computed via (3.37)-(3.43).

As an excerpt of the $\mathcal{X}_1$ linear motor, the field of a permanent magnet array with six magnets is presented in Figures 3.5 and 3.6. On the right of Figure 3.5 the three dimensional surface plots are shown for the corresponding vector components. In order to get a good impression of which effect occurs at which location, with regard to the permanent magnet array, the latter is also indicated on the left hand side of the Figure. Additionally, Figure 3.6 illustrates the respective side views along the translational axes q_x and q_y in the same manner.

Apparently, as can be seen in Figures 3.5 (e), (f) and 3.6 (e), (f) the vertical flux density distribution $B_z(q_x, q_y)$, crucial for the generation of translational forces, shows indeed a sinusoidal relationship with respect to the translational axis q_x, as desired. It shows a magnitude of approximately $0.5\,\mathrm{T}$ and has its maxima and minima perfectly aligned with the centerlines of the individual magnets. Along the direction of

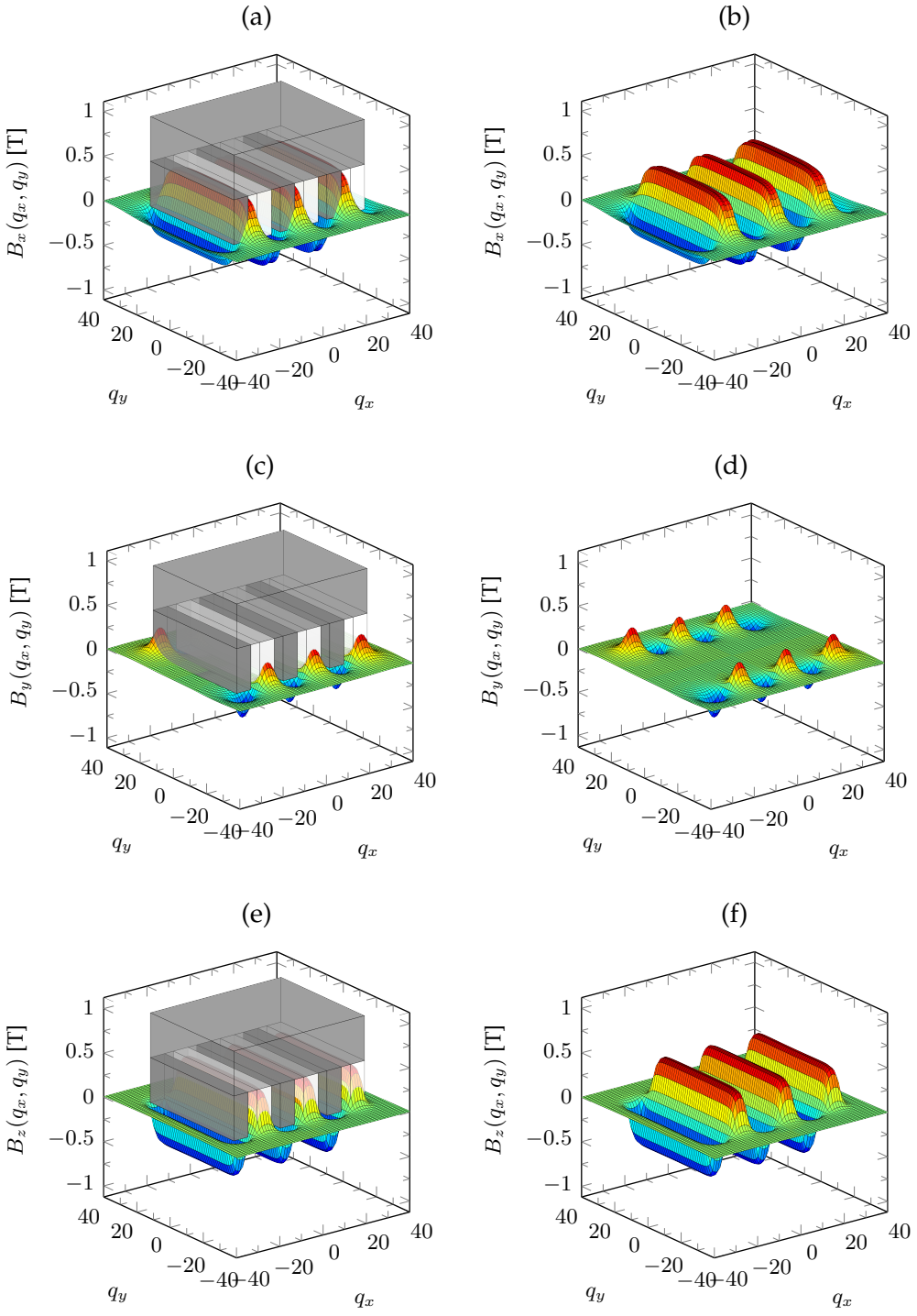

FIGURE 3.5: Computed 3d flux density distribution of components $B_x(q_x, q_y)$, $B_y(q_x, q_y)$, $B_z(q_x, q_y)$ for an example of six permanent magnets in NS configuration according to Table 3.1.

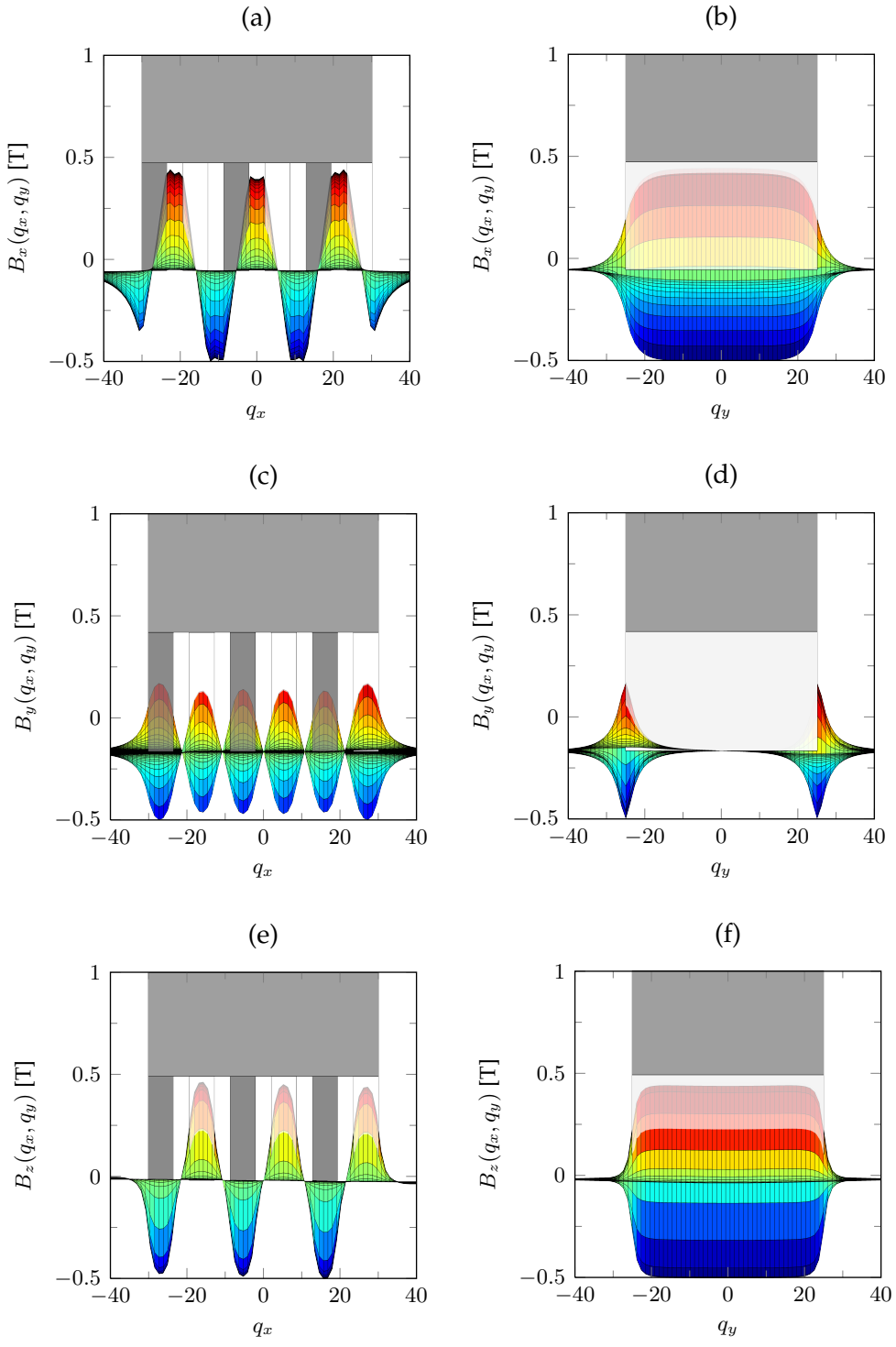

FIGURE 3.6: Respective side views of flux density components along q_x and q_y.

q_y it is almost constant except at the edges of the permanent magnets. Accordingly, component B_y along q_y is zero almost everywhere, except at the corners/edges of the permanent magnets. There, the maximum and minimum peaks show a relatively small magnitude of approximately $0.2\,\mathrm{T}$ and are equally aligned with the centerlines of the magnets. The flux density component B_x shows a wave form that is akin to that of the vertical components with similar amplitude but sharper edges. It additionally exhibits a phase shift of a quarter of the magnet period, i.e. $T_m/4$, with respect to the vertical component. Hence, maxima and minima occur in between two magnets. Along the direction of q_y it is likewise constant except at the edges of the magnets.

For comparing the model with real world data, measurements were undertaken at the PPS1405 platform. In these experiments a Hall effect sensor was used for measuring the vertical flux density distribution of the permanent magnet arrays of the $\mathcal{X}_1$ and $\mathcal{Y}_1$ motors. For the $\mathcal{X}_1$ motor the sensor was placed in parallel to the q_y axis, next to the driving coil. Thereby, the tip of the sensor was placed at the height of the working air gap and it was centered with respect to the magnet depth. With reference to Figure 3.5 the tip was exactly at $q_y = 0$. Then the motor was displaced and the flux density was measured. The same experiment was similarly conducted for the $\mathcal{Y}_1$ motor. The results of these investigations are illustrated in Figure 3.7, where the measured flux is compared to the proposed model and an ideal sinusoid. The model shows a very good match and the first impression is that the real field of the motors is very close to a pure sinusoid with only minor nonlinear distortions around the top and the zero crossings.

The flux density model presented in (3.37)-(3.43) is very nice for building complex simulation models. It is also very useful during the design and evaluation phase of a motor with regard to an optimization of the geometrical dimensions of a magnet array. Comparisons of this model with finite element analysis in [82] show a nearly perfect alignment of the field solutions such that this model provides a computationally effective means for a first design.

However, since we are mainly concerned in deriving a model suitable for controller design we must admit, that this model is indeed too detailed and needs some further simplification.

To this end, let us firstly restrict our analysis on the vertical flux density component $B_z(q_x, q_y)$ only since this is the component responsible for the generation of planar propulsion forces in the (q_x, q_y)-plane. Then, let us confine on a constant air gap $q_{z,0}$ such that the position dependency of q_z in the vertical flux density vanishes. Let us further introduce the variables $B_{x_{ij}}(q_x, q_y)$ and $B_{y_{ij}}(q_x, q_y)$ with $i, j = 1, 2$ representing the vertical flux density components with respect to the corresponding coil phases and motors $\mathcal{X}_{ij}$, $\mathcal{Y}_{ij}$.

individual magnets	number	6
	magnetization	$M_s = 1.02 \times 10^5 \mathrm{A/m}$
	air gap	$q_{z,0} = 1.2\,\mathrm{mm}$
	width	$6.6\,\mathrm{mm}$
	depth	$50\,\mathrm{mm}$
	height	$16\,\mathrm{mm}$
array	distance of adjacent magnets	$4.1\,\mathrm{mm}$

TABLE 3.1: Modeling parameters for the permanent magnet array with partially virtual geometrical dimensions for the accommodation of back-iron effects (cf. Table 2.2).

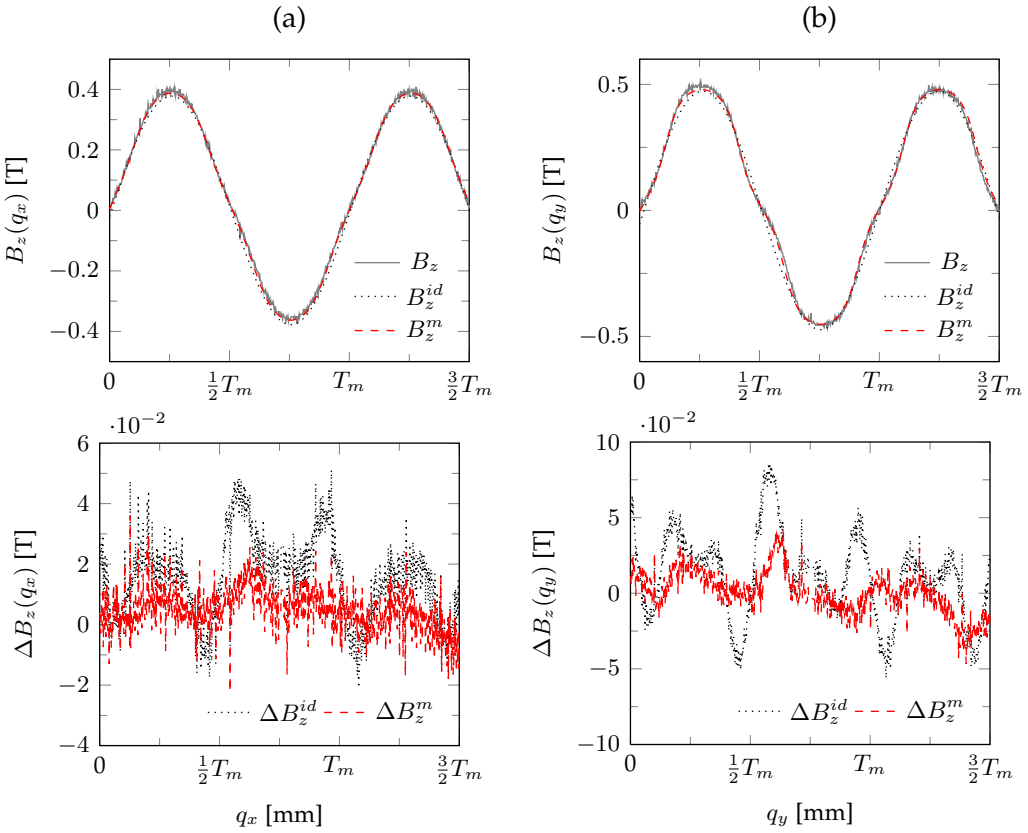

FIGURE 3.7: Comparison of measured (B_z), modeled (B_z^m) and ideal sinusoidal (B_z^{id}) flux density distribution along the q_x (left) and along the q_y (right) directions with respective modeling deviations $\Delta B_z^m = B_z - B_z^m$ and $\Delta B_z^{id} = B_z - B_z^{id}$. NRMSE^m = 1.14 %, NRMSE^{id} = 2.63 % (left); NRMSE^m = 1.47 %, NRMSE^{id} = 3.13 % (right)

Next, and in view of Figure 3.5 we introduce the following simplifying assumptions regarding $B_{x_{ij}}$ and $B_{y_{ij}}$:

Assumption 3.1.6. *We assume that $B_{x_{ij}}(q_x, q_y)$ above the $\mathcal{X}_{ij}$-coil is constant along the q_y-axis. That is, $B_{x_{ij}}(q_x, q_y) = B_{x_{ij}}(q_x)$.*

Assumption 3.1.7. *Similarly we assume that $B_{y_{ij}}(q_x, q_y)$ above the $\mathcal{Y}_{ij}$-coil is constant along the q_x-axis such that $B_{y_{ij}}(q_x, q_y) = B_{y_{ij}}(q_y)$.*

Due to the fact that the vertical flux density components are very close to a pure sinusoid for the time being we also assume so. Then,

$$B_{x_{ij}}(q_x) = \bar{B}\sin(\tfrac{2\pi}{T_m}q_x + \rho_{p,j} + \varphi_x) \tag{3.44}$$

$$B_{y_{ij}}(q_y) = \bar{B}\sin(\tfrac{2\pi}{T_m}q_y + \rho_{p,j} + \varphi_y) \tag{3.45}$$

with magnitude $\bar{B}$, magnet period $T_m > 0$, phase pitch $\rho_{p,j} = \frac{\pi}{2}(j-1)$, and $\varphi_x, \varphi_y > 0$ phase shifts with respect to i-frame. The mismatch between the ideal and the actual distribution will be treated in Section 3.1.5, where parasitic phenomena are considered.

According to (A.23) the Lorentz force imparted on an energized coil inside a magnetic field $\vec{B}$ results from

$$\vec{F} = I \int_C d\vec{l} \times \vec{B} \tag{3.46}$$

evaluated over the wire length C of the coil along the direction of current flow $I\, d\vec{l}$. The Lorentz forces of the planar motor are modeled under the assumptions:

Assumption 3.1.8. *We assume that the coils are perfectly orthogonally aligned with respect to the q_x- and q_y-axes. Furthermore, coils are assumed sufficiently long with respect to the permanent magnet width l such that end effects can be excluded. Finally, also the permanent magnet array is assumed sufficiently long with respect to its corresponding motion direction such that the number of current carrying wires inside the magnetic field is always constant.*

Assumption 3.1.9. *Due to tight sensor constraints (see 2.1) and very small tilting motion (see [139]), the mover's roll, pitch and yaw motion is small such that its influence on the electromagnetic forces is negligible. For the maximum yaw angle $q_{\phi,max} \in [-0.25°, 0.25°]$ with roll and pitch angles in between $\pm 0.01°$. Therefore, $(B_{x_{ij}}(q_x), B_{y_{ij}}(q_y))$ of the magnetic field are assumed perfectly perpendicular to the respective coil surfaces, hence, also to every single coil winding.*

These assumptions imply that the Lorentz forces are acting in q_x and q_y direction only, perpendicularly with respect to the coil (windings), regardless of the mover's orientation q_ϕ (Figure 3.8). Thus, the forces in q_x and q_y direction are decoupled from one another.

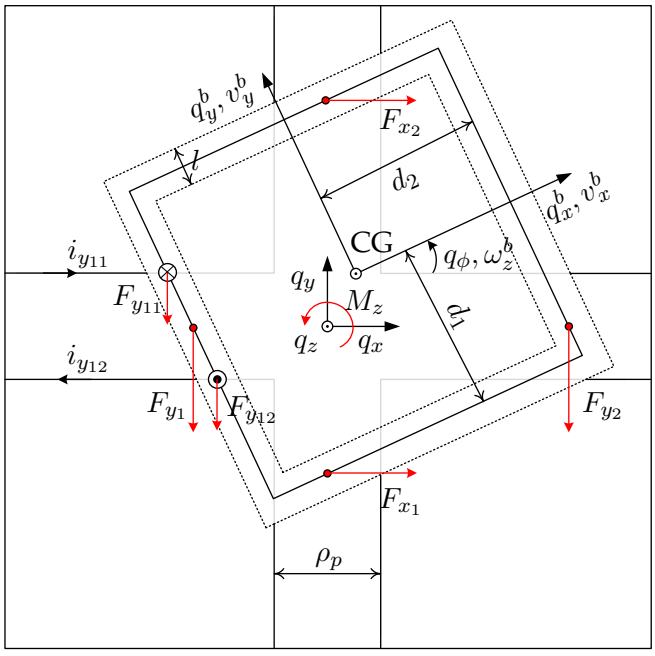

FIGURE 3.8: Planar electromagnetic forces/torques on the mover: For simplicity, coil phases are depicted as conductors. Dotted lines indicate the location of the permanent magnet arrays, the solid line spots the line of the applied electromagnetic forces. Forces $F_{x_i} = F_{x_{i1}} + F_{x_{i2}}$ act between the corresponding two coil phases, similarly F_{y_i}. Quantities v_x^b, v_y^b, ω_z^b are longitudinal, transversal and angular (around the q_z-axis) body velocities with respect to i-frame.

Due to Assumption 3.1.8 the solution for the line integral of the Lorentz force equation will result in constant values $\bar{l}_{x_{ij}}$ and $\bar{l}_{y_{ij}}$, respectively, representing the effective lengths of the dedicated coil phases inside the magnetic field. Taking into account the respective directions of current flow, the electromagnetic forces between the permanent magnet arrays and the single coil phases read

$$F_{x_{ij}}(q_x) = |i_{x_{ij}}\bar{l}_{x_{ij}}B_{x_{ij}}(q_x)\vec{e}_y \times \vec{e}_z| = |i_{x_{ij}}\bar{l}_{x_{ij}}B_{x_{ij}}(q_x)\vec{e}_x| = i_{x_{ij}}\bar{l}_{x_{ij}}B_{x_{ij}}(q_x) \quad (3.47)$$

$$F_{y_{ij}}(q_y) = |i_{y_{ij}}\bar{l}_{y_{ij}}B_{y_{ij}}(q_y)\vec{e}_x \times \vec{e}_z| = |i_{y_{ij}}\bar{l}_{y_{ij}}B_{y_{ij}}(q_y)\vec{e}_y| = i_{y_{ij}}\bar{l}_{y_{ij}}B_{y_{ij}}(q_y). \quad (3.48)$$

Note that solving the line integral is not necessary, since the motor constants $K_{mx_{ij}} = \bar{l}_{x_{ij}}\bar{B}$ may be obtained experimentally. Thus, with regard to Figure 3.8, the total sums of forces in the respective directions are

$$F_x(q_x, i_{x_{ij}}) = \sum_{i=1}^{2}\sum_{j=1}^{2} F_{x_{ij}}, \quad F_y(q_y, i_{y_{ij}}) = \sum_{i=1}^{2}\sum_{j=1}^{2} F_{y_{ij}}. \quad (3.49)$$

Notice, that for the computation of torque around the normal axis we should consider the fact that the lever arms depend on the yawing angle q_ϕ. Namely,

$$M_z = d_{x_1}(q_\phi)\, F_{x_1} - d_{x_2}(q_\phi)\, F_{x_2} + d_{y_2}(q_\phi)\, F_{y_2} - d_{y_1}(q_\phi)\, F_{y_1}, \quad (3.50a)$$

with lever arms

$$d_{x_1}(q_\phi) = \frac{d_1}{\cos(q_\phi)} + x\tan(q_\phi), \quad d_{x_2}(q_\phi) = \frac{d_1}{\cos(q_\phi)} - x\tan(q_\phi) \quad (3.50b)$$

$$d_{y_1}(q_\phi) = \frac{d_2}{\cos(q_\phi)} - y\tan(q_\phi), \quad d_{y_2}(q_\phi) = \frac{d_2}{\cos(q_\phi)} + y\tan(q_\phi) \quad (3.50c)$$

and the dedicated forces per coil system

$$F_{x_i} = \sum_{j=1}^{2} F_{x_{ij}}, \quad F_{y_i} = \sum_{j=1}^{2} F_{y_{ij}}, \quad i = 1, 2. \quad (3.50d)$$

Due to very small yaw angles of $q_{\phi,\max} = \pm 0.25°$ (see Assumption 3.1.9) we apply the small-angle approximation and drop the dependency on q_ϕ such that

$$M_z = d_2 \sum_{i,j=1}^{2} F_{y_{ij}}(-1)^i - d_1 \sum_{i,j=1}^{2} F_{x_{ij}}(-1)^i, \quad (3.51)$$

with d_1, d_2 denoting the distances from the mover's center of gravity to the centerline of the permanent magnet arrays. For brevity, we omit the dependencies in forces and torques on currents and positions, respectively.
Let us now drop the $\vec{(\cdot)}$-notation for vectors and vector valued functions. Doing so, and gathering the forces and torques in a vector $\tau = (F_x, F_y, M_z)^{\mathrm{T}}$ yields

$$\begin{pmatrix} F_x \\ F_y \\ M_z \end{pmatrix} = \begin{pmatrix} F_{x_{11}} + F_{x_{12}} + F_{x_{21}} + F_{x_{22}} \\ F_{y_{11}} + F_{y_{12}} + F_{y_{21}} + F_{y_{22}} \\ d_1\left(F_{x_{11}} + F_{x_{12}} - F_{x_{21}} - F_{x_{22}}\right) + d_2\left(F_{y_{21}} + F_{y_{22}} - F_{y_{11}} - F_{y_{12}}\right) \end{pmatrix}.$$

Since the currents are linear in the forces, the last statement forms a system of linear equations with matrix $\mathcal{B} : i \to \tau$, such that

$$\tau = \mathcal{B}i, \tag{3.52}$$

i.e.

$$\begin{pmatrix} F_x \\ F_y \\ M_z \end{pmatrix} = \begin{pmatrix} \bar{l}_{x11} B_{x11}(q_x) & 0 & d_1 \bar{l}_{x11} B_{x11}(q_x) \\ \bar{l}_{x12} B_{x12}(q_x) & 0 & d_1 \bar{l}_{x12} B_{x12}(q_x) \\ \bar{l}_{x21} B_{x21}(q_x) & 0 & -d_1 \bar{l}_{x21} B_{x21}(q_x) \\ \bar{l}_{x22} B_{x22}(q_x) & 0 & -d_1 \bar{l}_{x22} B_{x22}(q_x) \\ 0 & \bar{l}_{y11} B_{y11}(q_y) & -d_2 \bar{l}_{y11} B_{y11}(q_y) \\ 0 & \bar{l}_{y12} B_{y12}(q_y) & -d_2 \bar{l}_{y12} B_{y12}(q_y) \\ 0 & \bar{l}_{y21} B_{y21}(q_y) & d_2 \bar{l}_{y21} B_{y21}(q_y) \\ 0 & \bar{l}_{y22} B_{y22}(q_y) & d_2 \bar{l}_{y22} B_{y22}(q_y) \end{pmatrix}^T \begin{pmatrix} i_{x11} \\ i_{x12} \\ i_{x21} \\ i_{x22} \\ i_{y11} \\ i_{y12} \\ i_{y21} \\ i_{y22} \end{pmatrix} \tag{3.53}$$

where $\mathcal{B}$ is the control allocation matrix that expresses the position dependency of the field and the electromagnetic coupling of forces. Note that in terms of the magnetic flux density model this is the most general form. For simplicity, we assume further that $\forall i, j$ the effective lengths $\bar{l}_x = \bar{l}_{x_{ij}}$ and $\bar{l}_y = \bar{l}_{y_{ij}}$ such that the motor constants are given by $K_{mx} = \bar{l}_x \bar{B}$ as well as $K_{my} = \bar{l}_y \bar{B}$. Taking further the simplified flux density model into account yields

$$\mathcal{B}(q)^{\mathrm{T}} = \begin{pmatrix} K_{mx} \sin(\zeta_x) & 0 & d_1 K_{mx} \sin(\zeta_x) \\ K_{mx} \cos(\zeta_x) & 0 & d_1 K_{mx} \cos(\zeta_x) \\ K_{mx} \sin(\zeta_x) & 0 & -d_1 K_{mx} \sin(\zeta_x) \\ K_{mx} \cos(\zeta_x) & 0 & -d_1 K_{mx} \cos(\zeta_x) \\ 0 & K_{my} \sin(\zeta_y) & -d_2 K_{my} \sin(\zeta_y) \\ 0 & K_{my} \cos(\zeta_y) & -d_2 K_{my} \cos(\zeta_y) \\ 0 & K_{my} \sin(\zeta_y) & d_2 K_{my} \sin(\zeta_y) \\ 0 & K_{my} \cos(\zeta_y) & d_2 K_{my} \cos(\zeta_y) \end{pmatrix} \tag{3.54}$$

where $\zeta_x = \frac{2\pi}{T_m} q_x + \varphi_x$ and $\zeta_y = \frac{2\pi}{T_m} q_y + \varphi_y$. This completes the computation of forces.

Remark 3.1.2. Note that the assumptions on the ideal sinusoidal wave form distribution of the vertical flux density component may appear restrictive at first sight. However, they have a practical relevance. In fact, in practice sine and cosine functions are used for a commutation of the motor (see among others [35, 57, 121]). These commutation laws used throughout in practice directly stem from the assumption of an ideal sinusoidal field component. Such a sine-cosine commutation law is also applied in the PPS1405. Hence, we will use this assumption for the derivation of the commutation law, but at the same time, we study its impact in the presence of uncertain field distributions in Section 3.1.5.

Remark 3.1.3. Under ideal conditions the B_y component has zero force contribution because it is in parallel with the direction of current flow. Hence, the vector product in the Lorentz force equation is zero. This of course changes if there is a rotation of the magnet, or equally the mover, because the field direction gets more and more anti parallel with respect to the current flow. However, in accordance with the vector product this force component would be normal on the (q_x, q_y)–plane pointing in the direction of q_z. It will thus not influence translational motion. Due to the hard sensor constraints

on the yawing angle of $\pm 0.25^\circ$ encountered in the PPS1405 this influence is negligible.

Remark 3.1.4. Although we restricted our analysis to the translational forces and therefore the vertical flux density only, it is important to notice that the flux density component $B_x(q_x)$ has also a force contribution. Indeed, it gives rise to vertical forces along q_z. In practice this is sometimes used to actively levitate the mover of a planar motor. However, in the PPS1405 the vertical position cannot be controlled because of the following reasons. First, the vertical position is not measured which results in a lack of feedback information necessary for control. And second, the force necessary for levitation is not high enough. So, we must accept it as a parasitic effect. For a rough estimate of its effect it can be shown that the vertical force makes approximately 10 % of the translational force applied. According to [123] this results in a variation of the air gap of $\pm 1\,\mu\mathrm{m}$, which is acceptable. But these effects should be kept in mind. In practice one tries to optimize the magnet geometry such that these effects are minimized, while at the same time translational forces are maximized.

3.1.3 Commutation Law

The previous analysis shows that the electromagnetic forces/torques (3.52) depend on the position in a nonlinear, nonuniform manner. Furthermore, in view of the control task of Figure 2.2 (Section 2.1) we favor to specify reference forces $\tau^\star$ with respect to the physical degree of freedoms rather than reference currents $i^\star$ (actual control inputs). These issues are resolved with the so-called motor commutation law

$$i^\star = C_o(q)\,\tau^\star \tag{3.55}$$

that distributes the phase currents for obtaining the desired force independent from the mover position. For the generation of perfectly constant or homogeneous forces this ideally requires the exact knowledge of the field distributions with respect to the q_x and q_y axes, the exact knowledge of motor constants K_{mx}, K_{my} as well as the absence of current offsets, i.e. $p_0 = 0$.

In fact, composing the commutation law and the control allocation (3.52) indicates that the commutation law results from inversion of $\mathcal{B}(q)$. Since the system is *overactuated* with 8 control inputs for 3 degrees of freedom, we follow the ideas of [121] for deriving a commutation law that minimizes the electric power $\|i\|^2 = i_{x_{11}}^2 + \ldots + i_{y_{22}}^2$ subject to the equality constraint $\mathcal{B}\,i = \tau$, see [121]. Or written as a minimization problem

$$\begin{aligned} \min_{i} \quad & \|i\|^2 \\ s.t. \quad & \mathcal{B}i = \tau. \end{aligned}$$

This poses a least norm problem that may for instance be solved with the method of Lagrange multipliers. The classical solution reads

$$i^\star(t) = \mathcal{B}(q)^{\mathrm{T}} \left(\mathcal{B}(q)\mathcal{B}(q)^{\mathrm{T}}\right)^{-1} \tau^\star(t) = C_o(q)\,\tau^\star(t), \tag{3.56}$$

where of course $C_o(q)$ represents the Moore-Penrose pseudoinverse of $\mathcal{B}(q)$. For the field distribution according to (3.44) and (3.45) this yields

$$C_o(q) = \begin{pmatrix} \frac{\sin(\zeta_x)}{2K_{mx}} & 0 & \frac{d_1 K_{mx}\sin(\zeta_x)}{2\left(d_1^2K_{mx}^2+d_2^2K_{my}^2\right)} \\ \frac{\cos(\zeta_x)}{2K_{mx}} & 0 & \frac{d_1 K_{mx}\cos(\zeta_x)}{2\left(d_1^2K_{mx}^2+d_2^2K_{my}^2\right)} \\ \frac{\sin(\zeta_x)}{2K_{mx}} & 0 & -\frac{d_1 K_{mx}\sin(\zeta_x)}{2\left(d_1^2K_{mx}^2+d_2^2K_{my}^2\right)} \\ \frac{\cos(\zeta_x)}{2K_{mx}} & 0 & -\frac{d_1 K_{mx}\cos(\zeta_x)}{2\left(d_1^2K_{mx}^2+d_2^2K_{my}^2\right)} \\ 0 & \frac{\sin(\zeta_y)}{2K_{my}} & -\frac{d_2 K_{my}\sin(\zeta_y)}{2\left(d_1^2K_{mx}^2+d_2^2K_{my}^2\right)} \\ 0 & \frac{\cos(\zeta_y)}{2K_{my}} & -\frac{d_2 K_{my}\cos(\zeta_y)}{2\left(d_1^2K_{mx}^2+d_2^2K_{my}^2\right)} \\ 0 & \frac{\sin(\zeta_y)}{2K_{my}} & \frac{d_2 K_{my}\sin(\zeta_y)}{2\left(d_1^2K_{mx}^2+d_2^2K_{my}^2\right)} \\ 0 & \frac{\cos(\zeta_y)}{2K_{my}} & \frac{d_2 K_{my}\cos(\zeta_y)}{2\left(d_1^2K_{mx}^2+d_2^2K_{my}^2\right)} \end{pmatrix}. \tag{3.57}$$

It turns out that the minimum power commutation coincides with the well-known sine-cosine-commutation in motion control and electric machine engineering [57, 117, 121]. The intuition behind this commutation law is the trigonometric identity $\sin^2(x) + \cos^2(x) = 1$.

This becomes clear, if e.g. equation (3.52) is considered for the generation of $F_x^\star$. Substituting $i^\star$ for i in (3.52) with $i^\star$ according to (3.56) yields

$$F_x = b_1^{\mathrm{T}} c_1 F_x^\star, \tag{3.58}$$

where b_1^{T} and c_1 denote respectively, the first row of $\mathcal{B}(q)$ and the first column of $C_o(q)$. Inserting the respective expressions for b_1 and c_1 we finally obtain

$$F_x = b_1^T c_1 F_x^\star = \left(\sin^2(\zeta_x) + \cos^2(\zeta_x)\right) F_x^\star = F_x^\star.$$

The fact that the motor constants K_{mx} and K_{my} appear inside the commutation matrix is not appealing from a practical point of view because these parameters are somehow hidden inside of this matrix. This fact renders it complicated to analyze uncertainties in the motor constants. Therefore, we next introduce a mathematically equivalent scheme that allows us to have direct access on the motor constants. The equivalent commutation scheme is given by equations

$$i^\star = \bar{C}_o\, i_c^\star, \quad i_c^\star = K_m^{-1}\tau^\star, \tag{3.59}$$

where

$$\bar{C}_o(q) = \begin{pmatrix} \sin(\zeta_x) & 0 & \frac{d_1 \sin(\zeta_x)}{\left(d_1^2+d_2^2\right)} \\ \cos(\zeta_x) & 0 & \frac{d_1 \cos(\zeta_x)}{\left(d_1^2+d_2^2\right)} \\ \sin(\zeta_x) & 0 & -\frac{d_1 \sin(\zeta_x)}{\left(d_1^2+d_2^2\right)} \\ \cos(\zeta_x) & 0 & -\frac{d_1 \cos(\zeta_x)}{\left(d_1^2+d_2^2\right)} \\ 0 & \sin(\zeta_y) & -\frac{d_2 \sin(\zeta_y)}{\left(d_1^2+d_2^2\right)} \\ 0 & \cos(\zeta_y) & -\frac{d_2 \cos(\zeta_y)}{\left(d_1^2+d_2^2\right)} \\ 0 & \sin(\zeta_y) & \frac{d_2 \sin(\zeta_y)}{\left(d_1^2+d_2^2\right)} \\ 0 & \cos(\zeta_y) & \frac{d_2 \cos(\zeta_y)}{\left(d_1^2+d_2^2\right)} \end{pmatrix} \tag{3.60}$$

is a "gainless" commutation matrix without any motor constants and

$$K_m = \begin{pmatrix} 2K_{mx} & 0 & 0 \\ 0 & 2K_{my} & 0 \\ 0 & 0 & 2K_{m\phi} \end{pmatrix} \tag{3.61}$$

is a constant diagonal matrix with the doubled motor constants representing each pair of the linear motors for the respective motion axes, while

$$K_{m\phi} = \frac{(d_1^2 K_{mx} + d_2^2 K_{my})}{d_1^2 + d_2^2}. \tag{3.62}$$

In fact it is easy to show that

$$\tau^\star = \mathcal{B}(q)\, i^\star = \mathcal{B}(q)\bar{C}_o(q)\, i_c^\star = K_m\, i_c^\star = \tau^\star \tag{3.63}$$

and is hence equivalent to (3.56). With this law, apparently the inversion of the motor constants appears from outside such that the effect of uncertainties with respect to these quantities is more visible. The effect of matrix $\bar{C}_o$ on $\mathcal{B}$ is the mere compensation of the nonlinearities of the flux density distribution leaving outside the motor constants.

Since the elements of K_m have the physical units of Newton per Ampere

$$i_c^\star = \begin{pmatrix} i_x^\star & i_y^\star & i_\phi^\star \end{pmatrix}^{\mathrm{T}} \tag{3.64}$$

represents a vector of (virtual) currents, one for each axis. In the literature variable i_c is also referred to as input current command [35]. Intuitively, this version of the commutation law resembles an analogy to rotary DC-motors.

By virtue of the fact that both laws are equivalent they might be used interchangeably. So, if we are concerned with the analysis of a nominal or an ideal system then we will use the version from (3.56). Otherwise we make use of (3.59).

Remark 3.1.5. Note that $\bar{C}_o(q)$ may be derived by the Moore-Penrose-inverse of $\bar{\mathcal{B}}(q)$, where

$$\bar{\mathcal{B}}(q) = \mathcal{B}(q)\Big|_{\substack{K_{mx}=1/2 \\ K_{my}=1/2}}. \tag{3.65}$$

Remark 3.1.6. It is important to notice that the commutation matrices not necessarily

need to be made up of sine and cosine functions. If the knowledge of the field distribution is better than only sine and cosine, then this knowledge might be included inside $\mathcal{B}$ or $\bar{\mathcal{B}}$ respectively. In practice it is also possible to measure the flux density distribution online by means of Hall effect sensors [57]. The commutation matrices can thus be fed directly by these values.

3.1.4 Mechanical Equations of Motion

Rigid Body Dynamics

We refer to [41] for the mover's mechanical equations of motion. This includes the velocity transformation

$$\dot{q}(t) = R(q_\phi)\,\nu(t), \tag{3.66}$$

and the well-known Newton-Euler-equations with respect to the body fixed frame (b-frame)

$$m\,(\dot{v}_c(t) + \omega(t) \times v_c(t)) = f_c(t) \tag{3.67}$$

$$I_c\,\dot{\omega}(t) + \omega(t) \times (I_c\,\omega(t)) = m_c(t). \tag{3.68}$$

In these equations, $\dot{q} \in \mathbb{R}^3$ is the velocity in the inertial frame and

$$R(q_\phi) = \begin{pmatrix} \cos(q_\phi) & -\sin(q_\phi) & 0 \\ \sin(q_\phi) & \cos(q_\phi) & 0 \\ 0 & 0 & 1 \end{pmatrix} \in \mathrm{SO}(3) \tag{3.69}$$

is an orthogonal matrix transforming b-frame velocity $\nu = (v_x^b, v_y^b, \omega_z^b)^{\mathrm{T}}$ into i-frame (Figure 3.8). Moreover, $v_c = (v_x^b, v_y^b, 0)^{\mathrm{T}}$, $\omega = (0, 0, \omega_z^b)^{\mathrm{T}}$, $f_c = (f_x^b, f_y^b, 0)^{\mathrm{T}}$, $m_c = (0, 0, m_z^b)^{\mathrm{T}}$ are linear velocity, angular velocity, propelling forces and torques of the mover, respectively, all defined in b-frame. Variables m and $I_c \in \mathbb{R}^{3\times3}$ are the mover's mass and inertia tensor. Assumption 3.1.9 and planar motion imply the zeros in ω, m_c, v_c and f_c. Since the b-frame origin coincides with the center of gravity (CG) and the principle axes of rotation [41], the inertia tensor I_c is diagonal. Inserting v_c, ω, f_c and m_c in (3.67), (3.68) and enhancement by a linear damping $\tau_d^b(t) = -D\,\nu(t)$ yields

$$M\,\dot{\nu}(t) + C(\nu)\,\nu(t) + D\,\nu(t) = \tau^b(t) \tag{3.70}$$

as the dynamics in b-frame coordinates with

$$M = \begin{pmatrix} m & 0 & 0 \\ 0 & m & 0 \\ 0 & 0 & I_z \end{pmatrix},\ C(\nu) = \begin{pmatrix} 0 & -m\,\omega_z^b(t) & 0 \\ m\,\omega_z^b(t) & 0 & 0 \\ 0 & 0 & 0 \end{pmatrix} \tag{3.71}$$

as mass and Coriolis matrix, respectively, $D = \mathrm{diag}(d_x, d_y, d_\phi)$ the damping matrix and $\tau^b = (f_x^b, f_y^b, m_z^b)^{\mathrm{T}}$ forces/torque in b-frame. Inverting the velocity transformation and using

$$\dot{\nu}(t) = R^{-1}(q_\phi)\left(\ddot{q}(t) - \dot{R}(q_\phi)\,R^{-1}(q_\phi)\,\dot{q}(t)\right), \tag{3.72}$$

where $\dot{R}(q_\phi) = R(q_\phi)\, S(\omega)$ the dynamics of the mover can partially be expressed in the i-frame coordinates:

$$R^{-1}(q_\phi)\left(M\ddot{q}(t) + \bar{C}(\dot{q})\dot{q}(t) + D\dot{q}(t)\right) = \tau^b(t). \tag{3.73}$$

Note that the Coriolis term $\bar{C}(\dot{q}) = (mI - M)\, S(\dot{q}) \in \mathbb{R}^{3\times 3}$ made up of I as identity matrix and the skew symmetric cross product operator $S(\dot{q})$ [41] vanishes. Note further that $S(\dot{q}) = \frac{1}{m}C(\dot{q})$ and $S(\omega) = \frac{1}{m}C(\nu)$ since $\dot{q}_\phi = \omega_z^b$ (see last row of $R(q_\phi)$).

As we have assumed that the electromagnetic forces always act perpendicularly to the coils (see Assumption 3.1.9 and Figure 3.8) the forces propelling the mover act in i-frame. Their expression in b-frame requires the rotation $\tau^b = R^{-1}(q_\phi)\tau$. This finally yields the dynamics now in i-frame

$$M\ddot{q}(t) + D\dot{q}(t) = \tau(t) = B(q)\, i(t). \tag{3.74}$$

Note that for planar motion no gravitational terms occur. Inserting the commutation law

$$i^\star(t) = C_o(q)\tau^\star(t) \tag{3.75}$$

from (3.56) and C_o as in (3.57) into the right hand side of (3.74) we obtain

$$M\ddot{q}(t) + D\dot{q}(t) = \tau^\star(t) \tag{3.76}$$

constituting the rigid body dynamics of the mover, being completely linear. Due to the special structure of matrices M and D, it is obvious that under ideal conditions axes are naturally decoupled from each other such that we can treat every individual axis as a simple single input single output system. Doing so and dropping the $\cdot^\star$ superscript yields

$$m\ddot{q}_x(t) + d_x\dot{q}_x(t) = F_x(t) \tag{3.77}$$
$$m\ddot{q}_y(t) + d_y\dot{q}_y(t) = F_y(t) \tag{3.78}$$
$$I_c\ddot{q}_\phi(t) + d_\phi\dot{q}_\phi(t) = M_z(t) \tag{3.79}$$

Due to the fact that all axes share the same dynamics but possess different parameters, we introduce a one dimensional generic axis model given by

$$m_l\ddot{q}_l(t) + d_l\dot{q}_l(t) = F_l(t), \tag{3.80}$$

that shall represent every individual axis of the stage. Thereby, we use the following definitions

$$l \in \{x, y, \phi\}, \quad m_x = m_y := m, \quad m_\phi := I_c, \quad F_\phi := M_z. \tag{3.81}$$

Remark 3.1.7. Note that we did not use the model of the DCAs yet. Here we simply assumed ideal conditions, i.e. the fact that the commanded or desired current is equal to the current through the coils. The effect of imperfect DCAs is explained in Section 3.1.5.

Flexible Dynamics

Besides the rigid body dynamics it is also important to take flexibilities and structural modes into account. Following reference [114] mainly three sources of flexibilities are encountered in electromechanical drives/devices. That is

- actuator flexibilities
- guiding system flexibilities and
- stator or machine frame flexibilities.

Due to the simple and flat, integrated design of planar actuators the effect of the former two sources is relatively small and therefore neglected at first sight (see discussion in Section 2.3.3). However, inherent flexibilities in the machine frame (stator) and the inextricably linked lightly damped vibrations of the latter have an immense influence on the mover dynamics. In fact, they pose critical challenges in achieving performance specifications such as high tracking bandwidth or low settling times of servo errors [114, 125].

Indeed, the main cause of such vibrations is the reaction force of the mover imparted on the stator. Due to the fact that the stator constitutes a mass with limited stiffness and low damping, it is exited by these forces and caused to vibrate. Since the mover moves on the stator base and relative to it, these vibrations appear as input perturbations acting on the mover. They are characterized by long-tailed transients with typical frequencies between 1–10 Hz [125]. Of course, any other external disturbance can excite the frame resulting in the same detrimental effects.

Due to a relatively low mass ratio of the PPS1405 of $300/20$ between base (stator) and load (mover), exactly these effects have been experienced throughout the experiments. This fact is illustrated in Figure 3.9. It shows the tracking error of a servo controller in a point-to-point motion task. The controller, which was designed on the basis of the rigid body dynamics, clearly shows the long-tailed oscillations having a detrimental impact on positioning accuracy and settling time. For a sufficient reduction of these oscillations they must be taken into consideration.

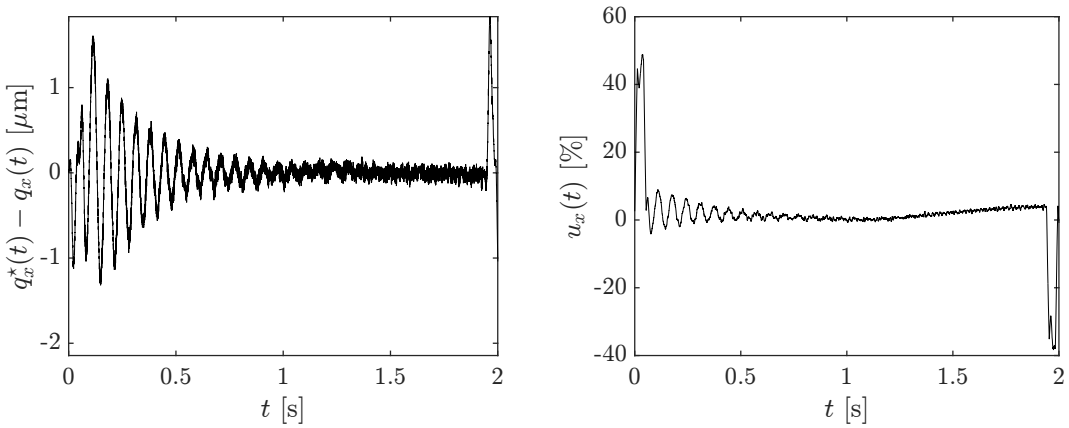

FIGURE 3.9: Tracking error (left) and control input (right) for a servo controller in a point-to-point motion task.

In order to account for these effects and structural modes in general, the biggest moving masses of a machine are typically modeled as individual masses coupled by springs

and dampers [13, 114, 125, 133]. In doing so, an abstract model representation, accounting for the frame vibration, may be given by the mass spring damper system shown in Figure 3.10. The figure presents the generic one axis model of the motion stage with

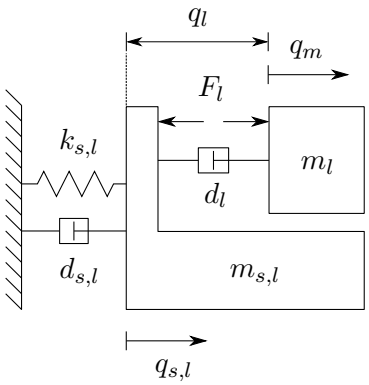

FIGURE 3.10: Abstract mass spring damper model for the description of compliance between stator and mover, analogues to models presented in [114, 125].

additional compliance of the stator. The equations of motion for the simple model are given by

$$m_{s,l}\ddot{q}_{s,l}(t) = -d_{s,l}\dot{q}_{s,l}(t) - k_{s,l}q_{s,l}(t) + d_l\left(\dot{q}_m(t) - \dot{q}_{s,l}(t)\right) - F_l(t) \tag{3.82}$$

$$m_l\ddot{q}_m(t) = -d_l\left(\dot{q}_m(t) - \dot{q}_{s,l}(t)\right) + F_l(t) \tag{3.83}$$

where $m_{s,l}$ and m_l are stator and mover mass/inertia, $k_{s,l}$ and $d_{s,l}$ are stator stiffness and damping, while q_m, $q_{s,l}$ and q_l denote, position/angle of mover mass, position/angle of stator mass and measured output as the relative displacement between stator and mover given by

$$q_l(t) = q_m(t) - q_{s,l}(t). \tag{3.84}$$

Differentiating the last equation twice with respect to time and substitution into (3.83) yields

$$\ddot{q}_l(t) = -\frac{d_l}{m_l}\dot{q}_l(t) + \frac{1}{m_l}F_l(t) - \ddot{q}_{s,l}(t) \tag{3.85}$$

$$\ddot{q}_{s,l}(t) = -\frac{d_{s,l}}{m_{s,l}}\dot{q}_{s,l}(t) - \frac{k_{s,l}}{m_{s,l}}q_{s,l}(t) + \frac{d_l}{m_{s,l}}\dot{q}_l(t) - \frac{1}{m_{s,l}}F_l(t) \tag{3.86}$$

as a generic model for an individual axis.

Remark 3.1.8. Apparently, from equations (3.85) and (3.86) the effect of stator motion on the mover dynamics is visible. Indeed, the differential equation with respect to the measured output q_l constitutes the rigid body dynamics of the mover (cf. (3.80)) that is perturbed by the stator acceleration. Hence, the effect can also be interpreted as an external perturbation, affecting the mover.

Note further that in the frequency domain the stator dynamics creates a complex conjugate pair of poles and zeros in the transfer function from F_l to q_l of (3.85) and (3.86). It thus represents the so-called internal dynamics of the system. On the other hand, the differential equation (3.85) constitutes the external dynamics. This terminology will be treated more precisely in Section 3.2.

Another interesting observation is the fact that due to the existence of only one control input, one has to trade high performance positioning control of the mover off for vibration damping of the stator or vice versa [125].

Remark 3.1.9. In view of the model abstraction the following should be noted. For a more precise modeling of structural modes one would actually model every single element inside the machine by means of a coupled mass spring damper approach because every mechanical element attached to the machine has its own resonance frequency contributing to some extend to the frequency characteristics of the motion stage. So, this approach would actually involve that in addition to stator and mover the following elements should also be considered in a coupled mass spring damper modeling approach: the sensor head, the sensor grid, the coils, the magnet arrays and the air bearings. Since every element contributes with a model order of two the model order of the resulting model grows fast as each of these elements is added. Owing to the fact that these elements have a wide range of time constants usually such a model is numerically stiff and consequently complicates controller design due to numerical issues. Hence, we try to keep the modeling complexity low by restricting on the most significant dynamics. Another problem of these more complex models is the fact that model parameters appear unmatched, which means that they are not in the span of the input matrix. This in fact is undesirable in terms of adaptive control approaches.

3.1.5 Phenomenological Disturbance Models

Disturbances encountered in the motion system in question may be classified as environmental disturbances, e.g. floor vibration or other external forces on the mover or stator, and system inherent disturbances or parasitic effects. This section is dedicated to the latter class. These disturbances generally arise due to the imperfectness of the magnetic field wave form distribution as a result of component tolerances as well as parasitic forces caused by magnetization and eddy current effects [123] of ferromagnetic components. Since in accordance with [123] the analytical computation of eddy current and magnetization effects is expensive, in this section we propose phenomenological models for describing the phenomena that have been observed throughout the experiments. Some typical disturbances in the context of planar motors are also presented in [57, 117, 118, 135].

Firstly, commutation errors occur if the actual flux density distribution deviates from the theoretical design captured in $\mathcal{B}(q)$. The analytical model for the permanent magnet array (3.37)-(3.43) derived earlier is very well suited for describing such effects in a high fidelity simulation environment. Another very simple one dimensional model was presented in our work in [141] which accounts for these effects in a phenomenological manner.

The key idea of this model basically stems from the observation that the wave form of the real flux density distribution often shows distortions at the top and the zero crossings. This effect has been recreated by the use of tangent-hyperbolic and sine-hyperbolic functions, respectively. These are successively applied to the nominally expected sinusoidal flux density distribution, namely

$$B^p_{x_{ij}} = \alpha_1 \tanh\left(\alpha_2 \sinh(\alpha_3 B_{x_{ij}}(q_x))\right) \tag{3.87}$$

$$B^p_{y_{ij}} = \alpha_1 \tanh\left(\alpha_2 \sinh(\alpha_3 B_{y_{ij}}(q_y))\right). \tag{3.88}$$

The free parameters $\alpha_1, \alpha_2, \alpha_3 \in \mathbb{R}$ are for shaping the waveform. Figure 3.11 shows a comparison of the model with another flux density measurement (black), measured with a Hall effect sensor. Despite the extreme simplicity of the model a very good model fit (red) with the real flux density is achieved. It could also be modeled by a sine wave with higher harmonics similar to the approach in [118].

Inserting this magnetic field model or the one from (3.37)-(3.43) in $\mathcal{B}(q)$, yields the parasitic control allocation matrix $\mathcal{B}^p(q)$ such that $\Delta\mathcal{B}(q) = \mathcal{B}^p(q) - \mathcal{B}(q)$ may denote its deviation from the ideal description.

However, most significant is the influence from external forces due to magnetization-effects of ferromagnetic components in the traversing range (see Figure 3.14). These forces mainly arise from cogging/reluctance forces. Further external forces are spring forces of air supply hoses and downhill-slope forces due to an inaccurate adjustment of the stator.

A closed-loop experiment was conducted with the mover operated in constant velocity. We identified the external disturbances during the experiment through analysis of the control signal in a velocity controller as a measure of the external disturbances. Figure 3.12 indicates a strong correlation between force ripple and ferromagnetic coil-screw positions. The external parasitic forces are direction dependent and linearly scale with the magnitude of the velocity. In this regard, we propose the following phenomenological model for the generic axes:

$$F_{p,l}(q_l, \dot{q}_l) = \begin{cases} d_{p,l}\,\dot{q}_l + \bar{F}^{+}_{p,l}(q_l), & \text{for } \dot{q}_l \geq 0 \\ d_{p,l}\,\dot{q}_l + \bar{F}^{-}_{p,l}(q_l), & \text{for } \dot{q}_l < 0 \end{cases} \tag{3.89}$$

with direction dependent $\bar{F}^{+}_{p,l}(q_l)$ and $\bar{F}^{-}_{p,l}(q_l)$ (Figure 3.12), damping coefficient $d_{p,l} > 0$ and l as defined in (3.81). As a result of aerostatic levitation, static friction effects are absent. Therefore, for a softer transition between the direction dependent terms we use

$$F_{p,l}(q_l, \dot{q}_l) = d_{p,l}\,\dot{q}_l + \tfrac{1}{2}\left(\tanh(\delta\dot{q}_l) + 1\right)\,\bar{F}^{+}_{p,l}(q_l) - \tfrac{1}{2}\left(\tanh(\delta\dot{q}_l) - 1\right)\,\bar{F}^{-}_{p,l}(q_l) \tag{3.90}$$

with $\delta > 0$. Note that this implements a smooth kind of coulomb plus viscous friction model [4].

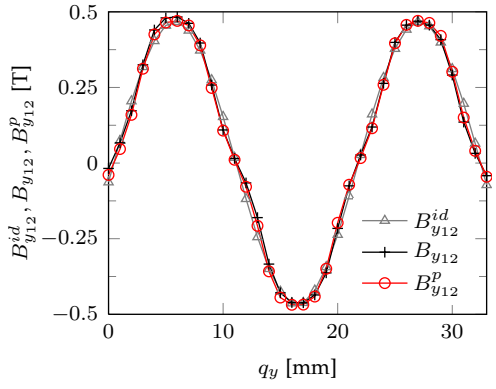

FIGURE 3.11: Comparison of ideal (sinusoidal) B^{id}_{y12}, measured B_{y12} and simulated/modeled B^{p}_{y12} magnetic flux density distributions of the $\mathcal{Y}_1$-PMA along the q_y-axis. The phenomenological magnetic flux model uses parameters $\bar{B} = 0.4677$, $\alpha_1 = 0.4851$, $\alpha_2 = 0.1877$, $\alpha_3 = 6.6367$, $T_m = 21.3423$ and $\varphi_x = -0.1355$ obtained via curve fitting. The normalized root mean square error between measured and simulated distributions is 1.32%.

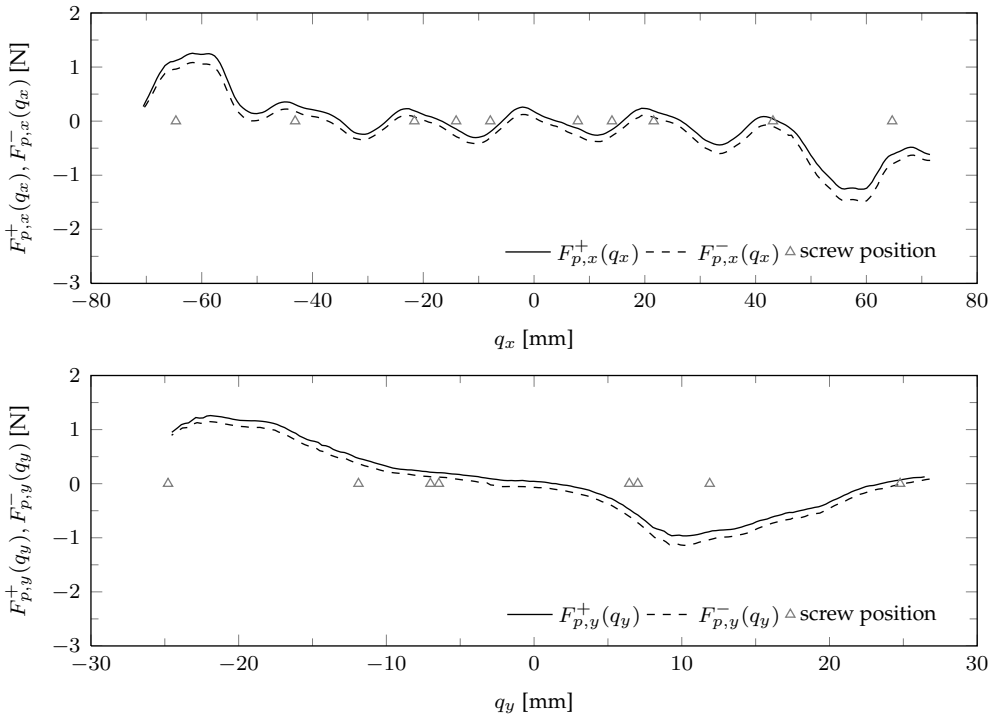

FIGURE 3.12: Experimentally identified parasitic forces for $q_x, q_\phi \equiv 0 \wedge q_y \in [-24, 24]$ mm (upper Figure) and $q_y, q_\phi \equiv 0$ and $q_x \in [-70, 70]$ mm due to magnetization of ferrous screws that fix the coils.

Stacking the parasitic forces $F_{p,l}$ for all l in consecutive order into the vector $\tau^p(q, \dot{q})$ these models combine to the total forces

$$\tau_{total} = (\mathcal{B}(q) + \Delta\mathcal{B}(q))\, i(t) - \tau^p(q, \dot{q}), \tag{3.91}$$

acting at the input of the motion stage. Taking also the DCA model (3.16) and the commutation law (3.59) into account, the total forces combine as per

$$\begin{aligned} \tau_{total} &= p_1 K_m i_c^\star + p_1 \Delta\mathcal{B}(q)\bar{C}_o(q) i_c^\star + (\mathcal{B}(q) + \Delta\mathcal{B}(q))p_0 - \tau^p(q, \dot{q}) \\ &= p_1 \tau^\star - f_d(q, \dot{q}), \end{aligned} \tag{3.92}$$

where $i_c^\star = K_m^{-1}\tau^\star$. Now let us briefly elaborate on the influence and the significance of these effects. Apparently, the DC-gain p_1 of the closed current loop constitutes the (force) input gain for the mechanical system that has been identified in Section 3.1.2. The second term represents force and torque ripple as a result of errors in the commutation scheme. Roughly speaking, these can be seen as modulations of the entries in $\Delta\mathcal{B}$ with sine and cosine functions. It thus constitutes a periodical disturbance dependent on position. Since it scales the control input in dependence of the actual position, this effect can also be interpreted as a fluctuation of the input gain which can greatly be addressed to adaptive control algorithms.

In order to get a rough idea on the extent of these effects, a typical force ripple is shown in Figure 3.13. In this example, on the basis of the analytical magnet model (3.37)-(3.43) (parameters see Table 3.1), the force ripple is computed for motion along q_y. Without loss of generality we set $K_{my} = 1$ and normalized the ideal sinusoidal and the true field distributions $B^p_{x_{1j}}$ (cf. Figure 3.13 (a)). Please note that the value of the

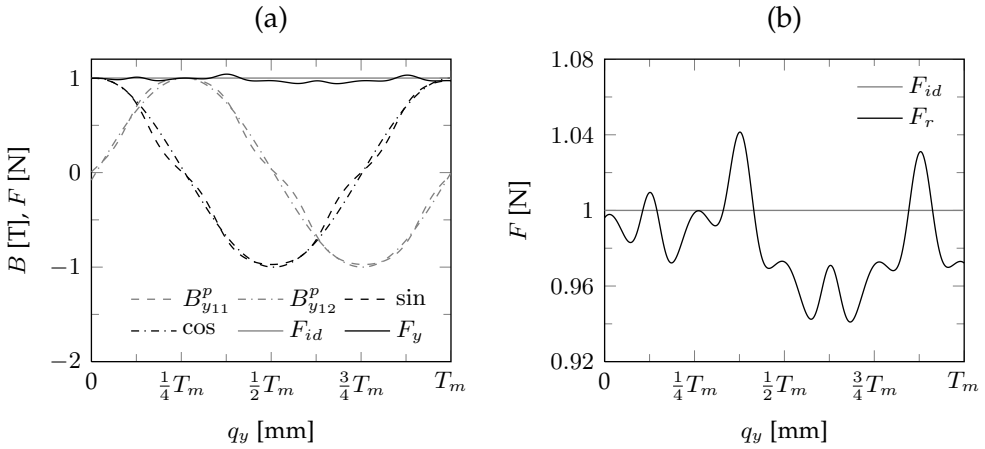

FIGURE 3.13: Force ripple due to commutation errors along q_y examined over one magnet period T_m. Magnetic field distributions $B^p_{y_{1j}}$ compared to ideal sine and cosine distributions and the resulting ideal F_{id} and actual applied force distribution F_y over q_y (a). Close up of the forces in (b).

motor constant has no effect on the value of the ripples since the motor constant itself is compensated inside the commutation law. Additionally, we commanded a constant translational force of $F_y^\star = 1\,\mathrm{N}$. With application of the sinusoidal commutation law from (3.56) the actual force F_y imparted on the mover slightly deviates from the commanded one. In fact, it shows ripples with peak values between 4–6% of the applied force which is tolerable (cf. Figure 3.13 (b)).

This shows that commutation errors do have an effect. However, during experiments and simulations it has been observed that when treated as an external input disturbance (lumped disturbance approach) these effects could greatly be suppressed by means of feedback control including integral action. Therefore, for simplicity we will treat it as a lumped input disturbance, lumped into $f_d(q, \dot{q})$.

Note that the control algorithms to follow will be designed to tolerate an even higher uncertainty in the input gain such that these relatively small fluctuations are dominated by these uncertainties. So, if the controller can handle these higher uncertainties it will also handle commutation errors considerably well.

The third term is only presented for the sake of completeness, in order to show that offsets or asymmetries p_0 in the power amplifiers also give rise to parasitic force ripples. As discussed in Section 3.1.2 the offset vector in our case is negligible. What is interesting about offsets, is the fact that they create linear combinations with the true force allocation matrix of the process. In reference [117] this remarkable property is used for an off-line identification of the entries in the force allocation matrix. Although not apparent in the case of the PPS1405 these disturbances can also be included in $f_d(q, \dot{q})$ without any problems.

The greatest influence however emanates from the last term of (3.92) as discussed earlier. Please note that the functions $\bar{F}^+_{p,l}$ and $\bar{F}^-_{p,l}$ also partially include commutation errors since these have been identified from a closed loop experiment that of course included these effects. We also lump this disturbance into $f_d(q, \dot{q})$.

Finally, from these observations we can conclude that the most prominent disturbances encountered in the motion stage system essentially occur at the control input,

where they appear as matched uncertainties. Obviously, for precise trajectory tracking the controller has to reject or suppress $f_d(q, \dot{q})$ in an application relevant frequency band. Indeed, this is challenging since the frequency of the periodic force ripples scales with mover velocity. A detailed discussion on that can be found in [117, 118].

Remark 3.1.10. In the face of our application luckily the influence of commutation errors turns out less. However, it should be noted that strictly speaking, commutation errors resemble fluctuations of the input gain. Moreover, it can be shown that commutation errors can lead to a parasitic coupling of control inputs. This should be checked from application to application in order to evaluate the impact on the system in question.

In order to transfer these insights to the generic axis model from (3.85) and (3.86), we define

$$f_d(q, \dot{q}) = \begin{pmatrix} \bar{f}_{1,x}(q_x, \dot{q}_x) & \bar{f}_{1,y}(q_y, \dot{q}_y) & \bar{f}_{1,\phi}(q_\phi, \dot{q}_\phi) \end{pmatrix}^{\mathrm{T}} \tag{3.93}$$

such that $\bar{f}_{1,l}(q_l, \dot{q}_l)$ represents one of these disturbances in the respective directions. We further define

$$x_1(t) := q_l(t), \quad x_2(t) := \dot{q}_l(t), \quad x_3(t) := q_{s,l}(t), \quad x_4(t) := \dot{q}_{s,l}(t) \tag{3.94}$$

as system states and substitute (3.86) into (3.85). Furthermore, we define $u_1(t) := i_l^\star(t)$ as an element of $i_c^\star$ as control input and $f_{1,l} := \bar{f}_{1,l}/(2p_1K_{ml})$. Finally, omitting index l for simplicity yields the following generic single axis LTI state space model

$$\begin{aligned} \dot{x}(t) &= Ax(t) + B(u_1(t) - f_1(x,t)), \quad x(0) = x_0 \\ y(t) &= Cx(t)\,, \end{aligned} \tag{3.95}$$

where

$$A = \begin{pmatrix} 0 & 1 & 0 & 0 \\ 0 & -a_1 & a_2 & a_3 \\ 0 & 0 & 0 & 1 \\ 0 & a_4 & -a_2 & -a_3 \end{pmatrix}, \quad B = \begin{pmatrix} 0 \\ b_1 \\ 0 \\ -b_2 \end{pmatrix}, \quad C^{\mathrm{T}} = \begin{pmatrix} 1 \\ 0 \\ 0 \\ 0 \end{pmatrix}, \tag{3.96}$$

while

$$a_1 = \left(\frac{d_l}{m_l} + \frac{d_l}{m_{s,l}}\right), \qquad a_2 = \frac{k_{s,l}}{m_{s,l}}, \qquad a_3 = \frac{d_{s,l}}{m_{s,l}}, \tag{3.97}$$

$$a_4 = \frac{d_l}{m_{s,l}}, \qquad b_1 = 2p_1K_{ml}\left(\frac{1}{m_{s,l}} + \frac{1}{m_l}\right), \qquad b_2 = \frac{2p_1K_{ml}}{m_{s,l}}, \tag{3.98}$$

Note that due to the linearity of the term $d_{p,l}\dot{q}_l$ in (3.90), this term is directly inserted into A and absorbed by a_1.

A comparison of experimental position data to the overall motion stage model is shown in Figure 3.14. It shows several open loop step responses of the process along the translational motion axes. These step responses have been applied at the very beginning of our investigations for gaining first insights and some intuition over the process. Clearly, the influence of external forces can be recognized by the waviness of the position signals. However, the overall model match is nearly perfect.

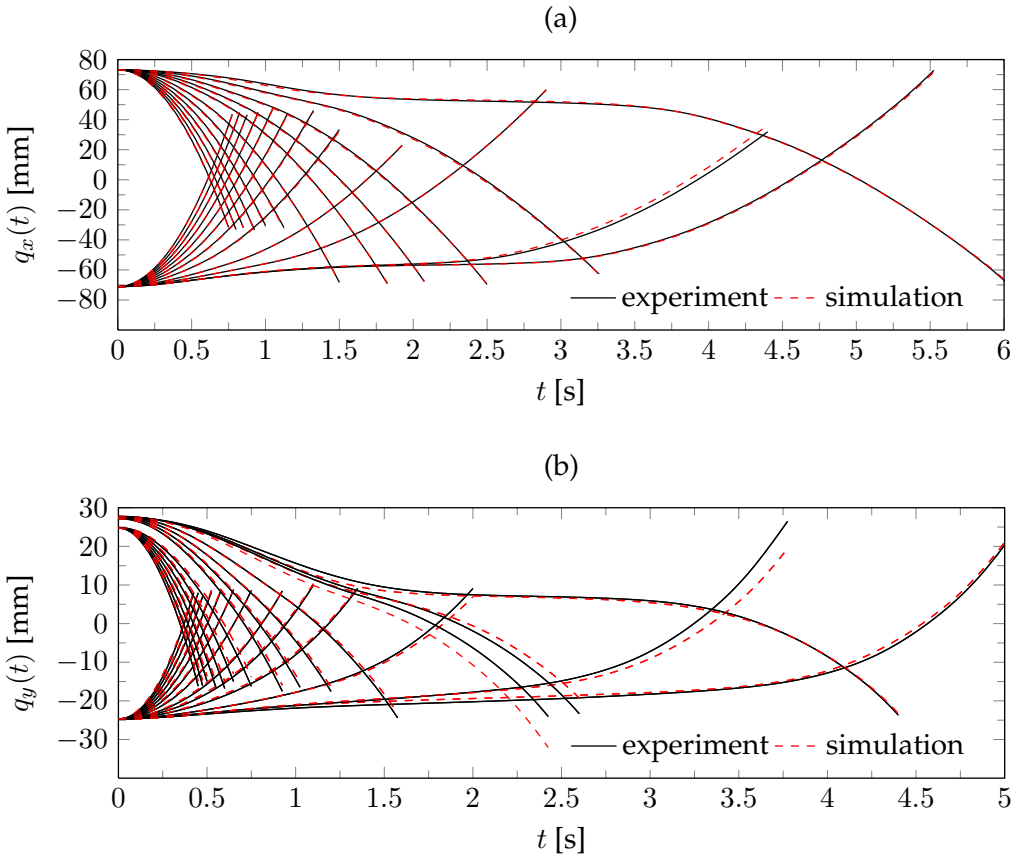

FIGURE 3.14: Comparison of experimental position data with simulations on the proposed model for current/force step responses (in whole current/force range of 0–3 A,0–10 N) over the entire traversing range along the q_x and q_y-axes.

3.1.6 Closed Loop Frequency Response Measurements

Although the open loop responses show an excellent match, these experiments show no visible evidence for the occurrence of vibration of the stator part. However, as discussed in Section 3.1.4 and as shown in Figure 3.9, closed loop experiments revealed that there are substantial effects due to structural modes.

Since the dynamics of the motion stage is dominantly linear, a simple and effective means of identifying resonances is the measurement of the frequency response function (FRF) of the process. This is also to validate the theoretical modeling approach and verify whether there are further effects not taken into consideration so far.

By virtue of the fact that the process is not BIBO stable the measurement of the FRF can only be accomplished in a closed loop experiment. Such an experiment was designed in the work of [93]. To this end, three simple PID controllers, one for each axis, were designed for the mere stabilization of the process. For the excitation of the process a crested multi-sine signal with logarithmic frequency spacing was used due to the remarkable properties of these signals [110].

In a closed loop experiment a bias free estimate of the open loop process FRF might be obtained via indirect FRF measurements [110]. Roughly speaking, this means that either the sensitivity or the complementary sensitivity function is measured, while the transfer function of the process is recomputed via the known controller transfer function and the equations of the standard feedback loop (see [7, 93, 110] and references

therein).

Remark 3.1.11. The presence of nonlinear perturbations and input disturbances at the motion stage raises doubts about the validity of the FRF, and at first sight, leads to the intuition of a corrupted FRF or the existence of bias errors such that the FRF has no useful meaning. However, in the work of [93], the influence of exactly these effects on the motion stage's FRF has been investigated. It was found that these disturbances do affect the result of the FRF but only in the low frequency range up to $1\,\mathrm{Hz}$. For frequencies greater than $1\,\mathrm{Hz}$ the FRF "converges" to its expected/nominal behavior which is sufficient for us.

Figure 3.15 illustrates the results of the measurements from 1–$500\,\mathrm{Hz}$ for all three axes. The measured FRFs are indicated with gray solid lines. The FRF of the theoretical model (3.95) (without disturbances) is shown with a black dotted line and the theoretical model in series with a fitted transfer function is illustrated with red dashed lines. Until a frequency of approximately $200\,\mathrm{Hz}$ all the magnitude plots show the behavior that one would expect from the theoretical model. That is a slope of $-40\,\mathrm{dB/decade}$ and (partially) in the range of $10\,\mathrm{Hz}$ to $20\,\mathrm{Hz}$ an anti-resonance followed by a resonance peak. The latter characteristic stems from a colocated sensor-actuator configuration as discussed in 2.3.3 and results from compliance between mover and stator representing the first resonance mode of the machine. Interestingly, in that range there is no distinct resonance in the dynamics of q_ϕ. This is traced back to very small rotational motion and a relatively stiff stator with respect to reaction torques. Owing to the low damping properties of the mover, the influence of viscose damping is only visible below $1\,\mathrm{Hz}$ which is not shown here.

Normally, from the theoretical model it would be expected that the phase will not fall below $-180°$. However, in all three Figures it can be seen that after the resonance peak at $\omega \approx 20\,\mathrm{Hz}$ the phase creeps slowly downwards until a frequency of $\omega \approx 200\,\mathrm{Hz}$, where it reaches a value of approximately $-220°$ to $-230°$. After that point, the phase abruptly drops a further $-180°$, where it finally reaches a value between $-360°$ and $-450°$. In the magnitude plots this phase drop is accompanied by a second resonance peak. It is believed that this second peak /structural mode originates from compliance between the sensor and the actuators and/or the guiding system. It is important to notice that the current control loop of the actuators has a phase lag of $-16°$ at a frequency of $\omega = 500\,\mathrm{Hz}$. Therefore, it contributes only very little to the observed phase lag such that the source is definitely not the current loop dynamics of the actuator but a different one.

Eventually, the Figure indicates a good model match of the theoretical model with the measured FRF. This is a first important step towards adaptive controller design. Indeed, although it is possible that parameters like masses, damping coefficients, stiffnesses etc. may change, for the application in question it is rather unlikely that the fundamental physical structure of the system will change. Therefore, the identification of the physical structure of the machine is a first insight in the configuration of parametric uncertainties and hence a first step towards parameter adaptation and adaptive control. However, the observed creep in phase and the high frequency resonance is not represented by the theoretical model.

In order to make use of both, i.e. the theoretical model as well as the experimental results, we suggest to split the FRF into two frequency bands. Thus, the overall input output behavior of an individual axis of the motion stage maybe represented by the

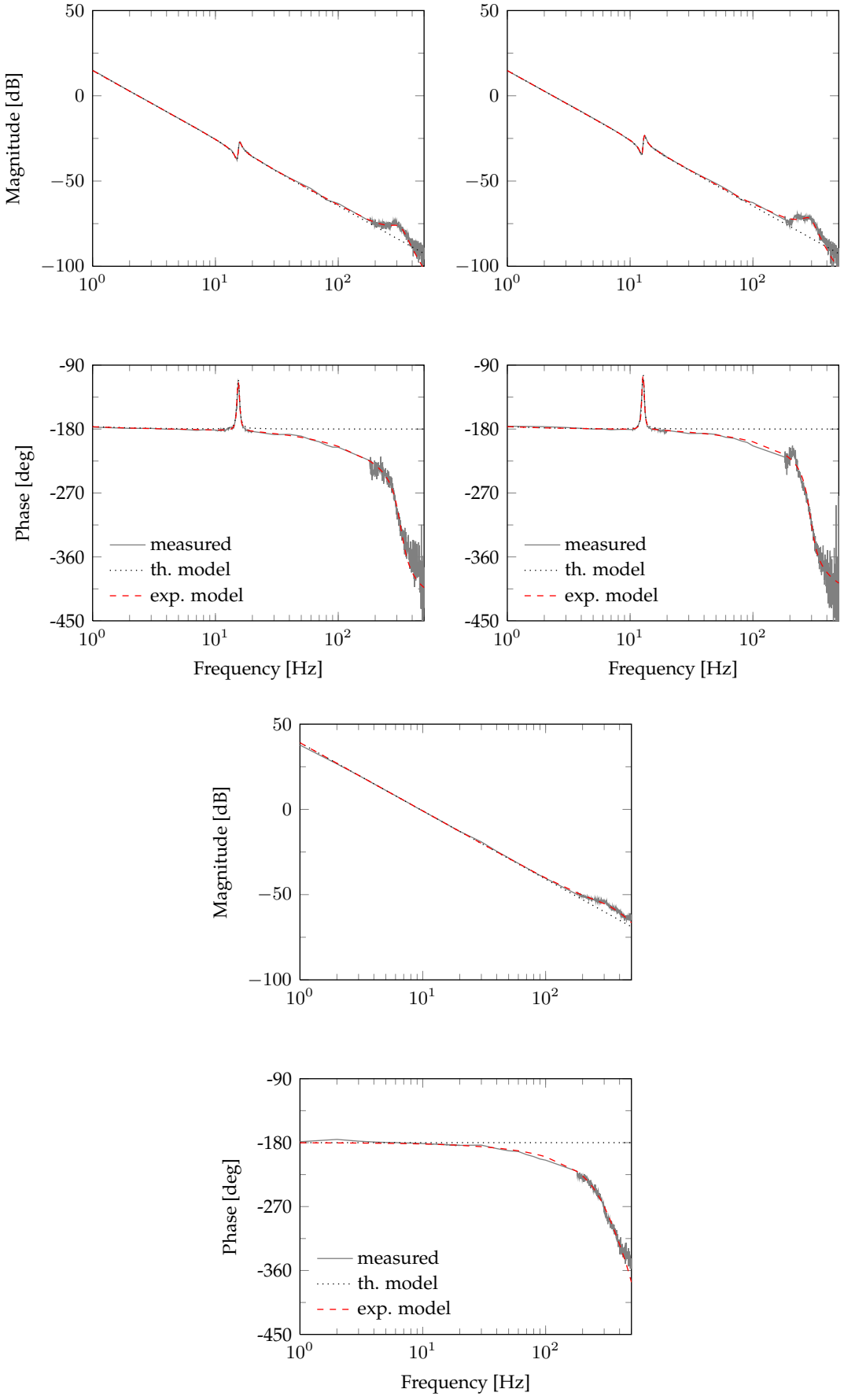

FIGURE 3.15: comparison of measured and identified FRFs for q_x (a), q_y (b), q_ϕ (c) (input current [A], output position [mm])

following transfer function

$$y(s) = \Sigma(s)u(s) = \Sigma_1(s)\Sigma_2(s)u(s), \tag{3.99}$$

where $\Sigma_1(s)$ denotes the transfer function in the first frequency band ranging from $1\,\mathrm{Hz}$ to $200\,\mathrm{Hz}$, while $\Sigma_2(s)$ represents the remaining higher frequency parts of $\Sigma(s)$ including the creeping drop in phase. Thus intuitively, $\Sigma_2(s)$ plays the role of a virtual actuator model. Hence, the output of $\Sigma_2(s)$ is the input of $\Sigma_1(s)$, i.e.

$$y(s) = \Sigma_1(s)u_1(s) \tag{3.100}$$

$$u_1(s) = \Sigma_2(s)u(s). \tag{3.101}$$

In that way it is possible to relate $\Sigma_1(s)$ to the state space realization given in (3.95) (without disturbances), i.e.

$$\Sigma_1(s) = C(sI - A)^{-1}B, \tag{3.102}$$

driven by the output $u_1(t)$ of the input dynamics $\Sigma_2(s)$. Let the minimal state space realization of the virtual actuator dynamics $\Sigma_2(s)$ be given by

$$\begin{aligned} \dot{x}_a(t) &= A_a\, x_a(t) + B_a\, u(t), \quad x_a(0) = x_a^0 \\ u_1(t) &= C_a\, x_a(t). \end{aligned} \tag{3.103}$$

For the parameter identification of $\Sigma_2(s)$ a 4th order transfer function with one left half plane zero for both, the translational axes, and two left half plane zeros for the rotational axis was fitted by solving a complex curve fitting problem. The FRFs of the complete model are shown in Figure 3.15 in red dashed lines. The overall model match is very good. The numerical results of the parameter identification are illustrated in tables C.4–C.6 in Appendix C.

For the sake of reference and summary we introduce the following definition completing the modeling of the motion stage:

Definition 3.1.1 (Generic axis model (GAM))**.** *The generic axis model is given by the set of differential equations*

$$\Sigma : \begin{cases} \dot{x}(t) = A\, x(t) + B\left(u_1(t) - f_1(x,t)\right), \quad x(0) = x_0 \\ y(t) = C\, x(t), \\ \dot{x}_a(t) = A_a\, x_a(t) + B_a\, u(t), \quad x_a(0) = x_a^0 \\ u_1(t) = C_a\, x_a(t) \end{cases} \tag{3.104}$$

where $x(t) \in \mathbb{R}^4$ is the state, $u(t) \in \mathbb{R}$ is the control input, and $f_1(x(t), t) \in \mathbb{R}$ is a disturbance. The state space realization $(A, B, C, 0)$ represents the motion stages rigid body dynamics including the first structural mode. The respective matrices have the following structure

$$A = \begin{pmatrix} 0 & 1 & 0 & 0 \\ 0 & -a_1 & a_2 & a_3 \\ 0 & 0 & 0 & 1 \\ 0 & a_4 & -a_2 & -a_3 \end{pmatrix}, \quad B = \begin{pmatrix} 0 \\ b_1 \\ 0 \\ -b_2 \end{pmatrix}, \quad C^{\mathrm{T}} = \begin{pmatrix} 1 \\ 0 \\ 0 \\ 0 \end{pmatrix}, \quad a_i, b_j > 0. \tag{3.105}$$

The parameters are given by

$$a_1 = \left(\frac{d_l}{m_l} + \frac{d_l}{m_{s,l}}\right), \qquad a_2 = \frac{k_{s,l}}{m_{s,l}}, \qquad a_3 = \frac{d_{s,l}}{m_{s,l}}, \tag{3.106}$$

$$a_4 = \frac{d_l}{m_{s,l}}, \qquad b_1 = 2p_1K_{ml}\left(\frac{1}{m_{s,l}} + \frac{1}{m_l}\right), \qquad b_2 = \frac{2p_1K_{ml}}{m_{s,l}}, \tag{3.107}$$

where d_l, m_l and $d_{s,l}$, $m_{s,l}$ denote the damping coefficient and mass of the mover and stator, respectively, while $k_{s,l}$ is the stator stiffness. Quantities p_1 and K_{ml} represent the DC-gain of the current amplifiers and motor constants with index $l \in \{x, y, \phi\}$. The numerical values of these parameters are listed in tables C.4–C.6 in Appendix C. The second realization $(A_a, B_a, C_a, 0)$ resembles high frequency dynamics. The Laplace transform of Σ is given by

$$y(s) = \Sigma(s)u(s) = \Sigma_1(s)\Sigma_2(s)u(s) \tag{3.108}$$

with

$$\Sigma_1(s) = C(sI - A)^{-1}B, \quad \Sigma_2(s) = C_a(sI - A_a)^{-1}B_a, \tag{3.109}$$

where the dynamics of $\Sigma_2(s)$ is minimum phase, BIBO stable and $\Sigma_2(0) = 1$. The numerical values for $\Sigma_2(s)$ are also given in tables C.4–C.6 in Appendix C. ▼

For a simplified control design, at first sight, we exclude the high frequency dynamics $\Sigma_2(s)$ and treat them as unmodeled dynamics.

Remark 3.1.12. Mostly the DC-gain of high frequency dynamics is assumed different from one. However, in a series connection of transfer functions like $\Sigma_1(s)\Sigma_2(s)$ it is always possible to rewrite the product such that $\Sigma_2(s)$ has DC-gain one and the true DC-gain of the series connection is only governed by $\Sigma_1(s)$.

3.2 System Model Analysis

From the theoretical and experimental modeling procedures we arrived at the class of system as given in Definition 3.1.1. Apparently, the generic axis model without disturbance can be cast into a linear time invariant system of the form

$$\Sigma_\ell : \begin{cases} \dot{x}(t) = Ax(t) + Bu(t), \quad x(0) = x_0 \\ y(t) = Cx(t) \end{cases} \tag{3.110}$$

with state $x(t) \in \mathbb{R}^n$, input $u(t) \in \mathbb{R}$, output $y(t) \in \mathbb{R}$ and A, B, C system, input and output matrices of appropriate size. In order to identify potentially possible control algorithms, it is important to firstly analyze the system with respect to its system theoretic nature and its fundamental properties.

To this end, let us firstly notice that it is easy to show that (3.104) is completely controllable and also completely observable. Next, as already discussed, mover and stator relate to each other as external and internal dynamics of the overall system. For an analysis of these dynamics it is convenient to separate them from each other. This can be achieved with the aid of a similarity transformation. Especially for feedforward design the stability of the internal dynamics is crucial. The latter is easier to study in the input-output normal form. In this respect the relative degree of an LTI system, defined next, plays an important role.

Definition 3.2.1 (Relative degree of an LTI system [72])**.** *Given a single input single output LTI system of the form Σ_ℓ (3.110) with $x(t) \in \mathbb{R}^n$, $u(t), y(t) \in \mathbb{R}$ and A, B, C with appropriate size. Σ_ℓ or the output y is said to have relative degree $r \leq n$ if*

$$\begin{aligned} CA^k B &= 0, \quad \forall\, k < r-1 \\ CA^{r-1}B &\neq 0. \end{aligned}$$

The integer r satisfying this condition is equivalent to the difference between the degree of the denominator polynomial and the degree of the numerator polynomial of the transfer function

$$C\left(sI - A\right)^{-1} B$$

▼

Intuitively, the relative degree relates the control input $u(t)$ to the output $y(t)$ and gives information on through how many states the input needs to propagate to directly affect the output. The relative degree may be obtained by differentiating the output $y(t)$ with respect to time until $u(t)$ appears explicitly for the first time.

The next theorem provides necessary and sufficient conditions for the existence of a similarity transformation, transforming the system into input-output normal form. It is related to the Byrnes-Isidori normal form [72].

Theorem 3.2.1 (Linear input-output normal form [72, 150])**.** *Consider the linear system Σ_ℓ with relative degree $r \leq n$, state $x(t) \in \mathbb{R}^n$, input and output signals $u(t), y(t) \in \mathbb{R}$, and matrices/vectors $A \in \mathbb{R}^{n\times n}$, $B \in \mathbb{R}^{n\times 1}$, $C \in \mathbb{R}^{1\times n}$, respectively.*

Let

$$T_\xi = \begin{pmatrix} C \\ CA \\ \vdots \\ CA^{r-1} \end{pmatrix} \in \mathbb{R}^{r\times n}. \tag{3.111}$$

For any T_ξ there exists $T_\eta \in \mathbb{R}^{n-r\times n}$ such that

$$T := \begin{pmatrix} T_\xi \\ T_\eta \end{pmatrix} \in \mathbb{R}^{n\times n}$$

is regular. The similarity transformation

$$z(t) = Tx(t)$$

with $z(t)$ composed of

$$\xi(t) = \begin{pmatrix} z_1(t) \\ z_2(t) \\ \vdots \\ z_r(t) \end{pmatrix} = \begin{pmatrix} \xi_1(t) \\ \xi_2(t) \\ \vdots \\ \xi_r(t) \end{pmatrix} = \begin{pmatrix} y(t) \\ \dot{y}(t) \\ \vdots \\ y^{(r-1)}(t) \end{pmatrix} \in \mathbb{R}^r,$$

that is, the first $(r-1)$ *time derivatives of the output* $y(t)$ *and*

$$\eta(t) = \begin{pmatrix} z_{r+1}(t) \\ z_{r+2}(t) \\ \vdots \\ z_n(t) \end{pmatrix} = \begin{pmatrix} \eta_1(t) \\ \eta_2(t) \\ \vdots \\ \eta_{n-r}(t) \end{pmatrix} \in \mathbb{R}^{n-r}$$

transforms Σ_ℓ *into a system with the following normal form*

$$\dot{\xi}(t) = \check{A}_{11}\,\xi(t) + \check{A}_{12}\,\eta(t) + \check{B}_1\,u(t), \quad \xi(0) = \xi_0 \tag{3.112}$$

$$\dot{\eta}(t) = \check{A}_{21}\,\xi(t) + \check{A}_{22}\,\eta(t) + \check{B}_2\,u(t), \quad \eta(0) = \eta_0. \tag{3.113}$$

The respective matrices and vectors are given by

$$\begin{aligned} \begin{pmatrix} \check{A}_{11} & \check{A}_{12} \end{pmatrix} &:= T_\xi A T^{-1} \in \mathbb{R}^{r\times n}, & \check{B}_1 &:= T_\xi B \in \mathbb{R}^{r\times 1} \\ \begin{pmatrix} \check{A}_{21} & \check{A}_{22} \end{pmatrix} &:= T_\eta A T^{-1} \in \mathbb{R}^{(n-r)\times n}, & \check{B}_2 &:= T_\eta B \in \mathbb{R}^{(n-r)\times 1} \end{aligned}$$

and

$$\check{A}_{11} \in \mathbb{R}^{r\times r}, \quad \check{A}_{12} \in \mathbb{R}^{r\times(n-r)}, \quad \check{A}_{21} \in \mathbb{R}^{(n-r)\times r}, \quad \check{A}_{22} \in \mathbb{R}^{(n-r)\times(n-r)}.$$

Furthermore, equation (3.112) *has the particular normal form*

$$\begin{cases} \dot{\xi}_1(t) &= \xi_2(t) \\ &\vdots \\ \dot{\xi}_{r-1}(t) &= \xi_r(t) \\ \dot{\xi}_r(t) &= a_\xi^{\mathrm{T}}\,\xi(t) + a_\eta^{\mathrm{T}}\,\eta(t) + b_y u(t) \end{cases}$$

that may equivalently be expressed in terms of the input and output signals

$$y^{(r)}(t) = a_\xi^{\mathrm{T}} \begin{pmatrix} y(t) \\ \dot{y}(t) \\ \vdots \\ y^{(r-1)}(t) \end{pmatrix} + a_\eta^{\mathrm{T}} \begin{pmatrix} \eta_1(t) \\ \eta_2(t) \\ \vdots \\ \eta_{n-r}(t) \end{pmatrix} + b_y\,u(t), \tag{3.114}$$

where

$$\begin{pmatrix} a_\xi^{\mathrm{T}} & a_\eta^{\mathrm{T}} \end{pmatrix} := CA^rT^{-1} \in \mathbb{R}^{1\times n}, \quad b_y := CA^{r-1}B \in \mathbb{R}.$$

■

The correctness of the theorem may easily be verified by comparing the first r time derivatives of the output $y(t)$ with the applied transformation. Please note that equation (3.112) plays the role of the external dynamics, while (3.113) represents the so-called internal dynamics of system Σ_ℓ.

Let us now compute the transformation matrix T in order to apply the similarity transformation from Theorem 3.2.1 to the generic axis model without actuator dynamics. Using the definitions of the matrices in (3.105) and noting that the state space

realization $(A, B, C, 0)$ has relative degree $r = 2$, we obtain for T_ξ

$$T_\xi = \begin{pmatrix} C \\ CA \end{pmatrix} = \begin{pmatrix} 1 & 0 & 0 & 0 \\ 0 & 1 & 0 & 0 \end{pmatrix}.$$

For the choice of T_η we have some design freedom. Apparently, the simplest choice is given by

$$T_\eta = \begin{pmatrix} 0 & 0 & 1 & 0 \\ 0 & 0 & 0 & 1 \end{pmatrix}$$

rendering the transformation superfluous, since

$$T = T^{-1} = I \quad \Rightarrow \quad TAT^{-1} = A, \quad TB = B.$$

Consequently, the system appears naturally in the input-output normal form such that x_1 and x_2 (position and velocity of the mover) resemble the states of the external dynamics, while x_3 and x_4 (position and velocity of the stator) represent the states of the internal dynamics, respectively. However, with regard to vector B from (3.105) it is apparent that the control input also enters the internal dynamics. From a control design/stability perspective this fact is not appealing. Therefore, we use the design freedom in T_η in order to introduce a change of coordinates that renders the internal dynamics independent of any control inputs. Hence, T_η must satisfy

$$\check{B}_2 = T_\eta B = 0, \tag{3.115}$$

while having full row rank such that T is invertible. In view of (3.105), one possible choice is e.g.

$$T_\eta = \begin{pmatrix} 0 & \frac{b_2}{b_1} & 1 & 1 \\ 0 & \frac{b_2}{b_1} & 0 & 1 \end{pmatrix}. \tag{3.116}$$

Hence, the change of coordinates might be accomplished by

$$T = \begin{pmatrix} 1 & 0 & 0 & 0 \\ 0 & 1 & 0 & 0 \\ 0 & \frac{b_2}{b_1} & 1 & 1 \\ 0 & \frac{b_2}{b_1} & 0 & 1 \end{pmatrix} \quad \Leftrightarrow \quad T^{-1} = \begin{pmatrix} 1 & 0 & 0 & 0 \\ 0 & 1 & 0 & 0 \\ 0 & 0 & 1 & -1 \\ 0 & -\frac{b_2}{b_1} & 0 & 1 \end{pmatrix} \tag{3.117}$$

Applying the similarity transformation $z(t) = Tx(t)$ to the realization $(A, B, C, 0)$ of (3.104) yields the equivalent dynamics in the z coordinates which might be decomposed according to

$$\Sigma_z : \begin{cases} \dot{\xi}(t) = \check{A}_{11}\,\xi(t) + \check{A}_{12}\,\eta(t) + \check{B}_1 u_1(t) \\ \dot{\eta}(t) = \check{A}_{21}\,\xi(t) + \check{A}_{22}\,\eta(t), \end{cases} \tag{3.118}$$

where the block matrices are computed as in Theorem 3.2.1 and have the following structure

$$\check{A}_{11} := \begin{pmatrix} 0 & 1 \\ 0 & \check{a}_1 \end{pmatrix}, \quad \check{A}_{12} := \begin{pmatrix} 0 & 0 \\ \check{a}_2 & \check{a}_3 \end{pmatrix}, \tag{3.119}$$

$$\check{A}_{21} := \begin{pmatrix} 0 & \check{a}_4 \\ 0 & \check{a}_5 \end{pmatrix}, \quad \check{A}_{22} := \begin{pmatrix} \check{a}_6 & \check{a}_7 \\ \check{a}_8 & \check{a}_9 \end{pmatrix}. \tag{3.120}$$

The parameters $\check{a}_i$ are given by

$$\begin{cases} \check{a}_1 = -\frac{a_1 b_1 + b_2 a_3}{b_1} \\ \check{a}_2 = a_2 \\ \check{a}_3 = -a_2 + a_3 \\ \check{a}_4 = -\frac{b_2 a_1 b_1 - a_4 b_1^2 + b_2 b_1 + b_2^2 a_3 - b_2 a_3 b_1}{b_1^2} \\ \check{a}_5 = -\frac{b_2 a_1 b_1 - a_4 b_1^2 + b_2^2 a_3 - b_2 a_3 b_1}{b_1^2} \\ \check{a}_6 = -\frac{a_2(-b_2 + b_1)}{b_1} \\ \check{a}_7 = \frac{b_1 - b_2 a_2 + a_2 b_1 + b_2 a_3 - a_3 b_1}{b_1} \\ \check{a}_8 = -\frac{a_2(-b_2 + b_1)}{b_1} \\ \check{a}_9 = \frac{-b_2 a_2 + a_2 b_1 + b_2 a_3 - a_3 b_1}{b_1}. \end{cases} \tag{3.121}$$

Moreover, the input vector reads

$$\check{B}_1 := \begin{pmatrix} 0 \\ \check{b}_1 \end{pmatrix}, \tag{3.122}$$

where $\check{b}_1 = b_1$.

Since we are only interested in controlling the dynamics related to the output y of our system, i.e. the external dynamics, the internal dynamics is of minor interest. However, since it can be seen that the internal dynamics is coupled to the external dynamics by the term $\check{A}_{12}\eta(t)$ it is crucial that the internal dynamics remains bounded for all time so that the output will do so. If we can proof that the internal dynamics is asymptotically stable we can leave the internal dynamics aside and concentrate on the design of the controller controlling the external dynamics. The controller can then be designed such that undesired coupling between internal and external dynamics is compensated.

3.2.1 Analysis of the zero dynamics

In order to study the stability of the internal dynamics the concept of the so-called zero dynamics was introduced by [14]. The general definition of zero dynamics is given as follows

Definition 3.2.2 (Zero dynamics [72, 124])**.** *The zero dynamics of a system is the internal dynamics of the respective system under the constraint that its output y is kept identically zero for all time, i.e. $y \equiv 0$.* ▼

It is well known that in the linear case, when the system is controllable and observable, the zero dynamics coincide with the dynamics related to the zeros of the transfer function of the linear system. In classical control theory, the property of minimum or non-minimum phaseness is directly attributed to the location of the zeros in the complex

plane. Equivalently this property might be addressed in terms of the zero dynamics as stated next.

Definition 3.2.3 (Minimum phase system [72, 124])**.** *A system is called minimum phase if its zero dynamics is asymptotically stable and non-minimum phase otherwise.* ▼

Remark 3.2.1. It is well-known that the property of minimum or non-minimum phaseness of nonlinear systems might be related to special equilibrium points only. Hence, it is possible that a single nonlinear system exhibits both minimum and non-minimum phase behavior in dependence of its operating point or its regarded equilibrium point. Thus, the definition of minimum phaseness in the context of nonlinear systems is sometimes addressed locally around a special equilibrium point [124].

To study the stability of the internal dynamics of $(A, B, C, 0)$ of the generic motion stage model, without loss of generality, we consider the unperturbed plant in z coordinates without input dynamics as given in (3.118). Imposing the constraint $y \equiv 0$ leads to $\xi \equiv 0 \Rightarrow \dot{\xi} \equiv 0$ and hence to the autonomous zero dynamics

$$\dot{\eta}(t) = \check{A}_{22}\,\eta(t), \quad \eta(0) = \eta_0. \tag{3.123}$$

It can be shown that the characteristic polynomial of (3.123) reads

$$p(\lambda) = \lambda^2 + a_3\left(1 - \frac{b_2}{b1}\right)\lambda + a_2\left(1 - \frac{b_2}{b1}\right). \tag{3.124}$$

Hence, and by virtue of the fact that the constants $a_2, a_3, b_1, b_2 > 0$, the zero dynamics is asymptotically (in fact exponentially) stable if the inequality

$$\frac{b_2}{b_1} < 1 \tag{3.125}$$

holds.

In order to get a physical interpretation of the stability constraint we next substitute the parameters from (3.107) giving

$$\frac{m_l}{m_{s,l} + m_l} < 1 \tag{3.126}$$

Obviously, as long as $m_{s,l} > 0$, that is the mass of the stator, the stability condition is always fulfilled. In practice the stator is designed such that $m_{s,l} >> m_l$. Consequently, the zero dynamics of the motion stage is always asymptotically stable. This result of course makes sense because it is unlikely that the position of the stator gets unbounded as a force is applied to the mover.

Remark 3.2.2. Note that it is also possible to show the stability of the zero dynamics in the original coordinates. To this end let $x_\xi := \begin{pmatrix} x_1 & x_2 \end{pmatrix}^{\mathrm{T}}$ and $x_\eta := \begin{pmatrix} x_3 & x_4 \end{pmatrix}^{\mathrm{T}}$. Then the dynamics in original coordinates may be decomposed as

$$\dot{x}_\xi(t) = A_{11}\,x_\xi(t) + A_{12}\,x_\eta(t) + B_1 u_1(t) \tag{3.127}$$

$$\dot{x}_\eta(t) = A_{21}\,x_\xi(t) + A_{22}\,x_\eta(t) + B_2 u_1(t). \tag{3.128}$$

Imposing the constraint $y \equiv 0$ leads to $x_\xi \equiv 0 \Rightarrow \dot{x}_\xi \equiv 0$ and hence to

$$0 = a_\eta^{\mathrm{T}}\, x_\eta(t) + b_y u_1^\star(t) \tag{3.129}$$

$$\dot{x}_\eta(t) = A_{22}\, x_\eta(t) + B_2 u_1^\star(t). \tag{3.130}$$

The input required for keeping the output constant at zero might be obtained by solving (3.129) for $u_1^\star$. This special input is also referred to as output-zeroing control input [72, 124] and it reads

$$u_1^\star(t) = -\frac{a_\eta^{\mathrm{T}}\, x_\eta(t)}{b_y}. \tag{3.131}$$

Substituting the last equation into (3.130) finally yields the autonomous zero dynamics

$$\dot{x}_\eta(t) = A_\eta\, x_\eta(t), \quad x_\eta(0) = x_\eta^0, \tag{3.132}$$

where

$$A_\eta = \left(A_{22} - B_2\, b_y^{-1} a_\eta^{\mathrm{T}}\right) \in \mathbb{R}^{(n-r)\times(n-r)}. \tag{3.133}$$

In view of (3.105) and the respective decomposition this yields

$$\dot{x}_\eta(t) = \begin{pmatrix} 0 & 1 \\ -\left(1 - \frac{b_2}{b1}\right) a_2 & -\left(1 - \frac{b_2}{b1}\right) a_3 \end{pmatrix} x_\eta(t), \quad x_\eta(0) = x_\eta^0. \tag{3.134}$$

This of course leads to the same characteristic polynomial and thus to the same result.

Remark 3.2.3. If the zero dynamics is asymptotically stable this implies that the internal dynamics is BIBS stable. Therefore, all further inputs such as states of the external dynamics, control inputs, uncertainties and other perturbations do not alter the stability as long as these inputs are itself bounded. Moreover, from (3.106) it can be seen that constants

$$a_2 = \frac{k_{s,l}}{m_{s,l}}, \qquad a_3 = \frac{d_{s,l}}{m_{s,l}} \tag{3.135}$$

are related to mechanical stiffness and damping of the stator system. In the practical application these parameters are always positive and non-zero.

3.2.2 Analysis of Uncertainty Structure

In order to account for modeling errors or parametric uncertainty due to variation of loads or other parameters, we next analyze the mathematical structure of parametric uncertainties. To this end, we consider the state space realization Σ_z in the z coordinates as given in (3.118), but now together with the parasitic disturbances $f_1(x,t)$. Precisely speaking, f_1 is a function of mover position and mover velocity, i.e. a function of $\xi(t)$ only. Then,

$$\Sigma_z : \begin{cases} \dot{\xi}(t) = \check{A}_{11}\, \xi(t) + \check{A}_{12}\, \eta(t) + \check{B}_1(u_1(t) + f_1(\xi,t)) \\ \dot{\eta}(t) = \check{A}_{21}\, \xi(t) + \check{A}_{22}\, \eta(t). \end{cases} \tag{3.136}$$

Let the matrices/vectors with $\check{(\cdot)}$ denote the matrices of the nominal model. In order to describe the deviation of the model with respect to the true plant, we introduce the following assumptions on (additive) parameter perturbations:

Assumption 3.2.1 (Additive, constant parameter perturbations)**.** *We assume that the parameters of the true plant a_i^p and b_1^p ($i = 1, \ldots, 9$) have the following structure*

$$a_i^p = \check{a}_i + \Delta a_i, \quad b_1^p = \check{b}_1 + \Delta b_1 > 0, \tag{3.137}$$

where $\check{a}_i$ and $\check{b}_1$ model the nominally/a priori known (best guess) parameter estimates, while Δa_i and Δb_1 denote the uncertainty of the actual parameters, respectively. Without loss of generality, we assume that the input gain b_1^p is positive.

Assumption 3.2.2 (Boundedness of uncertainty)**.** *We assume further that the uncertainties are bounded by*

$$|\Delta a_i| \leq \delta_a, \quad |\Delta b_1| \leq \delta_b. \tag{3.138}$$

Assumption 3.2.3 (BIBS stability of the internal dynamics)**.** *We assume that the parameter perturbations Δa_i ($i = 1, \ldots, 9$) are such that the internal dynamics is BIBS stable, both with respect to initial conditions η_0 and input ξ (see Section 3.2.1).*

Assumption 3.2.4 (Invariance of controllability and observability)**.** *We further assume that the parameter perturbations Δa_i ($i = 1, \ldots, 9$) and Δb_1 are such that the properties on controllability and observability of the system are not altered.*

Taking the parameter perturbations into account leads to the following plant description

Definition 3.2.4 (Perturbed generic axis model (PGAM) in z coordinates)**.** *The perturbed generic axis model in z-coordinates is given by the set of differential equations*

$$\Sigma_{z,\Delta} : \begin{cases} \dot{\xi}(t) = \check{A}_{11}\, \xi(t) + \check{A}_{12}\, \eta(t) + \check{B}_1 \left(u_1(t) + d_\xi(t)\right), & \xi(0) = \xi_0 \\ \dot{\eta}(t) = \check{A}_{21}\, \xi(t) + \check{A}_{22}\, \eta(t) + d_\eta(t), & \eta(0) = \eta_0 \end{cases} \tag{3.139}$$

where $\xi(t) \in \mathbb{R}^2$, $\eta \in \mathbb{R}^2$ and matrices $\check{A}_{ij}$, for $i, j = 1, 2$, are given by (3.119)–(3.120) *with parameters* (3.121)*, while $\check{B}_1$ is defined by* (3.122)*. The perturbations d_η and d_ξ are defined as*

$$d_\eta(t) := \Delta A_{21} \xi(t) + \Delta A_{22} \eta(t) \tag{3.140}$$

$$d_\xi(t) := \beta u_1(t) + \theta_1^{\mathrm{T}} z(t) + f(\xi, t), \tag{3.141}$$

while

$$\beta := \Delta b_1 / \check{b}_1 \tag{3.142}$$

$$f(\xi, t) := (1 + \beta)\, f_1(\xi, t) \tag{3.143}$$

$$\theta_1^{\mathrm{T}} := \begin{pmatrix} 0 & \Delta a_1/\check{b}_1 & \Delta a_2/\check{b}_1 & \Delta a_3/\check{b}_1 \end{pmatrix} \tag{3.144}$$

and

$$\Delta A_{21} := \begin{pmatrix} 0 & \Delta a_4 \\ 0 & \Delta a_5 \end{pmatrix}, \quad \Delta A_{22} := \begin{pmatrix} \Delta a_6 & \Delta a_7 \\ \Delta a_8 & \Delta a_9. \end{pmatrix} \tag{3.145}$$

Or in equivalent form

$$\begin{cases} \dot{z}(t) = \check{A}z(t) + \check{B}\left(u_1(t) + d_\xi(t)\right) + \check{E}d_\eta(t), \quad z(0) = z_0 \\ y(t) = \check{C}z(t) \end{cases} \tag{3.146}$$

where

$$\check{A} = TAT^{-1}, \quad \check{B} = TB, \quad \check{C} = CT^{-1} = C \tag{3.147}$$

and these matrices/vectors are partitioned as

$$\check{A} = \begin{pmatrix} \check{A}_{11} & \check{A}_{12} \\ \check{A}_{21} & \check{A}_{22} \end{pmatrix}, \quad \check{B} = \begin{pmatrix} \check{B}_1 \\ 0 \end{pmatrix}, \quad \check{C} = C, \quad \check{E} = \begin{pmatrix} 0 \\ I \end{pmatrix}. \tag{3.148}$$

▼

Please notice the fact that the parameters in $\check{A}_{11}$ and $\check{A}_{12}$ lie both in the span of $\check{B}_1$. Hence, the parameter perturbations with respect to the external dynamics naturally appear as matched uncertainties. In other words, the uncertainties lie directly within the reach of the control channel. This fact is favorable for all sorts of disturbance rejection algorithms, including disturbance observers and adaptive control.

Note, however, that the parametric uncertainty in view of the internal dynamics is unmatched. This is not a problem, because we are primarily interested in shaping the external dynamics to our needs and specifications. However, it is clear that due to the coupling between external and internal dynamics the uncertainties regarding the internal dynamics, namely $d_\eta(t) := \Delta A_{21}\xi(t) + \Delta A_{22}\eta(t)$, propagate into the external dynamics through the solution $\eta(t)$. In order to understand how this influences the output dynamics, we make use of the linearity of the system and consider the general solution of the perturbed internal dynamics (3.139) from $\Sigma_{z,\Delta}$, i.e.

$$\eta(t) = e^{\check{A}_{22}(t-t_0)}\eta_0 + \int_{t_0}^{t} e^{\check{A}_{22}(t-\tau)}\left(\check{A}_{21}\xi(\tau) + d_\eta(\tau)\right)d\tau. \tag{3.149}$$

Now we can separate the inhomogeneous part of the solution into

$$\eta(t) = \underbrace{e^{\check{A}_{22}(t-t_0)}\eta_0 + \int_{t_0}^{t} e^{\check{A}_{22}(t-\tau)}\check{A}_{21}\xi(\tau)d\tau}_{\eta_n(t)} + \underbrace{\int_{t_0}^{t} e^{\check{A}_{22}(t-\tau)}d_\eta(\tau)d\tau}_{\eta_\Delta(t)} \tag{3.150}$$

which can be seen as a superposition of a nominal or an ideal solution $\eta_n(t)$ satisfying

$$\dot{\eta}_n(t) = \check{A}_{22}\eta_n(t) + \check{A}_{21}\xi(t), \quad \eta_n(0) = \eta_0, \tag{3.151}$$

with a perturbed solution $\eta_\Delta(t)$ satisfying

$$\dot{\eta}_\Delta(t) = \check{A}_{22}\eta_\Delta(t) + d_\eta(t), \quad \eta_\Delta(0) = 0. \tag{3.152}$$

Note that $\eta_\Delta(0) = 0$. Replacing $\eta(t)$ in (3.139) by $\eta(t) = \eta_n(t) + \eta_\Delta(t)$ and using (3.151) and (3.152) the system of equations from (3.139) can be equivalently expressed by

$$\Sigma_{z,d} : \begin{cases} \dot{\xi}(t) = \check{A}_{11}\xi(t) + \check{A}_{12}\eta_n(t) + \check{B}_1\left(u_1(t) + d_\xi(t) + d_\Delta(t)\right), \quad \xi(0) = \xi_0 \\ \dot{\eta}_n(t) = \check{A}_{21}\xi(t) + \check{A}_{22}\eta_n(t), \quad \eta_n(0) = \eta_0 \\ \dot{\eta}_\Delta(t) = \check{A}_{22}\eta_\Delta(t) + d_\eta(t), \quad \eta_\Delta(0) = 0 \\ d_\Delta(t) = \check{b}_1^{-1} a_\eta^{\mathrm{T}} \eta_\Delta(t), \end{cases} \tag{3.153}$$

where we additionally used the fact that $\check{A}_{12}\eta_\Delta(t) = \check{B}_1\check{b}_1^{-1}a_\eta^{\mathrm{T}}\eta_\Delta(t)$. Hence, also the influence of perturbations with respect to the internal dynamics is matched in the external dynamics. Intuitively, the first two equations represent the ideal motion stage dynamics (without the virtual actuator), perturbed by parameter uncertainties and external disturbances. The third differential equation plays the role of a disturbance generator system whose output, given by the fourth equation, is $d_\Delta(t)$. The disturbance generator is driven by the states η_n and ξ and the parameter perturbations of the internal dynamics. Assumption 3.2.3 and the BIBO stability of the nominal internal dynamics implies that the disturbance generator is also BIBO stable. The disturbances d_Δ are thus bounded if ξ is bounded which will be accomplished by feedback control.

For simplicity and for the time being, we ignore the disturbance generator and treat $d_\Delta(t)$ as a bounded time varying external disturbance. We than define a new state $z_n = (\xi \;\; \eta_n)^{\mathrm{T}}$ and rewrite the last set of equations to

$$\Sigma_{z_n} : \begin{cases} \dot{z}_n(t) = \check{A}\, z_n(t) + \check{B}(u_1(t) + d(t)), \quad z_n(0) = z_n^0 \\ y(t) = \check{C}\, z_n(t), \end{cases} \tag{3.154}$$

where the block matrices are given as in (3.148) and $d(t)$ is defined as

$$d(t) := d_\xi(t) + d_\Delta(t). \tag{3.155}$$

Remark 3.2.4. The representation of the motion stage in the form (3.154) is useful for the validation of output feedback designs, where only the output y is available for feedback. Indeed, the output has not changed. If for instance the observer is designed for the nominal system without disturbances, than it is interesting to notice that the state η_n in (3.153) represents exactly the state the observer would estimate. Due to the perturbation term d_Δ that is matched in the external dynamics, estimation errors rendered by the uncertainty of the internal dynamics and their influence on the external dynamics is more visible.

If full state information is available, i.e. both ξ and η can be measured, then the formulation in Definition 3.2.4 is appropriate, since the perturbations are already included in the measurement of η.

Remark 3.2.5. From a physical point of view Assumption 3.2.3 is reasonable because the instability of the internal dynamics would imply that the stator position could get unbounded which is unrealistic. As exposed in Section 3.2.1, in practice the stator dynamics is always BIBO stable and it is expected that the variation of parameters will not violate this property. Otherwise, from the coupling between internal and external dynamics, it is clear that nothing could be done, if the internal dynamics was unstable.

3.3 Fundamental Performance Limitations

Since it is crucial for the performance of a tracking task that reference trajectories are designed for meeting fundamental limitations of the machine, this section is dedicated to a short note on dynamic constraints and reference trajectories.

3.3.1 Dynamic Constraints

As every electromechanical device underlies several static and dynamic restrictions, also the motion stage exhibits such constraints. In particular we distinguish between constraints on position p, velocity v, acceleration a and jerk j, i.e.

$$\begin{aligned} p &\in [-p_{\max}, p_{\max}], \quad v \in [-v_{\max}, v_{\max}] \\ a &\in [-a_{\max}, a_{\max}], \quad j \in [-j_{\max}, j_{\max}]. \end{aligned}$$

Most obvious, position constraints are determined by the traversing range of the motor or the measurement range of the sensor system. The position constraints of the PPS1405 are summarized in Table 2.3.

Despite the sensor constraints on velocity as given in Table 2.1, additionally the maximum attainable velocity is influenced by the following three further sources

- friction/damping
- motion EMF
- position and acceleration constraints

The first source is easily understood by considering the simplified rigid body dynamics of the mover along one direction. Let for simplicity the current command for the respective axis be $i_l(t) = i_l^\star(t)$. Then the rigid body dynamics reads

$$m_l \dot{v}(t) + d_l v(t) = 2p_1 K_{ml} i_l(t). \tag{3.156}$$

This constitutes a BIBO stable system with a DC-gain of $2p_1 K_{ml}/d_l$. So, after all transients have decayed, it is easy to see that the maximum velocity will settle at a value of

$$v_{\max} = \frac{2p_1 K_{ml}}{d_l} i_{\max} \tag{3.157}$$

which of course also depends on the maximum current rating $i_{\max}$, supplied by the respective current amplifiers (cf. Table 2.3). With the identified parameters of $p_1 = 1.08$, $K_{ml} = 1.6\ \mathrm{N/A}$, $d_l = 7.2\ \mathrm{kg/s}$ and a maximum current range of $\pm 3\mathrm{A}$ this results in a maximum velocity of $v_{\max} = 1.44\ \mathrm{m/s}$.

The second bullet point considers the effect of back-EMF voltages, induced inside the driving coils, as a consequence of mover motion. For illustrating this effect, consider the following simplified coil model for a single phase, where coil and phase indexes are omitted for brevity:

$$L\frac{di(t)}{dt} = -Ri(t) - K_{emf} v(t) + u_s(t) \tag{3.158}$$

Therein, $L > 0$ and $R > 0$ are inductance and winding resistance, respectively, while u_s denotes the input or supply voltage. For the sake of simplicity we assume that

parameter K_{emf} is constant, denoting the back-EMF constant. Now, apparently, if the velocity takes values such that the induced voltage $K_{emf}v(t)$ equals the maximum of the input voltage $u_{s,\text{max}}$ then the last equation turns into

$$\frac{di(t)}{dt} = -\frac{R}{L}i(t) \tag{3.159}$$

with the current $i(t)$ converging exponentially to zero such that there is no generation of electromagnetic forces. Thus, the maximum velocity constraint by motion EMF can be computed according to

$$v_{\text{max}} = \frac{u_{s,\text{max}}}{K_{emf}}. \tag{3.160}$$

With a supply-/PWM-voltage of $\pm 24\,\text{V}$ and a back-EMF constant of $K_{emf} = 1.6\,\text{V}\,\text{s/m}$ this finally leads to $v_{\text{max}} = 15\,\text{m/s}$.

However, the largest constraint on the maximum velocity is imposed by the available positioning range in conjunction with the maximum acceleration. Of course, the fastest trajectory for moving from point $-p_{\text{max}}$ to $+p_{\text{max}}$ is typically achieved by a so-called bang-bang strategy, where the mover is accelerated by constant a_{max} for half of the distance and decelerated by $-a_{\text{max}}$ for the second half of the distance. The duration t_a of the acceleration phase is thus given by

$$t_a = \sqrt{\frac{2p_{\text{max}}}{a_{\text{max}}}}, \tag{3.161}$$

where p_{max} is one half of the total distance. Obviously, the maximum velocity will be obtained at the end of the acceleration phase which is hence given by

$$v_{\text{max}} = a_{\text{max}}t_a. \tag{3.162}$$

In view of equation (3.156), while assuming $d_l = 0$ for simplicity, quantity a_{max} can be computed as per

$$a_{\text{max}} = \frac{2p_1K_{ml}}{m_l}i_{\text{max}} \tag{3.163}$$

and results in a value of $a_{\text{max}} = 538.9\,\text{mm/s}^2$. Then considering the smallest positioning range of the mover along q_y with $q_y \in [-25, 25]\,\text{mm}$, the maximum velocity of the mover is calculated as $v_{\text{max}} = 164.15\,\text{mm/s}$. This clearly shows that although physically, the motor could be operated at even higher linear velocities, in the context of the planar motion stage, the greatest impact on velocity constraints emanates from the maximum ratings of positions and accelerations.

Finally, jerk represents the rate of change of acceleration. Since in the electromechanical actuator acceleration is directly proportional to current $i_l(t)$, the jerk is accordingly limited by the maximal rate of change of current $i_l(t)$. This, of course, relates to the rise-time of the closed loop current dynamics. Computing the rate of change of the normalized step responses from Figure 3.2 (a), (b) yields values for the maximum of the current change of $5000\,\text{A/s}$ to $8000\,\text{A/s}$. Taking the lower value and using equation 3.163, this translates into an upper bound of $j_{\text{max}} = 898.13\,\text{m/s}^3$.

Remark 3.3.1. Please note that the constraints computed above constitute theoretical or nominal values that might be obtained in the best case. However, some aspects have

not been considered yet. First, for a suitable allocation and limitation of control inputs, $80\,\%$ of the coil currents (i_{max}) is reserved for the translational axes, while the remaining $20\,\%$ are provided for the rotational axis. This is due to the fact that both, translational forces, and torque, are commanded over the same coils. Additionally, the presence of external disturbances (see Section 3.1.5) requires a certain amount of headroom for the control inputs. The controller needs at least $20\,\%$ to $30\,\%$ for an appropriate compensation of the disturbances encountered in the PPS1405. This lowers the amount of acceleration that can be provided to the actual tracking task to approximately $56\,\%$ to $64\,\%$ of the nominal value. Thus, accordingly the maximum velocities also reduce. The latter are also heavily dependent on the acceleration profile that is used. In practice the time optimal bang-bang trajectory is only rarely used, because for most systems a stepwise change in acceleration is not feasible. Due to these reasons, the motor manufacturer specifies a maximum velocity of $v_{\text{max}} = 50\ \text{mm/s}$.

3.3.2 Trajectory Design

The design of smooth and feasible reference trajectories plays a very important role in motion control and is as relevant as the design of sophisticated motion controllers. Since there is a vast literature on the topic, see e.g. [2, 8, 59, 89, 120], we only give a brief comment.

In fact, the reference trajectory specifies the desired motion of the motion control system, i.e. the position of the mover. In order to track this motion with a suitable amount of precision the reference trajectory must ensure that the desired motion is feasible, i.e. the given motion system is physically able to perform the desired motion. Therefore, it is inevitable that the trajectory is designed such that machine constraints are met. Indeed, it makes no sense to demand more from a system than it is capable of doing. If, nonetheless, fundamental machine limitations are violated this unavoidably results in poor performance.

As shown in references [8, 89], the choice of the motion profile has a strong impact on the position accuracy of motion control systems. A crucial parameter in this respect is the order of the trajectory [89]. This parameter basically relates to the number of time derivatives of the position trajectory and thus to the smoothness of the trajectory. For instance, according to [89], a second order trajectory is a trajectory with a piecewise continuous, i.e. step-like, acceleration profile. On the other hand, third and fourth order trajectories constitute trajectories with a step-like jerk or derivative of jerk/snap profile, respectively.

Along with [8, 89], higher order trajectories have the advantage that they inherently provide lower energy content at higher frequencies and thus vitally reduce the excitation of structural modes and eigenfrequencies in a motion system. Linking this with the requirement for the feasibility of a desired motion, it can be concluded that the smoother the trajectory, the less is the chance of demanding a motion which is physically impossible to perform by a given motion system [89]. In the presence of actuator dynamics, for instance, it is obviously impossible to produce a step-like change in force. Hence, it makes no sense to demand a step-like acceleration profile.

On the other hand, a disadvantage of higher order trajectories is the execution time for the trajectory which might be sub-optimal. However, solutions to this problem have been found for fourth-order trajectories in [2, 89].

The fourth-order algorithms presented in [2, 89] constitute the state-of-the-art algorithms for high-end applications. They are based on the construction of a derivative of

jerk/snap profile which via integration in time yields the respective profiles for jerk, acceleration, velocity and position.

However, a widely used standard in industry is a third order trajectory also known as *bell*, *seven segments* or *double S* trajectory [8]. This particular kind of trajectory is also used in the NC/CNC trajectory generator of the PPS1405 motion stage. In [8] also other approaches are presented exploiting polynomials, trigonometric and exponential functions for the generation of trajectories. In Section 5 we compare the *double S* trajectory with a degree 5 polynomial and consider the impact on position accuracy based on experimental results.

A completely different approach is the approach of *input shaping* [8, 120]. Roughly speaking, the main idea of *input shaping* is based on the convolution of the reference trajectory with a suitably chosen train of impulses, forming the so-called *input shaper*. In fact, the impulses are chosen such that when convolved with the reference signal, a signal is produced that when applied to the motion system, completely cancels the vibration in the system. Intuitively, this approach resembles a special kind of notch filtering [120]. It equivalently aims at reducing the energy content at higher frequencies, especially in the range of resonance frequencies, for reducing the effect of structural vibration. These approaches typically take the time-optimal bang-bang trajectory and smooth it accordingly. Along with [89] and references therein, the results of this approach can be very good but also lead to a considerable increase in execution time of the trajectory, without clear tuning mechanisms for obtaining time optimality.

Due to the significance of the trajectory generator it can and should be considered as a further DOF of the motion controller, having a strong influence on servo-error performance.

3.4 Summary–Formulation of Controller Specifications

We conclude this chapter by summarizing the most important properties of the motion stage system that have been discovered during the process of modeling and the experimental results. From that we deduce specifications for the motion controller yet to be devised.

- **Double integrating nature of the plant:** Obviously, the process of the motion stage essentially constitutes a double integrator with low damping. Hence, the system is not BIBO stable. Due to the low phase which is mostly less or equal to -180° (except at the resonance frequency of the stator) for proper stabilization the controller must essentially be of type PID. In view of the input disturbances described in Section 3.1.5 the integral action is needed for providing a proper compensation of these disturbances.

- **Low frequency resonances of stator:** As discussed in Sections 3.1.4 and 3.1.6 there are low frequency resonances of the stator in the range of $10\,\mathrm{Hz}$ to $20\,\mathrm{Hz}$ that are detrimental to positioning accuracy and pose serious problems on settling times of servo errors. Experiments revealed that for a sufficient reduction of oscillations in position error, the loop gain needs a minimum of $30\,\mathrm{dB}$, i.e. the sensitivity function needs $-30\,\mathrm{dB}$, at that frequency.

- **High frequency dynamics:** As discussed in Section 3.1.6, high frequency resonance modes occur in a range of approximately $200\,\mathrm{Hz}$ to $300\,\mathrm{Hz}$ and lead to a

considerable phase drop, limiting the achievable performance of the motion system. Since the excitation of these dynamics may lead to undesired high frequency oscillations and also instability, these dynamics should be handled with care. To limit the amount of excitation, the bandwidth of the controller should be chosen sufficiently below these modes, where we require a maximum peak of the sensitivity function of less than 2 ($6\,\mathrm{dB}$). This is a common value in practice. This requirement corresponds to a phase margin of at least 30° and thus also takes care of the fact that the controller should have sufficient phase lead around the crossover frequency. Moreover, to limit the control energy at high frequencies the controller needs sufficient high frequency roll off. Please note that the compensation of these dynamics is possible but represents a non-robust solution and is therefore not pursued.

- **Measurement noise:** The noise amplitude of position signals is below $50\,\mathrm{nm}$. We want that the measurement noise amplified by the controller is less than $10\,\%$ of the maximum control signal. This requires that the controller gain is less than $75\,\mathrm{dB}$. That is $20\log(0.3/50 \times 10^{-6}) \approx 75.56\,\mathrm{dB}$, when the position error is measured in mm.

- **Position error:** A stringent time domain requirement of the motor manufacturer is that during trajectory tracking the maximum position error stays below $1\,\mu\mathrm{m}$. For achieving perfect tracking in the nominal, case a feedforward controller is needed. To suppress disturbances and modeling errors, the feedback controller needs sufficiently high bandwidth. It is experienced that for achieving this goal, the controller bandwidth should at least be around $40\,\mathrm{Hz}$.

- **Available measurement signals:** Notice that only the position measurements $(q_x(t), q_y(t), q_\phi(t))$ are available for control. Hence, the specifications deduced above must be accomplished in an output feedback kind of manner.

- **Parametric uncertainty:** Due to the fact that the motion controller should be applicable to similar motion stage systems with different dimension and size, and tuning should only be done once based on a priori known system parameters, parametric uncertainties due to tolerances of diverse elements are expected. The controller should be able to cope with these uncertainties, while retaining sufficient performance.

Chapter 4

Control Design

Based on the model derived in Chapter 3 and the controller specifications given in Section 3.4, in this chapter we derive a motion controller for accurate trajectory tracking. For achieving this goal in the face of the given requirements and challenges, we separate the controller design into two design stages. That is, first, the stage of nominal or baseline tracking controller design in Section 4.1 and second, in view of parametric uncertainty, the stage of robust adaptive control design addressed in Section 4.2.

The design of the nominal controller is based on a two-degree-of-freedom (2-DOF) control architecture, comprising an inversion-based feedforward controller derived in Sections 4.1.1 and 4.1.2 and a feedback controller.

For meeting the requirement of output feedback control, we first derive a state feedback controller based on the assumption of full state measurements in Section 4.1.3. From that, in Section 4.1.4, an observer-based output feedback controller is deduced. For the purpose of reducing the effect of external disturbances on the state estimates of the observer, the latter is designed as an composite state and disturbance observer in the spirit of *disturbance accommodating control*. This also incorporates good disturbance rejection capabilities and essentially leads to a generalized PID type of controller with possibly multiple integrators.

The model based nature of the nominal controller provides a nice way of completely incorporating the available a priori knowledge of the motion stage. It thus allows the continuous improvement of the controller performance through the addition of further knowledge that might be available at a later stage.

Although the observer-based controller shows good robustness with respect to parametric uncertainties in the A matrix, it is sensitive with respect to uncertainties in the input gain, i.e. uncertainties in the B matrix. Therefore, we propose to augment this controller by an adaptive controller in order to recover the nominal performance in the presence of parametric uncertainty.

Towards this end, in Section 4.2, we apply the recent methodology of $\mathcal{L}_1$ adaptive control, as it offers outstanding performance and robustness features and, as one of the few methods in adaptive control, allows to directly incorporate bandwidth limitations within the design of the adaptive controller. Indeed, this is essential to limit the frequency content of the adaptive control signal, in order to avoid excitation of high frequency (unmodeled) dynamics.

Although not implementable on the PPS1405 platform, for the sake of exposition and completeness, we first present an $\mathcal{L}_1$ adaptive augmentation with full state feedback in Section 4.2.1. Followed by this, Section 4.2.2 is addressed to the final $\mathcal{L}_1$ output feedback design. Simulation results illustrate the effectiveness of the respective designs.

4.1 Nominal Tracking Control

In the diverse applications of nano and micropositioning it is essential that the moving element of a positioning stage precisely tracks predefined reference trajectories. Dependent on the application, these trajectories may be simple or highly complex. The problem of devising a controller for achieving accurate tracking is known as tracking control problem.

Basically, the design of tracking controllers can roughly be divided into two classes. That is first, the class of internal model based methods, resorting to the celebrated *internal model principle* of Francis and Wonham [42, 43], and second, the class of inversion based methods.

In accordance with the *internal model principle* (IMP), controllers belonging to the first class, achieve asymptotic output tracking by a one-degree-of-freedom (1-DOF) control architecture due to an explicit implementation of an internal model of the class of reference signal [29, 51]. Intuitively, these controllers can be seen as generalizations of proportional integral controllers with either state or output feedback. According to [29] the design of these controllers is also referred to as *robust servomechanism problem*. An advantage of the IMP approach is the fact that additionally to reference tracking, also asymptotic disturbance rejection to the same class of signals is achieved [29, 51]. This renders these controllers robust with respect to parametric plant uncertainty and does not require an accurate model of the plant [29]. However, the necessity of a model of the reference signal renders the design complicated in the case of complex and possibly changing reference trajectories. Since these models are typically unstable, they further impose the same performance limitations on the closed loop as if these unstable modes were part of the plant [51]. Hence, there is no separation of tracking performance and stabilization as a result of the 1-DOF configuration.

Inversion-based tracking control approaches, however, attain such a separation, while resorting to 2-DOF control architectures [65]. Classically, the 2-DOF structure comprises a feedback and a feedforward part [27, 34]. The latter is to steer the nominal system output y, assumed devoid of disturbances and modeling mismatch, along a reference trajectory $y^\star(t)$. The former is to attenuate disturbances, compensate unmodeled dynamics, stabilize and speed up tracking error convergence. Please note that basically two kinds of feedforward architectures may be distinguished [27]. Namely, the closed-loop inversion scheme, where the feedforward controller inverts a closed-loop system, and the plant inversion scheme, where the feedforward controller ideally constitutes an exact inverse of the plant. The benefit of the closed loop inversion approach is the fact that the usage of feedback before inversion may attenuate model uncertainty and thus relief the necessity of an accurate model as compared to the direct plant inversion [27]. However, as the controller gets more complex, the whole complexity must also be considered in the feedforward controller, while the inverse of the plant might be more simple. Moreover, along with [27] the plant inversion scheme tends to have better performance since it does not share the performance limitations of the closed loop system. Due to these reasons we will consider the plant inversion scheme only.

There are various benefits of 2-DOF control structures. Optimizing the tracking performance and disturbance attenuation may be done independently [65]. The major portion of the control amplitude (up to 90%) is provided by the feedforward part of the controller, i.e. in a clean and noise-free manner. The remaining portion is dedicated to the feedback part. For sufficiently smooth reference trajectories this fruitful combination may significantly reduce the excitation of resonant frequencies, and thus, vibration in a mechanical system. As a result, the controller design may be decisively

simplified and turn out attractive even in applications that require set-point regulation, only. Eventually, feedforward does not conflict with stability of the closed-loop system [34, 65]. It thus overcomes limitations imposed by trading off high-bandwidth (performance) and robust stability [27] in traditional 1-DOF feedback designs. It can thus lead to a substantial improvement of tracking performance when compared to 1-DOF feedback configurations. The feedforward controller may hence be seen as an add-on to feedback controlled systems for enhancing the tracking performance. Due to these reasons inversion based approaches are widely used (see [27, 34, 129, 136] among others).

Numerous methods exist for feedforward design, both for linear [27, 126, 150], and nonlinear systems [33, 52, 53]. Additional to these methods, the notion of differential flatness [40, 129], also applying for linear and nonlinear systems, became very popular for feedforward design, see [52, 53, 55] for recent results.

However, a disadvantage of the inversion based approach is the need for an accurate model and the difficulty of finding bounded solutions for non-minimum phase systems.

Although it can be shown that when subject to (parameter) uncertainties, feedforward together with feedback performs better than feedback alone [27], tracking performance, however, is highly dependent on the accuracy of model parameters [136]. This may inhibit the application of these controllers for highly uncertain plants.

The non-minimum phase issue might be addressed with a flatness based approach [129] or the acausal feedforward approach with pre and post actuation by [33] and [150].

4.1.1 Feedforward Design Preliminaries

According to the results of Section 3.2, the motion stage is controllable, observable, and minimum phase. For simplicity we impose the following assumption

Assumption 4.1.1. *For the ease of controller design, we exclude the virtual actuator dynamics from* Σ (3.104) *and assume that the control input* $u(t)$ *directly enters the motion stage.*

Moreover, we consider the nominal case such that external disturbances $f_1(x(\cdot), \cdot) \equiv 0$. Then, Σ reduces to

$$\Sigma_n : \begin{cases} \dot{x}(t) = A\,x(t) + B\,u(t), \quad x(0) = x_0 \\ y(t) = C\,x(t), \end{cases} \tag{4.1}$$

representing the nominal case. Next we give a precise definition of the nominal tracking control problem:

Definition 4.1.1 (Nominal (trajectory) tracking control problem)**.** *Consider system* (4.1) *(at least stabilizable) and an arbitrary, bounded reference trajectory* $y^\star(\cdot) \in \mathcal{C}^k$*, with* $k \geq r$*, where* r *denotes the relative degree. Devise a control law* u *such that the system output* y *tracks the desired reference trajectory* $y^\star$ *exactly, while the control input* u *stays uniformly bounded, i.e.*

$$|u(t)| \leq \delta_u < \infty, \quad \forall t \geq 0,$$

and the tracking error defined by $y_e(t) := y(t) - y^\star(t)$ asymptotically vanishes as $t \to \infty$, that is

$$\lim_{t\to\infty} y_e(t) = 0.$$

▼

An elegant way to solve the trajectory tracking problem is to reformulate it into a standard regulation problem as in [150]. This can be achieved by a simple change of coordinates. To this end, we first need to find a desired solution pair $(x^\star, u^\star)$, satisfying the set of equations

$$\begin{aligned} \dot{x}^\star(t) &= A\,x^\star(t) + B\,u^\star(t), \quad x^\star(0) = x_0^\star \\ y^\star(t) &= C\,x^\star(t). \end{aligned} \tag{4.2}$$

Next, we introduce the tracking error variables

$$e_x(t) := x(t) - x^\star(t) \tag{4.3}$$
$$u_e(t) := u(t) - u^\star(t) \tag{4.4}$$
$$y_e(t) := y(t) - y^\star(t) \tag{4.5}$$

and subtract (4.2) from (4.1). The resulting dynamics read

$$\begin{aligned} \dot{e}_x(t) &= A\,e_x(t) + B\,u_e(t), \quad e_x(0) = e_x^0 \\ y_e(t) &= C\,e_x(t) \end{aligned} \tag{4.6}$$

and represent the so-called trajectory tracking error dynamics. Apparently, asymptotic stabilization of the tracking error, or in other words, regulation of the tracking error e_x to zero, solves the tracking control problem. Thus, any standard control design method such as state or output feedback might be applied as illustrated by the following example.

Example 4.1.1. *Consider the tracking error dynamics from equation* (4.6) *and the simple state feedback law*

$$u_e(t) = -k^{\mathrm{T}} e_x(t). \tag{4.7}$$

Substituting the last equation into (4.6) *yields*

$$\dot{e}_x(t) = \left(A - Bk^{\mathrm{T}}\right) e_x(t) \tag{4.8}$$

for the closed loop tracking error dynamics. Using standard techniques, the feedback gain k^{T} is designed such that $A - Bk^{\mathrm{T}}$ is Hurwitz. Thus, the tracking error state $e_x(t)$ is regulated to zero asymptotically, i.e.

$$\lim_{t\to\infty} e_x(t) = 0. \tag{4.9}$$

Hence, $x(t) \to x^\star(t)$ and also $y(t) \to y^\star(t)$ as desired. ▲

Along with equation (4.4) it can be observed that the actual control input is composed of

$$u(t) = u^\star(t) + u_e(t). \tag{4.10}$$

Therein, u_e obviously resembles an error–based feedback controller, while $u^\star$ plays the role of a feedforward controller, inverting the dynamics of (4.1). Even though the stabilization of the tracking error dynamics is relatively easy, the computation of a suitable, bounded system inverse and feedforward law $u^\star(t)$ is more demanding, especially for non-minimum phase systems [150].

As discussed in the introductory part of this section, there are many methods for computing $u^\star(t)$. Since the nominal process in question is linear and minimum phase, a broad spectrum of algorithms apply. Potentially interesting methods are the approaches of [150] for general, stabilizable linear systems and those presented in [129] for differentially flat systems.

Due to the fact that the system Σ_n is linear and controllable, according to [129] the existence of a flat output can be concluded. However, since the flat output y_f does not coincide with the real output y of Σ_n a change of coordinates is necessary to obtain y_f and its respective dynamics. Indeed, finding the flat output for linear controllable systems is easy. It is simply given by the last row of the inverse of the Kalman controllability matrix modulo a constant factor multiplied by the system state [129]. Note, however, that the analytical computation of the flat output leads to cumbersome expressions. Yet, such a change of coordinates is unnecessary because the system in its original coordinates naturally appears in normal form (see Theorem 3.2.1) which by itself constitutes the basis for the computation of exact inverses as exposed in [150].

From a practical perspective it is believed that it is better to save the effort of applying the coordinate transformation in order to prevent numerical sensitivity problems and the fact that the transformation itself might rely on uncertain system parameters. Consequently, we will use the approach from [150] for the computation of the nominal inverse of Σ_n which for the case of linear, minimum phase systems is summarized in the following theorem.

Theorem 4.1.1 (Exact inverse for SISO minimum phase LTI systems [150])**.** *Consider the stabilizable system* (4.1) *with relative degree $r \leq n$ and an arbitrary, bounded reference trajectory $y^\star(\cdot) \in \mathcal{C}^r$. If there exists a regular similarity transformation $T^{\mathrm{T}} = (T_\xi^{\mathrm{T}} \quad T_\eta^{\mathrm{T}}) \in \mathbb{R}^{n\times n}$ as given in Theorem 3.2.1 and the system is minimum phase, then the systems exact inverse is given by*

$$\Sigma_n^{-1} : \begin{cases} \dot\eta^\star(t) = \check{A}_\eta \eta^\star(t) + \check{B}_\eta Y^\star(t), \quad \eta^\star(0) = \eta_0^\star \\ u^\star(t) = b_y^{-1}\left(\overset{(r)}{y^\star}(t) - a_\xi^{\mathrm{T}}\xi^\star(t) - a_\eta^{\mathrm{T}}\eta^\star(t)\right) \\ x^\star(t) = T^{-1}z^\star(t), \end{cases} \tag{4.11}$$

where the respective reference signals are partitioned as

$$z^\star(t) = \begin{pmatrix}\xi^\star(t)\\ \eta^\star(t)\end{pmatrix} \in \mathbb{R}^n, \quad \xi^\star(t) = \begin{pmatrix} y^\star(t) \\ \vdots \\ \overset{(r-1)}{y^\star}(t)\end{pmatrix} \in \mathbb{R}^r, \quad Y^\star(t) = \begin{pmatrix}\overset{(r)}{y^\star}(t)\\ \xi^\star(t)\end{pmatrix} \in \mathbb{R}^{r+1}.$$

The matrices for the internal dynamics are given by

$$\check{A}_\eta = \left(\check{A}_{22} - \check{B}_2 b_y^{-1} a_\xi^{\mathrm{T}}\right) \in \mathbb{R}^{(n-r)\times(n-r)}, \quad \check{B}_\eta = \left(\check{B}_2 b_y^{-1} \quad \check{A}_{21} - \check{B}_2 b_y^{-1} a_\xi^{\mathrm{T}}\right) \in \mathbb{R}^{(n-r)\times(r+1)},$$

while

$$\begin{aligned}\begin{pmatrix}\check{A}_{21} & \check{A}_{22}\end{pmatrix} &= T_\eta A T^{-1} \in \mathbb{R}^{(n-r)\times n}, \quad \check{B}_2 = T_\eta B \in \mathbb{R}^{(n-r)\times 1}\\ \begin{pmatrix}a_\xi^{\mathrm{T}} & a_\eta^{\mathrm{T}}\end{pmatrix} &= C A^r T^{-1} \in \mathbb{R}^{1\times n}, \qquad b_y = C A^{r-1} B \in \mathbb{R}.\end{aligned}$$

The reference system for (4.1) *can thus be constructed from the solution pair* $(x^\star, u^\star)$ *and the matrices of the process, i.e.*

$$\begin{aligned}\dot{x}^\star(t) &= A\, x^\star(t) + B\, u^\star(t), \quad x^\star(0) = x_0^\star\\ y^\star(t) &= C\, x^\star(t).\end{aligned}$$

■

Remark 4.1.1. In Definition 4.1.1 we imposed a condition on the smoothness of the reference trajectory in terms of the relative degree, which states that at least the r-th time derivative of the reference trajectory should be continuous. This condition may be explained by the following example:

Example 4.1.2. *Consider a linear process* $P(s)$ *with relative degree* $r = 2$ *and the following input-output relation*

$$y(s) = \frac{b_0}{s^2 + a_1 s + a_0} u(s), \quad a_0, a_1, b_0 > 0 \tag{4.12}$$

The exact inverse of $P(s)$ *is simply given by* $P^{-1}(s)$*, i.e.*

$$u^\star(s) = \frac{s^2 + a_1 s + a_0}{b_0} y^\star(s) \tag{4.13}$$

which is improper. However, the exact inverse can be implemented in the time domain by the algebraic relation

$$u^\star(t) = \frac{1}{b_0}\left(\ddot{y}^\star(t) + a_1 \dot{y}^\star(t) + a_0 y^\star(t)\right). \tag{4.14}$$

Apparently, the reference $y^\star$ *must at least be* $r = 2$ *times differentiable with respect to time which is a necessary condition such that the process can track the trajectory with finite inputs (see [27] and references therein). Since it is better to have rather smooth trajectories, we impose the condition of* $y^\star(\cdot) \in \mathcal{C}^r$ *which is more strict.* ▲

Remark 4.1.2. Note that the reference input $u^\star$ represents a compensation based feed-forward law that directly stems from the input-output normal form of the external dynamics as given in equation (3.114). Therein, $\eta^\star(t)$ denotes the reference solution of the internal dynamics. The latter is represented by the first equation of (4.11). Strictly speaking, this equation expresses the zero dynamics forced by the reference trajectories $Y^\star(t)$ (cf. matrix A_η in (3.133)).

Obviously, the above inverse yields a bounded solution $(x^\star, u^\star)$ if and only if the zero dynamics is asymptotically stable, i.e. $\check{A}_\eta$ is Hurwitz, or in other words, if the system is minimum phase.

Remark 4.1.3. In [150] the approach is also extended to non-minimum phase systems. Here the basic idea is to separate the internal dynamics into a stable part and an unstable part. Whereas bounded solutions for the stable part might be obtained by simple forward integration of the dynamics, the unstable part must be integrated backwards in

time to get bounded solutions. In fact, this results in acausal feedforward schemes that need pre- and/or post-actuation or some preview time (see also [33]). Since a detailed treatment of exact inverses for non-minimum phase systems goes beyond the scope of this text, the interested reader is referred to references [27, 33, 150] and references therein.

Remark 4.1.4. Note that the exclusion of the virtual actuator dynamics as proposed in Assumption 4.1.1 is actually a standard approach in control, in order to obtain a relatively simple abstraction of the real process, for an appropriate controller design. This assumption is also motivated by the following observations. First, it is expected that the modeling uncertainty in the high frequency range is quite high. Therefore, inversion of the high frequency dynamics is not recommended in order to avoid the excitation of high frequency unmodeled dynamics. Second, experiments with an approximate inversion of the actuator dynamics have not shown considerable benefits over not inverting the actuator dynamics. It rather showed worse performance since the inversion of some high frequency poles of the actuator dynamics led to a massive amplification of noise and an enormous increase of control effort. This consequently led to problems with meeting the actuator position limits. Finally, the high frequency dynamics $\Sigma_2(s)$ constitutes a system with relative degree three. That means that for the computation of an exact inverse of the overall system we would need a reference trajectory $y^\star(\cdot) \in \mathcal{C}^5$. This is problematic because reference trajectory generators used in industry usually provide $\mathcal{C}^2$ or at best $\mathcal{C}^4$ trajectories. Due to these reasons, we suggest to only invert the dynamics of the mechanical plant and avoid the inversion of the actuator dynamics. As a nice side-effect this keeps the controller complexity low. However, since there is a considerable phase drop due to the high frequency dynamics, the controller will be designed with sufficient phase lead to ensure robust stability.

4.1.2 Derivation of Nominal Feedforward Controller

We start our derivation with the design of the nominal feedforward controller. To this end, we consider the nominal plant Σ_n as given in (4.1). Recall that Σ_n appears naturally in normal form such that according to Theorem 4.1.1 an exact inverse may be derived in the original coordinates. In order to distinguish between the states of the external and internal dynamics we use the notation

$$x_\xi(t)^{\mathrm{T}} := \begin{pmatrix} x_1(t) & x_2(t) \end{pmatrix}, \quad x_\eta(t)^{\mathrm{T}} := \begin{pmatrix} x_3(t) & x_4(t) \end{pmatrix}. \tag{4.15}$$

Hence, the nominal plant may be written as

$$y^{(r)}(t) = a_\xi^{\mathrm{T}} x_\xi(t) + a_\eta^{\mathrm{T}} x_\eta(t) + b_y u(t) \tag{4.16}$$

$$\dot{x}_\eta(t) = A_{21} x_\xi(t) + A_{22} x_\eta(t) + B_2 u(t), \tag{4.17}$$

where A and B were partitioned as

$$A = \begin{pmatrix} A_{11} & A_{12} \\ A_{21} & A_{22} \end{pmatrix}, \quad B = \begin{pmatrix} B_1 \\ B_2 \end{pmatrix}. \tag{4.18}$$

Applying Theorem 4.1.1, the exact inverse of the nominal system reads

$$\Sigma_n^{-1}: \begin{cases} \dot{x}_\eta^\star(t) = A_\eta x_\eta^\star(t) + B_\eta Y^\star(t), \quad x_\eta^\star(0) = x_{\eta,0}^\star \\ u^\star(t) = b_y^{-1}\left(\overset{(r)}{y^\star}(t) - a_\xi^{\mathrm{T}} x_\xi^\star(t) - a_\eta^{\mathrm{T}} x_\eta^\star(t)\right) \\ x^\star(t) = \begin{pmatrix} x_\xi^\star(t) & x_\eta^\star(t) \end{pmatrix}^{\mathrm{T}}, \end{cases} \tag{4.19}$$

where A_η, B_η, b_y, a_ξ and a_η are defined as in Theorem 4.1.1, while noting that $T = I$.

4.1.3 Derivation of Nominal State Feedback Controller

As discussed in Section 3.2, in view of feedback controller design and the assessment of closed loop stability, it is convenient to use coordinates in which the internal dynamics is free of any control inputs. To this end, we introduced the transformation (3.117) that transforms the system into equivalent z coordinates. Next, recall the perturbed generic axis model in z coordinates from Definition 3.2.4 given by

$$\Sigma_{z,\Delta}: \begin{cases} \dot{z}(t) = \check{A} z(t) + \check{B}\left(u(t) + d_\xi(t)\right) + \check{E} d_\eta(t), \quad z(0) = z_0 \\ y(t) = \check{C} z(t), \end{cases} \tag{4.20}$$

where we also excluded the high frequency dynamics and assumed that the control input u directly enters the system (cf. Assumption 4.1.1 and Remark 4.1.4). We further assume that the full state $z(t) = Tx(t)$ is available for control.

The next step is to define a nominal trajectory reference system in the same coordinates given by

$$\Sigma_z^\star: \begin{cases} \dot{z}^\star(t) = \check{A} z^\star(t) + \check{B} u^\star(t), \quad z^\star(0) = z_0^\star \\ y^\star(t) = \check{C} z^\star(t). \end{cases} \tag{4.21}$$

Thereby, the solution pair $(z^\star, u^\star)$ is obtained via the nominal feedforward law Σ_n^{-1} in (4.19) derived in the original x coordinates and the transformation $z^\star(t) = Tx^\star(t)$ with T as in (3.117). Note that inputs and outputs are invariant under similarity transformation. Therefore, $u^\star$ can directly be applied as a feedforward controller.

Subtracting (4.21) from (4.20) and defining $e(t) := z(t) - z^\star(t)$ yields the perturbed nominal system in tracking error coordinates, i.e.

$$\begin{aligned} \dot{e}(t) &= \check{A}\, e(t) + \check{B}\left(u_e(t) + d_\xi(t)\right) + \check{E}\, d_\eta(t), \quad e(0) = e_0 \\ y_e(t) &= \check{C}\, e(t). \end{aligned} \tag{4.22}$$

This can again be separated into the external and internal tracking error dynamics

$$\dot{e}_1(t) = \check{A}_{11}\, e_1(t) + \check{A}_{12}\, e_2(t) + \check{B}_1\left(u_e(t) + d_\xi(t)\right) \tag{4.23}$$

$$\dot{e}_2(t) = \check{A}_{21}\, e_1(t) + \check{A}_{22}\, e_2(t) + d_\eta(t), \tag{4.24}$$

where $e(t) = \begin{pmatrix} e_1(t) & e_2(t) \end{pmatrix}^{\mathrm{T}}$ with $e_1(t) := \xi(t) - \xi^\star(t)$ and $e_2(t) := \eta(t) - \eta^\star(t)$. Since we have already seen that, under practical conditions, the internal dynamics is always asymptotically stable, and due to Assumption 3.2.3, with our control design, we can thus concentrate on the stabilization of the external dynamics only and leave the internal ones aside. In this regard we aim for three goals, namely

- find a stabilizing feedback law for the external dynamics
- compensate the coupling from the internal on the external dynamics
- compensate for the perturbation $d_\xi(t)$

To this end, we split the control input u_e made up of $u_e(t) = u(t) - u^\star(t)$ into three control portions, i.e.

$$u_e(t) = u_s(t) + u_c(t) + u_d(t) \tag{4.25}$$

meant for stabilization, and the compensation of couplings as well as disturbances. Although in the nominal model the matrices $\check{A}, \check{B}, \check{C}$ and $\check{E}$ are known, actually the disturbance terms d_ξ and d_η in general are unknown. However, since we are concerned with the nominal case, for the time being, we assume that at least the disturbance $d_\xi(t)$ is completely known.

A straight forward choice of the respective control portions is as per

$$\begin{cases} u_s(t) = -k_1^{\mathrm{T}} e_1(t) \\ u_c(t) = -\check{B}_1^\dagger \check{A}_{12}\, e_2(t) \\ u_d(t) = -d_\xi(t), \end{cases} \tag{4.26}$$

where

$$\check{B}_1^\dagger = \left(\check{B}_1^{\mathrm{T}} \check{B}_1\right)^{-1} \check{B}_1^{\mathrm{T}} \tag{4.27}$$

denotes the Moore-Penrose pseudoinverse. Substitution of $u_e(t)$ into the external tracking error dynamics leads to

$$\dot{e}_1(t) = \left(\check{A}_{11} - \check{B}_1 k_1^{\mathrm{T}}\right)\, e_1(t) + \left(\check{A}_{12} - \check{B}_1 \check{B}_1^\dagger \check{A}_{12}\right)\, e_2(t). \tag{4.28}$$

Due to the structure of $\check{A}_{12}$, $\check{B}_1$ it can easily be proven that

$$\left(\check{A}_{12} - \check{B}_1 \check{B}_1^\dagger \check{A}_{12}\right) = 0$$

and hence the resulting closed loop error dynamics behaves as per

$$\dot{e}_1(t) = \left(\check{A}_{11} - \check{B}_1 k_1^{\mathrm{T}}\right) e_1(t), \quad e_1(0) = e_1^0. \tag{4.29}$$

Via standard methods feedback gain k_1^{T} is designed such that matrix $\check{A}_{11} - \check{B}_1 k_1^{\mathrm{T}}$ is Hurwitz. Then the tracking error $e_1(t) \to 0$ as $t \to \infty$. Since the internal dynamics is asymptotically stable, for $t \to \infty$ also $e_2(t) \to 0$ and hence $e(t) \to 0$. This means that $z(t) \to z^\star(t)$ and consequently also $x(t) \to x^\star(t)$, as desired.

The complete nominal control law can thus be summarized by the following theorem:

Theorem 4.1.2. *Consider system* (4.20) *and* $e(t) := z(t) - z^\star(t)$, *with*

$$e^{\mathrm{T}}(t) = \begin{pmatrix} e_1^{\mathrm{T}}(t) & e_2^{\mathrm{T}}(t) \end{pmatrix}, \quad e_1(t) \in \mathbb{R}^r, \quad e_2(t) \in \mathbb{R}^{n-r}. \tag{4.30}$$

The nominal tracking controller composed of the exact inverse feedforward law

$$\Sigma_n^{-1}: \begin{cases} \dot{x}_\eta^\star(t) = A_\eta x_\eta^\star(t) + B_\eta Y^\star(t), \quad x_\eta^\star(0) = x_{\eta,0}^\star \\ u^\star(t) = b_y^{-1}\left(\overset{(r)}{y^\star}(t) - a_\xi^{\mathrm{T}} x_\xi^\star(t) - a_\eta^{\mathrm{T}} x_\eta^\star(t)\right) \\ x^\star(t) = \begin{pmatrix} x_\xi^\star(t) & x_\eta^\star(t) \end{pmatrix}^{\mathrm{T}}, \\ z^\star(t) = T x^\star(t) \end{cases} \tag{4.31}$$

and the nominal feedback control portions

$$\Sigma_{u,n}: \begin{cases} u_s(t) = -k_1^{\mathrm{T}} e_1(t) \\ u_c(t) = -\check{B}_1^\dagger \check{A}_{12}\, e_2(t) \\ u_d(t) = -d_\xi(t), \end{cases} \tag{4.32}$$

with control law

$$u(t) = u^\star(t) + u_s(t) + u_c(t) + u_d(t), \tag{4.33}$$

asymptotically stabilizes the tracking error dynamics and thus solves the nominal tracking control problem in the original coordinates, if the feedback gain k_1 is designed such that $\check{A}_{11} - \check{B}_1 k_1^{\mathrm{T}}$ is Hurwitz. ■

Remark 4.1.5. The compensation of the coupling term from the internal onto the external dynamics prevents that undesired motion of the stator is carried into the mover dynamics. Note that in the case of full state feedback and the compensation of the coupling term, the perturbation d_η on the internal dynamics has no further influence on the external dynamics. This is because the perturbation is included in the measurement of $\eta(t)$ which in this case is assumed to be available. It is thus canceled automatically.

4.1.4 Robust Output Feedback Design

Due to the fact that only the output y is available for feedback rather than the complete state z, we next derive an appropriate output feedback controller that might be implemented on the PPS1405 platform. For the extension of the nominal full state feedback tracking controller from Theorem 4.1.2 to an output feedback design, we propose to employ a state observer for providing estimates $\hat{z}$ of the full state z. In order to reduce the effect of unknown input disturbances and parameter uncertainty on the estimation error, the observer should also be able to cope with these uncertainties to some extent.

In this regard, in the literature of state and disturbance observers, (see e.g. the survey papers of [113] and [23]) there exists a wide range of approaches that can simultaneously estimate states as well as matched input disturbances, by exploiting IMP ideas.

In this respect, so called *Generalized Proportional Integral Observers* (GPIO) [95, 127] and *Generalized Extended State Observers* (GESO) [98, 113] have recently attracted researchers due to the simplicity of the design and a vast number of successful practical applications such as flight control [70], web tension regulation [66], robotics [128, 134], motion control [130] and power electronics [127] among others.

Although both approaches originate from different directions of control theory, they are essentially equivalent. In fact, these ideas are not new and actually resemble special

cases of the (more general) observers established in C.D. Johnson's theory of *disturbance accommodating control* (DAC) [76, 78] developed in the late 1960s.

The main idea of Johnson's approach stems from the observation that most disturbances encountered in practice posses a certain deterministic waveform structure which might be mathematically described by a linear combination of unknown constant coefficients $\theta_{w,i}$ with a set of completely known waveform basis functions $\phi_{w,i}(t)$ in the form

$$d_w(t) = \theta_{w,m}\phi_{w,m}(t) + \cdots + \theta_{w,1}(t)\phi_{w,1} + \theta_{w,0}\phi_{w,0}(t) = \theta_w^{\mathrm{T}}\phi_w(t), \tag{4.34}$$

where the $\phi_{w,i}(t)$ are typically chosen as $1, t, t^2, \sin(\omega t), e^{-\alpha t}, te^{-\alpha t} \ldots$ [77]. For exploiting the ideas of the IMP, from this so-called waveform model, an autonomous dynamic system of the from

$$\Sigma_w : \begin{cases} \dot{x}_w(t) = A_w\, x_w(t), \quad x_w(0) = x_w^0 \\ d_w(t) = C_w\, x_w(t), \end{cases} \tag{4.35}$$

is constructed. Therein, $x_w(t) \in \mathbb{R}^m$ denotes the disturbance state and $(A_w, 0, C_w, 0)$ are of appropriate dimension. This system, also known as disturbance generator or exosystem, exactly produces the disturbance $d_w(t)$ (here assumed scalar) at its output, while its initial conditions and state relate to the unknown constant coefficients $\theta_{w,i}$. Please note that the exosystem might be obtained via the Laplace transform of (4.34) and a successive solution of the state space realization problem.

Appending Σ_w to the original system results in an extended state space model of the process implementing an internal model of the expected disturbance. If the extended system is completely observable, both the system state as well as the disturbance state might be estimated from a Luenberger type of observer, designed for the extended system. In accordance with the IMP, this rejects or at least reduces the influences of external disturbances on the state estimate and additionally provides an estimate of the disturbance itself. The latter is then often used for active disturbance rejection in an appropriately designed feedback controller.

It is interesting to notice that the disturbance state x_w has a direct relation to the unknown coefficients of the waveform model (4.34) (see e.g. [58]). Hence, the estimation of x_w in an observer based setting can also be interpreted as an adaptive tuning of coefficients $\theta_{w,i}$ of the waveform model for adapting to the disturbance $d_w(t)$ as it evolves in time. Therefore, this approach has also been put in the perspective of adaptive control in references [74, 75, 77].

For the selection of waveform models t-polynomial or spline as well as sinusoidal waveform structures play a special role because these are the ones encountered in most applications [77]. A key benefit of spline basis functions is the fact that no special knowledge about disturbances is necessary. This is due to the fact that almost any practical disturbance might be approximated locally by a spline polynomial. Moreover, it is experienced that DAC is robust to mismatches between the disturbance model with respect to the true disturbance. Indeed, in [58] it is shown that the spline model can also adapt to a sinusoidal disturbance quite well. Therefore, this waveform model is extremely powerful. For this reason the GPIO and GESO methodologies exclusively use spline polynomials with very good results, also in the context of nonlinear, chaotic systems, see e.g. [95].

Notice that along with [31] the disturbance observer based DAC controllers are dual to the well known approach of *robust servomechanism* of Davison [29]. Moreover,

these controllers represent a generalization of PID and PID-notch-filter controllers with multiple integrators in an observer based state-feedback framework as exposed in the excellent paper [78]. However, an advantage of the observer based designs over the compensator design is its natural windup protection, when driven by a saturated control input [63]. On the other hand, the observer based controller is more sensitive to uncertainty in the input gain [63]. However, this drawback will be addressed by an augmentation of the DAC controller by an $\mathcal{L}_1$ adaptive output feedback controller.

In the following we apply the ideas of DAC and synthesize a robust output feedback baseline controller with active disturbance rejection capabilities, for solving the tracking problem. To this end, recall that the system (3.139) might equivalently be expressed as

$$\Sigma_{z,d}: \begin{cases} \dot{\xi}(t) = \check{A}_{11}\xi(t) + \check{A}_{12}\eta_n(t) + \check{B}_1\left(u_1(t) + d_\xi(t) + d_\Delta(t)\right), \quad \xi(0) = \xi_0 \\ \dot{\eta}_n(t) = \check{A}_{21}\xi(t) + \check{A}_{22}\eta_n(t), \quad \eta_n(0) = \eta_0 \\ \dot{\eta}_\Delta(t) = \check{A}_{22}\eta_\Delta(t) + d_\eta(t), \quad \eta_\Delta(0) = 0 \\ d_\Delta(t) = \check{b}_1^{-1} a_\eta^{\mathrm{T}} \eta_\Delta(t), \end{cases} \tag{4.36}$$

with d_ξ and d_η as defined in Definition 3.2.4, $\eta = \eta_n + \eta_\Delta$ and application of Assumption 4.1.1. With $z_n^{\mathrm{T}} = (\xi^{\mathrm{T}} \;\; \eta_n^{\mathrm{T}})$ we rewrite this into

$$\begin{aligned} \dot{z}_n(t) &= \check{A}\, z_n(t) + \check{B}(u(t) + d(t)), \quad z_n(0) = z_n^0 \\ y(t) &= \check{C}\, z_n(t), \end{aligned} \tag{4.37}$$

where we also omitted the disturbance generator for brevity. This is legitimate due to the reasons given in Section 3.2.2. Owing to the fact that the controller, yet to be devised, sees only the output of the system, which is unchanged, with a slight abuse of notation we drop the index n in z_n.

As the difference between η and η_n becomes more important in the stability proof of the $\mathcal{L}_1$ controller, we will thoroughly comment on that issue.

Subtracting next the trajectory reference system $\Sigma_z^\star$ from the last set of equations yields the tracking error dynamics as per

$$\begin{aligned} \dot{e}(t) &= \check{A}\, e(t) + \check{B}\left(u_e(t) + d(t)\right), \quad e(0) = e_0 \\ y_e(t) &= \check{C}\, e(t). \end{aligned} \tag{4.38}$$

Although we know that the 4-tupel $(A, B, C, 0)$ and consequently $(\check{A}, \check{B}, \check{C}, 0)$ are completely observable one could pose the question, whether the disturbance term $d(t)$ is observable at the output. According to [36], a condition for the observability of a disturbance can intuitively be formulated as follows:

A disturbance d is observable if it can algebraically be expressed in terms of the measured output y and a finite number of time derivatives of y as well as the control input u and a finite number of time derivatives of u.

Using the normal form from Theorem 3.2.1 it can be shown that for some disturbance $d_0(t) \in \mathbb{R}$ the differential equation with respect to the output reads

$$y^{(r)}(t) - a_\xi^{\mathrm{T}}\xi(t) - b_y u(t) = a_\eta^{\mathrm{T}}\eta(t) + d_0(t). \tag{4.39}$$

From that we concluded that the term $a_\eta^{\mathrm{T}}\eta(t) + d_0(t)$ can be reconstructed from the knowledge of input and output signals $u(t)$ and $y(t)$, respectively. That means, external disturbances d_0 acting on the external dynamics, parameter perturbations with respect to $a_\eta^{\mathrm{T}}\eta$, as well as perturbations of the internal dynamics that propagate through the solution $\eta(t)$ can be observed. Moreover, since there is no input u in the internal dynamics (z-coordinates) and none of the elements in η is measured it can further be concluded, that disturbances that act directly on the internal dynamics cannot be observed. However, this is not required for the solution of our problem. It suffices that at least the effect of these perturbations on the external dynamics via $\eta(t)$ is observable which is the case. Thus, intuitively, the disturbance must first propagate through the entire internal dynamics until its influence will be visible through $a_\eta^{\mathrm{T}}\eta$. This fact also justifies the usage of the model above, where this influence is represented by d_Δ.

Remark 4.1.6. Let us shortly comment on the reasoning behind using the model in the format of (4.36) and (4.37) instead of the one from Definition 3.2.4. The reason for this is the fact that, strictly speaking, only the disturbance with respect to the external dynamics is observable. Disturbances acting on the internal dynamics are not observable. However, during simulations of the observer based output feedback controller the following observation has been made. Besides the estimation of disturbances with respect to the external dynamics, the disturbance observer additionally estimated a second component of the disturbance. This particular component represented the perturbation of the internal dynamics, carried through the solution of $\eta(t)$ into the external ones. The model given above lets us exactly compute this influence and validate the disturbance rejection capabilities of the disturbance observer. This justifies the usage of the above model.

Knowing that the disturbances encountered in our application are observable, we go on with the derivation of the controller. Doing so, in the spirit of DAC, we impose the following assumption

Assumption 4.1.2 (Waveform structure of disturbances)**.** *Assume that parts of the lumped disturbance $d(t)$ affecting the external dynamics can be expressed by*

$$d(t) = d_w(t) + d_r(t),$$

where $d_w(t)$ is described by a waveform model of type

$$d_w(t) = \theta_w^{\mathrm{T}}\,\phi_w(t), \quad \theta_w, \phi_w(t) \in \mathbb{R}^m$$

with a vector θ_w of constant, unknown parameters and $\phi_w(t)$, a vector of completely known waveform basis functions, while $d_r(t) \in \mathbb{R}$ denotes an unknown, but uniformly bounded residuum term. Moreover, $d_w(t)$ constitutes the output signal of the following dynamic system

$$\Sigma_w : \begin{cases} \dot{x}_w(t) = A_w\, x_w(t), \quad x_w(0) = x_w^0 \\ d_w(t) = C_w\, x_w(t) \end{cases} \tag{4.40}$$

with disturbance state $x_w(t) \in \mathbb{R}^m$ and $A_w \in \mathbb{R}^{m\times m}$ and $C_w \in \mathbb{R}^m$.

Remark 4.1.7. According to reference [77], practical experience has shown that a t-polynomial waveform structure of order $(m-1)$ as per

$$d_w(t) = c_{m-1}t^{m-1} + \cdots + c_1 t + c_0 \tag{4.41}$$

with values $1 \leq m \leq 4$ is adequate for most disturbances encountered in practical applications. Additionally, in the case of sinusoidal disturbances or vibration, the waveform basis functions may also be chosen as $\sin(\omega_1 t)$, or $e^{-at}\sin(\omega_1 t)$, with ω_1 the dominant frequency of the disturbance or the resonance frequency of the process. Interestingly, the introduction of internal models with sinusoidal waveform structures implicitly leads to the realization of notch filters.

Using Assumption 4.1.2 and substitution of the output equation of (4.40) into (4.38) yields

$$\begin{aligned}\dot{e}(t) &= \check{A}\, e(t) + \check{B}\,(u_e(t) + C_w x_w(t) + d_r(t))\\ y_e(t) &= \check{C} e(t).\end{aligned}$$

Appending the state of the disturbance model to the existing tracking error state gives the extended tracking error dynamics

$$\begin{aligned}\begin{pmatrix}\dot{e}(t)\\ \dot{x}_w(t)\end{pmatrix} &= \begin{pmatrix}\check{A} & \check{B}C_w\\ 0 & A_w\end{pmatrix}\begin{pmatrix}e(t)\\ x_w(t)\end{pmatrix} + \begin{pmatrix}\check{B}\\ 0\end{pmatrix}(u_e(t) + d_r(t))\\ y_e(t) &= \begin{pmatrix}\check{C} & 0\end{pmatrix}\begin{pmatrix}e(t)\\ x_w(t)\end{pmatrix}\end{aligned}$$

or in shorter notation

$$\begin{aligned}\dot{\varepsilon}(t) &= \bar{A}\,\varepsilon(t) + \bar{B}\,(u_e(t) + d_r(t))\\ y_e(t) &= \bar{C}\varepsilon(t).\end{aligned} \tag{4.42}$$

The choice of $(A_w, 0, C_w, 0)$ must ensure that the pair $(\bar{A}, \bar{C})$ is observable. If this condition is met then we can next design a standard Luenberger observer with respect to the extended system. The observer is given by

$$\Sigma_{\hat{\varepsilon}}: \begin{cases}\dot{\hat{\varepsilon}}(t) = \bar{A}\,\hat{\varepsilon}(t) + \bar{B}\,u_e(t) + \ell(y_e(t) - \hat{y}_e(t)), \quad \hat{\varepsilon}(0) = \hat{\varepsilon}_0\\ \hat{y}_e(t) = \bar{C}\hat{\varepsilon}(t).\end{cases} \tag{4.43}$$

It provides estimates

$$\hat{\varepsilon}(t) = \begin{pmatrix}\hat{e}(t)\\ \hat{x}_w(t)\end{pmatrix}, \quad \hat{d}_w(t) = C_w\hat{x}_w(t) \tag{4.44}$$

that is, estimates of the tracking error variables as well as the whole disturbance state. The estimation error dynamics with estimation error defined as $\tilde{\varepsilon} := \varepsilon - \hat{\varepsilon}$ then reads

$$\dot{\tilde{\varepsilon}}(t) = \left(\bar{A} - \ell\bar{C}\right)\tilde{\varepsilon}(t) + \bar{B}\,d_r(t), \tag{4.45}$$

where observer gain $\ell \in \mathbb{R}^{n+m}$ might be designed with any standard method such that matrix $\bar{A} - \ell\bar{C}$ is Hurwitz.

Obviously, the estimation error dynamics is driven be the residuum $d_r(t)$. In the total absence of $d_r(t)$ the estimation error asymptotically converges to the origin of the estimation error state space. For uniformly bounded $d_r(t)$, the estimation error will converge asymptotically to a near vicinity of the origin of the estimation error state space. The deeper the eigenvalues of $\bar{A} - \ell\bar{C}$ lie in the open left half complex plain and the better the waveform model approximates the true disturbance, the smaller the

bound on the estimation error gets. For more details in this respect we refer to our work published in [142].

For the time being, we assume that the residuum term d_r is uniformly bounded (cf. Assumption 4.1.2). Under which assumptions this is true will be shown in the stability proof for the adaptive augmentation in Section 4.2.2.

In a *certainty equivalence* kind of manner the estimated disturbance and state variables are next used within the feedback and compensation parts of the nominal control law from Theorem 4.1.2 such that the control input u_e reads

$$u_e(t) = -k_1^{\mathrm{T}} \hat{e}_1(t) - \check{B}_1^{\dagger} \check{A}_{12}\, \hat{e}_2(t) - \hat{d}_w(t) \tag{4.46}$$

which is equivalent to

$$u_e(t) = -\begin{pmatrix} k_1^{\mathrm{T}} & \check{B}_1^{\dagger} \check{A}_{12} \end{pmatrix} \hat{e}(t) - C_w \hat{x}_w(t) = -K \hat{\varepsilon}(t), \tag{4.47}$$

where

$$K = \begin{pmatrix} k_1^{\mathrm{T}} & \check{B}_1^{\dagger} \check{A}_{12} & C_w \end{pmatrix} \tag{4.48}$$

denotes the composite feedback gain. Decomposing (4.38) into external and internal dynamics and inserting the observer-based controller given by (4.43) and (4.47) with (4.48) into the external tracking error dynamics, while noting that $\hat{\varepsilon} = \varepsilon - \tilde{\varepsilon}$ we get

$$\begin{cases} \dot{e}_1(t) & = \left(\check{A}_{11} - \check{B}_1 k_1^{\mathrm{T}}\right) e_1(t) + \check{B}_1 K \tilde{\varepsilon}(t) + \check{B}_1 d_r(t) \\ \dot{\tilde{\varepsilon}}(t) & = \left(\bar{A} - \ell \bar{C}\right) \tilde{\varepsilon}(t) + \bar{B}\, d_r(t) \end{cases} \tag{4.49}$$

for the closed loop tracking error dynamics. Or in block matrix form

$$\begin{pmatrix} \dot{e}_1(t) \\ \dot{\tilde{\varepsilon}}(t) \end{pmatrix} = \begin{pmatrix} \check{A}_{11} - \check{B}_1 k_1^{\mathrm{T}} & \check{B}_1 K \\ 0 & \bar{A} - \ell \bar{C} \end{pmatrix} \begin{pmatrix} e_1(t) \\ \tilde{\varepsilon}(t) \end{pmatrix} + \begin{pmatrix} \check{B}_1 \\ \bar{B} \end{pmatrix} d_r(t). \tag{4.50}$$

Assuming that the waveform model completely describes the occurring disturbances, i.e. $d_r \equiv 0$, then obviously the controller is able to completely reject these disturbances and the closed loop dynamics is asymptotically stable with the characteristic polynomial

$$p_{cl}(\lambda) = \det\left(\lambda I - (\check{A}_{11} - \check{B}_1 k_1^{\mathrm{T}})\right) \det\left(\lambda I - (\bar{A} - \ell \bar{C})\right). \tag{4.51}$$

The latter is a Hurwitz polynomial, if the matrices $\check{A}_{11} - \check{B}_1 k_1^{\mathrm{T}}$ and $\bar{A} - \ell \bar{C}$ are Hurwitz—a well known result from the separation theorem for LTI systems [51].

The resulting controller can be summarized by the following theorem

Theorem 4.1.3. *Let a system be given as* (4.20) *and* $e(t) := z(t) - z^{\star}(t)$*, with*

$$e^{\mathrm{T}}(t) = \begin{pmatrix} e_1^{\mathrm{T}}(t) & e_2^{\mathrm{T}}(t) \end{pmatrix}, \quad e_1(t) \in \mathbb{R}^r, \quad e_2(t) \in \mathbb{R}^{n-r}. \tag{4.52}$$

Consider the nominal output feedback tracking controller composed of the exact inverse feedforward law

$$\Sigma_n^{-1}: \begin{cases} \dot{x}_\eta^\star(t) = A_\eta x_\eta^\star(t) + B_\eta Y^\star(t), \quad x_\eta^\star(0) = x_{\eta,0}^\star \\ u^\star(t) = b_y^{-1}\left(\overset{(r)}{y^\star}(t) - a_\xi^{\mathrm{T}} x_\xi^\star(t) - a_\eta^{\mathrm{T}} x_\eta^\star(t)\right) \\ x^\star(t) = \begin{pmatrix} x_\xi^\star(t) & x_\eta^\star(t) \end{pmatrix}^{\mathrm{T}}, \\ z^\star(t) = T x^\star(t) \end{cases} \tag{4.53}$$

and the dynamic output feedback controller

$$\Sigma_c: \begin{cases} \dot{\hat{\varepsilon}}(t) = \left(\bar{A} - \ell\bar{C}\right)\hat{\varepsilon}(t) + \bar{B}\, u_e(t) + \ell\, y_e(t), \quad \hat{\varepsilon}(0) = \hat{\varepsilon}_0 \\ u_e(t) = -K\hat{\varepsilon}(t), \end{cases} \tag{4.54}$$

with

$$K = \begin{pmatrix} k_1^{\mathrm{T}} & \check{B}_1^\dagger \check{A}_{12} & C_w \end{pmatrix} \tag{4.55}$$

and overall control law

$$u(t) = u^\star(t) + u_e(t). \tag{4.56}$$

For $d_r \equiv 0$ the controller asymptotically stabilizes the tracking error dynamics and thus solves the nominal tracking control problem in the original coordinates if the feedback and observer gains k_1 and ℓ are designed such that matrices $\check{A}_{11} - \check{B}_1 k_1^{\mathrm{T}}$ and $\bar{A} - \ell\bar{C}$ are Hurwitz.

In the presence of uniformly bounded input disturbances $d_r \neq 0$ the controller asymptotically stabilizes the tracking error dynamics to a vicinity of the origin of the tracking error state space. ■

4.1.5 Controller Tuning and Frequency Domain Analysis

For the design of the controller, parameters ℓ and k_1 must be computed and the disturbance model $(A_w, 0, C_w, 0)$ must be specified.

Due to the outstanding robustness properties of Linear Quadratic Regulators (LQR) [61, 92] and the nice time domain properties of minimum energy estimators such as the Kalman-Bucy filter [61], we will use both of these approaches for the parameterization of both, controller and observer. The combination of LQR and a Kalman-Bucy filter is also known as Linear Quadratic Gaussian (LQG) control [61, 92]. Since the properties of these controllers are extensively studied in any standard text book on linear systems, see e.g. [51, 61] and many others, we will not elaborate any deeper on them and just apply them from a practical point of view.

A common problem of tuning an observer-based controller, with the performance assessment in the time domain, is the fact that one tends to tune the parameters such that very good state and/or disturbance estimates are obtained. Of course this is intuitive, because it implies good time domain performance and good disturbance rejection properties. However, with this approach one looses sight of robustness.

In order to get some insights on how to tune the controller to get sufficient robustness we proceed with a frequency domain analysis of the presented control scheme. In this way, the observer-based controller is rather interpreted as a dynamic output feedback compensator. Towards this end, it is convenient to rewrite the output feedback

controller to

$$\Sigma_c : \begin{cases} \dot{\hat{\varepsilon}}(t) = \left(\bar{A} - \ell\bar{C} - \bar{B}K\right)\hat{\varepsilon}(t) + \ell\, y_e(t), \quad \hat{\varepsilon}(0) = \hat{\varepsilon}_0 \\ u_e(t) = -K\hat{\varepsilon}(t) \end{cases} \tag{4.57}$$

Taking the Laplace transform yields

$$\hat{\varepsilon}(s) = \left(sI - \left(\bar{A} - \ell\bar{C} - \bar{B}K\right)\right)^{-1} \ell\, y_e(s) \tag{4.58}$$

$$u_e(s) = -K\hat{\varepsilon}(s) \tag{4.59}$$

and hence

$$u_e(s) = -\Sigma_c(s)\, y_e(s), \tag{4.60}$$

with $\Sigma_c(s) = K\left(sI - \left(\bar{A} - \ell\bar{C} - \bar{B}K\right)\right)^{-1}\ell$. Next, let $\Sigma_n^{-1}(s)$ denote the Laplace transform of the nominal feedforward controller Σ_n^{-1} (see e.g. Theorem 4.1.3) with input signal $y^\star(s)$ and output $u^\star(s)$, respectively. Apparently, the proposed output feedback controller can be cast into the 2-DOF architecture presented in Figure 4.1. Please note,

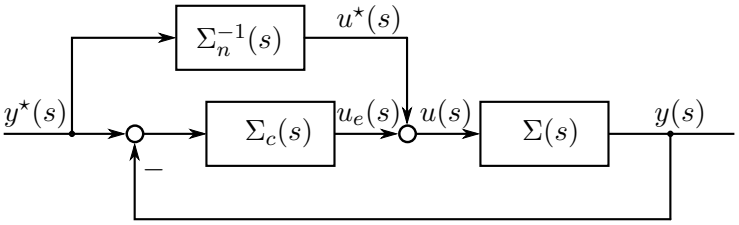

FIGURE 4.1: 2-DOF control architecture.

that in contrast to the tracking error $y_e(t)$ in our design, the tracking error in the 2-DOF architecture is given by $y^\star(t) - y(t) = -y_e(t)$, such that the input/output behavior of the controller is simply given by

$$u_e(s) = \Sigma_c(s)(y^\star(s) - y(s)). \tag{4.61}$$

By virtue of the fact that the feedforward controller does not influence the stability of the closed loop system, we can thus concentrate on the design of the feedback controller only. To study its frequency domain behavior, we consider the standard feedback configuration (without feedforward) as shown in Figure 4.2. For our analysis we further

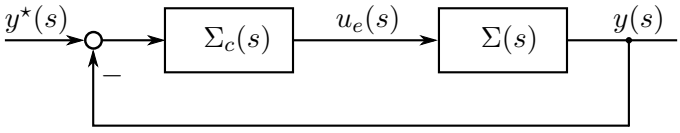

FIGURE 4.2: Standard feedback configuration.

consider the so-called gang of four of the feedback loop system

$$S(s) = \frac{1}{1+\Sigma_c(s)\Sigma(s)}, \quad T(s) = \frac{\Sigma_c(s)\Sigma(s)}{1+\Sigma_c(s)\Sigma(s)},$$
$$S_u(s) = \frac{\Sigma_c(s)}{1+\Sigma_c(s)\Sigma(s)}, \quad S_i(s) = \frac{\Sigma(s)}{1+\Sigma_c(s)\Sigma(s)},$$

that is sensitivity $S(s)$, complementary sensitivity $T(s)$, noise sensitivity $S_u(s)$ as well as process sensitivity $S_i(s)$. Furthermore, the loop gain

$$L(s) = \Sigma_c(s)\Sigma(s) \tag{4.62}$$

gives valuable insight on robustness margins like gain and phase margin. Due to the 2-DOF control architecture, the tracking performance is completely specified by the feedforward controller. Therefore, feedback controller design is exclusively dedicated to disturbance rejection. Therefore, we will mainly concentrate on $L(s)$, $S(s)$, $S_i(s)$ and $S_u(s)$.

The following simulation example illustrates the effectiveness of the proposed control scheme and shows that robustness is sacrificed, if the controller performance is only assessed in the time domain:

Example 4.1.3. *Consider system* (4.37) *and the controller from Theorem 4.1.3. For illustration purposes, the input dynamics is first excluded from the simulation and all parametric uncertainties are set to zero. Only the external disturbances are present at the system input, i.e.* $d(t) = f_1(\xi, t)$.

We assume that the disturbance d *may be approximated by a first order polynomial given by*

$$d_w(t) = c_1 t + c_0. \tag{4.63}$$

The disturbance model $(A_w, 0, C_w, 0)$ *is thus given by a pair of integrators, i.e.*

$$\Sigma_w : \begin{cases} \dot{x}_w(t) = \begin{pmatrix} 0 & 1 \\ 0 & 0 \end{pmatrix} x_w(t), \quad x_w(0) = 0 \\ d_w(t) = \begin{pmatrix} 1 & 0 \end{pmatrix} x_w(t) \end{cases} \tag{4.64}$$

Let further $Q_c \in \mathbb{R}^{r\times r}$, $Q_o \in \mathbb{R}^{(n+m)\times(n+m)}$, *symmetric and positive semidefinite, and* $R_c \in \mathbb{R}^+$, $R_o \in \mathbb{R}^+$ *be the weights for the LQR controller and the minimum energy observer, respectively. Tuning the weights solely on time domain observations, while aiming for an almost perfect fit of the disturbance estimate with the true disturbance, yields the following weights*

$$Q_c = \mathit{diag}(10, 0), \quad R_c = 1, \tag{4.65}$$

and

$$Q_o = \mathit{diag}(1, 1\mathrm{e}6, 1, 1\mathrm{e}6, 1\mathrm{e}12, 1\mathrm{e}22), \quad R_o = 1, \tag{4.66}$$

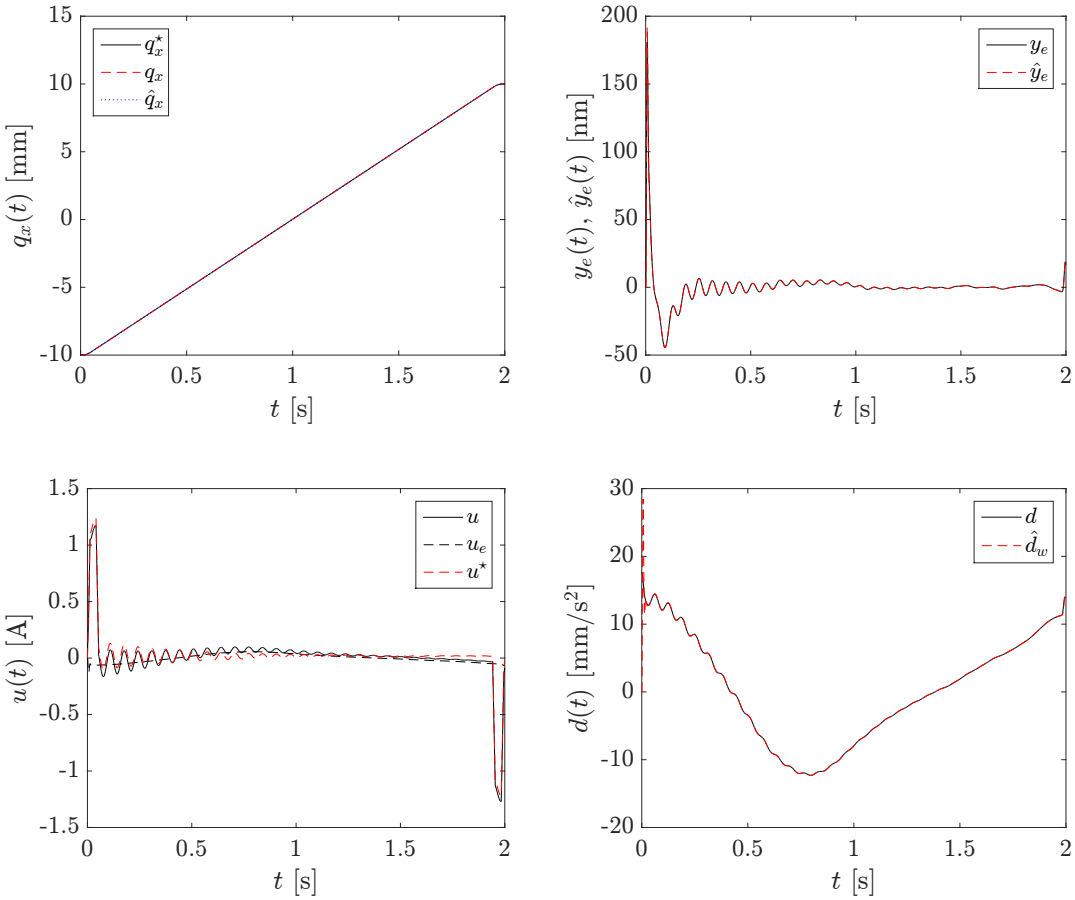

FIGURE 4.3: Simulation results for Example 4.1.3 with reference trajectory $y^\star = q_x^\star$, regulated position $y = q_x$ and position estimate $\hat{y} = \hat{q}_x$ (top left), dedicated tracking and estimation errors y_e, $\hat{y}_e$ (top right), control input u and portions $u^\star$, u_e (bottom left) such as true disturbance d and disturbance estimate $\hat{d}_w$.

specified in the original coordinates. This leads to the following eigenvalues of $A_c := \check{A}_{11} - \check{B}_1 k_1^{\mathrm{T}}$ *and* $A_o := \bar{A} - \ell \bar{C}$*, i.e.*

$$\lambda(A_c) = -19.18 \pm j19.18$$
$$\lambda(A_o) \in \{-215.20 \pm j519.54, -519.53 \pm j215.20, -2.50 \pm j98.10\}.$$

The resulting performance is illustrated on a point-to-point positioning problem along the q_x*-axis, where the mover is positioned from* $-10\,\mathrm{mm}$ *to* $10\,\mathrm{mm}$ *in* $2\,\mathrm{s}$*. For solving this problem, a standard double S trajectory is adopted. Figure 4.3 depicts the simulation results.*

Observing the tracking error (top right) and the quality of the disturbance estimate (bottom right), it can be concluded that the time domain performance of the proposed controller is excellent. After a short transient of the observer estimation error dynamics on $t \in [0, 0.2]\,\mathrm{s}$*, the tracking error settles down to a near vicinity of the origin of the tracking error state space and its magnitude takes values below* $10\,\mathrm{nm}$*. The disturbance is estimated nearly perfectly, and also the estimates for velocity and the stator states, not shown here for brevity, are excellent as well.*

However, if we examine the frequency domain performance of the controller with this particular parameterization, shown in Figure 4.4, it is evident that the frequency domain performance

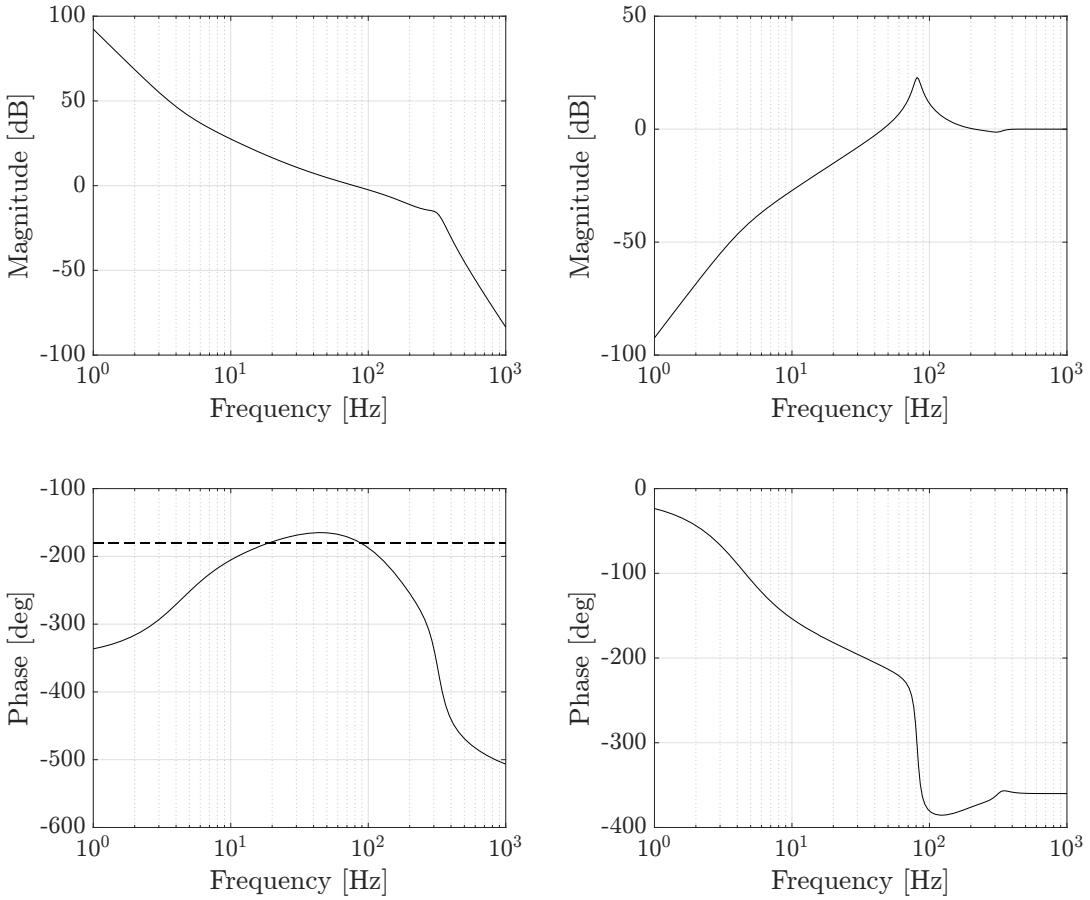

FIGURE 4.4: Loop gain $L(s)$ (left) with a phase margin of $\phi_m = 4.92°$ and a gain margin of $g_m = 1.12$ dB; Sensitivity function $S(s)$ (right) with a peak value of $M_s = 23$ dB. The dotted line indicates the line of $-180°$.

is poor in terms of robustness. Although the loop gain $L(s)$ has its typical and desirable shape, the controller has insufficient phase lead resulting in phase and gain margins of $\phi_m = 4.92°$ and $g_m = 1.12$ dB, respectively. That means that a perturbation of the input gain parameter at a factor of 1.14 renders the closed loop system unstable which is not tolerable. Additionally, the sensitivity shows a peak value of $M_s = 23$ dB which amplifies noise too much and thus may excite unmodeled dynamics.

Please note that the effect of input dynamics $\Sigma_2(s)$ is included in the bode plots in order to illustrate the effect of unmodeled dynamics. ▲

The example clearly shows that good time domain performance does not necessarily imply good frequency domain performance, nor robustness. The contrary may also be true, that is, good frequency domain performance in terms of robustness is only gained at the expense of (time domain) performance. So, we have to find a good compromise between these two contrary goals.

Indeed, this trade-off is not new. It is well known (see e.g. [61, 92]) that LQG controllers suffer from poor frequency domain properties. In order to recover some of the outstanding robustness properties and loop shapes of full state-feedback LQR controllers the so-called method of loop transfer recovery (LTR) proposed by [38, 132] is often employed. However, although the LTR procedure provided quite good results

our impression was that better results could be obtained when the weights were adjusted manually in order to obtain the desired loop shapes.

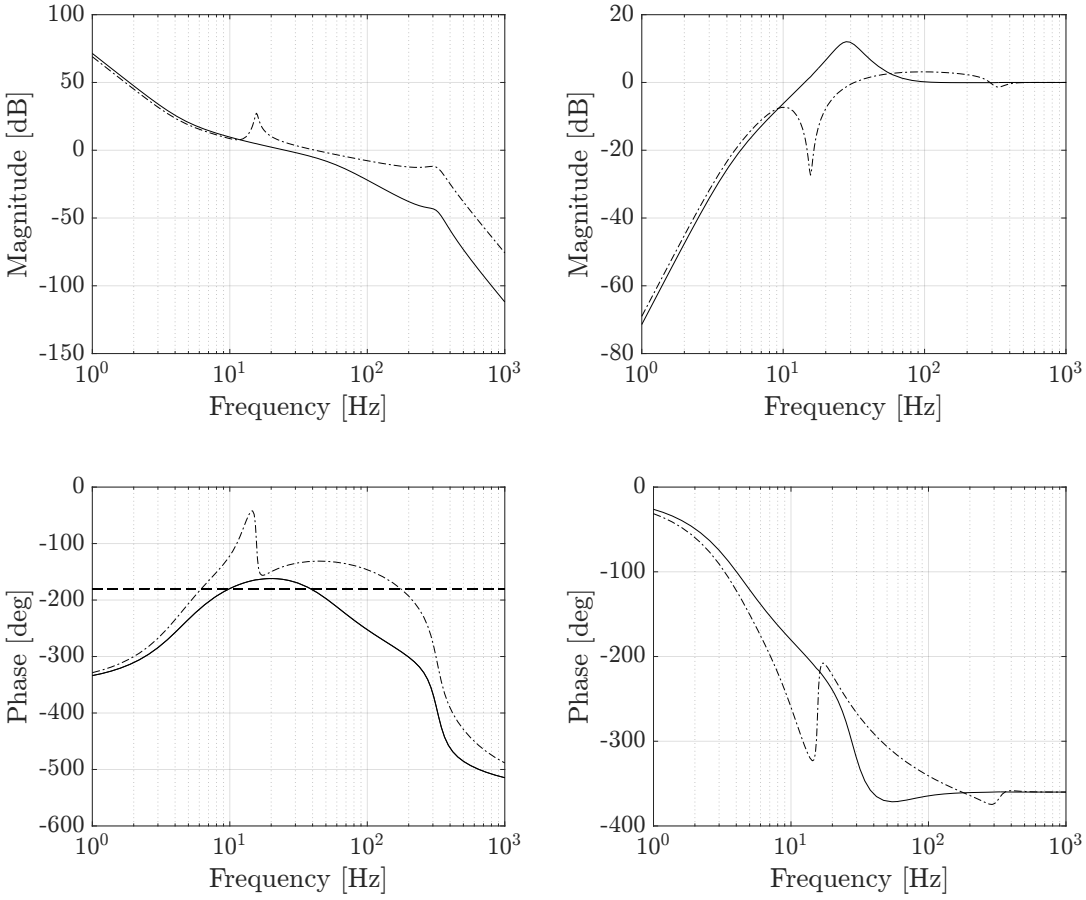

FIGURE 4.5: Loop gain $L(s)$ (left) of the initial design with reduced bandwidth (solid) and the final design (dash-dotted). The two designs provide respectively, the following phase and gain margins, $\phi_m = 16°$, $g_m = 4.53$ dB (solid) and $\phi_m = 48.8\,°$, $g_m = 11.7$ dB (dash-dotted); Sensitivity function $S(s)$ (right) of the respective designs with peak values of $M_s = 12$ dB (solid) $M_s = 3$ dB (dash-dotted). The dotted line indicates the line of $-180°$.

Doing so, the controller from example 4.1.3 can be rendered more robust by reducing the bandwidth of the controller. Choosing the controller weights as

$$Q_c = \text{diag}(10, 0), \quad R_c = 1, \tag{4.67}$$

and

$$Q_o = \text{diag}(1, 1e6, 1, 1e6, 1e12, 1e18), \quad R_o = 1, \tag{4.68}$$

leads to the loop shapes presented in Figure 4.5 in solid lines. Note, that for the following Figures, the input dynamics $\Sigma_2(s)$ is always included. The choice of weighting matrix Q_o reduces the bandwidth of the initial design heavily from $80\,\text{Hz}$ to approximately $25\,\text{Hz}$. Despite the massive reduction of bandwidth the provided phase and gain margins of $\phi_m = 16°$ and $g_m = 4.53$ dB are still unacceptable. Also the sensitivity

peak showing a value of $12\,\mathrm{dB}$ is still too high. Additionally, due to the fact that the loop gain has a gain of approximately $5\,\mathrm{dB}$ in the range of the resonance frequency of the stator, the time domain behavior is accompanied by undesired long tailed oscillations. This effect is shown in Figure 4.6 (A), where the output response to unit steps in the input disturbance is shown, again in solid lines.

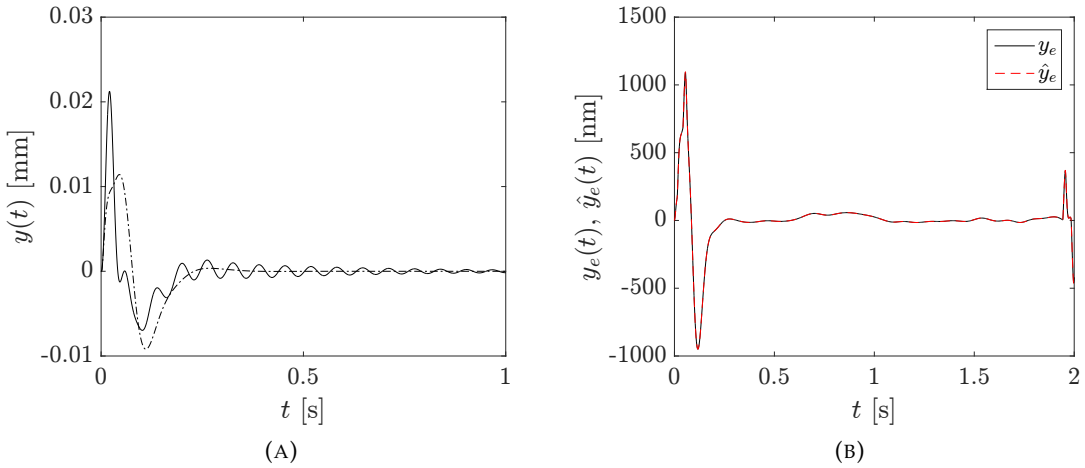

(A) (B)

FIGURE 4.6: (A) Output response to unit step in the input disturbance for the initial design with reduced bandwidth (solid), and the final design (dash-dotted); (B) tracking error for the final design applied to the tracking task of Example 4.1.3 but now with input dynamics.

For reducing this effect it has been experienced that the loop gain should have a gain of approximately $30\,\mathrm{dB}$ around the resonance frequency. Moreover, due to the aspired $\mathcal{L}_1$ augmentation of the nominal design, and a desired phase margin of at least $30°$ for the complete scheme, we experienced that the nominal controller should have a phase margin between $45°$ and $50°$. Shaping the loop to these specifications leads to the final design with weighting matrices (with respect to original coordinates)

$$Q_c = \mathrm{diag}(10, 0), \quad R_c = 1, \tag{4.69}$$

as well as

$$Q_o = \mathrm{diag}(0, 2\mathrm{e}13, 3\mathrm{e}9, 1\mathrm{e}13, 1\mathrm{e}14, 1\mathrm{e}21), \quad R_o = 1, \tag{4.70}$$

and the loop shapes presented in Figure 4.5 in dash-dotted lines. The eigenvalues of $A_c := \check{A}_{11} - \check{B}_1 k_1^{\mathrm{T}}$ and $A_o := \bar{A} - \ell \bar{C}$ are given by

$$\begin{aligned}
&\lambda(A_c) = -19.18 \pm j19.18 \\
&\lambda(A_o) \in \{-1494.18 \pm j1496.51, -81.10 \pm j79.10, -34.15 \pm j64.34\}.
\end{aligned}$$

With this particular design, the loop shapes have sufficient phase and gain margins of $\phi_m = 48.8\,°$ and $g_m = 11.7\,\mathrm{dB}$, as desired. Also the sensitivity peak with a value of $M_s = 3\,\mathrm{dB}$ lies within the specification.

Interestingly, through the third and fourth weight of Q_o an implicit notch filter has been formed, providing a loop gain of $28\,\mathrm{dB}$ in the range of the resonance frequency. As evident from Figure 4.6 (A), this completely removes the influence of frame vibrations

when subject to input step disturbances. Note that also the noise sensitivity, not shown for brevity, fulfills the specification with a peak value of $65\,\mathrm{dB}$.

If this controller is applied for the tracking task of Example 4.1.3 the tracking error performance presented in Figure 4.6 (B) is obtained. Again, the large peaking at the beginning is only due to the transient of the observer estimation error dynamics and of course only appears once. After this transient has decayed, the tracking error stays always below $500\,\mathrm{nm}$ and therefore fulfills the specification on the tracking error in a realistic kind of manner.

Although the derived controller is quite robust it has been observed that in the presence of parametric uncertainty, the tracking error performance deteriorates. To handle these uncertainties, it is proposed to make use of a further control input, dedicated for an adaptive augmentation of the nominal control loop. This will be presented in the next section.

4.2 $\mathcal{L}_1$ Adaptive Tracking Control

For controlling systems with unknown and possibly time-varying parameters, the concept of adaptive control emerged in the early 1950s, where it was primarily conceived for autopilots of high performance aircraft. It was proposed to automatically adjust the controller parameters in order to adapt to changing aircraft dynamics and parametric variations (see e.g. [5, 68, 92] for a detailed historical overview).

In this regard, in particular, model reference adaptive control (MRAC) became famous [5, 71, 102]. However, in the early 1980s Rohrs' well-known counterexample [119] revealed that MRAC such as most of the hitherto existing adaptive controllers lacks robustness with respect to unmodeled dynamics and disturbances, thwarting its practical use. In view of these problems, many modifications have been proposed so as to robustify existing adaptation schemes [71]. Most of these modifications yet only led to ensure the boundedness of the adaptive estimates [147] but did not affect the bandwidth and phase margin of the control loop, as suggested by [119].

For resolving the performance and robustness trade-off, a recent methodology is the so-called $\mathcal{L}_1$ adaptive control theory, see overview in [68]. The philosophy of $\mathcal{L}_1$ adaptive control is based on the understanding that uncertainties may be compensated within the available controller bandwidth, only [68, 147]. Bandwidth limitations, e.g. due to actuator dynamics, may be included into the controller design by inserting a low-pass filter at a particular point of the control loop [68].

This filter, interestingly, lets achieve a (frequency) decoupling of the control from the estimation loop by shielding high frequency content of the adaptation from the plant input. The approach enables fast parameter adaptation, thus performance, without sacrificing robustness of the closed-loop, only constraint by hardware limitations [68]. Furthermore, the approach helps take into account the three time-scales of an adaptive system, crucial for stability [3], and solves Rohrs' benchmark problem [147].

The fast adaptation loop in $\mathcal{L}_1$ adaptive controllers lets quantify the transient performance of the closed-loop, a priori, without need of persistency of excitation arguments and high gain feedback [68]. This makes it attractive for an adaptive augmentation of 2-DOF control architectures in tracking problems, where trajectories usually need to be smooth, in contrast to persistently exciting.
In particular $\mathcal{L}_1$ adaptive control can be considered as a modified version of an indirect or predictor-based MRAC approach. Thus, the control architecture of an $\mathcal{L}_1$ controller

essentially comprises the same elements, namely a state predictor, an adaptation law and a control law, as shown in Figure 4.7.

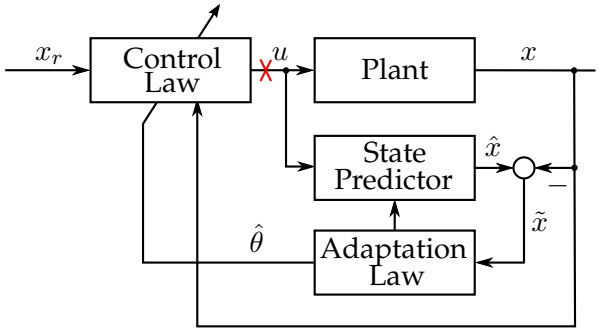

FIGURE 4.7: Predictor-based MRAC architecture, with x_r as reference, u as control input, x as plant state, $\hat{x}$ as predictor state, $\tilde{x}$ as prediction error and $\hat{\theta}$ as adaptive estimate. The red cross marks the position for possible modifications.

Essentially, the state predictor, also known as companion system [16], constitutes an observer like system that captures the desired reference dynamics of the closed loop system. It thus plays an equivalent role as the reference models in direct MRAC schemes (see e.g. [68, 71, 92]). Due to this fact, we will sometimes use the terms state predictor and reference model interchangeably. Being an observer like system, the predictor mimics the desired closed loop behavior and substitutes all unknown parameters by its adaptive estimates [68]. The latter are provided by the adaptation law which itself is driven by the prediction error (or equivalently reference model-tracking error) computed from the difference of plant and predictor state (cf. Figure 4.7).

These estimates are also used in the control law, which attempts to compensate for the uncertainties in a *certainty equivalence* kind of manner. The key difference between the predictor-based MRAC scheme and $\mathcal{L}_1$ adaptive control is the control law. While in MRAC one tries to compensate for all disturbances, which in fact assumes an infinite bandwidth of the control channel, in $\mathcal{L}_1$ adaptive control, compensation of uncertainties only takes place in the achievable bandwidth of the control channel. As discussed earlier, the limitation of bandwidth in $\mathcal{L}_1$ adaptive control is addressed by means of a low-pass filter placed at a particular point in the control loop. This special point is marked by the red cross in Figure 4.7.

Interestingly, this shows parallels to classical control and loop shaping ideas, where it is natural to incorporate low-pass filters for obtaining high frequency roll-off. When properly designed, this in fact avoids the excitation of high frequency unmodeled dynamics which is advantageous in the face of our application.

Note that the insertion of the filter is only possible due to the observer like architecture and the fact that it renders the predictor error dynamics (reference model-tracking error dynamics) independent of the control input. In fact this leaves also room for numerous other modifications, including hedging, the treatment of input time delays and others [86]. Hence, this architecture is favorable and the key to the concept of $\mathcal{L}_1$ adaptive control.

Note that in view of the predictor-based MRAC the bandwidth of the controller is only adjustable via the adaptation gain, where high gains imply good performance but poor robustness and vice versa. That means that there is no separation of robustness and performance which renders tuning of these controllers very difficult [68]. However, the low-pass filter in $\mathcal{L}_1$ adaptive control achieves a decoupling of the control

from the adaptation loop. This means that theoretically, infinitely high adaptation rates are possible, without sacrificing robustness. This in turn results in superior transient performance.

Due to this fact, the authors of [68] suggest to choose the adaptation rate as high as the hardware limitations (of the CPU) permit. Thus, the design of an $\mathcal{L}_1$ adaptive controller basically comes down to the design of the reference dynamics, i.e. the state predictor, and the design of a low-pass filter.

In the authors opinion the best way of applying adaptive control is to augment a nominal/baseline controller that has been carefully designed and obtains desired performance with respect to nominal conditions. Thus, the state predictor is simply given by the closed loop dynamics of the baseline control loop. Consequently, the design of the $\mathcal{L}_1$ controller simply reduces to the design of a low-pass filter which is then designed for addressing bandwidth limitations and for obtaining considerable roll-off at high frequencies.

Finally, note that there exists also a modification for direct MRAC schemes, for addressing limitations with respect to control authority. This also includes bandwidth limitations. In particular, this modification is referred to as pseudo control hedging (PCH) or simply hedging (see e.g. [9, 79, 80]). Roughly speaking, PCH modifies the reference model by a so-called hedging signal such that actuator characteristics such as saturations or input dynamics are not visible to the adaptive element and do not appear in the reference model tracking error dynamics. Interestingly, as shown in the work of [9] this particular modification, at least for known input gains, is equivalent to $\mathcal{L}_1$ adaptive control. While according to [9] stability proofs for hedging in dircet MRAC schemes have not yet been available, $\mathcal{L}_1$ adaptive control constitutes the "*[...] mathematically correct framework that provides a stability proof/condition [...]*"[9].

4.2.1 $\mathcal{L}_1$ Adaptive Augmentation with Full State Feedback

Although not implementable on the PPS1405 platform, for the sake of completeness we next comment on the design of an $\mathcal{L}_1$ adaptive augmentation with full state feedback based on our work presented in [140]. To this end, let us consider the nominal state feedback controller derived in Section 4.1.3. For the design of the nominal controller, so far, we assumed d_ξ to be perfectly known. Of course this assumption is not realistic. For unknown d_ξ we propose to replace the control portion u_d of the nominal controller by a new (adaptive) input u_{ad} that is capable of providing a reasonable estimate $\hat{d}_\xi$ to compensate for d_ξ. The new control law is thus given by

$$u(t) = u^\star(t) + u_s(t) + u_c(t) + u_{ad}(t), \tag{4.71}$$

where all control portions are as in Theorem 4.1.2 and u_{ad} is yet to be devised. In view of the high frequency dynamics $\Sigma_2(s)$, limiting the bandwidth of the control channel, the complete rejection of d_ξ is not a realistic goal. Note that even if d_ξ would be perfectly known, it could not be rejected entirely due to the presence of unmodeled high frequency dynamics. Thus, we take these limitations into account and only try to compensate for d_ξ within the achievable bandwidth. This is the best that one can hope to achieve in this situation. To this end, we employ the recently established $\mathcal{L}_1$ adaptive control theory from Hovakimyan and Cao [68].

Remark 4.2.1. In contrast to the $\mathcal{L}_1$ schemes presented in [68], where the reference signal also enters the low-pass filter, we let the nominal controller including reference feedforward enter the system directly. This is evident from equation (4.71). Only in this

way the nominal tracking performance is independent of the low-pass filter of the $\mathcal{L}_1$ controller.

In view of the understanding that uncertainties can only be compensated for within a feasible bandwidth of the control channel also the problem of (perfect) asymptotic output tracking is not feasible. Therefore, we adapt the nominal tracking problem from Definition 4.1.1 to

Definition 4.2.1 (Robust (trajectory) tracking control problem)**.** *Consider system* (4.20) *and an arbitrary, bounded reference trajectory $y^\star(\cdot) \in \mathcal{C}^k$, with $k \geq r$, where r denotes the relative degree. Devise a control law for u such that in the presence of system uncertainties d_ξ and d_η the system output y tracks the desired reference trajectory $y^\star$ as best as possible, while the control input u stays uniformly bounded, i.e.*

$$|u(t)| \leq \delta_u < \infty, \quad \forall t \geq 0,$$

and the tracking error defined by $y_e(t) := y(t) - y^\star(t)$ stays uniformly ultimately bounded

$$|y_e(t)| \leq \epsilon_t, \quad \forall\, t \geq T_0,$$

where $\epsilon_t > 0$ is a desired tracking tolerance and T_0 is a finite time instant. ▼

For solving the robust tracking control problem, we next begin with the derivation of the $\mathcal{L}_1$ controller. Towards this end, we consider the dynamics in (4.20) with inserted control law (4.71), together with the definition of d_ξ, as given in (3.141). That is,

$$\begin{cases} \dot{e}_1(t) = A_m\, e_1(t) + B_m \left(u_{ad}(t) + \beta u(t) + \theta_1^{\mathrm{T}} z(t) + f(\xi, t)\right), \quad e_1(0) = e_1^0 \\ \dot{e}_2(t) = \check{A}_{21}\, e_1(t) + \check{A}_{22}\, e_2(t) + d_\eta(t), \quad e_2(0) = e_2^0 \\ y_e(t) = C_m e_1(t), \end{cases} \tag{4.72}$$

where we used the definitions $A_m := \check{A}_{11} - \check{B}_1 k_1^{\mathrm{T}}$ (Hurwitz), $B_m := \check{B}_1$ and C_m the first two rows of $\check{C}$. In view of Assumption 4.1.1, u_1 has been replaced by u.

This constitutes the perturbed closed loop tracking error dynamics. We assume that k_1 is designed such that in the absence of d_ξ and d_η desired performance and robustness specifications are met such that these dynamics constitute the desired closed loop dynamics under nominal conditions. The task of the adaptive controller is thus to compensate for d_ξ in order to recover the nominal performance in the face of unexpected changes in the parameter values or unknown external disturbances.

In view of Assumption 3.2.3, let us again concentrate on the external dynamics. To this end, additionally to Assumptions 3.2.1 and 3.2.2 consider the following assumption:

Assumption 4.2.1. *We assume, that the disturbance term $f(\xi, t)$ may be modeled as*

$$f(\xi, t) := \theta_2^{\mathrm{T}}(t)\xi(t) + \sigma(t), \tag{4.73}$$

where $\theta_2(t) \in \mathbb{R}^2$ is a time-varying vector of unknown parameters and $\sigma \in \mathbb{R}$ is an unknown time-varying residuum.

Then the external dynamics of (4.72) becomes

$$\begin{cases} \dot{e}_1(t) = A_m\, e_1(t) + B_m \left(u_{ad}(t) + \beta u(t) + \theta^{\mathrm{T}}(t) z(t) + \sigma(t)\right), \quad e_1(0) = e_1^0 \\ y_e(t) = C_m e_1(t). \end{cases} \tag{4.74}$$

where $\theta(t)$ is partitioned as per

$$\theta^{\mathrm{T}}(t) = \begin{pmatrix}\theta_1^{\mathrm{T}} + \begin{pmatrix}\theta_2^{\mathrm{T}}(t) & 0\end{pmatrix}\end{pmatrix} =: \begin{pmatrix}\theta_\xi^{\mathrm{T}}(t) & \theta_\eta^{\mathrm{T}}\end{pmatrix} \tag{4.75}$$

in order to account for the parameter perturbations with respect to $\xi(t)$ and $\eta(t)$. Moreover, β, $\theta(t)$ and $\sigma(t)$ are subject to the following assumptions [68]:

Assumption 4.2.2. *The unknowns $\theta(t)$ and $\sigma(t)$ are assumed to be uniformly bounded, i.e.*

$$\theta(t) \in \Omega_{\theta,0}, \quad |\sigma(t)| \leq \sigma_{max,0}, \quad \forall\, t \geq 0 \tag{4.76}$$

and continuously differentiable with respect to time t, obeying

$$\|\dot{\theta}(t)\| \leq \delta_\theta < \infty, \quad |\dot{\sigma}(t)| \leq \delta_\sigma < \infty, \quad \forall\, t \geq 0. \tag{4.77}$$

Therein $\Omega_{\theta,0}$ is a known convex compact set and $\sigma_{max,0}$ is a known (conservative) bound on $\sigma(t)$ such that $\sigma(t)$ securely lies within the set $\Omega_{\sigma,0} := [-\sigma_{max,0}, \sigma_{max,0}]$.

Applying next the Assumptions 3.2.1 and 3.2.2 on parameter β leads to the following assumption:

Assumption 4.2.3. *Let the unknown input gain perturbation $\beta > -1$ and let it belong to a known (conservative) convex compact set $\beta \in \Omega_{\beta,0} := [\beta_{l,0}, \beta_{u,0}] \subset \mathbb{R}$ where $-1 < \beta_{l,0} < \beta_{u,0}$ are known lower and upper bounds on β.*

Remark 4.2.2. Assumption 4.2.1 is imposed for simplicity and has a reasonable physical interpretation to it. Indeed, the main part of the disturbances $f(\xi, t)$ encountered in our application can be physically interpreted as stiffness and damping coefficients that depend on position and velocity, respectively (cf. Figure 3.12). Therefore, modeling these coefficients with a time-varying component $\theta_2^{\mathrm{T}}(t)\xi(t)$ and an additional time-varying residuum $\sigma(t)$ forms a reasonable model.

Of course, in the case of more complex nonlinearities on could use the approach presented in [92] that is widely used throughout the MRAC and neuro-adaptive control community. There, the nonlinearity $f(\xi, t)$ is modeled by $\theta_2^{\mathrm{T}}\phi(\xi)$ with $\phi(\xi) \in \mathbb{R}^N$ an N dimensional regressor vector of known nonlinear, locally Lipschitz continuous basis functions. Therein, θ_2 is again a constant vector or matrix of unknown parameters.

Another alternative is the application of Lemma A.9.1 of reference [68]. Roughly speaking, it states that for $\xi(\cdot) \in \mathcal{L}_\infty$ and $\dot{\xi}(\cdot) \in \mathcal{L}_\infty$, there exist constants $\theta_2(t) \in \mathbb{R}$ and $\sigma(t) \in \mathbb{R}$ such that on a finite time interval $t \in [0, \tau]$ the nonlinearity $f(\xi, t)$ may be expressed as

$$f(\xi, t) = \theta_2(t)\, \|\xi_t\|_{\mathcal{L}_\infty} + \sigma(t). \tag{4.78}$$

However, in view of the physical interpretation and the weak nonlinearity the suggested model suffices our needs.

The $\mathcal{L}_1$ adaptive controller is then given by the following elements:

- state predictor
- adaptation law
- control law

The state predictor is given by

$$\Sigma^{p}_{\mathcal{L}_1} : \begin{cases} \dot{\hat{e}}_1(t) = A_m\, \hat{e}_1(t) + B_m \left(u_{ad}(t) + \hat{\beta} u(t) + \hat{\theta}^{\mathrm{T}}(t) z(t) + \hat{\sigma}(t) \right) \\ \hat{y}_e(t) = C_m \hat{e}_1(t), \quad \hat{e}_1(0) = e_1^0, \end{cases} \tag{4.79}$$

where $\hat{e}_1 \in \mathbb{R}^r$ is the predictor state and $\hat{\beta} \in \mathbb{R}$, $\hat{\theta} \in \mathbb{R}^n$ and $\hat{\sigma} \in \mathbb{R}$ denote the estimates of the respective unknowns.

Remark 4.2.3. Note that (4.79) indicates a perfect initialization of the predictor state $\hat{e}_1$ with the error state of the plant. However, this is not as restrictive as it seems and does not sacrifice stability, as shown in the proof of [17]. In fact, non-zero initialization errors will contribute to an exponentially decaying component within the initial transient phase. During this transient phase the performance may slightly degrade [17].

The state predictor system is a simple simulator, mimicking the dynamics of the controlled system. For rendering the observation dynamics faster than the control loop dynamics, as suggested in [68], the state predictor may be augmented on the right hand side of (4.79) by a Luenberger type of correction term, i.e. $-L_m \left(\hat{e}(t) - e(t) \right)$ with appropriate gain $L_m \in \mathbb{R}^{r \times r}$. On the one hand, this helps speed up the decay rate of the initialization error, leaving transient performance almost unaffected. On the other hand, it lets adjust the damping properties of the adaptation loop and thus helps reduce high frequency content in the estimates and peaking phenomena. For details see the thorough discussions in [68, 85]. Due to the observer-like architecture in $\mathcal{L}_1$ adaptive control this modification appears somehow naturally. Interestingly, it shows equivalences to recent results on closed-loop reference models in direct MRAC schemes [47, 92] used for improving the transient performance of MRAC controllers.

The adaptive estimates inside the state predictor are provided by the adaptation law [18, 68] given by

$$\Sigma^{a}_{\mathcal{L}_1} : \begin{cases} \dot{\hat{\beta}}(t) = \Gamma\, \mathrm{Proj}(\hat{\beta}(t), -\tilde{e}_1^{\mathrm{T}}(t) P B_m u(t)) \\ \dot{\hat{\theta}}(t) = \Gamma\, \mathrm{Proj}(\hat{\theta}(t), -z(t)\, \tilde{e}_1^{\mathrm{T}}(t) P B_m) \\ \dot{\hat{\sigma}}(t) = \Gamma\, \mathrm{Proj}(\hat{\sigma}(t), -\tilde{e}_1^{\mathrm{T}}(t) P B_m) \end{cases} \tag{4.80}$$

with associated initial conditions $\hat{\beta}(0) = \hat{\beta}_0$, $\hat{\theta}(0) = \hat{\theta}_0$, $\hat{\sigma}(0) = \hat{\sigma}_0$ as best initial guesses for the unknowns to be estimated. Furthermore, $\tilde{e}_1(t) = \hat{e}_1(t) - e_1(t)$ is the prediction error, $\Gamma > 0$ the adaptation gain and $P = P^{\mathrm{T}} > 0$ is the unique solution of Lyapunov equation

$$A_m^{\mathrm{T}} P + P A_m = -Q \tag{4.81}$$

for some $Q = Q^{\mathrm{T}} > 0$. The projection operator $\mathrm{Proj}(\cdot, \cdot)$ is to keep estimates uniformly bounded within a compact convex set, i.e.

$$\hat{\beta}(t) \in \Omega_\beta \supset \Omega_{\beta,0} \tag{4.82}$$

$$\hat{\theta}(t) \in \Omega_\theta \supset \Omega_{\theta,0} \tag{4.83}$$

$$\hat{\sigma}(t) \in \Omega_\sigma \supset \Omega_{\sigma,0} \tag{4.84}$$

for all $t \geq 0$. For the sake of clarity, note that

$$\Omega_\beta := [\beta_l, \beta_u],\ \beta_l < \beta_{l,0} < \beta_{u,0} < \beta_u \tag{4.85}$$

$$\Omega_\sigma := [-\sigma_{\max}, \sigma_{\max}],\ 0 < \sigma_{\max,0} < \sigma_{\max}. \tag{4.86}$$

Sets with subindex 0 capture a priori known bounds of the unknowns, while respective supersets denote the tolerance bound of the projection operator, see [68, 91, 111]. We have implemented the projection operator as in [68]. For the ease of exposition we use the control law

$$\dot{u}_{ad}(t) = -k\, u_{ad}(t) - k\, \hat{\chi}_u(t), \quad u_{ad}(0) = 0 \tag{4.87}$$

$$u_{ad}(s) = -C_u(s)\, \hat{\chi}_u(s) \tag{4.88}$$

where $\hat{\chi}_u(t) := \hat{\beta} u(t) + \hat{\theta}^{\mathrm{T}}(t) z(t) + \hat{\sigma}(t)$,

$$C_u(s) = \frac{k}{s+k}, \quad k > 0, \tag{4.89}$$

and $u_{ad}(s)$ denotes the Laplace transform of $u_{ad}(t)$. Please note that this notation is used throughout this text.

In a *certainty equivalence* manner it aims to compensate χ_u by means of the estimate $\hat{\chi}_u$. Thereby, compensation only occurs within a predefined bandwidth specified by the low-pass filter $C_u(s)$ and design parameter k. Of course more complex filtering structures are also possible, given that $C_u(s)$ is BIBO stable, strictly proper and satisfies $C_u(0) = 1$. The choice of parameter k will be clarified in the remainder of this section. Eventually, the proposed complete $\mathcal{L}_1$ adaptive tracking controller is given by (4.71), (4.31), (4.32), and (4.79)–(4.88).

Discussion

When comparing the proposed control law (4.88) with the one given in [18] the first impression is that both are different. In contrast to the $\mathcal{L}_1$ adaptive controller in [18] the filter of (4.88) seems to be independent of the input gain. Yet this is due to the fact that until now we have not made explicit use of $u(t)$ in (4.74), (4.79) and (4.88). As we will see, in doing so the Lyapunov-based stability proof turns out simpler and the number of adaptation laws is minimized.

For illustrating the relation to the control law in [18, 68], we compute the control structure by making explicit use of $u(t)$. Inserting (4.71) together with (4.31), (4.32) in (4.74), (4.79) and (4.87) yields the equivalent error dynamics

$$\dot{e}_1(t) = A_m e_1(t) + B_m\, (\omega\, u_{ad}(t) + \chi_{ou}(t)), \quad e_1(0) = e_1^0, \tag{4.90}$$

the equivalent state predictor model

$$\dot{\hat{e}}_1(t) = A_m \hat{e}_1(t) + B_m\, (\hat{\omega}\, u_{ad}(t) + \hat{\chi}_{ou}(t)), \quad \hat{e}_1(0) = e_1^0, \tag{4.91}$$

as well as the equivalent adaptive input

$$\dot{u}_{ad}(t) = -k\, \hat{\omega}(t)\, u_{ad}(t) - k\, \hat{\chi}_{ou}(t), \quad u_{ad}(0) = 0. \tag{4.92}$$

Within these equations, we have used the abbreviations

$$\chi_{ou}(t) := \Theta_1^{\mathrm{T}}(t)\, z(t) + \Theta_2^{\mathrm{T}}\, z^\star(t) + \beta u^\star(t) + \sigma(t) \tag{4.93}$$

$$\hat{\chi}_{ou}(t) := \hat{\Theta}_1^{\mathrm{T}}(t)\, z(t) + \hat{\Theta}_2^{\mathrm{T}}\, z^\star(t) + \hat{\beta} u^\star(t) + \hat{\sigma}(t) \tag{4.94}$$

with

$$\omega := 1 + \beta, \qquad \Theta_1^{\mathrm{T}}(t) := \theta^{\mathrm{T}}(t) - \beta K^{\mathrm{T}}, \qquad \Theta_2^{\mathrm{T}} := \beta K^{\mathrm{T}}, \tag{4.95}$$

$$\hat{\omega}(t) := 1 + \hat{\beta}(t), \quad \hat{\Theta}_1^{\mathrm{T}}(t) := \hat{\theta}^{\mathrm{T}}(t) - \hat{\beta}(t) K^{\mathrm{T}}, \quad \hat{\Theta}_2^{\mathrm{T}}(t) := \hat{\beta}(t) K^{\mathrm{T}}, \tag{4.96}$$

where

$$K^{\mathrm{T}} = \begin{pmatrix} k_1^{\mathrm{T}} & k_2^{\mathrm{T}} \end{pmatrix}, \quad k_2^{\mathrm{T}} := \check{B}_1^{\dagger} \check{A}_{12} \tag{4.97}$$

is the state feedback vector from the nominal controller. In the line of thought with [18, 68] the control law may be further generalized by rewriting (4.92) as per

$$\dot{u}_{ad}(t) = -k \left(\hat{\omega}(t)\, u_{ad}(t) + \hat{\chi}_{ou}(t) \right) = -k\, \hat{\chi}(t) \tag{4.98}$$

$$u_{ad}(s) = -\frac{k}{s}\, \hat{\chi}(s) = -k\, D(s)\, \hat{\chi}(s). \tag{4.99}$$

This reveals that the proposed $\mathcal{L}_1$ controller (4.87) implicitly leads to a similar one as given in [18]. In the simplest case, $D(s)$ is an integrator. However, generally and for the purpose of admitting more complex filtering structures, $D(s)$ may be any strictly proper transfer function such that

$$C(s) = \frac{\omega k D(s)}{1 + \omega k D(s)}, \quad \forall\, \omega \in \Omega_\omega \tag{4.100}$$

is BIBO stable, strictly proper, $C(0) = 1$ and the $\mathcal{L}_1$-norm stability condition

$$\left\| (sI - A_m)^{-1} B_m \left(1 - C(s)\right) \right\|_{\mathcal{L}_1} L < 1 \tag{4.101}$$

holds. Thereby,

$$L := \max_{\theta \in \Omega_\theta} \|\theta_\xi\|_1 + \|k_1\|_1 \max_{\beta \in \Omega_\beta} |\beta| + L_{z,1} \left(\max_{\theta \in \Omega_\theta} \|\theta_\eta\|_1 + \|k_2\|_1 \max_{\beta \in \Omega_\beta} |\beta| \right), \tag{4.102}$$

where

$$L_{z,1} := \|H_z(s)\|_{\mathcal{L}_1}, \quad H_z(s) := \left(sI - (\check{A}_{22} + \Delta A_{22}) \right)^{-1} (\check{A}_{21} + \Delta A_{21}) \tag{4.103}$$

Remark 4.2.4. From (4.90) and (4.92) it is not directly clear how the uncertainties are compensated. Deeper insight is gained when considering the steady state of (4.92), see [67], i.e.

$$u_{ad}^{ss}(t) = -\frac{1}{\hat{\omega}(t)} \hat{\chi}_{ou}(t). \tag{4.104}$$

Evidently, in steady state all uncertainties are compensated by means of their estimates.

Note that the proposed control law in steady state is equivalent to its MRAC counterpart. However, in contrast to the MRAC controller the explicit inversion of $\hat{\omega}$ in (4.92) or (4.87) is avoided. The inversion of $\hat{\omega}$ is rather accomplished dynamically, as discussed in [67].

Furthermore, consider (4.92) with a $\hat{\omega}$ that is varying slowly in time. This leads to the intuition that compensation takes place within a bandwidth $\omega_b = k\hat{\omega} > 0$, that is, dependent on the estimate $\hat{\omega}$, see [147]. Thus, adaptation may change ω_b with time, while the projection operator ensures that it changes within the following interval

$$\omega_b \in [k\,(1+\beta_l)\,, k\,(1+\beta_u)]\,. \tag{4.105}$$

Hence, the design parameter k may be seen to adjust the lower and upper filter bandwidth to the given limitations.

The remarkable feature of $\mathcal{L}_1$ adaptive controllers, to adaptively change its bandwidth, is exceptional when compared with existing adaptive control algorithms and is also the key for the robustness properties of the scheme, when subject to unmodeled dynamics (see [18, 147]).

Remark 4.2.5. Omitting the low-pass filter in (4.87) leads to the well-known predictor-based MRAC controller, where the inversion of $\hat{\omega}$ happens to appear explicitly. Hence, projection-based adaptation laws or similar methods must be used to ensure that $\hat{\omega} > 0$, $\forall\, t \geq 0$. Note, however, that the same applies for the $\mathcal{L}_1$ controller, since also in steady state singularities must be prohibited.

Ideal Closed Loop System

Due to the insertion of the low-pass filter $C(s)$ (or equivalently $C_u(s)$) in the $\mathcal{L}_1$ scheme, the controller will not be able to track the standard reference model known from MRAC, because this assumes infinite bandwidth of the control channel and therefore does not include any filtering structures. Instead, it is clear that the model tracking performance and thus the disturbance rejection properties of the $\mathcal{L}_1$ controller will heavily depend upon the choice of the bandwidth of the low-pass filter. A feasible reference model for $\mathcal{L}_1$ adaptive control, for predicting the best possible performance that could be achieved under ideal conditions, must therefore directly incorporate the filtering structure $C(s)$. For computing a model for this ideal case, in accordance with [68], it is simply assumed that all unknowns are perfectly known and compensated within the bandwidth of $C(s)$. Hence, the ideal control system is given by the set of the following equations

$$\Sigma_{\mathcal{L}_1}^{id}\,:\begin{cases}\dot{e}_{1,id}(t) = A_m e_{1,id}(t) + B_m\left(\omega\, u_{id}(t) + \chi_{ou,id}(t)\right)\\ \dot{e}_{2,id}(t) = \check{A}_{21}\, e_{1,id}(t) + \check{A}_{22}\, e_{2,id}(t) + d_{\eta,id}(t), \quad e_{2,id}(0) = e_2^0\\ y_{e,id}(t) = C_m e_{1,id}(t), \quad e_{1,id}(0) = e_1^0\\ u_{id}(t) = -\frac{1}{\omega}C(s)\chi_{ou,id}(t)\end{cases} \tag{4.106}$$

The first equation of $\Sigma_{\mathcal{L}_1}^{id}$ may equivalently be expressed in the frequency domain as

$$e_{1,id}(s) = H(s)\,(1 - C(s))\,\chi_{ou,id}(s) + e_{in}(s), \tag{4.107}$$

where

$$H(s) := (sI - A_m)^{-1} B_m, \quad e_{in}(s) := (sI - A_m)^{-1} B_m \, e_1^0 \tag{4.108}$$

and $\chi_{ou,id}(s)$ denotes the Laplace transform of $\chi_{ou,id}(t)$. Please notice that the control objective is to bring $e_{1,id}$ to zero. As apparent from equation (4.107) perfect cancellation of $\chi_{ou,id}(s)$ can only be achieved with $C(s) = 1$. This of course corresponds to an infinite bandwidth of the control channel and is not feasible in practice. Note that for $C(s) = 1$, (4.106) resembles the reference system in MRAC. Instead, (4.107) and the fact that $C(s)$ is a low-pass filter with $C(0) = 1$ imply that for frequencies below the bandwidth ω_b of $C(s)$, $C(s) \approx 1$ such that perfect cancellation is achieved in that frequency range. However, for frequencies above ω_b, $C(s) \approx 0$ such that there is no contribution of the $\mathcal{L}_1$ controller in that frequency band such that high frequency oscillations from the adaptation law are shielded from the plant input. Instead, in that range the disturbances are rejected by the capabilities of the nominal controller.

Applying the final value theorem of the Laplace transform to (4.107) and recalling that $C(0) = 1$, reveals that even in the case of constant unknowns these will only be canceled in steady state and not during the transient phase. In view of the aspired tracking control objective, at first glance, this fact may be seen as a drawback of the scheme. However, if the controlled plant exhibits actuator dynamics as in our case and $C(s)$ is designed accordingly, one cannot get any better with or without the filter due to the actuator dynamics. Thus, the $\mathcal{L}_1$ controller achieves the best possible result in this situation. Obviously, increasing the bandwidth of $C(s)$ leads to better performance but lower robustness and vice versa.

In the spirit of [68] we will also exploit the ideal system description $\Sigma_{\mathcal{L}_1}^{id}$ for deriving transient and steady state performance bounds of the proposed controller. To this end, we next provide a stability analysis of the proposed $\mathcal{L}_1$ controller.

Stability Analysis

According to the literature on $\mathcal{L}_1$ adaptive control [68] the procedure for proving the stability of a closed loop system with any $\mathcal{L}_1$ controller can basically be described as a three step procedure.

In the first step, the stability of the ideal (non-adaptive) closed loop system is considered which in fact provides $\mathcal{L}$–stability conditions for the choice of $C(s)$ under which the system is stable with respect to ideal conditions, i.e. when all uncertainties are perfectly known.

In the second step, the stability of the closed loop adaptive system is considered. This is typically done in terms of a Lyapunov proof of the predictor error dynamics. In fact this is equivalent to the reference model error dynamics in terms of MRAC. The result of this analysis provides upper bounds for the prediction error state and/or output.

Due to the insertion of the low-pass filter in $\mathcal{L}_1$ adaptive control and the fact that the stability of the predictor error dynamics is independent of the choice of adaptive control input, the stability/boundedness of this error alone does not imply stability of the closed loop system and boundedness of control inputs. Thus, in the final step the results of step one and two are combined.

At this stage it is shown that the error between the actual state (control input) and the ideal state (control input) is bounded. From that, stability of the overall closed loop system and boundedness of control inputs can be concluded, completing the proof.

The last step additionally provides transient and steady state performance bounds. These bounds show that the performance of the closed loop adaptive system can come arbitrarily close to that of the ideal system, if the adaptation gain Γ for gradient-based adaptation laws, or the sampling time T_s in the case of piecewise constant adaptive laws are chosen arbitrarily large, or arbitrarily small, respectively.

Following this three step procedure and the lines of thought of [68], we next provide a proof for the stability of the ideal closed loop system.

Proof. Take (4.107) and let $G(s) := H(s)(1 - C(s))$. Then

$$e_{1,id}(s) = G(s)\chi_{ou,id}(s) + e_{in}(s). \tag{4.109}$$

Since A_m is Hurwitz, it follows that $e_{in}(t)$ is uniformly bounded. Next, a bound on $e_{1,id}(t)$ is obtained by taking the truncated $\mathcal{L}_\infty$ norm, i.e. $\|(\cdot)_\tau\|_{\mathcal{L}_\infty}$, on both sides of the last expression, i.e.

$$\|(e_{1,id})_\tau\|_{\mathcal{L}_\infty} \leq \|G(s)\|_{\mathcal{L}_1} \|(\chi_{ou,id})_\tau\|_{\mathcal{L}_\infty} + \|e_{in}\|_{\mathcal{L}_\infty}. \tag{4.110}$$

Next, note that $\chi_{ou}(t)$ from (4.93) can be rewritten in terms of $e_1(t)$. Replacing $e_1(t)$ by $e_{1,id}(t)$ yields

$$\chi_{ou,id}(t) = \bar{\theta}_1^{\mathrm{T}}(t)e_{1,id}(t) + \bar{\theta}_2^{\mathrm{T}}e_{2,id}(t) + \theta^{\mathrm{T}}(t)z^\star(t) + \beta u^\star(t) + \sigma(t) \tag{4.111}$$

where

$$\bar{\theta}_1^{\mathrm{T}}(t) := \theta_\xi^{\mathrm{T}}(t) - \beta k_1^{\mathrm{T}}, \quad \bar{\theta}_2^{\mathrm{T}} := \theta_\eta^{\mathrm{T}} - \beta k_2^{\mathrm{T}}. \tag{4.112}$$

Taking the truncated $\mathcal{L}_\infty$ norm of $\chi_{ou,id}$ yields

$$\begin{aligned}\|(\chi_{ou,id})_\tau\|_{\mathcal{L}_\infty} \leq& \left\|(\bar{\theta}_1^{\mathrm{T}}e_{1,id})_\tau\right\|_{\mathcal{L}_\infty} + \left\|(\bar{\theta}_2^{\mathrm{T}}e_{2,id})_\tau\right\|_{\mathcal{L}_\infty} \\ &+ \left\|(\theta^{\mathrm{T}}z^\star)_\tau\right\|_{\mathcal{L}_\infty} + \|(\beta u^\star)_\tau\|_{\mathcal{L}_\infty} + \|\sigma_\tau\|_{\mathcal{L}_\infty} \\ \leq& L_1 \|(e_{1,id})_\tau\|_{\mathcal{L}_\infty} + L_2 \|(e_{2,id})_\tau\|_{\mathcal{L}_\infty} \\ &+ L_3 \|z_\tau^\star\|_{\mathcal{L}_\infty} + L_4 \|u_\tau^\star\|_{\mathcal{L}_\infty} + \sigma_{\max}\end{aligned} \tag{4.113}$$

where

$$L_1 := \max_{\theta\in\Omega_\theta,\beta\in\Omega_\beta} \left\|\bar{\theta}_1\right\|_1, \; L_2 := \max_{\theta\in\Omega_\theta,\beta\in\Omega_\beta} \left\|\bar{\theta}_2\right\|_1, \; L_3 := \max_{\theta\in\Omega_\theta} \|\theta\|_1, \; L_4 := \max_{\beta\in\Omega_\beta} |\beta| \tag{4.114}$$

For deriving a bound on the tracking error $e_{2,id}(t)$ of the internal dynamics, we note that from the second equation of (4.106) and the definition of d_η as in (3.140) it follows that

$$e_{2,id}(s) = H_z(s)\, e_{1,id}(s) + H_{\Delta_1}(s)\, \xi^\star(s) + H_{\Delta_2}(s)\, \eta^\star(s) + e_{2,in}(s), \tag{4.115}$$

where we used the following definitions for the respective transfer functions and signals

$$H_z(s) := \left(sI - (\check{A}_{22} + \Delta A_{22})\right)^{-1} (\check{A}_{21} + \Delta A_{21}) \tag{4.116}$$

$$H_{\Delta_1}(s) := \left(sI - (\check{A}_{22} + \Delta A_{22})\right)^{-1} \Delta A_{21} \tag{4.117}$$

$$H_{\Delta_2}(s) := \left(sI - (\check{A}_{22} + \Delta A_{22})\right)^{-1} \Delta A_{22} \tag{4.118}$$

$$e_{2,in}(s) := \left(sI - (\check{A}_{22} + \Delta A_{22})\right)^{-1} e_2^0. \tag{4.119}$$

Assumption 3.2.3 implies that matrix $\check{A}_{22} + \Delta A_{22}$ is Hurwitz such that the transfer functions $H_z(s), H_{\Delta_1}(s), H_{\Delta_2}(s)$ are BIBO stable and the signal $e_{2,in}(t)$ is uniformly bounded. Moreover, we note that the reference signals $\xi^\star(t)$ and $\eta^\star(t)$ are of course uniformly bounded also. Hence, the following upper bound

$$\left\|(e_{2,id})_\tau\right\|_{\mathcal{L}_\infty} \leq L_{z,1} \left\|(e_{1,id})_\tau\right\|_{\mathcal{L}_\infty} + L_{z,2} \tag{4.120}$$

holds uniformly for all $\tau \geq 0$ and there exist constants $L_{z,1}, L_{z,2} > 0$ given by

$$L_{z,1} := \left\|H_z(s)\right\|_{\mathcal{L}_1} \tag{4.121}$$

$$L_{z,2} := \left\|H_{\Delta_1}(s)\right\|_{\mathcal{L}_1} \left\|\xi_\tau^\star\right\|_{\mathcal{L}_\infty} + \left\|H_{\Delta_2}(s)\right\|_{\mathcal{L}_1} \left\|\eta_\tau^\star\right\|_{\mathcal{L}_\infty} + \left\|(e_{2,in})_\tau\right\|_{\mathcal{L}_\infty}. \tag{4.122}$$

Note that this bound is also in accordance with [68] and the norm bounds imposed on unknown internal dynamics. Substituting this bound back into (4.113) yields

$$\left\|(\chi_{ou,id})_\tau\right\|_{\mathcal{L}_\infty} \leq (L_1 + L_2 L_{z,1}) \left\|(e_{1,id})_\tau\right\|_{\mathcal{L}_\infty} + \rho_\chi \tag{4.123}$$

with uniformly bounded $\rho_\chi := L_2 L_{z,2} + L_3 \left\|z_\tau^\star\right\|_{\mathcal{L}_\infty} + L_4 \left\|u_\tau^\star\right\|_{\mathcal{L}_\infty} + \sigma_{\max}$. Further, notice that

$$L_1 = \max_{\theta\in\Omega_\theta, \beta\in\Omega_\beta} \left\|\theta_\xi - \beta k_1\right\|_1 \tag{4.124}$$

$$\leq \max_{\theta\in\Omega_\theta} \left\|\theta_\xi\right\|_1 + \max_{\beta\in\Omega_\beta} \left\|\beta k_1\right\|_1 \tag{4.125}$$

$$= \max_{\theta\in\Omega_\theta} \left\|\theta_\xi\right\|_1 + \left\|k_1\right\|_1 \max_{\beta\in\Omega_\beta} |\beta| \tag{4.126}$$

and similarly

$$L_2 = \max_{\theta\in\Omega_\theta, \beta\in\Omega_\beta} \left\|\theta_\eta - \beta k_2\right\|_1 \leq \max_{\theta\in\Omega_\theta} \left\|\theta_\eta\right\|_1 + \left\|k_2\right\|_1 \max_{\beta\in\Omega_\beta} |\beta|. \tag{4.127}$$

Then

$$L_1 + L_2 L_{z,1} \leq \max_{\theta\in\Omega_\theta} \left\|\theta_\xi\right\|_1 + \left\|k_1\right\|_1 \max_{\beta\in\Omega_\beta} |\beta| + L_{z,1} \left(\max_{\theta\in\Omega_\theta} \left\|\theta_\eta\right\|_1 + \left\|k_2\right\|_1 \max_{\beta\in\Omega_\beta} |\beta| \right).$$

Defining the last inequality as

$$L := \max_{\theta\in\Omega_\theta} \left\|\theta_\xi\right\|_1 + \left\|k_1\right\|_1 \max_{\beta\in\Omega_\beta} |\beta| + L_{z,1} \left(\max_{\theta\in\Omega_\theta} \left\|\theta_\eta\right\|_1 + \left\|k_2\right\|_1 \max_{\beta\in\Omega_\beta} |\beta| \right) \tag{4.128}$$

and substitution of L and (4.123) into (4.110) yields

$$\|(e_{1,id})_\tau\|_{\mathcal{L}_\infty} \leq \frac{\|G(s)\|_{\mathcal{L}_1}\,\rho_\chi + \|e_{in}\|_{\mathcal{L}_\infty}}{1 - \|G(s)\|_{\mathcal{L}_1}\,L}. \tag{4.129}$$

Then $e_{1,id}(t)$ is uniformly bounded on $t \in [0, \tau]$ for all $\tau \geq 0$ if the filter parameters k and $D(s)$ verify the $\mathcal{L}_1$-norm stability condition in (4.101). Then also the ideal closed loop system given in (4.106) is BIBS stable. □

Now that we know that under ideal conditions the closed loop system is stable, in the following, we adhere to the lines of proof in [68] to show stability of the closed loop adaptive system with the proposed tracking controller. This constitutes the second step of the three step procedure.

Proof. Subtracting (4.74) from (4.79) yields the prediction error dynamics

$$\dot{\tilde{e}}_1(t) = A_m\tilde{e}_1(t) + B_m(\tilde{\beta}\,u(t) + \tilde{\theta}^{\mathrm{T}}(t)\,z(t) + \tilde{\sigma}(t)), \tag{4.130}$$

where we have used the denotation $\tilde{e}_1 = \hat{e}_1 - e_1$, $\tilde{\theta} = \hat{\theta} - \theta$, $\tilde{\beta} = \hat{\beta} - \beta$ and $\tilde{\sigma} = \hat{\sigma} - \sigma$ for the respective estimation error variables. Now, take the Lyapunov function candidate

$$V(\tilde{e}_1, \tilde{\beta}, \tilde{\theta}, \tilde{\sigma}) = \tilde{e}_1^{\mathrm{T}} P \tilde{e}_1 + \frac{1}{\Gamma}\left(\tilde{\beta}^2 + \tilde{\theta}^{\mathrm{T}}\tilde{\theta} + \tilde{\sigma}^2\right), \tag{4.131}$$

where time dependencies are dropped, for brevity. Recall that $\Gamma > 0$ and P is the unique positive definite solution of Lyapunov equation $A_m^{\mathrm{T}}P + PA_m = -Q$ for some $Q = Q^{\mathrm{T}} > 0$. Using the adaptation law in (4.80) we obtain

$$\begin{aligned}
\dot{V} =& -\tilde{e}_1^{\mathrm{T}}Q\tilde{e}_1 + 2\tilde{\beta}\left(\frac{1}{\Gamma}\dot{\hat{\beta}} + \tilde{e}_1^{\mathrm{T}}PB_m u\right) + 2\tilde{\theta}^{\mathrm{T}}\left(\frac{1}{\Gamma}\dot{\hat{\theta}} + z\,\tilde{e}_1^{\mathrm{T}}PB_m\right) \\
&+ 2\tilde{\sigma}\left(\frac{1}{\Gamma}\dot{\hat{\sigma}} + \tilde{e}_1^{\mathrm{T}}PB_m\right) - \frac{2}{\Gamma}\left(\tilde{\theta}^{\mathrm{T}}\dot{\theta} + \tilde{\sigma}\dot{\sigma}\right) \\
=& -\tilde{e}_1^{\mathrm{T}}Q\tilde{e}_1 + \underbrace{2\tilde{\beta}\big(\mathrm{Proj}(\hat{\beta}, -\tilde{e}_1^{\mathrm{T}}PB_m u) + \tilde{e}_1^{\mathrm{T}}PB_m u\big)}_{\leq 0} \\
&+ \underbrace{2\tilde{\theta}^{\mathrm{T}}\big(\mathrm{Proj}(\hat{\theta}, -z\,\tilde{e}_1^{\mathrm{T}}PB_m) + z\,\tilde{e}_1^{\mathrm{T}}PB_m\big)}_{\leq 0} \\
&+ \underbrace{2\tilde{\sigma}\big(\mathrm{Proj}(\hat{\sigma}, -\tilde{e}_1^{\mathrm{T}}PB_m) + \tilde{e}_1^{\mathrm{T}}PB_m\big)}_{\leq 0} - \frac{2}{\Gamma}\big(\tilde{\theta}^{\mathrm{T}}\dot{\theta} + \tilde{\sigma}\dot{\sigma}\big) \\
\leq& -\tilde{e}_1^{\mathrm{T}}Q\tilde{e}_1 - \frac{2}{\Gamma}\big(\tilde{\theta}^{\mathrm{T}}\dot{\theta} + \tilde{\sigma}\dot{\sigma}\big).
\end{aligned} \tag{4.132}$$

The projection operator keeps the estimates of the unknowns within compact convex sets for all time, i.e.

$$\hat{\theta}(t) \in \Omega_\theta,\;\; \hat{\beta}(t) \in \Omega_\beta,\;\; \hat{\sigma}(t) \in \Omega_\sigma,\;\; \forall\, t \geq 0. \tag{4.133}$$

This helps derive a bound for the second term in (4.132), i.e.

$$\tilde{\theta}^{\mathrm{T}}\dot{\theta} + \tilde{\sigma}\dot{\sigma} \leq 2\Big(\max_{\theta\in\Omega_\theta}\|\theta\|_2\,\delta_\theta + \sigma_{\max}\,\delta_\sigma\Big), \tag{4.134}$$

which yields

$$\dot{V} \leq -\tilde{e}_1^{\mathrm{T}} Q \tilde{e}_1 + \frac{4}{\Gamma} \left(\theta_{\max} \delta_\theta + \sigma_{\max} \delta_\sigma \right). \tag{4.135}$$

Consequently $\dot{V} \leq 0$, whenever

$$\tilde{e}_1^{\mathrm{T}} Q \tilde{e}_1 \geq \frac{4}{\Gamma} \left(\theta_{\max} \delta_\theta + \sigma_{\max} \delta_\sigma \right) \tag{4.136}$$

and hence we have the bound

$$\|\tilde{e}_1\|_2^2 \geq \frac{4 \left(\theta_{\max} \delta_\theta + \sigma_{\max} \delta_\sigma \right)}{\Gamma \lambda_{\min}(Q)} =: \tilde{e}_{1,\max}^2 \tag{4.137}$$

on the radius of a ball out of which $\dot{V} \leq 0$. All trajectories that start outside the sphere will eventually converge to its interior or its surface and stay there for all time. The prediction-error $\tilde{e}_1$ is thus uniformly bounded, staying in a vicinity of the origin of the state space. Increasing the gain Γ will decrease the norm of $\tilde{e}_1$.

An upper bound on the prediction error $\|\tilde{e}_1\|_2$ may be obtained by computing an upper bound $V_{\max}$ on V via (4.137). Hence,

$$\begin{aligned} V &= \tilde{e}_1^{\mathrm{T}} P \tilde{e}_1 + \frac{1}{\Gamma} \left(\tilde{\beta}^2 + \tilde{\theta}^{\mathrm{T}} \tilde{\theta} + \tilde{\sigma}^2 \right) \\ &\leq \lambda_{\max}(P) \|\tilde{e}_1\|_2^2 + \frac{1}{\Gamma} \left(4 \theta_{\max}^2 + (\beta_u - \beta_l)^2 + 4 \sigma_{\max}^2 \right). \end{aligned} \tag{4.138}$$

The second summand follows from the parameter projection since the projection operator ensures that for all time

$$\tilde{\beta}^2 + \tilde{\theta}^{\mathrm{T}} \tilde{\theta} + \tilde{\sigma}^2 \leq 4 \theta_{\max}^2 + (\beta_u - \beta_l)^2 + 4 \sigma_{\max}^2. \tag{4.139}$$

Inserting (4.137) into inequality (4.138) yields

$$V_{\max} = \frac{\theta_m}{\Gamma} \tag{4.140}$$

with

$$\theta_m = \frac{4 \lambda_{\max}(P)}{\lambda_{\min}(Q)} \left(\theta_{\max} \delta_\theta + \sigma_{\max} \delta_\sigma \right) + 4 \theta_{\max}^2 + (\beta_u - \beta_l)^2 + 4 \sigma_{\max}^2. \tag{4.141}$$

The former assumption $\hat{e}_1(0) = e_1^0$ implies

$$\begin{aligned} V(0) &= \frac{1}{\Gamma} \left(\tilde{\beta}^2(0) + \tilde{\theta}^{\mathrm{T}}(0) \, \tilde{\theta}(0) + \tilde{\sigma}^2(0) \right) \\ &\leq \frac{1}{\Gamma} \left(4 \theta_{\max}^2 + (\beta_u - \beta_l)^2 + 4 \sigma_{\max}^2 \right) < V_{\max}. \end{aligned} \tag{4.142}$$

Therefore, V initially starts within the $V_{\max}$ region. Function V may increase exceeding $V(0)$, however, it cannot exceed $V_{\max}$ since outside the ball $\dot{V} < 0$. Hence, using (4.138) and (4.140) we conclude that for all $t \geq 0$

$$\lambda_{\min}(P) \|\tilde{e}_1\|_2^2 \leq V(t) \leq \frac{\theta_m}{\Gamma} \tag{4.143}$$

implying that the prediction error obeys

$$\|\tilde{e}_1\|_2 \leq \sqrt{\frac{\theta_m}{\Gamma \lambda_{\min}(P)}}. \tag{4.144}$$

Now as we have shown that $\tilde{e}_1(t)$ is uniformly ultimately bounded, it remains to show that one of the variables, either $\hat{e}_1(t)$ or $e_1(t)$ is bounded, avoiding that they diverge at the same rate. To this end, we rewrite the adaptive control signal (4.99) as

$$u_{ad}(s) = -k\, D(s)\, (\omega\, u_{ad}(s) + \chi_{ou}(s) + \tilde{\chi}(s))\,, \tag{4.145}$$

where $\tilde{\chi}(t) = \hat{\chi}(t) - \chi(t)$ and $\chi(t) = \omega\, u_{ad}(s) + \chi_{ou}(s)$. Solving for $u_{ad}(s)$ leads to

$$u_{ad}(s) = -\frac{C(s)}{\omega}\, (\chi_{ou}(s) + \tilde{\chi}(s)) \tag{4.146}$$

with $C(s)$ as defined in (4.100). Next, consider the Laplace transform of (4.90) given by

$$e_1(s) = G(s)\, \chi_{ou}(s) - H(s)\, C(s)\, \tilde{\chi}(s) + e_{in}(s) \tag{4.147}$$

where $e_{in}(s) = (sI - A_m)^{-1}\, e_1^0$, $H(s) = (sI - A_m)^{-1}\, B_m$ and $G(s) = H(s)\,(1 - C(s))$. Assuming $\hat{e}_1^0 = e_1^0$, the prediction error dynamics such as its Laplace transform read

$$\dot{\tilde{e}}_1(t) = A_m \tilde{e}_1(t) + B_m\, \tilde{\chi}(t) \tag{4.148}$$

$$\tilde{e}_1(s) = H(s)\, \tilde{\chi}(s). \tag{4.149}$$

Using (4.149) in (4.147) and by virtue of the fact that $C(s)$ is scalar valued we obtain

$$e_1(s) = G(s)\, \chi_{ou}(s) - C(s)\, \tilde{e}_1(s) + e_{in}(s). \tag{4.150}$$

Now, as we know that the ideal closed loop system is stable with $e_{1,id}(\cdot) \in \mathcal{L}_{\infty e}$ we can conclude the boundedness of $e_1(t)$, if the norm $\|(e_{1,id} - e_1)_\tau\|_{\mathcal{L}_\infty}$ exists. Additionally to this information, we obtain a bound for the transient performance.

From (4.150), (4.109) and (4.111) it follows that

$$e_{1,id}(s) - e_1(s) = G(s)\chi_e(s) + C(s)\tilde{e}_1, \tag{4.151}$$

with

$$\chi_e = \bar{\theta}_1^{\mathrm{T}}(e_{1,id}(t) - e_1(t)) + \bar{\theta}_2^{\mathrm{T}}(e_{2,id}(t) - e_2(t)). \tag{4.152}$$

Taking the truncated $\mathcal{L}_\infty$-norm, yields

$$\|(e_{1,id} - e_1)_\tau\|_{\mathcal{L}_\infty} \leq \|G(s)\|_{\mathcal{L}_1}\, \|\chi_{e\tau}\|_{\mathcal{L}_\infty} + \|C(s)\|_{\mathcal{L}_1}\, \|\tilde{e}_{1\tau}\|_{\mathcal{L}_\infty}\,. \tag{4.153}$$

Note that the term χ_e can be likewise bounded as (4.123) with L as defined in (4.102). Then $\|\chi_{e\tau}\|_{\mathcal{L}_\infty} \leq L\, \|(e_{1,id} - e_1)_\tau\|_{\mathcal{L}_\infty}$ such that (4.153) turns to

$$\|(e_{1,id} - e_1)_\tau\|_{\mathcal{L}_\infty} \leq \frac{\|C(s)\|_{\mathcal{L}_1}}{1 - \|G(s)\|_{\mathcal{L}_1}\, L} \sqrt{\frac{\theta_m}{\Gamma \lambda_{\min}(P)}}, \tag{4.154}$$

where we also used the bound on $\tilde{e}_1$ from (4.144). Consequently, e_1 is uniformly bounded for all $\tau \geq 0$ if k and $D(s)$ are designed such that $C(s)$, as defined in (4.100), is

a BIBO stable strictly proper transfer function with DC-gain $C(0) = 1$ and the $\mathcal{L}_1$ norm condition

$$\|G(s)\|_{\mathcal{L}_1} \; L < 1 \tag{4.155}$$

is satisfied. To proof the boundedness of the adaptive control signal u_{ad}, we subtract (4.146) from u_{id} as given in (4.106) giving

$$u_{id}(s) - u_{ad}(s) = -\frac{C(s)}{\omega}\chi_e + \frac{C(s)}{\omega}\tilde{\chi} \tag{4.156}$$

Along with [68] we make use of Lemma A.12.1 from [68] that implies that there exists a vector $c_0 \in \mathbb{R}^r$ such that $c_0^{\mathrm{T}} H(s)$ has relative degree one and is minimum phase, i.e. transfer function

$$H_1(s) := \frac{C(s)}{c_0^{\mathrm{T}} H(s)} c_0^{\mathrm{T}}, \tag{4.157}$$

is proper and BIBO stable. Then using the definition of $H_1(s)$ and (4.149) we rewrite

$$\frac{C(s)}{\omega}\tilde{\chi} = \frac{1}{\omega}\frac{C(s)}{c_0^{\mathrm{T}} H(s)} c_0^{\mathrm{T}} H(s)\tilde{\chi}(s) = \frac{H_1(s)}{\omega} H(s)\tilde{\chi}(s) = \frac{H_1(s)}{\omega}\tilde{e}_1(s). \tag{4.158}$$

Thus it follows that

$$\|(u_{id} - u_{ad})_\tau\|_{\mathcal{L}_\infty} \leq \left\|\frac{C(s)}{\omega}\right\|_{\mathcal{L}_1} L \, \|(e_{1,id} - e_1)_\tau\|_{\mathcal{L}_\infty} + \left\|\frac{H_1(s)}{\omega}\right\|_{\mathcal{L}_1} \|\tilde{e}_{1\tau}\|_{\mathcal{L}_\infty} \tag{4.159}$$

which is uniformly bounded for all $\tau \geq 0$ due to strictly proper and BIBO stable $C(s)$, proper and BIBO stable $H_1(s)$ and the uniform boundedness of (4.154) and (4.144). □

Due to the fact that we assumed the availability of the complete state z for adaptive state feedback control, this controller is not implementable on the PPS1405 platform, because only the output y is measurable. Note, however, that this assumption is not unrealistic, in [136] and references therein the use of accelerometers for similar motion control applications is reported. These could be attached to mover and stator such that full state information might be recalculated.

However, in order to illustrate the performance that could be achieved by this controller, we next give a small simulation example.

Example 4.2.1 (Simulation of proposed $\mathcal{L}_1$ augmentation with full state feedback)**.** *For demonstrating the tracking performance of the proposed scheme, we again adopt a point-to-point tracking control problem along the q_x-axis. This time, a degree five polynomial is used as reference trajectory, illustrated in Figure 4.8. During this task, the mover is first transitioned from $-10\,\mathrm{mm}$ to $10\,\mathrm{mm}$ in $2\,\mathrm{s}$. After an idle time of a further $2\,\mathrm{s}$, where the mover is at rest, the same transition is reversed.*

The motion stage is simulated according to the generic axis model in the original coordinates as given in Definition 3.1.1. Additionally, to each individual physical parameter, i.e. a_i, b_j, in A and B (see Table C.4) a parametric uncertainty of $+50\,\%$ is added.

For specifying the reference dynamics, A_m and B_m are chosen as

$$A_m = \begin{pmatrix} 0 & 1 \\ -735.9 & -38.4 \end{pmatrix}, \quad B_m = \begin{pmatrix} 0 \\ 232.6975 \end{pmatrix}. \tag{4.160}$$

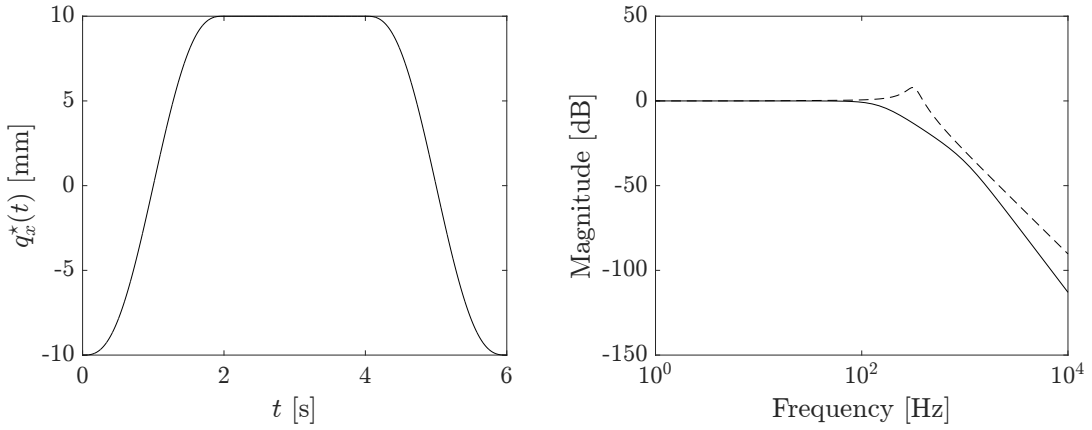

FIGURE 4.8: Point-to-point reference trajectory (left) and magnitude bodeplot (right) of $C_u(s)$ (solid) and $\Sigma_2(s)$ (dashed).

Note, that this corresponds to the same controller gain k_1 as in Example 4.1.3 and consequently leads to the same closed loop eigenvalues given by

$$\lambda(A_m) = -19.18 \pm j19.18.$$

For the ease of filter design we use the form of the control law as given in (4.88)*. The filter $C_u(s)$ is designed such that it respects the input dynamics $\Sigma_2(s)$. This is illustrated in the magnitude plot on the right of Figure 4.8. The transfer function of the filter is given by*

$$C_u(s) = \frac{3.507\text{e}13}{s^4 + 1.022\text{e}04s^3 + 5.221\text{e}07s^2 + 6.05\text{e}10s + 3.507\text{e}13} \tag{4.161}$$

constituting a series connection of two second order filters with each having a damping ratio of $\zeta_f = 0.707$ and natural frequencies of $\omega_{f,1} = 2\pi 150$ rad/s and $\omega_{f,2} = 2\pi 1000$ rad/s. Following the design approach presented above, this filter may also be cast into the equivalent form as in (4.99) *with $D(s)$ as per*

$$D(s) = \frac{1}{s^4 + 1.022\text{e}04s^3 + 5.221\text{e}07s^2 + 6.05\text{e}10s} \tag{4.162}$$

and $k = 3.507\text{e}13$.

In view of the perturbations, the convex compact sets for the projection bounds are set to

$$\Omega_\beta = [-0.6, 0.6], \quad \Omega_\sigma = [-1, 1], \quad \Omega_\theta = \{\theta \in \mathbb{R}^4 : \theta_i \in [-21, 21]\}. \tag{4.163}$$

Finally, the adaptation gain $\Gamma = 10000$ and the Luenberger modification term is set to $L_m = diag(1\text{e}3, 1\text{e}3)$.

Figure 4.9 illustrates the tracking errors (top) and control efforts (bottom) for the nominal state feedback controller (left) and for the $\mathcal{L}_1$ augmentation (right). Obviously, in the face of uncertainties, the nominal controller has difficulties in keeping the tracking error below $1\,\mu$m. However, the $\mathcal{L}_1$ augmentation suppresses these uncertainties remarkably well and keeps the tracking error below $1\,\mu$m, as desired. ▲

Remark 4.2.6. Filter design in $\mathcal{L}_1$ adaptive control is not a trivial task. Indeed, in the course of filter design it has been observed that the $\mathcal{L}_1$ norm sufficient condition for stability is quite restrictive. In fact, in the case of Example 4.2.1 it was not possible

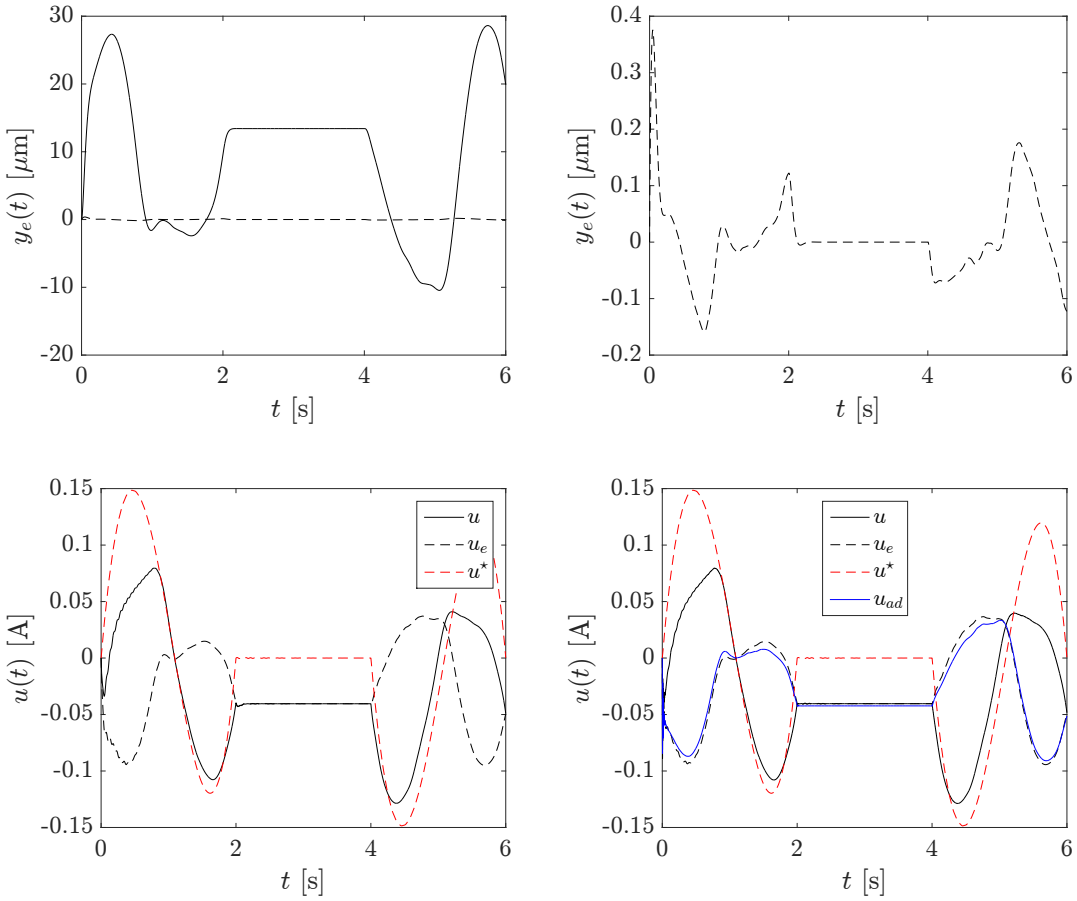

FIGURE 4.9: Tracking of a polynomial point-to-point trajectory: tracking errors (top) for nominal state feedback controller (solid, left) and proposed $\mathcal{L}_1$ augmentation (dashed). Control portions (bottom) for nominal controller (left) and adaptive controller (right).

to design a filter that first, verified the $\mathcal{L}_1$ norm condition and second, respected the virtual actuator dynamics $\Sigma_2(s)$.

Of course, in the case of no input dynamics, it is always possible to verify the $\mathcal{L}_1$ norm condition by choosing the bandwidth of the filter sufficiently large. But, in our case it is clear that this may violate the bandwidth limitations imposed by the unmodeled input dynamics and thus the robustness/stability of the closed loop system. Note that also for systems with unknown input dynamics, sufficient conditions for stability are presented in [68]. Adapting these conditions to our problem did not solve it either.

Note further that this issue seems to be a common problem and has also been reported in the work of [64]. In view of the theoretical overhead this is an unsatisfactory result.

However, since the $\mathcal{L}_1$ norm condition is only sufficient and not necessary for stability, still filters may be designed for obtaining a stable closed loop system. Aided by a few simulations the result presented above was obtained, showing satisfactory results.

Although Example 4.2.1 already shows quite good results, even better tracking performance is possible. In fact, this may be accomplished by augmenting a nominal controller with integral action. This will be investigated next.

4.2.2 $\mathcal{L}_1$ Adaptive Augmentation with Output Feedback

The derivation of adaptive output feedback schemes usually involves strictly positive real (SPR) conditions (see e.g. [71]) on the model tracking error dynamics or at least the addition of auxiliary filtering structures to render it SPR (see e.g. [148] and references therein). In fact, the SPR condition allows to invoke the celebrated Kalman-Yakubovich-Popov (KYP) Lemma (see e.g. [71]) at the stage of Lyapunov proof/design which enables the derivation of adaptation laws that solely require the knowledge of the measured output y, instead of the full state. Recent results on adaptive output feedback schemes are e.g. presented in [48, 83, 90] among others.

In the theory of $\mathcal{L}_1$ adaptive control, output feedback architectures for both, SPR [68] and non-SPR (see e.g. [19–21, 83, 94]) systems are addressed, where the latter is possible due to a piecewise constant adaptation law.

By virtue of the fact that the considered motion stage system naturally appears as a non-SPR system, and for the sake of keeping the design freedom with respect to the nominal controller, we adopt the non-SPR methodology for the derivation of an appropriate output feedback controller.

The design of these controllers may basically be distinguished by two design methodologies. That is first, a standalone design and second, an augmentation based design approach. Mostly, in the literature on $\mathcal{L}_1$ adaptive output feedback, the standalone approach is pursued, where the $\mathcal{L}_1$ controller alone controls the plant—as the name implies. A thorough guideline for the design of these controllers, based on pole placement ideas, is presented in [145]. There, roughly speaking, the design of low-pass filter and reference model, for meeting the $\mathcal{L}_1$ norm stability condition, is reformulated into an equivalent feedback stabilization problem. Thereby, the latter may be addressed by any standard LTI method, e.g. pole placement.

However, we experienced that the standalone controllers exhibit small steady state errors which is undesirable, especially in the context of our application. The reason for this will become clear in the further course of this section. Our solution to this problem is to exploit an augmentation approach. Indeed, when augmenting a nominal controller with integral action, no problems with steady state errors will occur and the performance and disturbance rejection capabilities of the nominal controller are added to those of the $\mathcal{L}_1$ controller. This is also consistent with our idea to exploit nominal controllers for the incorporation of plant knowledge. Therefore, we prefer the $\mathcal{L}_1$ augmentation approach.

For the baseline controller design in Section 4.1.4 we subdivided the control input u_e into three portions, where each portion had its individual task. Now, similar to the design in Section 4.2.1, we add a fourth input, namely u_{ad}, for the adaptive controller in order to compensate for the residuum perturbations d_r. In this residuum term especially parameter uncertainties with respect to the input gain are expected. These particular uncertainties are quite difficult to handle in the baseline design. Hence, the new control input is given by

$$u_e(t) = u_s(t) + u_c(t) + u_d(t) + u_{ad}(t) \tag{4.164}$$

making use of the observer-based baseline controller from Theorem 4.1.3 derived in Section 4.1.4 the control input with adaptive augmentation thus reads

$$u_e(t) = -K\hat{\varepsilon}(t) + u_{ad}(t) \tag{4.165}$$

with the composite feedback gain K as in (4.55). Now, taking into account that the baseline controller was actually designed for z_n rather then z, it is straight forward to show that the tracking error dynamics from (4.38) including the disturbance generator precisely read

$$\Sigma_{e_n} : \begin{cases} \dot{e}_1(t) = \check{A}_{11}\, e_1(t) + \check{A}_{12}\, e_{2n} + \check{B}_1\, (u_e(t) + d(t)), \quad e_1(0) = e_1^0 \\ \dot{e}_{2n}(t) = \check{A}_{21}\, e_1(t) + \check{A}_{22}\, e_{2n}, \quad e_{2n}(0) = e_2^0 \\ \dot{\eta}_\Delta(t) = \check{A}_{22}\, \eta_\Delta(t) + d_\eta(t), \quad \eta_\Delta(0) = 0 \\ d_\Delta(t) = \check{b}_1^{-1} a_\eta^{\mathrm{T}} \eta_\Delta, \end{cases} \tag{4.166}$$

where $e_1 = \xi - \xi^\star$, $e_2 = \eta - \eta^\star$ and $e_{2n} = \eta_n - \eta^\star$, while $\eta = \eta_n + \eta_\Delta$. Moreover, $d = d_\xi + d_\Delta = d_w + d_r$ and d_ξ as well as d_η are defined as in (3.141) and (3.140).

Then, strictly speaking, the states of the appended system dynamics and that of the baseline controller are defined as per

$$\varepsilon = \begin{pmatrix} e_1 \\ e_{2n} \\ x_w \end{pmatrix}, \quad \hat{\varepsilon} = \begin{pmatrix} \hat{e}_1 \\ \hat{e}_{2n} \\ \hat{x}_w \end{pmatrix}. \tag{4.167}$$

The control law u_e is then given by

$$u_e(t) = k_1^{\mathrm{T}} e_1(t) - \check{B}_1^\dagger \check{A}_{12} e_{2n}(t) - d_w(t) + K\tilde{\varepsilon}(t) + u_{ad}(t). \tag{4.168}$$

Inserting this control law into Σ_{e_n} and using further the observer estimation error dynamics from (4.45) leads to

$$\begin{cases} \dot{e}_1(t) = \left(\check{A}_{11} - \check{B}_1 k_1^{\mathrm{T}}\right) e_1(t) + \check{B}_1 K \tilde{\varepsilon}(t) + \check{B}_1\, (u_{ad}(t) + d_r(t)) \\ \dot{\tilde{\varepsilon}}(t) = \left(\bar{A} - \ell \bar{C}\right) \tilde{\varepsilon}(t) + \bar{B}\, d_r(t) \end{cases} \tag{4.169}$$

and thus to the desired closed loop tracking error dynamics for the external dynamics given by

$$\begin{aligned} \dot{\Xi}(t) &= A_m \Xi(t) + B_m u_{ad}(t) + E_m d_r(t), \quad \Xi(0) = \Xi_0 \\ y_e(t) &= C_m \Xi(t) \end{aligned} \tag{4.170}$$

where $\Xi^{\mathrm{T}} = \begin{pmatrix} e_1^{\mathrm{T}} & \tilde{\varepsilon}^{\mathrm{T}} \end{pmatrix}$ and

$$A_m := \begin{pmatrix} \check{A}_{11} - \check{B}_1 k_1^{\mathrm{T}} & \check{B}_1 K \\ 0 & \bar{A} - \ell \bar{C} \end{pmatrix}, \quad B_m := \begin{pmatrix} \check{B}_1 \\ 0 \end{pmatrix}, \quad C_m^{\mathrm{T}} = \begin{pmatrix} \check{C}^{\mathrm{T}} \\ 0^{\mathrm{T}} \end{pmatrix}, \quad E_m = \begin{pmatrix} \check{B}_1 \\ \bar{B} \end{pmatrix}$$

For convenience, let $n_m = r + n + m$. Then $A_m \in \mathbb{R}^{n_m \times n_m}$, $B_m \in \mathbb{R}^{n_m \times 1}$, $C_m \in \mathbb{R}^{1 \times n_m}$, $B_m \in \mathbb{R}^{n_m \times 1}$. Let further

$$e_1(t) = F \Xi(t), \tag{4.171}$$

then

$$\Sigma_m : \begin{cases} \dot{\Xi}(t) = A_m \Xi(t) + B_m u_{ad}(t) + \Delta(t), \quad \Xi(0) = \Xi_0 \\ y_e(t) = C_m \Xi(t) \\ \dot{e}_{2n}(t) = \check{A}_{21} F \Xi(t) + \check{A}_{22}\, e_{2n}, \quad e_{2n}(0) = e_2^0 \\ \dot{\eta}_\Delta(t) = \check{A}_{22}\, \eta_\Delta(t) + d_\eta(t), \quad \eta_\Delta(0) = 0, \\ d_\Delta(t) = \check{b}_1^{-1} a_\eta^{\mathrm{T}} \eta_\Delta \end{cases} \tag{4.172}$$

where in view of the definition of $d(t)$ in (3.155) and Assumption 4.1.2 we defined

$$\Delta(t) := E_m(d_\xi(t) + d_\Delta(t) - d_w(t)). \tag{4.173}$$

Σ_m constitutes the class of uncertain system for which the $\mathcal{L}_1$ controller shall be designed. The system is also subject to assumptions 3.2.1, 3.2.2, 3.2.3, 4.2.1, 4.2.2. We additionally introduce

Assumption 4.2.4 (Stability of waveform model)**.** *We assume that the waveform model (see Assumption 4.1.2) included in the baseline controller is asymptotically stable such that*

$$|d_w(t)| \leq d_{w_{max}} < \infty. \tag{4.174}$$

It can be easily shown that due to the control architecture of the baseline controller, the transfer function from $u_{ad}(s)$ to $y_e(s)$ of the desired closed loop dynamics has relative degree $r = 2$. Consequently, this constitutes a non strictly positive real (non-SPR) system. For non-SPR reference models in [19, 68, 83] $\mathcal{L}_1$ adaptive output feedback controllers are presented. These controllers use a so-called piecewise constant adaptive law. In the following lines we adopt the ideas of [68, 83] to our problem.

In accordance with [68, 83], the $\mathcal{L}_1$ control architecture is composed of the following elements

- output predictor
- adaptation law
- control law

The output predictor is given by

$$\Sigma_{\mathcal{L}_1}^{op} : \begin{cases} \dot{\hat{\Xi}}(t) = A_m \hat{\Xi}(t) + B_m u_{ad}(t) + \hat{\Delta}(t), \quad \hat{\Xi}(0) = \Xi_0 \\ \hat{y}_e(t) = C_m \hat{\Xi}(t), \end{cases} \tag{4.175}$$

where $\hat{\Delta}(t) \in \mathbb{R}^{n_m}$ denotes the estimate of $\Delta(t)$. The former is computed via the piecewise constant adaptation law given by

$$\hat{\Delta}(t) = -\Phi(T_s)^{-1} \mu_1(kT_s) = K_\Delta(T_s) \tilde{y}_e(kT_s), \tag{4.176}$$

where $T_s > 0$ denotes the available sampling time of the CPU, $\hat{\Delta}(t) = \hat{\Delta}(kT_s)$ takes constant values on $t \in [kT_s, (k+1)T_s)$ for $k = 0, 1, 2, \ldots$ and

$$\mu_1(kT_s) := e^{\Lambda A_m \Lambda^{-1} T_s} \mathbf{1}_1 \tilde{y}_e(kT_s) \tag{4.177}$$

$$\Phi(T_s) := \int_0^{T_s} e^{\Lambda A_m \Lambda^{-1}(T_s - \tau)} \Lambda d\tau = \Lambda A_m^{-1} \left(e^{A_m T_s} - I \right). \tag{4.178}$$

Therein $\mathbf{1}_1 = (1,\, 0,\, \ldots,\, 0)^{\mathrm{T}} \in \mathbb{R}^{n_m}$, $\tilde{y}_e(t) = \hat{y}_e(t) - y_e(t)$ and

$$\Lambda := \begin{pmatrix} C_m \\ D\sqrt{P} \end{pmatrix}, \tag{4.179}$$

is a regular state transformation matrix, where

$$P = \left(\sqrt{P}\right)^{\mathrm{T}} \sqrt{P}, \quad P = P^{\mathrm{T}} > 0 \tag{4.180}$$

satisfies the algebraic Lypanuov equation

$$A_m^{\mathrm{T}} P + P A_m = -Q, \quad \text{for arbitrary} \quad Q = Q^{\mathrm{T}} > 0. \tag{4.181}$$

Furthermore, the vector $C_m(\sqrt{P})^{-1}$ lies in the kernel of $D \in \mathbb{R}^{n_m - 1 \times n_m}$, i.e.

$$D \left(C_m \left(\sqrt{P}\right)^{-1} \right)^{\mathrm{T}} = 0. \tag{4.182}$$

Finally, the control law is given by

$$u_{ad}(s) = -C(s) H_{ym}^{-1}(s) H_{yum}(s) \hat{\Delta}(s), \tag{4.183}$$

where $C(s)$ is a BIBO stable strictly proper low-pass filter verifying $C(0) = 1$ with relative degree greater or equal to r and

$$H_{\Xi m}(s) := (sI - A_m)^{-1} B_m, \quad H_{\Xi um}(s) := (sI - A_m)^{-1} \tag{4.184}$$

define the transfer functions from u_{ad} to Ξ and from Δ to Ξ, respectively, while

$$H_{ym}(s) := C_m H_{\Xi m}, \quad H_{yum}(s) := C_m H_{\Xi um} \tag{4.185}$$

denote the respective (minimum phase) maps from these inputs to the output y_e. Along the lines of [83] and adapted to our problem, the selection of $C(s)$ must ensure that

$$H_w(s) := \left(I + E_m \beta C(s) H_{ym}^{-1}(s) H_{yum}(s) \right)^{-1} \tag{4.186}$$

is stable and the following $\mathcal{L}_1$-norm stability condition is satisfied

$$\|G_{um}\|_{\mathcal{L}_1} L < 1, \tag{4.187}$$

where

$$G_{um} := \left(I - H_{\Xi m}(s) C(s) H_{ym}^{-1}(s) C_m \right) H_{\Xi um}(s) H_w(s) \tag{4.188}$$

and

$$L := L_1 + L_2 + L_{z,1} + L_3 L_{z,3} \tag{4.189}$$

while

$$L_1 := \max_{\theta\in\Omega_\theta,\beta\in\Omega_\beta} \left\| E_m \theta_K^{\mathrm{T}} \right\|_\infty, \quad \theta_K^{\mathrm{T}} := \begin{pmatrix} \theta_\xi^{\mathrm{T}}(t) - \beta k_1^{\mathrm{T}} & \beta K^{\mathrm{T}} \end{pmatrix} \tag{4.190}$$

$$L_2 := \max_{\theta\in\Omega_\theta,\beta\in\Omega_\beta} \left\| E_m \bar{\theta}_2^{\mathrm{T}} \right\|_\infty, \quad \bar{\theta}_2^{\mathrm{T}} := \begin{pmatrix} \theta_\eta^{\mathrm{T}}(t) - \beta k_2^{\mathrm{T}} \end{pmatrix} \tag{4.191}$$

$$L_3 := \max_{\theta\in\Omega_\theta} \left\| E_m \theta_\Delta^{\mathrm{T}} \right\|_\infty, \qquad \theta_\Delta^{\mathrm{T}} := \begin{pmatrix} \theta_\eta^{\mathrm{T}}(t) + \check{b}_1^{-1} a_\eta^{\mathrm{T}} \end{pmatrix}. \tag{4.192}$$

Eventually,

$$L_{z,1} := \left\| H_{z,1}(s) \right\|_{\mathcal{L}_1}, \quad H_{z,1}(s) := \left(sI - \check{A}_{22} \right)^{-1} \check{A}_{21} F \tag{4.193}$$

$$L_{z,3} := \left\| H_{z,2}(s) \right\|_{\mathcal{L}_1}, \quad H_{z,2}(s) := H_{\Delta_1}(s) + H_{z,1}(s) H_{\Delta_3}(s) \tag{4.194}$$

with

$$H_{\Delta_1}(s) := \left(sI - (\check{A}_{22} + \Delta A_{22}) \right)^{-1} \Delta A_{21} F \tag{4.195}$$

$$H_{\Delta_3}(s) := \left(sI - (\check{A}_{22} + \Delta A_{22}) \right)^{-1} \Delta A_{22} \tag{4.196}$$

The complete $\mathcal{L}_1$ output feedback controller is given by (4.175), (4.176) and (4.183), subject to the $\mathcal{L}_1$-norm stability condition (4.187).

Remark 4.2.7. Please notice that Assumption 4.2.4 is needed for the stability proof. It implies, that spline type wave form models as exploited in Example 4.1.3, i.e.

$$d_w(t) = c_{m-1} t^{m-1} + \cdots + c_1 t + c_0 \tag{4.197}$$

are not allowed because they obviously violate the assumption. Though, in accordance with Assumption 4.2.4, we may approximate the spline model via

$$d_w(t) = e^{-\alpha t}(c_{m-1} t^{m-1} + \cdots + c_1 t + c_0) \tag{4.198}$$

with α being an arbitrary (small) positive constant. In fact, for an approximation of a first order polynomial as in Example 4.1.3, this leads to a state space model of the form

$$\Sigma_w : \begin{cases} \dot{x}_w(t) = \begin{pmatrix} 0 & 1 \\ -\alpha^2 & -2\alpha \end{pmatrix} x_w(t), \quad x_w(0) = x_w^0 \\ d_w(t) = \begin{pmatrix} 1 & 0 \end{pmatrix} x_w(t) \end{cases} \tag{4.199}$$

For small α this intuitively approximates a pair of integrators. Note, however, that Assumption 4.2.4 is rather technical. Indeed, in practice it has been experienced that the true spline model, i.e. a true chain of integrators, may be combined with the proposed $\mathcal{L}_1$ controller without any problems. However, from a practical point of view, for sufficiently small α, there is no considerable difference between a true pair of integrators and the approximated ones. In fact, it was even experienced that the approximated model showed better numerical properties during frequency domain analysis. Therefore, the waveform model Σ_w as given above is applied with $\alpha = 1 \times 10^{-4}$.

Remark 4.2.8. The intuition behind the piecewise constant adaptation law is discussed in detail in reference [85]. It is also apparent in view of equation (4.262) and the consecutive lines. Roughly speaking, the adaptation law inverts the discretized solution of the continuous time predictor output error dynamics and thus according to [85] provides estimates that completely compensate for the output prediction error accumulated in the previous time step. Indeed, the terms $\mu_1(kT_s)$ and $\Phi(T_s)$ relate to the homogeneous and the inhomogeneous parts of the discretized solution. Note that the piecewise constant character is crucial because this enables the fact that $\hat{\Delta}(kT_s)$ may be written outside the integral of the inhomogeneous solution such that it is possible to solve for it.

Remark 4.2.9. Please note that for the sake of simplicity we assumed a perfect initialization of the output predictor with the plant. Strictly speaking, this assumption is quite restrictive because for most applications such an initialization is simply not possible. Moreover, it is well known that initialization errors typically lead to undesired peaking phenomena that must be prohibited. Note, however, that in the context of the motion stage, from a practical point of view, such an initialization is possible, at least in an approximate manner. In fact, due to the measurement principle of the position sensor a so-called homing procedure is required as exposed in Section 2.2.1. In particular, homing is accomplished by a dedicated motion controller which at the end of the procedure places the mover at $(q_x, q_y, q_\phi) = (0, 0, 0)$, where it is at rest. Consequently, the respective mover velocities such as the states of the machine frame are approximately zero also. At this stage the output predictor is continuously initialized with the measured output error $y_e(t)$ [1] while the resulting states are assumed zero. Experiments revealed that this procedure lead to satisfactory results for a save commissioning of the process, including the $\mathcal{L}_1$ controller, when switched from the homing controller to the $\mathcal{L}_1$ controller.

Ideal Closed Loop System

Similar to the analysis presented in section 4.2.1 an ideal closed loop system may be defined by

$$\Sigma_{\mathcal{L}_1}^{id} : \begin{cases} \dot{\Xi}_{id}(t) = A_m \Xi_{id}(t) + B_m u_{id}(t) + \Delta_{id}(t), \quad \Xi_{id}(0) = \Xi_0 \\ y_{e,id}(t) = C_m \Xi_{id}(t) \\ u_{id}(t) = -\mathcal{L}^{-1}\{C(s) H_{ym}^{-1}(s) H_{yum}(s)\} \Delta_{id}(t) \end{cases} \tag{4.200}$$

$$\Sigma_{int}^{id} : \begin{cases} \dot{e}_{2n,id}(t) = \check{A}_{21} F \Xi_{id}(t) + \check{A}_{22}\, e_{2n,id}, \quad e_{2n,id}(0) = e_2^0 \\ \dot{\eta}_{\Delta,id}(t) = \check{A}_{22}\, \eta_{\Delta,id}(t) + d_{\eta,id}(t), \quad \eta_{\Delta,id}(0) = 0, \\ d_\Delta(t) = \check{b}_1^{-1} a_\eta^{\mathrm{T}} \eta_{\Delta,id} \end{cases} \tag{4.201}$$

where $\mathcal{L}^{-1}\{\cdot\}$ denotes the inverse Laplace transform.

Stability Analysis

Rigorous proofs for the stability of $\mathcal{L}_1$ adaptive output feedback structures together with transient and steady state performance bounds are presented in references [68, 83]. The ideas and arguments of these proofs are directly applicable to our problem.

[1] Recall that $y_e(t)$ constitutes the measured output error rather than the measured output.

Therefore, instead of copying the proofs of references [68, 83] we rather give a sketch of proof and comment on the main differences that arise due to the considered class of system. Moreover, we try to give some intuitive remarks for the practitioner.

Towards this end, closely following the lines of proof of [68, pp. 192-207], [83, pp. 62-88] we begin with the first step of the three step procedure—the stability of the ideal closed loop system. For that purpose and in accordance with Lemma 4.2.3 [68, p. 198] and Lemma 5.3 [83, p. 71] we state the following lemma establishing the stability of the ideal closed loop system for our problem:

Lemma 4.2.1. *Let $C(s)$ verify the $\mathcal{L}_1$-norm condition in* (4.187)*. Then, the closed loop ideal system* (4.200)–(4.201) *is BIBS stable, where*

$$\|\Xi_{id}\|_{\mathcal{L}_\infty} \leq \rho_r \tag{4.202}$$

$$\|u_{id}\|_{\mathcal{L}_\infty} \leq \rho_{ur} \tag{4.203}$$

$$\|y_{e,id}\|_{\mathcal{L}_\infty} \leq \mu_c \rho_r \tag{4.204}$$

♦

Due to the fact that the main differences occur at this stage we next provide a complete proof of Lemma 4.2.1

Proof. Let us first shed some light on the perturbation Δ and its individual components. In view of (4.173) it is apparent that Δ is made up of d_ξ, d_Δ and d_w. Using the definition of d_ξ in (3.141), subject to Assumption 4.2.1, d_ξ may be written as

$$d_\xi(t) = \beta u(t) + \theta^{\mathrm{T}}(t) z(t) + \sigma(t). \tag{4.205}$$

Inserting the control input $u(t) = u^\star(t) + u_e(t)$ with $u_e(t)$ as in (4.168) and with K as in (4.55) into the last equation and decomposing θ as in (4.75) yields

$$d_\xi(t) = \beta u_{ad} + \beta u^\star + \bar{\theta}_1^{\mathrm{T}} e_1 + \beta K^T \tilde{\varepsilon} - \beta k_2^{\mathrm{T}} e_{2n} + \theta_\eta^{\mathrm{T}} e_2 + \theta^{\mathrm{T}} z^\star + \sigma - \beta d_w, \tag{4.206}$$

where we also used $k_2^{\mathrm{T}} := \check{B}_1^\dagger \check{A}_{12}$ and $\bar{\theta}_1$ as in (4.112). Time arguments are dropped for brevity.

Next, we note that stacking e_1 and $\tilde{\varepsilon}$ in a vector results in Ξ. Using this, the fact that $e_2 = e_{2n} + \eta_\Delta$ and the definitions of $\bar{\theta}_2$ in (4.112), d_Δ in (4.201), θ_K in (4.190) and θ_Δ in (4.192) results in

$$\Delta = E_m \left(\beta u_{ad} + \beta u^\star + \theta_K^{\mathrm{T}} \Xi - \bar{\theta}_2^{\mathrm{T}} e_{2n} + \theta_\Delta^{\mathrm{T}} \eta_\Delta + \theta^{\mathrm{T}} z^\star + \sigma - \omega d_w \right), \tag{4.207}$$

where additionally $w := 1 + \beta$. Now along the lines of [83], let

$$\vartheta_{id} := E_m \left(\beta u^\star + \theta_K^{\mathrm{T}} \Xi_{id} - \bar{\theta}_2^{\mathrm{T}} e_{2n,id} + \theta_\Delta^{\mathrm{T}} \eta_{\Delta,id} + \theta^{\mathrm{T}} z^\star + \sigma - \omega d_w \right) \tag{4.208}$$

such that

$$\Delta_{id} = E_m \beta u_{id} + \vartheta_{id}. \tag{4.209}$$

Substitution of u_{id} from (4.200) then yields

$$\begin{aligned}\Delta_{id}(s) &= -E_m\beta C(s)H_{ym}^{-1}(s)H_{yum}(s)\Delta_{id}(s) + \vartheta_{id}(s)\\ &= \left(I + E_m\beta C(s)H_{ym}^{-1}(s)H_{yum}(s)\right)^{-1}\vartheta_{id}\\ &= H_w(s)\vartheta_{id}(s).\end{aligned} \tag{4.210}$$

Next, we transform system (4.200) into the frequency domain giving

$$\Xi_{id}(s) = H_{\Xi m}(s)u_{id}(s) + H_{\Xi um}(s)\Delta_{id}(s) + \Xi_{in}(s). \tag{4.211}$$

The insertion of u_{id} yields

$$\begin{aligned}\Xi_{id}(s) &= -H_{\Xi m}(s)C(s)H_{ym}^{-1}(s)H_{yum}(s)\Delta_{id}(s) + H_{\Xi um}(s)\Delta_{id}(s) + \Xi_{in}(s)\\ &= \left(H_{\Xi um}(s) - H_{\Xi m}(s)C(s)H_{ym}^{-1}(s)H_{yum}(s)\right)\Delta_{id}(s) + \Xi_{in}(s).\end{aligned} \tag{4.212}$$

With $H_{yum} = C_m H_{\Xi um}$, Δ_{id} from (4.210) and the definition in (4.188) it follows that

$$\Xi_{id}(s) = G_{um}(s)\vartheta_{id}(s) + \Xi_{in}(s). \tag{4.213}$$

Next, we prove the first bound of Lemma 4.2.1. To this end, consider

$$\begin{aligned}\|(\vartheta_{id})_\tau\|_{\mathcal{L}_\infty} \leq{}& \|(E_m\beta u^\star)_\tau\|_{\mathcal{L}_\infty} + \left\|\left(E_m\theta_K^{\mathrm{T}}\Xi_{id}\right)_\tau\right\|_{\mathcal{L}_\infty} + \left\|\left(E_m\bar{\theta}_2^{\mathrm{T}}e_{2n,id}\right)_\tau\right\|_{\mathcal{L}_\infty}\\ &+ \left\|\left(E_m\theta_\Delta^{\mathrm{T}}\eta_{\Delta,id}\right)_\tau\right\|_{\mathcal{L}_\infty} + \left\|\left(E_m\theta^{\mathrm{T}}z^\star\right)_\tau\right\|_{\mathcal{L}_\infty} + \|(E_m\sigma)_\tau\|_{\mathcal{L}_\infty} + \|(E_m\omega d_w)_\tau\|_{\mathcal{L}_\infty}\\ \leq{}& L_0\|u^\star\|_{\mathcal{L}_\infty} + L_1\|(\Xi_{id})_\tau\|_{\mathcal{L}_\infty} + L_2\left\|(e_{2n,id})_\tau\right\|_{\mathcal{L}_\infty} + L_3\left\|(\eta_{\Delta,id})_\tau\right\|_{\mathcal{L}_\infty} \quad (4.214)\\ &+ L_4\|d_{w_\tau}\|_{\mathcal{L}_\infty} + L_5\|(z^\star)_\tau\|_{\mathcal{L}_\infty} + L_6\sigma_{\max}, \quad (4.215)\end{aligned}$$

where in addition to (4.190), (4.191) and (4.192) we used the following definitions

$$L_0 := \max_{\beta\in\Omega_\beta}|\beta|\,\|E_m\|_\infty, \quad L_4 := \left(1 + \max_{\beta\in\Omega_\beta}|\beta|\right)\|E_m\|_\infty, \tag{4.216}$$

$$L_5 := \max_{\theta\in\Omega_\theta}\left\|E_m\theta^{\mathrm{T}}\right\|_\infty, \quad L_6 := \|E_m\|_\infty. \tag{4.217}$$

In order to derive a bound on $e_{2n,id}$ we consider the Laplace transform of the internal dynamics from (4.201) together with the definition given in (4.193). That is

$$e_{2n,id}(s) = H_{z,1}(s)\Xi_{id}(s) + e_{2n,in}(s), \quad e_{2n,in}(s) := \left(sI - \check{A}_{22}\right)^{-1}e_2^0 \tag{4.218}$$

which might be bounded by

$$\left\|(e_{2n,id})_\tau\right\|_{\mathcal{L}_\infty} \leq \|H_{z,1}(s)\|_{\mathcal{L}_1}\|(\Xi_{id})_\tau\|_{\mathcal{L}_\infty} + \left\|(e_{2n,in})_\tau\right\|_{\mathcal{L}_\infty} \tag{4.219}$$

and consequently leads to

$$\left\|(e_{2n,id})_\tau\right\|_{\mathcal{L}_\infty} \leq L_{z,1}\|(\Xi_{id})_\tau\|_{\mathcal{L}_\infty} + L_{z,2}. \tag{4.220}$$

Note that the $\mathcal{L}_1$-norm of $H_{z,1}(s)$ exists and $e_{2n,in}$ is uniformly bounded, due to the stability of the (nominal) internal dynamics ($\check{A}_{22}$ is Hurwitz) discussed in Section 3.2.

Using the fact that $\xi_{id} = e_{1,id} + \xi^\star$ and $\eta_{id} = e_{2n,id} + \eta^\star + \eta_{\Delta,id}$ from (4.201) it follows that

$$\eta_{\Delta,id}(s) = H_{z,2}(s)\Xi_{id}(s) + H_{\Delta_2}(s)\xi^\star(s) + H_{\Delta_3}(s)\left(e_{2n,in}(s) + \eta^\star(s)\right), \tag{4.221}$$

where $H_{z,2}(s)$ and $H_{\Delta_3}(s)$ are defined in (4.194) and (4.196), respectively, while

$$H_{\Delta_2}(s) := \left(sI - (\check{A}_{22} + \Delta A_{22})\right)^{-1} \Delta A_{21}. \tag{4.222}$$

In view of Assumption 3.2.3, all transfer functions $H_{z,i}(s)$ and $H_{\Delta_i}(s)$ are BIBO stable and their $\mathcal{L}_1$-norms exist. Hence, the following bound holds

$$\begin{aligned}\left\|(\eta_{\Delta,id})_\tau\right\|_{\mathcal{L}_\infty} \leq \|H_{z,2}(s)\|_{\mathcal{L}_1} \|(\Xi_{id})_\tau\|_{\mathcal{L}_\infty} + \|H_{\Delta_2}(s)\|_{\mathcal{L}_1} \|\xi^\star\|_{\mathcal{L}_\infty} \\ + \|H_{\Delta_3}(s)\|_{\mathcal{L}_1} \left(\|e_{2n,in}\|_{\mathcal{L}_\infty} + \|\eta^\star\|_{\mathcal{L}_\infty}(s)\right).\end{aligned} \tag{4.223}$$

With

$$L_{z,4} := \|H_{\Delta_2}(s)\|_{\mathcal{L}_1} \|\xi^\star\|_{\mathcal{L}_\infty} + \|H_{\Delta_3}(s)\|_{\mathcal{L}_1} \left(\|e_{2n,in}\|_{\mathcal{L}_\infty} + \|\eta^\star\|_{\mathcal{L}_\infty}(s)\right) \tag{4.224}$$

and the definition of $L_{z,3}$ in (4.194) it follows that

$$\left\|(\eta_{\Delta,id})_\tau\right\|_{\mathcal{L}_\infty} \leq L_{z,3} \|(\Xi_{id})_\tau\|_{\mathcal{L}_\infty} + L_{z,4}. \tag{4.225}$$

By substituting the bounds in (4.220) and (4.225) into (4.215) and with regard to the definition of L in (4.189) we obtain

$$\|(\vartheta_{id})_\tau\|_{\mathcal{L}_\infty} \leq L \|(\Xi_{id})_\tau\|_{\mathcal{L}_\infty} + \rho_\vartheta \tag{4.226}$$

with

$$\rho_\vartheta := L_0 \|u^\star\|_{\mathcal{L}_\infty} + L_2 L_{z,2} + L_3 L_{z,4} + L_4 d_{w_{\max}} + L_5 \|z^\star\|_{\mathcal{L}_\infty} + L_6 \sigma_{\max}, \tag{4.227}$$

where we applied Assumption 4.2.4 to guarantee the boundedness of ρ_ϑ.

Substituting the bound in (4.226) back into (4.213) results in

$$\|(\Xi_{id})_\tau\|_{\mathcal{L}_\infty} \leq \|G_{um}(s)\|_{\mathcal{L}_1} \|(\vartheta_{id})_\tau\|_{\mathcal{L}_\infty} + \|(\Xi_{in})_\tau\|_{\mathcal{L}_\infty} \tag{4.228}$$

$$\leq \|G_{um}(s)\|_{\mathcal{L}_1} L \|(\Xi_{id})_\tau\|_{\mathcal{L}_\infty} + \|G_{um}(s)\|_{\mathcal{L}_1} \rho_\vartheta + \|(\Xi_{in})_\tau\|_{\mathcal{L}_\infty} \tag{4.229}$$

Using the $\mathcal{L}_1$-norm condition in (4.187) it follows that

$$\|(\Xi_{id})_\tau\|_{\mathcal{L}_\infty} \leq \rho_r := \frac{\|G_{um}(s)\|_{\mathcal{L}_1} \rho_\vartheta + \|(\Xi_{in})_\tau\|_{\mathcal{L}_\infty}}{1 - \|G_{um}(s)\|_{\mathcal{L}_1} L} < \infty, \tag{4.230}$$

which holds uniformly and hence, $\|(\Xi_{id})_\tau\|_{\mathcal{L}_\infty}$ is bounded. This proofs the first bound of Lemma 4.2.1. The third bound directly follows from the first one as per

$$\left\|(y_{e,id})_\tau\right\|_{\mathcal{L}_\infty} \leq \|(C_m \Xi_{id})_\tau\|_{\mathcal{L}_\infty} \leq \|C_m\|_1 \rho_r =: \mu_c \rho_r. \tag{4.231}$$

To proof the second bound of Lemma 4.2.1 we substitute (4.210) into u_{id}, that is

$$u_{id}(s) = -C(s) H_{ym}^{-1}(s) H_{yum}(s) H_w(s) \vartheta_{id}(s). \tag{4.232}$$

Taking the $\mathcal{L}_\infty$-norm and using the bound from (4.226) yields

$$\|(u_{id})_\tau\|_{\mathcal{L}_\infty} \leq \left\|C(s)H_{ym}^{-1}(s)\right\|_{\mathcal{L}_1} \|H_{yum}(s)H_w(s)\|_{\mathcal{L}_1} \left(L\,\|(\Xi_{id})_\tau\|_{\mathcal{L}_\infty} + \rho_\vartheta\right) =: \rho_{ur} < \infty. \tag{4.233}$$

This bound holds uniformly, if $\|(\Xi_{id})_\tau\|_{\mathcal{L}_\infty}$ is bounded, which is true, if the $\mathcal{L}_1$-norm condition in (4.187) is satisfied. This completes the proof. □

In the second step, in [68, pp. 201-205] and [83, pp. 74-80] a bound on the predictor error output is derived by Lyapunov type of arguments. For that purpose the output predictor error dynamics are considered. The latter is obtained by subtracting the desired external dynamics in (4.172) from the output predictor given in (4.175). This yields

$$\dot{\tilde{\Xi}}(t) = A_m\tilde{\Xi}(t) + \tilde{\Delta}(t), \quad \tilde{\Xi}(0) = 0. \tag{4.234}$$

Applying further the change of coordinates

$$\tilde{\varrho} = \Lambda\tilde{\Xi} \tag{4.235}$$

with Λ as given in (4.179) yields

$$\Sigma_{\mathcal{L}_1}^{\tilde{op}} : \begin{cases} \dot{\tilde{\varrho}}(t) = \Lambda A_m\Lambda^{-1}\tilde{\varrho}(t) + \Lambda\tilde{\Delta}(t), \quad \tilde{\varrho}(0) = 0 \\ \tilde{y}_e(t) = \tilde{\varrho}_1(t), \end{cases} \tag{4.236}$$

where $\tilde{\varrho}_1(t)$ denotes the first element of $\tilde{\varrho}(t)$ and

$$\tilde{\Xi}(t) := \hat{\Xi}(t) - \Xi(t), \quad \tilde{\Delta}(t) := \hat{\Delta}(t) - \Delta(t), \tag{4.237}$$

while due to the initialization of the output predictor $\tilde{\varrho}(0) = 0$. The state transformation plays a crucial role because it enables the separation of the predictor error output from the resulting states and thus forms the basis for the derivation of the piecewise constant adaptation law. In connection with Lemma 4.2.1 from [68, p.195] it additionally provides a Lyapunov function candidate associated with P, the solution of the algebraic Lyapunov equation with respect to matrix A_m in the original coordinates (see (4.180)–(4.182)), while maintaining this separation in the $\tilde{\varrho}$ coordinates which is needed later on. This is summarized by the following Lemma.

Lemma 4.2.2 ([68])**.** *For arbitrary $\varrho := (y \quad v^{\mathrm{T}})^{\mathrm{T}} \in \mathbb{R}^n$, $y \in \mathbb{R}$ and $v \in \mathbb{R}^{n-1}$, there exist $p_1 > 0$ and positive definite $P_2 \in \mathbb{R}^{(n-1)\times(n-1)}$ such that*

$$\varrho^{\mathrm{T}}(\Lambda^{-1})^{\mathrm{T}}P\Lambda^{-1}\varrho = p_1y^2 + v^{\mathrm{T}}P_2v. \tag{4.238}$$

♦

The proof of Lemma 4.2.2 can be found in [68].

Adopted to our problem, the result concerning the predictor output error bound from [68, 83] is summarized by the following Lemma.

Lemma 4.2.3 ([83])**.** *Consider the system in* (4.172) *and the $\mathcal{L}_1$ adaptive output feedback controller given by* (4.175), (4.176) *and* (4.183), *subject to the $\mathcal{L}_1$-norm stability condition* (4.187).

If we choose $T_s > 0$ to ensure

$$\gamma_0(T_s) < \bar{\gamma}_0, \tag{4.239}$$

where $\bar{\gamma}_0$ is an arbitrary positive constant, and if for arbitrary $\tau \geq 0$ the following bounds hold:

$$\|\Xi_\tau\|_{\mathcal{L}_\infty} < \rho, \quad \|u_{ad_\tau}\|_{\mathcal{L}_\infty} < \rho_u, \tag{4.240}$$

then

$$\|\tilde{y}_{e_\tau}\|_{\mathcal{L}_\infty} < \bar{\gamma}_0. \tag{4.241}$$

♦

Please note that according to [83] the bounds ρ and ρ_u are defined as

$$\rho := \rho_r + \bar{\gamma}_1, \quad \rho_u := \rho_{ur} + \bar{\gamma}_2, \tag{4.242}$$

where specific to our problem ρ_r and ρ_{ur} are defined in (4.230) and (4.233), respectively. Additionally, variables $\bar{\gamma}_1$ and $\bar{\gamma}_2$ are arbitrary (small) positive constants [83].

Proof. In [68, 83] the bound on the output prediction error is shown by reductio ad absurdum. Doing so, it is assumed that the bound in (4.241) does not hold, i.e. there exists t', for which

$$|\tilde{y}_e(t)| < \bar{\gamma}_0, \quad \forall t \in [0, t') \tag{4.243}$$

$$|\tilde{y}_e(t')| = \bar{\gamma}_0. \tag{4.244}$$

This leads to

$$\left\|\tilde{y}_{e'_t}\right\|_{\mathcal{L}_\infty} = \bar{\gamma}_0 \tag{4.245}$$

constituting the contradicting argument. Using the bounds in (4.240) and from the definitions in (4.216), (4.189), (4.227) the following bound specific to our problem can be derived:

$$\|\Delta_{t'}\|_{\mathcal{L}_\infty} \leq L_0 \left\|u_{ad_{t'}}\right\|_{\mathcal{L}_\infty} + L \|\Xi_{t'}\|_{\mathcal{L}_\infty} + \rho_\vartheta \tag{4.246}$$

$$\leq L_0\rho_u + L\rho + \rho_\vartheta =: \Delta_{\max} \tag{4.247}$$

Then, in accordance with [68, p. 202] from the general solution of (4.236) it follows that

$$\tilde{\varrho}(kT_s + t) = e^{\Lambda A_m \Lambda^{-1} t}\tilde{\varrho}(kT_s) + \int_0^t e^{\Lambda A_m \Lambda^{-1}(t-\tau)}\Lambda\hat{\Delta}(kT_s)d\tau \tag{4.248}$$

$$- \int_0^t e^{\Lambda A_m \Lambda^{-1}(t-\tau)}\Lambda\Delta(kT_s + \tau)d\tau$$

which, due to the properties of the $\tilde{\varrho}$ coordinates, might be decomposed as per

$$\tilde{\varrho}(kT_s + t) = \chi(kT_s + t) + \zeta(kT_s + t), \tag{4.249}$$

where

$$\chi(kT_s+t) = e^{\Lambda A_m \Lambda^{-1} t}\begin{pmatrix}\tilde{y}_e(kT_s)\\ 0\end{pmatrix} + \int_0^t e^{\Lambda A_m \Lambda^{-1}(t-\tau)}\Lambda\hat{\Delta}(kT_s)d\tau \tag{4.250}$$

$$\zeta(kT_s+t) = e^{\Lambda A_m \Lambda^{-1} t}\begin{pmatrix}0\\ \tilde{v}(kT_s)\end{pmatrix} - \int_0^t e^{\Lambda A_m \Lambda^{-1}(t-\tau)}\Lambda\Delta(kT_s+\tau)d\tau. \tag{4.251}$$

Then in [68, 83] it is proven by induction that the bounds

$$|\tilde{y}_e(kT_s)| \leq \varsigma(T_s) \tag{4.252}$$

$$\tilde{v}^{\mathrm{T}}(kT_s)P_2\tilde{v}(kT_s) \leq \alpha \tag{4.253}$$

hold for all $(kT_s) \leq t'$, where α and $\varsigma(T_s)$ in view of our problem are defined by

$$\alpha := \lambda_{\max}(\Lambda^{-\mathrm{T}}P\Lambda^{-1})\frac{2\left\|\Lambda^{-\mathrm{T}}P\right\|\Delta_{\max}}{\lambda_{\min}(\Lambda^{-\mathrm{T}}Q\Lambda^{-1})} \tag{4.254}$$

$$\kappa(T_s) := \int_0^{T_s}\left\|\mathbf{1}_1 e^{\Lambda A_m \Lambda^{-1}(T_s-\tau)}\Lambda\right\|_1 d\tau \tag{4.255}$$

$$\varsigma(T_s) := \|\nu_2(T_s)\|\sqrt{\frac{\alpha}{\lambda_{\max}(P_2)}} + \kappa(T_s)\Delta_{\max}, \tag{4.256}$$

and

$$\mathbf{1}_1 e^{\Lambda A_m \Lambda^{-1} t} = \begin{pmatrix}\nu_1(t) & \nu_2^{\mathrm{T}}(t)\end{pmatrix}, \quad \nu_1(t) \in \mathbb{R}, \quad \nu_2(t) \in \mathbb{R}^{n_m-1}. \tag{4.257}$$

The derivation of these bounds takes place in the inductive step. In particular, the derivation of α involves the dynamics associated with the solution (4.251) on $t \in [kT_s, (k+1)T_s]$, i.e.

$$\dot{\zeta}(t) = \Lambda A_m \Lambda^{-1}\zeta(t) - \Lambda\Delta(t), \tag{4.258}$$

and the dedicated Lyapunov function candidate supplied by Lemma 4.2.2, i.e.

$$V(t) = \zeta^{\mathrm{T}}(t)\Lambda^{-\mathrm{T}}P\Lambda^{-1}\zeta(t), \tag{4.259}$$

where $\zeta(t) = (0 \quad \tilde{v}(t)^{\mathrm{T}})^{\mathrm{T}}$. Indeed, by computing the rate of change of $V(t)$ it can be shown that $\dot{V}(t) < 0$, whenever

$$\|\zeta(t)\| > \frac{2\left\|\Lambda^{-\mathrm{T}}P\right\|\Delta_{\max}}{\lambda_{\min}(\Lambda^{-\mathrm{T}}Q\Lambda^{-1})} \tag{4.260}$$

which by virtue of this fact provides an upper bound on $V(t)$ and $\zeta(t)$ as per

$$V(t) \leq \alpha, \quad \|\zeta(t)\| \leq \sqrt{\frac{\alpha}{\lambda_{\max}(P_2)}}, \quad \forall t \in [kT_s, (k+1)T_s]. \tag{4.261}$$

Using the properties of Lemma 4.2.2 proves the bound in (4.253).

The bound in (4.252) is derived as follows. Due to the decomposition of $\tilde{\varrho}$, in the inductive step, $\chi(t) = (\tilde{y}_e(t) \;\; 0^{\mathrm{T}})^{\mathrm{T}}$ can be written as

$$\chi((k+1)T_s) = e^{\Lambda A_m \Lambda^{-1} T_s} \begin{pmatrix} \tilde{y}_e(kT_s) \\ 0 \end{pmatrix} + \int_0^{T_s} e^{\Lambda A_m \Lambda^{-1}(T_s-\tau)} \Lambda \hat{\Delta}(kT_s) d\tau \tag{4.262}$$

which intuitively constitutes a discrete time realization of the predictor output error dynamics associated with

$$\dot{\chi}(t) = \Lambda A_m \Lambda^{-1} \chi(t) - \Lambda \hat{\Delta}(t). \tag{4.263}$$

Recall that the goal of the adaptive controller is to closely follow the output predictor dynamics considered as reference model. Thus the adaptive law is chosen such that $\chi((k+1)T_s) = 0$. In view of the assumption on piecewise constant $\hat{\Delta}(kT_s)$ on $t \in [kT_s, (k+1)T_s)$, which lets us move $\hat{\Delta}(kT_s)$ outside the integral, and the fact that for $T_s > 0$ matrix

$$\Phi(T_s) = \int_0^{T_s} e^{\Lambda A_m \Lambda^{-1}(T_s-\tau)} \Lambda d\tau \tag{4.264}$$

is invertible, we can solve the equation (4.262) for $\hat{\Delta}(kT_s)$. This in fact results in the adaptation law given in (4.176). Then, due to $\chi((k+1)T_s) = 0$, and the decomposition of $\tilde{\varrho}$, $\tilde{y}_e((k+1)T_s)$ can be written as

$$\tilde{y}_e((k+1)T_s) = \mathbf{1}_1^{\mathrm{T}} \zeta((k+1)T_s) \tag{4.265}$$

which together with the general solution and the bounds on $\zeta(t)$ considered at time $(k+1)T_s \leq t'$ proves the bound in (4.252).

Following from here on the lines of proof of [68] applied to our problem finally leads to

$$|\tilde{y}_e(t)| \leq \gamma_0(T_s) \tag{4.266}$$

which holds for all $t \in [0, t']$. Along with (4.239) it follows that

$$\left\| \tilde{y}_{e_{t'}} \right\|_{\mathcal{L}_\infty} < \bar{\gamma}_0 \tag{4.267}$$

which contradicts (4.244) and thus proves the bound in (4.241). Eventually, the following result is obtained for $\gamma_0(T_s)$:

$$\gamma_0(T_s) := \beta_1(T_s)\varsigma(T_s) + \beta_2(T_s)\sqrt{\frac{\alpha}{\lambda_{\max}(P_2)}} + \beta_3(T_s)\varsigma(T_s) + \beta_4(T_s)\Delta_{\max}, \tag{4.268}$$

where

$$\beta_1(T_s) := \max_{t\in[0,T_s]} |\nu_1(t)|, \quad \beta_2(T_s) := \max_{t\in[0,T_s]} \|\nu_2(t)\|, \tag{4.269}$$

$$\beta_3(T_s) := \max_{t\in[0,T_s]} \nu_3(t), \quad \beta_4(T_s) := \max_{t\in[0,T_s]} \nu_4(t), \tag{4.270}$$

and

$$\nu_3(t) := \int_0^t |\mathbf{1}_1^{\mathrm{T}} e^{\Lambda A_m \Lambda^{-1}(t-\tau)} \Lambda \Phi^{-1}(T_s) e^{\Lambda A_m \Lambda^{-1} T_s} \mathbf{1}_1| d\tau \tag{4.271}$$

$$\nu_4(t) := \int_0^t \left\| \mathbf{1}_1 e^{\Lambda A_m \Lambda^{-1}(t-\tau)} \Lambda \right\|_1 d\tau. \tag{4.272}$$

□

Next, we comment on the final step of the three step procedure which combines the results of the first and the second step. Towards this end, consider the main result of [83] summarized by the following theorem.

Theorem 4.2.1 ([83]). *Consider the closed loop system with $\mathcal{L}_1$ adaptive output feedback controller defined via* (4.172), (4.175), (4.176) *and* (4.183), *subject to the $\mathcal{L}_1$-norm stability condition* (4.187) *and the ideal closed loop system* (4.200), (4.201). *If we choose $T_s > 0$ to ensure*

$$\gamma_0(T_s) < \bar{\gamma}_0, \tag{4.273}$$

where $\bar{\gamma}_0$ is an arbitrary positive constant we have

$$\|\Xi\|_{\mathcal{L}_\infty} \leq \rho, \quad \|u_{ad}\|_{\mathcal{L}_\infty} \leq \rho_u \tag{4.274}$$

and

$$\|\Xi_{id} - \Xi\|_{\mathcal{L}_\infty} < \gamma_1, \quad \|y_{e,id} - y_e\|_{\mathcal{L}_\infty} < \mu_c \gamma_1, \quad \|u_{id} - u_{ad}\|_{\mathcal{L}_\infty} < \gamma_2 \tag{4.275}$$

■

Proof. The proof is similar to the one presented in [83, pp. 80-83] and directly applicable to our problem. Similar to the proof of Lemma 4.2.3 this one is also accomplished by a contradicting argument assuming that the first and the third bound in (4.275) do not hold, i.e. there exists time $\tau \in \mathbb{R}^+$ such that

$$\|\Xi_{id}(t) - \Xi(t)\|_\infty < \gamma_1, \quad \|u_{id}(t) - u_{ad}(t)\|_\infty < \gamma_2, \qquad \forall t \in [0, \tau) \tag{4.276}$$

$$\|\Xi_{id}(\tau) - \Xi(\tau)\|_\infty = \gamma_1, \quad \|u_{id}(\tau) - u_{ad}(\tau)\|_\infty = \gamma_2, \tag{4.277}$$

Closely following the lines of proof of [83], while using the bounds presented in the stability proof of the ideal closed loop system, the following bounds can be established for our problem:

$$\gamma_1 := \frac{\left(\left\| G_{um}(s) E_m \beta C(s) H_{ym}^{-1}(s) \right\|_{\mathcal{L}_1} + \left\| H_{\Xi m}(s) C(s) H_{ym}^{-1}(s) \right\|_{\mathcal{L}_1} \right) \bar{\gamma}_0}{1 - \|G_{um}(s)\|_{\mathcal{L}_1} L} + \delta_1 \tag{4.278}$$

$$\begin{aligned} \gamma_2 := \left\| C(s) H_{ym}^{-1}(s) H_{yum}(s) H_w(s) \right\|_{\mathcal{L}_1} \left(L\gamma_1 + \left\| E_m \beta C(s) H_{ym}^{-1}(s) \right\|_{\mathcal{L}_1} \bar{\gamma}_0 \right) \\ + \left\| C(s) H_{ym}^{-1}(s) \right\|_{\mathcal{L}_1} \bar{\gamma}_0 + \delta_1, \end{aligned} \tag{4.279}$$

where δ_1 is an arbitrary (small) positive constant for enforcing the contradiction argument. Furthermore, ρ and ρ_u are defined as in (4.242) and (4.230), (4.233), respectively,

while the choice of $\bar{\gamma}_0$ and δ_1 must ensure that $\gamma_1 < \bar{\gamma}_1$, $\gamma_2 < \bar{\gamma}_2$. Finally, $\mu_c := \|C_m\|_1$. This completes the proof. □

Remark 4.2.10. Theorem 4.2.1 constitutes the most important result for $\mathcal{L}_1$ adaptive output feedback structures of the presented type. In conjunction with Lemma 4.2.2 from [68], i.e.

Lemma 4.2.4 ([68])**.** *The following limiting relationship is true:*

$$\lim_{T_s \to 0} \gamma_0(T_s) = 0 \tag{4.280}$$

♦

It implies that $\gamma_0(T_s)$ and hence $\bar{\gamma}_0$ and consequently $|\tilde{y}_e(t)|$ as well as $\|\Xi_{id} - \Xi\|_{\mathcal{L}_\infty}$ may be rendered arbitrarily small by letting T_s approach arbitrarily close to zero. In other words, the closed loop system can arbitrarily close approach the performance of the ideal system if $T_s \to 0$. This raises the question, whether it is possible to set $T_s = 0$, which basically asks for a continuous time realization of the piecewise constant adaptation law. However, in view of matrix $\Phi(T_s)$ as given in (4.178) and the requirement of its inverse, it is apparent that $\Phi(T_s)$ becomes singular if $T_s = 0$. Accordingly, there exists no continuous version of the adaptation law and the piecewise constant character is necessary for implementation reasons.

Controller Tuning and Frequency Domain Analysis

In a number of papers [62, 86, 108] researchers perceived that $\mathcal{L}_1$ adaptive control architectures with piecewise constant adaptive laws as presented in [68] in fact resemble LTI controllers, showing interesting parallels to disturbance observer structures [69, 86, 108]. The LTI nature becomes apparent if for instance the ideal closed loop system (4.200)–(4.201) is considered. Although mostly in the literature on $\mathcal{L}_1$ adaptive control the ideal control law $u_{id}(s)$ is termed non-implementable [68, 83], because it depends on the unknowns Δ_{id} assumed to be perfectly known, due to the insertion of the low-pass filter, it is possible to directly solve for u_{id} [86] which is demonstrated next. Towards this end, consider the Laplace transform of (4.200) with zero initial conditions given by

$$\begin{cases} y_{e,id}(s) = H_{ym}(s)u_{id}(s) + H_{yum}(s)\Delta_{id}(s) \\ u_{id}(s) = -C(s)H_{ym}^{-1}(s)H_{yum}(s)\Delta_{id}(s), \end{cases} \tag{4.281}$$

with $H_{ym}(s)$ and $H_{yum}(s)$ given in (4.184)– (4.185). Please note that the internal dynamics are not considered because their effect is captured inside $\Delta_{id}(s)$. Now, solving the first equation of (4.281) for $\Delta_{id}(s)$ and substitution into $u_{id}(s)$ leads to

$$u_{id}(s) = -\frac{C(s)}{H_{ym}(s)(1 - C(s))}\, y_{e,id}(s), \tag{4.282}$$

where we used the fact that in our case (SISO) $H_{ym}(s)$ is scalar. This constitutes the ideal control law which indeed is implementable.

In the particular case of the presented output feedback scheme, the LTI nature of the controller given by (4.175), (4.176) and (4.183) can be observed by the fact that for given $T_s > 0$ the term

$$K_\Delta(T_s) := -\Phi(T_s)^{-1} e^{\Lambda A_m \Lambda^{-1} T_s}\, \mathbf{1}_1 \tag{4.283}$$

of the adaptation law is a constant vector providing a proportional feedback of the sampled error variable $\tilde{y}_e(kT_s)$.

If we assume that the sampling frequency is above the Nyquist rate associated with the bandwidth of $\tilde{y}_e(t)$ [62] the sampled adaptation law is equivalent to an LTI system given by

$$\hat{\Delta}(s) = K_{\Delta}(s)\,\tilde{y}_e(s). \tag{4.284}$$

Since the remaining parts, i.e. the output predictor such as the control law, are also LTI, it follows that the complete controller resembles an LTI controller. Therefore, LTI techniques might be used for the design and the assessment of the controller. In view of Remark 4.2.6 this is especially useful for filter design which may be aided by frequency domain and loop shaping ideas.

To this end, firstly consider the Laplace transform of the output predictor that is

$$\hat{y}_e(s) = H_{ym}(s)u_{ad}(s) + H_{yum}(s)K_{\Delta}(s)\tilde{y}_e(s), \tag{4.285}$$

as well as the Laplace transform of the control law

$$u_{ad}(s) = -C(s)\frac{H_{yum}(s)}{H_{ym}(s)}K_{\Delta}(s)\tilde{y}_e(s). \tag{4.286}$$

Next, subtracting $y_e(s)$ from (4.285) noting that $\tilde{y}_e(s) = \hat{y}_e(s) - y_e(s)$ and substitution into (4.286) yields

$$u_{ad}(s) = \frac{H_{yum}(s)K_{\Delta}(s)C(s)}{H_{ym}(s)\left(H_{yum}(s)K_{\Delta}(s)C(s) - H_{yum}(s)K_{\Delta}(s) + 1\right)}y_e(s), \tag{4.287}$$

where we note that due to the considered SISO case also the product $H_{yum}(s)K_{\Delta}(s)$ is scalar. If we rewrite the last equation to

$$u_{ad}(s) = -\frac{C(s)}{H_{ym}(s)\left(1 - C(s) - \frac{1}{H_{yum}(s)K_{\Delta}(s)}\right)}y_e(s) \tag{4.288}$$

it can be seen that this control law approximates the ideal one from (4.282). Obviously, if $T_s \to 0$, $K_{\Delta} \to \infty$ and hence $u_{ad}(s) \to u_{id}(s)$. In [86] this behavior is described as limiting behavior.

Since $H_{ym}(s)$ and $H_{yum}(s)$ are completely known from the parameters (A_m, B_m, C_m, 0) of the nominal closed loop system, only the low-pass filter $C(s)$ and sampling time T_s must be tuned. According to [68] the sampling time should be chosen as small as the CPU permits. Following these lines of thought, we set T_s to the lowest possible value that is provided by the real-time platform, that is $T_s = 125$ µs. Indeed, a comparison with higher values on T_s revealed that the best disturbance rejection properties were obtained with $T_s = 125$ µs. The filter $C(s)$ is chosen as a series connection of two second order filters, i.e.

$$C(s) = C_1(s)C_2(s), \quad C_i(s) = \frac{\omega_i^2}{(s^2 + 2\zeta_i\omega_i s + \omega_i^2)}, \quad i = 1, 2 \tag{4.289}$$

with $\omega_1 = 500$ rad/s, $\zeta_1 = 1.5$, $\omega_2 = 10\omega_1$ rad/s, $\zeta_2 = 0.8$. This particular choice is motivated by the following facts. First, $C_1(s)$ is chosen such that the bandwidth of the filter lies significantly below the bandwidth of the input dynamics $\Sigma_2(s)$. This is done

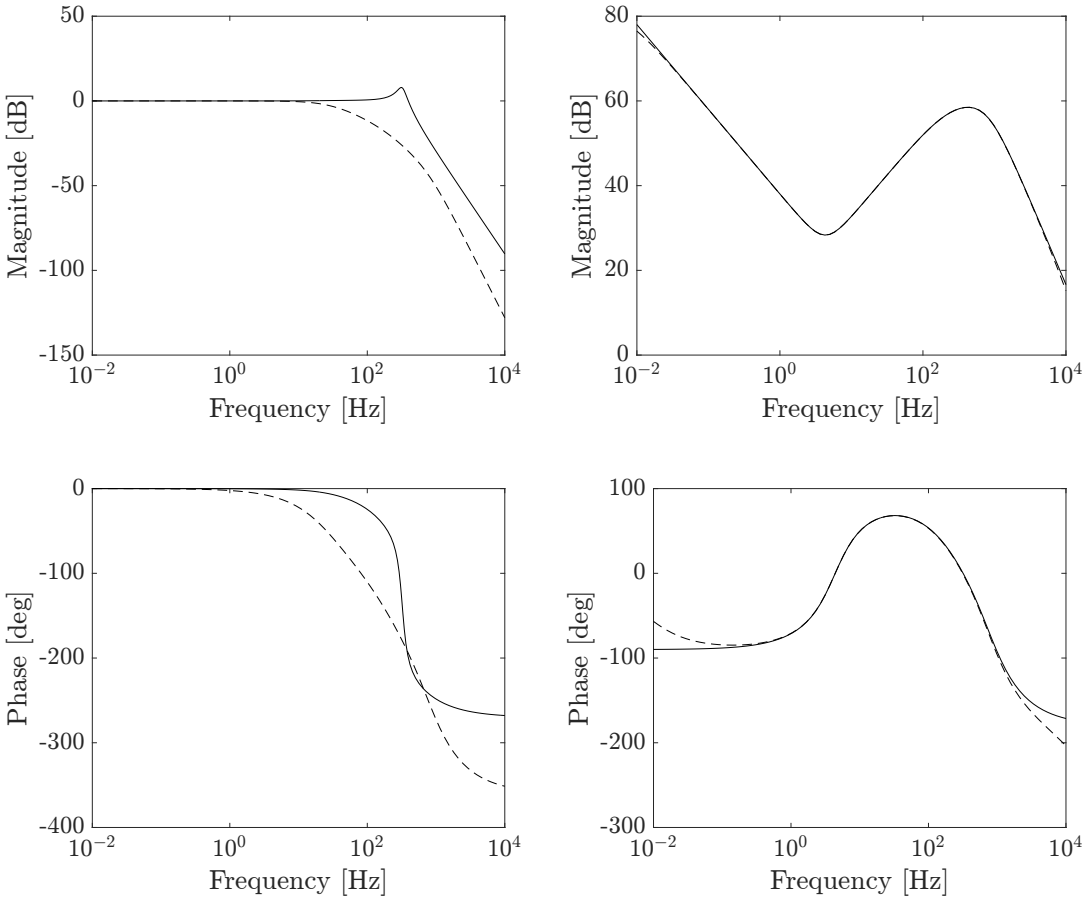

FIGURE 4.10: Input dynamics $\Sigma_2(s)$ (solid) and filter $C(s)$ (dashed) (left); ideal $\mathcal{L}_1$ controller (solid) and implemented $\mathcal{L}_1$ controller (dashed).

in order to avoid excitation of the high frequency dynamics and for posing a consistent control goal. Being concordant with this requirement, ω_1 is chosen as high as possible for gaining good disturbance rejection properties. Doing so, an eye is kept on the peak values and the specification of the noise sensitivity.

The role of the second filter is to introduce sufficient roll-off at higher frequencies. In fact, the filter is designed such that the high frequency behavior of the augmented loop converges to that of the nominal feedback loop. This avoids unnecessary high gains in higher frequency regions. The bode plots of filter $C(s)$ and the ideal and implemented $\mathcal{L}_1$ controllers are presented in Figure 4.10.

The bode plot of the ideal and the implemented $\mathcal{L}_1$ controllers reveal that the ideal controller essentially is of PID type with additional roll-off filtering. Moreover, the approximative nature of the implemented controller can be seen. Due to the fact that the latter only approximates the ideal controller small steady state errors are expected. However, since our approach incorporates both a baseline controller with integral action together with the augmenting $\mathcal{L}_1$ controller, the integral action incorporated by the baseline controller removes these steady state errors.

Note that although the ideal control law is implementable, we still will use the $\mathcal{L}_1$ control architecture because it is favorable from an architectural point of view [86]. In fact, with the $\mathcal{L}_1$ architecture it is very easy to apply modifications so as to incorporate known time-delays, such as known input nonlinearities and input dynamics [86].

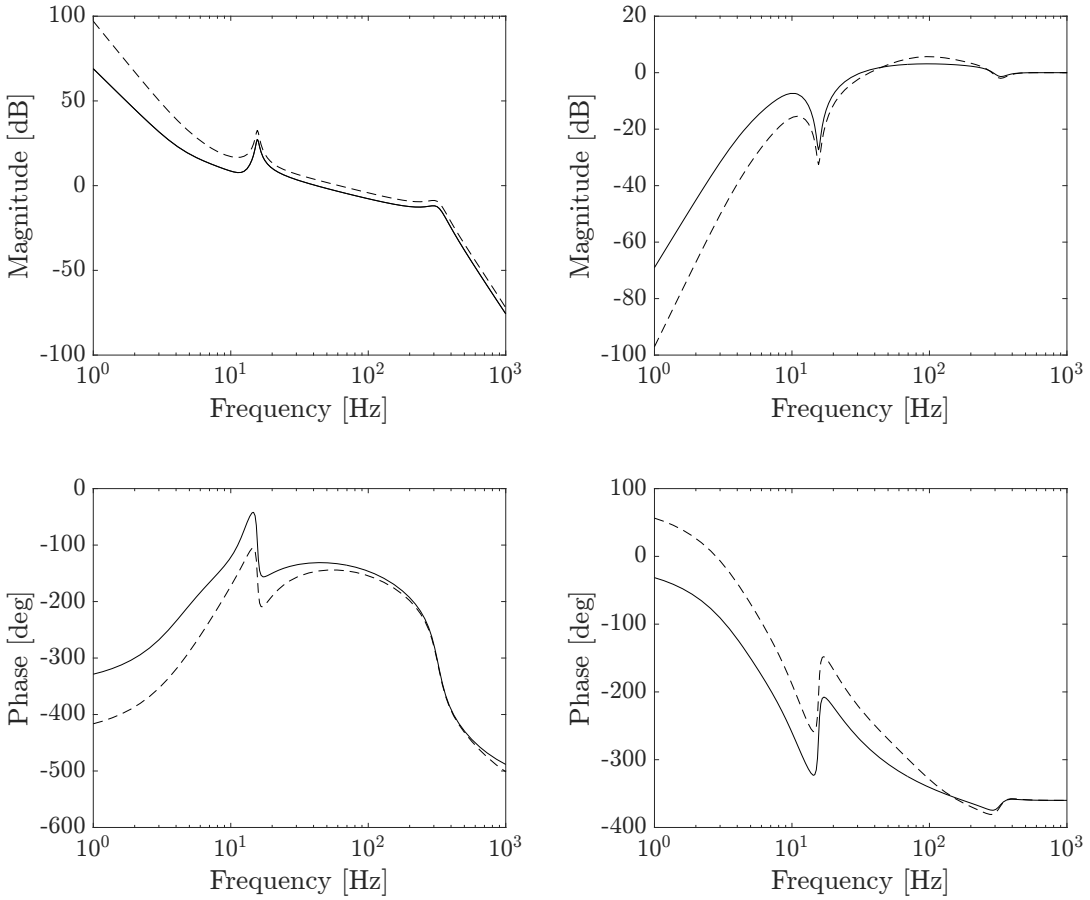

FIGURE 4.11: Loop gain (left) and Sensitivity (right) of nominal output feedback controller (solid) together with the proposed $\mathcal{L}_1$ adaptive augmentation (dashed).

Moreover, the initialization of observer states etc. can easily be accomplished. This might not be the case for the ideal control law as shown in [86].

Transferring the nominal controller including the $\mathcal{L}_1$ augmentation into the standard feedback loop, and computation of the loop gain and the relevant sensitivity functions finally yields the loop shapes (dotted) presented in Figures 4.11 and 4.12. For the sake of comparison, the loop shapes of the nominal controller (solid) are also shown.

Apparently, the loop gain of the $\mathcal{L}_1$ augmented feedback loop shows a considerable increase in gain for lower frequencies and thus better disturbance rejection and hence improved performance. This is also directly visible from the sensitivity plot on the right of Figure 4.11 and the process sensitivity shown on the left of Figure 4.12.

The overall controller has a bandwidth of $61\,\mathrm{Hz}$, a phase margin of $\phi_m = 35.6°$ and a gain margin of $g_m = 8\,\mathrm{dB}$. Moreover, it exhibits a sensitivity peak of $M_s = 5.7\,\mathrm{dB}$, as desired.

The noise sensitivity function, shown on the right of Figure 4.12, has its maximum at $68.5\,\mathrm{dB}$ which is a considerable increase of control effort of approximately $3.5\,\mathrm{dB}$ compared to the nominal controller. However, it still lies within the specifications and is justified by the increase in performance. Notice, how the augmented design rolls-off at higher frequencies and converges to the high frequency behavior of the nominal design.

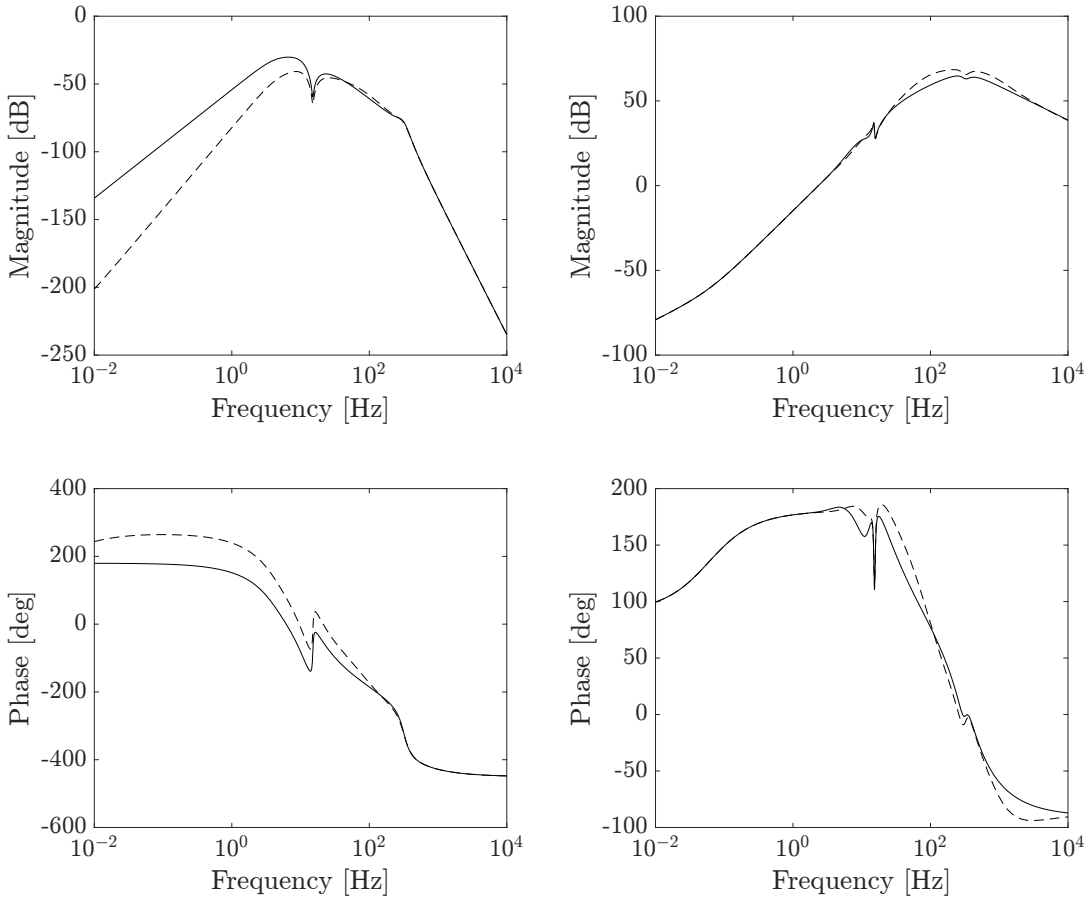

FIGURE 4.12: Process and noise sensitivity functions of final nominal output feedback controller (solid) together with the proposed $\mathcal{L}_1$ adaptive augmentation (dashed)

Finally, we conclude that all the desired frequency domain specifications are met. The time domain performance of the proposed scheme is assessed in Chapter 5 by experiments conducted at the motion stage platform.

Remark 4.2.11. The fact that in specific cases there exist LTI controllers that are equivalent to $\mathcal{L}_1$ adaptive control architectures has lead to controversial discussions, among members of the adaptive control community, on the benefits of $\mathcal{L}_1$ adaptive control (see e.g. [73, 106] and the response of [67]).

However, it is important to notice that $\mathcal{L}_1$ adaptive control is applicable to a much broader class of systems. This includes nonlinear systems [68] or linear time varying systems [68, 83] for which no equivalent LTI controllers exist. Moreover, with the generalization of adaptation laws as presented in [84],[144] and [143] also adaptation laws borrowing ideas from funnel control are possible.

4.2.3 A Note on a possible MIMO Approach

The $\mathcal{L}_1$ output feedback controller presented in Section 4.2.2 may straightforwardly be extended to MIMO systems as presented in reference [19].

Regarding the MIMO approach, the following question arises: Is there a benefit of using the $\mathcal{L}_1$ MIMO controller over three $\mathcal{L}_1$ augmented SISO controllers for the respective axes? And this, if the augmentation has been designed subject to the assumption of a completely decoupled motion stage?

In order to answer this question let us perform the following thought experiment. Firstly, recall that the physical modeling in Section 3.1 revealed that under a mild set of assumptions the motion axes of the PPS1405 can be seen as completely decoupled. Based on this fact we derived our baseline controllers, implementing three SISO controllers for the dedicated motion axes.

The closed loop behavior of each baseline controller thus forms the reference model for the respective SISO $\mathcal{L}_1$ controllers.

Now, let us stack up the three SISO reference models into one MIMO reference model and let $(\bar{A}_m, \bar{B}_m, \bar{C}_m)$ denote their respective matrices. Accordingly, we obtain a reference model with three inputs and three outputs, whose inputs and outputs are of course completely decoupled.

Further, recall that the main idea of the reference model is to capture the desired input/output behavior of the closed loop adaptive system. Hence, the decoupled nature of the reference model is without a doubt desired and could be used to enforce a decoupling of inputs and outputs for the closed loop adaptive system.

As opposed to the SISO case, where only the inputs and outputs of one axis are used at a time, in the MIMO approach we make use of all inputs and outputs simultaneously. Now recall, that the presented $\mathcal{L}_1$ output feedback controller also compensates for unmatched uncertainties. Consequently, one could think that with the MIMO approach, where all parasitic couplings between axes will be captured in the lumped disturbance term Δ there should be a better rejection of these couplings/disturbances.

However, it turns out that there is no benefit at all. Indeed, both approaches yield identical results.

The reason for this can be explained as follows. Since $(\bar{A}_m, \bar{B}_m, \bar{C}_m)$ of the stacked MIMO model are diagonal block matrices, it can easily be shown that all components of the MIMO $\mathcal{L}_1$ controller, i.e.

- output predictor
- adaptation law
- control law

will also be diagonal. Hence this MIMO controller can also be implemented by three dedicated SISO $\mathcal{L}_1$ output feedback controllers. Please notice that this issue has also been observed by [54]. According to [54] a true benefit of the MIMO approach can only be exploited, if the MIMO nature of the process in question is explicitly considered. Thus, for applying MIMO schemes in the context of the motion stage the MIMO nature of the latter should be explored more deeply in future works.

4.3 Implementation Issues

For a successful transition of $\mathcal{L}_1$ adaptive control into practice several obstacles must be tackled and some modifications should be considered.

4.3.1 Anti-Windup Modification

In almost any application plants underly several constraints. These can be static or also dynamic and mostly are targeted to plant inputs, states or outputs.

Normally, during the process of reference trajectory design, trajectories are planned such that all input, state or output dependent constraints are accommodated. Therefore, it is reasonable to assume that there is no violation of these constraints during normal operation. However, in the authors opinion a robust control design should always take at least constraints with respect to control authority into account, in order to be able to robustly react on unforeseen changes or initialization errors that might cause the control input to saturate. Not taking input constraints into consideration, could immediately render the closed loop motion system unstable, whenever the input saturates.

In this section we will thus concentrate on limitations with respect to control authority. In the simplest case these limitations are static nonlinearities possibly of the form

$$u_{sat}(t) = \mathrm{sat}(u(t)) = \begin{cases} u_{max}\,\mathrm{sign}(u(t)), & |u(t)| \leq u_{max} \\ u(t), & |u(t)| < u_{max} \end{cases} \tag{4.290}$$

that is the classical saturation function. However, besides actuator position constraints as captured by the $\mathrm{sat}(\cdot)$ function, real world actuators might also exhibit further limitations such as actuator position rate limits, hysteresis, backlash, input quantization or input dynamics [6, 63].

Since the modifications presented below are model based, taking the respective actuator characteristics into account, they will apply for all of these limits, regardless whether they are static or dynamic, as long as at least an adequate model of these characteristics is available. Hence, for the sake of simplicity it is convenient to firstly consider the simple actuator model $\mathrm{sat}(u(t))$ as given above.

It is well known [6, 63] that the effect of input saturation or rate limits causes so-called windup effects that can have disastrous consequences on the performance as well as the stability of the closed loop system. This is especially true, if the system is marginally stable or even unstable.

To accommodate for windup effects, numerous methods exist in the literature, see e.g. [63], [51], [6] and references therein.

A simple and systematic treatment of anti windup mechanisms is possible when observer-based controllers are considered. Indeed, these controllers exhibit an automatic windup protection if a respective actuator model is applied to the observer [6, 63]. This fact is illustrated by the following simple example.

Example 4.3.1. *Consider the following plant description with constraint control input, i.e.*

$$\begin{aligned} \dot{x}(t) &= A\,x(t) + B\,u_{sat}(t), \quad x(0) = x_0 \\ y(t) &= C\,x(t). \end{aligned} \tag{4.291}$$

A simple Luenberger observer with respective actuator model takes the form

$$\begin{aligned} \dot{\hat{x}}(t) &= A\,\hat{x}(t) + B\,u_{sat}(t) + \ell\,(y(t) - \hat{y}(t))\,, \quad \hat{x}(0) = \hat{x}_0 \\ \hat{y}(t) &= C\,\hat{x}(t), \end{aligned} \tag{4.292}$$

where ℓ is designed such that $A - \ell C$ is rendered Hurwitz. Now, assuming a perfect actuator model, it is easily verified that the implementation of $u_{sat}(t)$ instead of the unconstrained input $u(t)$ removes the actuator characteristics form the estimation error dynamics completely. The state equation of the estimation error then reads

$$\dot{\tilde{x}}(t) = (A - \ell C)\,\tilde{x}(t), \tag{4.293}$$

where we used $\tilde{x} := x - \hat{x}$ for the denotation of the estimation error. Consequently, $\tilde{x}(t) \to 0$ as $t \to \infty$ regardless of the input constraints. That means that the observer automatically corrects its estimates on states in a consistent manner with the plant, even in the case of input saturation. This holds also for all disturbance models (integrators) that have been appended to the observer.

From that we can conclude that when the observer state $\hat{x}(t)$ is used in a state feedback control setting, this automatically yields windup protection to this controller (see [6, 63] for a deeper treatment).

▲

This example demonstrates that observer-based control architectures are easily modified in order to account for input constraints and are in this respect favorable control architectures. Obviously, u_{sat} might be substituted by any available actuator model, or by a direct measurement of the actuator position (if available) to account also for other effects than only saturation.

This is exactly the reason why we pursued an observer-based implementation of the baseline controller. And this is also the reason, why the control architecture in $\mathcal{L}_1$ adaptive control is favorable and easily modified—because it is observer-based.

For applying the windup modification to the nominal controller, let us firstly consider the plant (4.37) with saturated control input u_{sat}, i.e.

$$\begin{aligned} \dot{z}(t) &= \check{A}\,z(t) + \check{B}(u_{sat}(t) + d(t)), \quad z(0) = z^0 \\ y(t) &= \check{C}\,z(t). \end{aligned} \tag{4.294}$$

Note that we dropped the index n in z_n, as in Section 4.1.4, for simplicity. Defining

$$u_e(t) := u_{sat}(t) - u^\star(t) \tag{4.295}$$

and applying exactly the same design steps as in Section 4.1.4, automatically leads to the modified output feedback controller given by

$$\Sigma_c^{AW} : \begin{cases} \dot{\hat{\varepsilon}}(t) = \left(\bar{A} - \ell\bar{C}\right)\hat{\varepsilon}(t) + \bar{B}\,\left(u_{sat}(t) - u^\star(t)\right) + \ell\,y_e(t), \quad \hat{\varepsilon}(0) = \hat{\varepsilon}_0 \\ u_e(t) = -K\hat{\varepsilon}(t), \\ u_{sat}(t) = \mathrm{sat}\left(u^\star(t) + u_e(t)\right) \end{cases} \tag{4.296}$$

and $u^\star$ as the output of the nominal feedforward controller Σ_n^{-1} (see Theorem 4.1.3).

It is straight forward to proof that with the definition of u_e as given in (4.295), the modified feedback controller and the nominal feedforward law Σ_n^{-1}, exactly the same tracking error dynamics is obtained as in (4.50).

4.3.2 Pseudo-Control Hedging

When considered in a set point regulation context, $\mathcal{L}_1$ adaptive control provides automatic windup protection due to its observer-based control architecture, if the predictor is modified respectively (see Example (4.3.1)). Modifications of this kind have been reported in references [54, 86]. However, although this property holds for the regulation problem, it is not so easy to get for the tracking problem. This is due to the fact that first, multiple control portions such as reference feedforward, a stabilizing feedback as well as an adaptive control portion are present, and second, the $\mathcal{L}_1$ controller is designed with respect to the tracking error dynamics rather then the original system dynamics. This implies that the $\mathcal{L}_1$ controller only sees parts of the control inputs. Precisely speaking, the predictor sees only the adaptive control portion u_{ad}. Therefore, it is not so easy to detect a saturation of the overall control input u inside the predictor.

In order to provide a windup protection for the adaptive part, we will use a methodology called pseudo-control hedging (PCH) introduced by [79, 80]. The main idea of PCH is to introduce a modification to the reference model, a so-called hedging signal v_h, in order to "hide" certain actuator characteristics from the adaptive element such that the latter will not adapt to these characteristics [80]. In other words, the PCH approach modifies the reference model, i.e. predictor, in such a way that the actuator characteristics will be removed completely from the model tracking/prediction error dynamics. This is exactly the same idea as discussed in Example 4.3.1.

According to [79, 80], the hedging signal may be computed by subtracting the vector fields of the considered system with unconstrained and constrained control inputs. That is,

$$v_{h_1} = g(e, u, u^\star, d) - g(e, u_{sat}, u^\star, d), \tag{4.297}$$

where

$$\begin{aligned} g(e, u, u^\star, d) &:= \check{A}_{11}\, e_1(t) + \check{A}_{12}\, e_2(t) + \check{B}_1\, (u(t) - u^\star(t)) + \check{B}_1\, d(t) \\ g(e, u_{sat}, u^\star, d) &:= \check{A}_{11}\, e_1(t) + \check{A}_{12}\, e_2(t) + \check{B}_1\, (u_{sat}(t) - u^\star(t)) + \check{B}_1\, d(t) \end{aligned}$$

represent the respective right hand sides of the external tracking error dynamics of (4.38). Then,

$$v_{h_1}(t) = \check{B}_1(u(t) - u_{sat}(t)). \tag{4.298}$$

Please note that v_{h_1} denotes the first component of the hedging signal v_h which corresponds to the state $e_1 =: \Xi_1$, i.e. the first component in Ξ (see (4.170)). The second component v_{h_2} of the hedging signal is dedicated to $\tilde{\varepsilon} =: \Xi_2$, being the second component of Ξ. Since $\tilde{\varepsilon}$ represents the estimation error of the observer which itself is already protected against windup effects, $v_{h_2} = 0$. Hence, the modified predictor including PCH reads

$$\Sigma_{\mathcal{L}_1}^{ph} : \begin{cases} \dot{\hat{\Xi}}(t) = A_m \hat{\Xi}(t) + B_m u_{ad}(t) + \hat{\Delta}(t) - v_h, \quad \hat{\Xi}(0) = \Xi_0 \\ \hat{y}_e(t) = C_m \hat{\Xi}(t) \end{cases} \tag{4.299}$$

with

$$v_h = \begin{pmatrix} \check{B}_1 \\ 0 \end{pmatrix} (u(t) - u_{sat}(t)). \tag{4.300}$$

Next, we demonstrate that the modified predictor with hedging works properly. Towards this end, we compute the prediction error dynamics and show that it is independent of any actuator characteristics. To do so, we split the output predictor into

$$\dot{\hat{e}}_1(t) = A_{m,1}\hat{e}_1(t) + \check{B}_1 K\hat{\tilde{\varepsilon}}(t) + \check{B}_1 u_{ad}(t) + \hat{\Delta}_1(t) - v_{h_1}(t) \tag{4.301}$$

$$\dot{\hat{\tilde{\varepsilon}}}(t) = A_{m,2}\hat{\tilde{\varepsilon}}(t) + \hat{\Delta}_2(t), \tag{4.302}$$

where we defined $A_{m,1} := \check{A}_{11} - \check{B}_1 k_1^{\mathrm{T}}$ and $A_{m,2} := \bar{A} - \ell\bar{C}$ for brevity. Consider further the external tracking error dynamics of the plant with constraint input given by

$$\dot{e}_1(t) := \check{A}_{11}\, e_1(t) + \check{A}_{12}\, e_2(t) + \check{B}_1\, (u_{sat}(t) - u^\star(t)) + \check{B}_1\, d(t). \tag{4.303}$$

Subtracting the last equation from (4.301), using the definition of v_{h_1} above and omitting time arguments for brevity yields

$$\dot{\hat{e}}_1 = A_{m,1}\hat{e}_1 + \check{B}_1 K\hat{\tilde{\varepsilon}} + \check{B}_1 u_{ad} + \hat{\Delta}_1 - \check{B}_1 u + \check{B}_1 u^\star - \check{A}_{11}\, e_1 - \check{A}_{12}\, e_2 - \check{B}_1\, d. \tag{4.304}$$

By inserting the control law

$$u = u^\star - k_1^{\mathrm{T}} e_1 - \check{B}_1^\dagger \check{A}_{12} e_2 - d_w + K\tilde{\varepsilon} + u_{ad} \tag{4.305}$$

and recalling that $\Delta_1 = \check{B}_1 d_r$ we obtain

$$\dot{\hat{e}}_1 = A_{m,1}\hat{e}_1 + \check{B}_1 K\hat{\tilde{\varepsilon}} + \check{B}_1 u_{ad} + \hat{\Delta}_1 - A_{m,1}\, e_1 - \check{B}_1 u_{ad} - \check{B}_1 K\tilde{\varepsilon} - \Delta_1 \tag{4.306}$$

$$\dot{\tilde{\Xi}}_1 = A_{m,1}\tilde{\Xi}_1 + \check{B}_1 K\tilde{\Xi}_2 + \tilde{\Delta}_1. \tag{4.307}$$

This constitutes the first differential equation of the prediction error dynamics. Notice, that it is independent of any actuator characteristics, as desired.

For computing the second equation of the prediction error dynamics we must consider the extended tracking error dynamics with constrained input. In view of (4.42) that is

$$\dot{\varepsilon} = \bar{A}\,\varepsilon + \bar{B}\,(u_{sat} - u^\star + d_r)\,. \tag{4.308}$$

Using further the observer with the anti windup protection (4.296) presented in the foregoing section, the estimation error dynamics of the observer may be computed as

$$\dot{\hat{\tilde{\varepsilon}}} = A_{m,2}\tilde{\varepsilon} + \Delta_2, \tag{4.309}$$

where $\tilde{\varepsilon} = \varepsilon - \hat{\varepsilon}$ and $\Delta_2 = \bar{B}d_r$. Subtracting the last equation from (4.302) and combing this result with (4.307) finally yields

$$\tilde{\Xi}(t) = A_m\tilde{\Xi}(t) + \tilde{\Delta}(t). \tag{4.310}$$

This of course coincides with the prediction error dynamics of the unconstrained case (cf. equation (4.234)). From this we conclude that the PCH modification works as expected.

Note that with PCH it is also possible to account for the high frequency dynamics $\Sigma_2(s)$. To do so, $\Sigma_2(s)$ must be included in v_h. However, on the one hand this is not necessary because bandwidth limitations due to $\Sigma_2(s)$ have already been accounted for during the design of the $\mathcal{L}_1$ controller, i.e. by the choice of the low-pass filter $C(s)$.

On the other hand, we experienced that when doing so, the tracking performance was unsatisfactory. For these reasons, the PCH approach is only applied to account for static actuator position limits.

4.3.3 Minimal vs. Non-Minimal Realizations

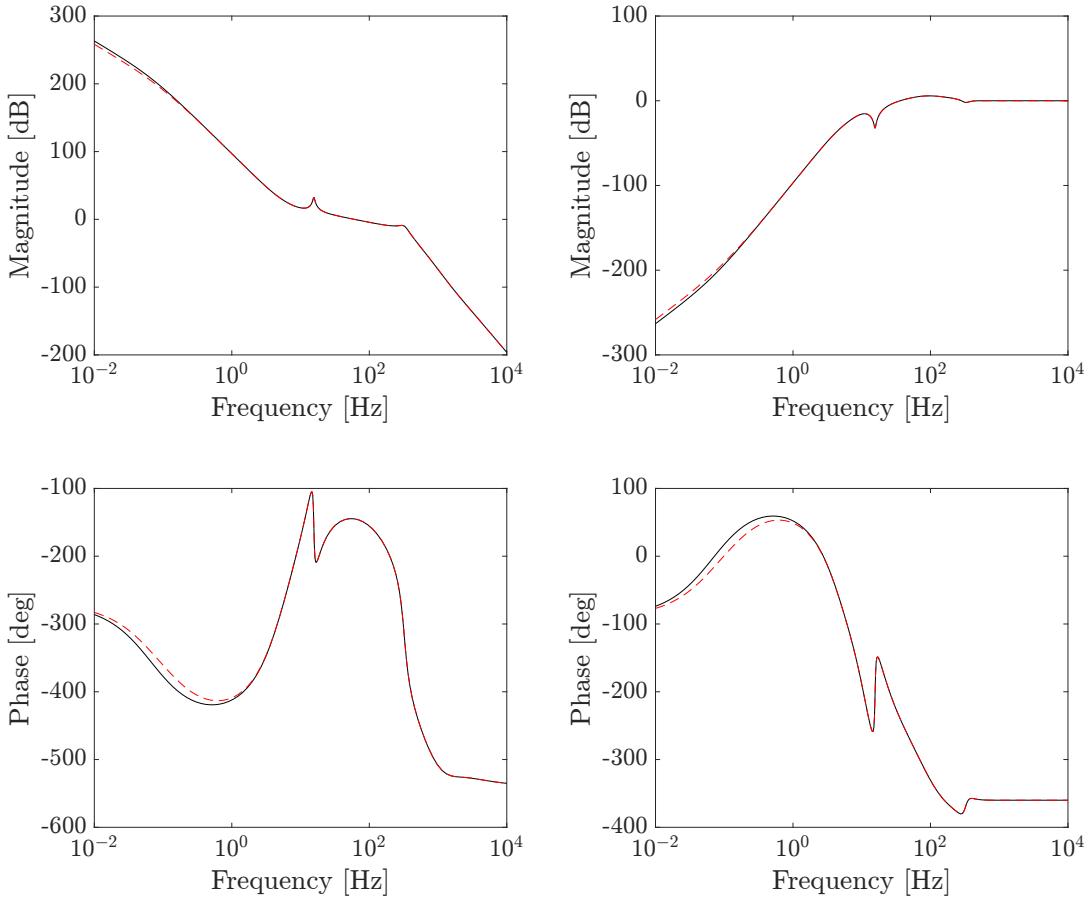

FIGURE 4.13: Loop gain (left) and sensitivity (right) of non-minimal $\mathcal{L}_1$ controller (solid) and minimal one (red dashed).

Apparently, the state space representation of the external reference dynamics from (4.172) is a non-minimal realization, where only the pair $(\check{A}_{11} - \check{B}_1 k_1^{\mathrm{T}}, \check{B}_1)$ is controllable. Thus, the transfer function from the adaptive control input u_{ad} to the tracking error output reads

$$y_e(s) = \check{C}(sI - \check{A}_{11} + \check{B}_1 k_1^{\mathrm{T}})^{-1}\check{B}_1 u_{ad}(s) = H_{ym}(s)u_{ad}(s). \tag{4.311}$$

By virtue of that fact, and the additional fact that we are only interested in tracking the output error dynamics, one could argue that it would be sufficient to only utilize a minimal state space realization of $H_{ym}(s)$ for the realization of the output predictor, as suggested in [68].

This, in fact, would contribute to a significant reduction of order 8 of the controller, to order 2. Note, however, that for the computation of the control law not only the transfer function from u_{ad} to y_e is needed, but also the one from Δ to y_e. Since the

latter one is different for the non-minimal and the minimal realization, the usage of the minimal state space realization within the output predictor would be technically incorrect with the aspired augmentation approach and the lines of proof presented above.
However, the frequency domain analysis presented in Figure 4.13 reveals that there is almost no difference between the two approaches. The non-minimal realization approach exhibits a little more gain in the low frequency range, below $0.3\,\mathrm{Hz}$. For frequencies greater than $0.3\,\mathrm{Hz}$ the frequency characteristics of both controllers are identical. Notice that the small amount of extra gain is not visible in the time domain performance. Therefore, taking the minimal realization of H_{ym} is a well suited method for order reduction of the presented $\mathcal{L}_1$ output feedback controller.

Indeed, the large order of the non-minimal controller posed problems during implementation of the scheme on the Beckhoff real-time system. In fact, it was not possible to run these controllers simultaneously on all three axis at a sampling rate of $125\,\mu\mathrm{s}$. A successful implementation was only possible after exploiting the minimal realization approach. In that case, the 4-tupel $(A_m, B_m, C_m, 0)$ of the predictor is determined by a minimal realization of $H_{ym}(s)$ as in [68]. The adaptation law and control law of the $\mathcal{L}_1$ controller are then accordingly computed, based on that realization.

4.3.4 Numerical Issues

Due to the complexity of the computations involved in the $\mathcal{L}_1$ adaptive output-feedback design the controller synthesis is quite prone to numerical difficulties. For instance it was found that the computation of matrix D involved in the coordinate transformation

$$\Lambda = \begin{pmatrix} C_m \\ D\sqrt{P} \end{pmatrix} \tag{4.312}$$

is vulnerable with respect to badly conditioned matrices A_m with higher dimension. Recall that Λ is needed for the derivation of a stable adaptive law (see equation (4.176)).

Indeed, if A_m is badly conditioned the resulting solution P of the algebraic Lyapunov equation

$$A_m^T P + P A_m = -Q$$

will so too. This leads to numerical roundoff errors that, in some cases, render the resulting matrix $\sqrt{P}$ and correspondingly matrix D complex and of course also badly conditioned. In the worst case this prevents the computation of $K_\Delta(T_s)$ or a numerically robust solution for Λ^{-1} and therefore, a feasible synthesis of the $\mathcal{L}_1$ controller.

Scaling

A solution to this issue is to improve the numerical conditioning of A_m by means of appropriate scaling of the desired (external) closed loop dynamics, i.e. the first to equations in (4.172). In particular, scaling is accomplished by a diagonal similarity transformation matrix $S \in \mathbb{R}^{n_m \times n_m}$ and the change of coordinates as per $\Xi_s(t) = S\Xi$. Accordingly, the scaled dynamics reads

$$\begin{aligned} \dot{\Xi}_s(t) &= A_m^s \Xi_s(t) + B_m^s u_{ad}(t) + \Delta^s(t), \quad \Xi_s(0) = \Xi_s^0 \\ y_s(t) &= C_m^s \Xi_s(t), \end{aligned} \tag{4.313}$$

where obviously

$$A_m^s = SA_mS^{-1}, \quad B_m^s = SB_m, \quad C_m^s = C_mS^{-1}, \quad \Delta_s = S\Delta.$$

The adaptive controller is then designed with respect to the scaled dynamics and reads

$$\Sigma_{\mathcal{L}_1}^s : \begin{cases} \dot{\hat{\Xi}}_s(t) = A_m^s \hat{\Xi}_s(t) + B_m^s u_{ad}(t) + \hat{\Delta}^s(t) - v_h^s, \quad \hat{\Xi}_s(0) = \hat{\Xi}_s^0 = S\Xi_0 \\ \hat{y}_s(t) = C_m^s \hat{\Xi}_s(t) \\ u_{ad}(t) = -C(s) \dfrac{C_m^s \left(sI - A_m^s\right)^{-1}}{C_m^s \left(sI - A_m^s\right)^{-1} B_m^s} \hat{\Delta}^s(t) \\ \hat{\Delta}^s(t) = -\Phi^s(T_s)^{-1} \mu_1^s(kT_s) = K_\Delta^s(T_s)\, \tilde{y}_s(kT_s), \end{cases} \tag{4.314}$$

where Φ^s such as μ_1^s are defined as in (4.177) and (4.178) but with respect to the scaled matrices, $v_h^s = Sv_h$ is the scaled hedging signal with v_h as in (4.300) and $\tilde{y}_s(t) = \hat{y}_s(t) - y_e(t)$.

Note that the approach of scaling is legitimate because the input/output behavior of a state space realization is invariant under similarity transformation. Although the similarity transformation changes the definition of states, this fact plays a minor role in the design of the $\mathcal{L}_1$ output feedback controller since the latter is first and foremost an input/output approach. In practice, the scaling procedure turned out very useful and enabled the feasible synthesis of $\mathcal{L}_1$ output feedback controllers for reference models with higher dimension.

It is also noteworthy that for the proper initialization of the output predictor the initial conditions must also be scaled correctly in order to avoid peaking phenomena of the controller.

4.3.5 LTI-Equivalent Architectures

Due to the equivalence of the $\mathcal{L}_1$ controller with LTI controllers, implementation might also be done in terms of the respective LTI equivalent (see e.g. [108]).

We note that due to the close connection of $\mathcal{L}_1$ adaptive control to disturbance observer architectures (see [69, 108]) it is very probable that similar performance might be obtained with a single DAC controller and a disturbance model made up of three integrators. The parameterization of this controller for obtaining similar performance will possibly be more demanding since it is not aided by design as in $\mathcal{L}_1$ adaptive control.

Chapter 5

Experiments

To demonstrate the effectiveness of the proposed control scheme, in this section we present experimental results obtained from measurements conducted at the PPS1405 platform. First, Section 5.1 is dedicated to introducing the considered reference trajectories and performance indexes for the assessment of controller performance. Second, in Section 5.2 we briefly comment on existing controllers and compare them with the proposed schemes in Section 5.3. Finally, we verify the robustness of the proposed schemes to parametric uncertainty and unforeseen saturations of the control input.

5.1 Trajectories and Performance Indexes

For the assessment of controller performance two standard path geometries in motion control are considered, namely line segments and circles.

The geometry of circles is of course simply obtained by respectively applying sine and cosine functions with equal amplitude, frequency and phase to either the q_x and the q_y axes. For the generation of line segments, we consider the two motion profiles presented in Figure 5.1. That is first, a trajectory with a so-called *double S* velocity profile, also known as *bell* or *seven segments* trajectory [8], illustrated in the left column of Figure 5.1. And second, a polynomial spline trajectory, shown in the right column. In either of the two columns from top to bottom position, velocity, and acceleration are shown over time.

The *double S* trajectory is adopted because it is widely used in industrial practice. In fact it is also used in the NC/CNC trajectory generator of Tetra's commercial positioning system. Therefore, the controller should fulfill the specifications on tracking errors of less than $1\,\mu\mathrm{m}$ during transitions for these trajectories. However, although the *double S* trajectory provides acceleration profiles that are continuous, these profiles are trapezoidal in shape, and therefore exhibit non-differentiable points. This in fact leads to an undesired excitation of resonance frequencies.

However, the excitation of resonance frequencies can drastically be reduced by exploiting smoother reference trajectories as discussed in 3.3. The benefits of a smoother acceleration profile will be illustrated by the polynomial spline trajectory. Here, a simple degree 5 polynomial is used, where coefficients are computed such that boundary conditions with respect to position, velocity and acceleration are met. Please note that due to the absence of a constant velocity phase for the polynomial spline trajectory used here, this trajectory actually narrows the set of possible applications. However, this is not our point. We consider these trajectories because they are simple to compute and they demonstrate quite well the benefits of applying smoother trajectories to a motion system over less smoother ones. Of course the composition of smooth trajectories with constant velocity phases is possible and considered in references [2, 8, 89] among others.

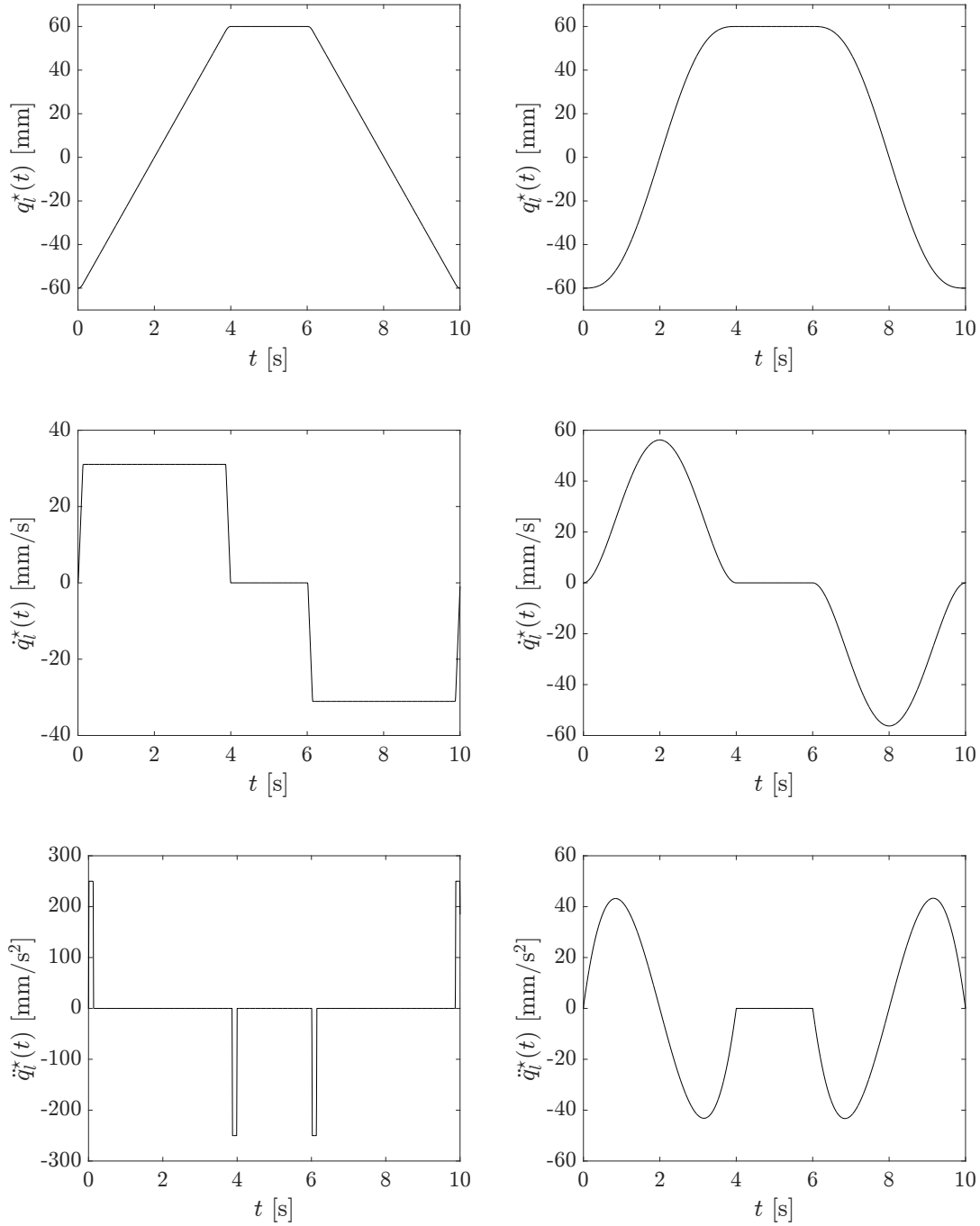

FIGURE 5.1: Point-to-point trajectories for the generation of line geometries: *double S* trajectory (left) and polynomial trajectory (right).

For the experiments the trajectories described above were used with different parameters on distance, transition time and velocity. In order to render the subsequent discussion on experiments transparent, Table 5.1 aims to classify the considered trajectories. Analogously, Table 5.2 summarizes the controllers investigated throughout the experiments. Identifiers for trajectories and controllers are introduced for the sake of clarity/discussion.

Since we experienced no considerable difference in the performance between the q_x and the q_y axis, for the sake of brevity, for trajectories A–D, controllers are validated along the q_x axis, only. Please note further that for all experiments the yaw angle q_ϕ was regulated to zero.
For comparing the performance of different controllers and expressing it in a single number, the following performance indexes are used

$$\text{RMSE} = \sqrt{\frac{1}{N}\sum_{i=1}^{N}\left(q_l^\star(i) - q_l(i)\right)^2} \tag{5.1}$$

$$\text{ISI} = \int_0^{t_f} u_l^2(t)dt. \tag{5.2}$$

The *root mean square error* (RMSE) is used for the assessment of tracking errors in individual axes and the *integral of squared input* (ISI) for the evaluation of control energy. In these equations N denotes the total number of samples in a measured data set, $q_l^\star(i)$ and $q_l(i)$ are respectively, samples of the reference trajectory and the measured output at sampling instant i, while $l \in \{x, y, \phi\}$ indexes the considered motion axis. Finally, $u_l(t)$ and t_f represent the control input and the final time of the data set. For evaluating the tracking error performance for the circular path geometry, we introduce the following performance index

$$\text{RMSE}_C = \sqrt{\frac{1}{N}\sum_{i=1}^{N}\left\|\begin{pmatrix} q_x^\star(i) - q_x(i) \\ q_y^\star(i) - q_y(i)\end{pmatrix}\right\|_2^2}, \tag{5.3}$$

representing the root mean square of the length of the tracking error vector concerning the translational motion axes.

5.2 Review of existing/former controllers

Before we begin with the discussion on measurement results for the proposed control scheme, we would like to give a brief overview on the performance of former controllers that have been implemented and tested at the testbed (see Table 5.2). To this end, consider Figure 5.2, where the tracking error (left) and the control input (right) are shown for controllers $\mathcal{C}_3$ and $\mathcal{C}_0$ performing trajectory B. Thereby, $\mathcal{C}_3$ represents a standard P-PI servo-controller with feedforward, widely used in industry and also presently in operation at Tetra and all of their planar motors. It essentially utilizes a cascaded controller setting with a PI-controller for the inner velocity loop and a P-controller for the outer position loop. However, both, feedforward and controller, are tuned by a trial and error approach by the manufacturer itself.

The second controller, controller $\mathcal{C}_0$, constitutes a well-tuned PID controller with acceleration feedforward presented in [12, 142]. This controller exploits a *generalized*

identifier	geometry	type	number of moving axes	parameter	
A	line	*double S*	1 (q_x)	distance	$20\,\mathrm{mm}$
				transition time	$2\,\mathrm{s}$
				velocity	$10\,\mathrm{mm/s}$
B	line	*double S*	1 (q_x)	distance	$120\,\mathrm{mm}$
				transition time	$4\,\mathrm{s}$
				velocity	$31\,\mathrm{mm/s}$
C	line	polynomial	1 (q_x)	distance	$20\,\mathrm{mm}$
				transition time	$2\,\mathrm{s}$
				max. velocity	$19\,\mathrm{mm/s}$
D	line	polynomial	1 (q_x)	distance	$120\,\mathrm{mm}$
				transition time	$4\,\mathrm{s}$
				max. velocity	$56\,\mathrm{mm/s}$
E	circle	sine/cosine	2 (q_x, q_y)	radius	$1\,\mu\mathrm{m}$
				velocity	$0.6\,\mu\mathrm{m/s}$

TABLE 5.1: Classification of reference trajectories used throughout the experiments.

identifier	controller
$\mathcal{C}_0$	PID with GESO [12]
$\mathcal{C}_1$	proposed nominal/baseline controller
$\mathcal{C}_2$	proposed $\mathcal{L}_1$ augmentation
$\mathcal{C}_3$	industrial P-PI servo-controller

TABLE 5.2: Classification of Controllers used throughout experiments

extended state observer (GESO) for the estimation of velocities and disturbances, while the latter estimates are used for a direct rejection of disturbances. $\mathcal{C}_0$ is basically derived as a *computed torque* controller, where tuning of controller gains is achieved by pole placement methods. It is important to notice that the design of $\mathcal{C}_0$ only uses the rigid body dynamics of the mover. Compliance and vibration of the stator is interpreted as an external disturbance and compensated for by the disturbance observer. The disturbance model of the observer is essentially a single integrator.

Despite the presence of integral action in $\mathcal{C}_3$, during transitions it shows large tracking errors of more than $\pm 15\,\mu\mathrm{m}$. Apparently, this tracking error is way beyond the specification of $1\,\mu\mathrm{m}$ and therefore absolutely unacceptable. Additionally, at the stop of the motion on the interval $t \in [4, 6]$ it shows large settling times which is also undesirable.

The bad performance is mainly attributed to the trial and error approach for tuning of the controller. This becomes also evident if one compares the control efforts of controllers $\mathcal{C}_3$ and $\mathcal{C}_0$. Indeed, $\mathcal{C}_0$ with analytically designed feedforward and feedback controller needs approximately $25\,\%$ less control effort in the acceleration and deceleration phases than $\mathcal{C}_3$ which indicates that the feedforward controller of $\mathcal{C}_3$ is not appropriate.

However, compared to $\mathcal{C}_3$ controller $\mathcal{C}_0$ shows a vital improvement of tracking performance. As illustrated in the left bottom plot of Figure 5.2 the tracking error stays below $500\,\mathrm{nm}$ during the constant velocity phases of the *double S* trajectories. However, in the acceleration and deceleration phases the tracking error reaches peak values of

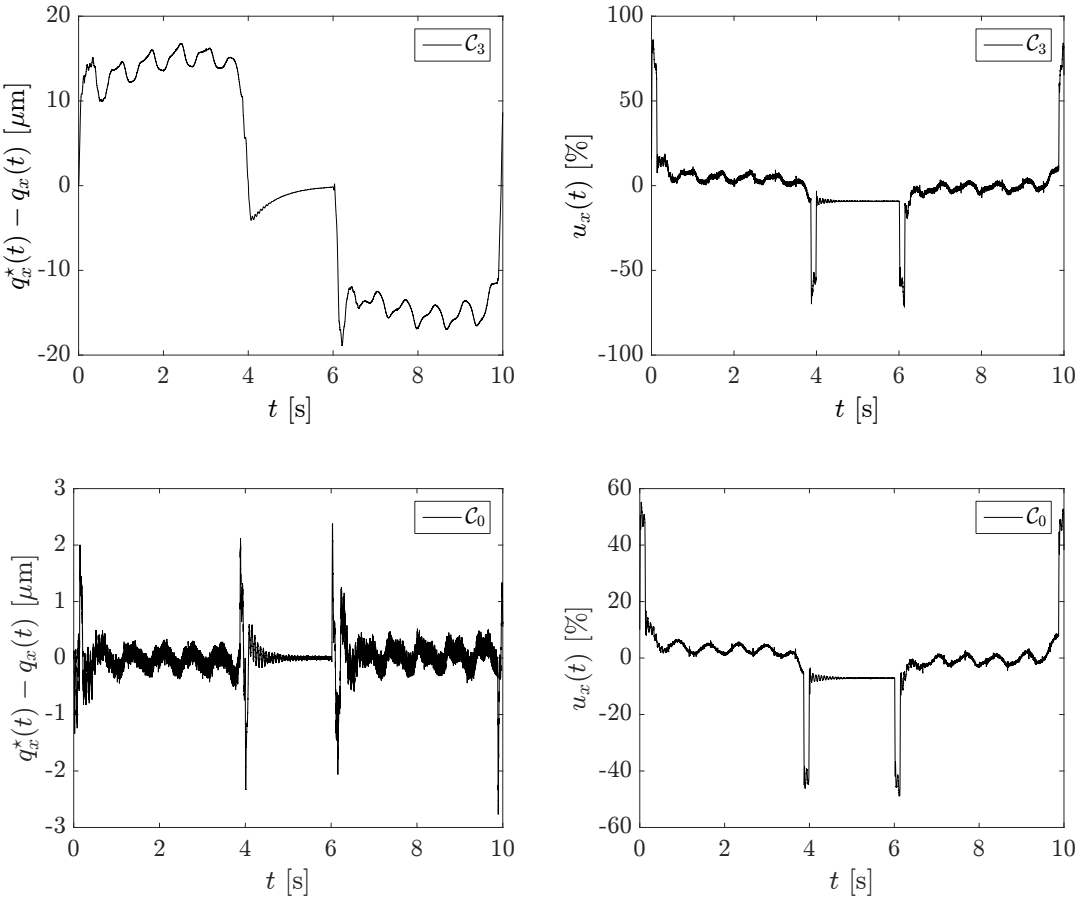

FIGURE 5.2: Tracking error (left) and control effort (right) for controllers $\mathcal{C}_3$ (top) and $\mathcal{C}_0$ (bottom) and trajectory B.

more than $2\,\mu\mathrm{m}$ which also violates the requirements on tracking errors. Large peaking in these phases has basically two reasons. First, compliance of the stator is not explicitly accounted for in the design of the feedback and the feedforward controllers. This means that essentially the acceleration of the reference trajectory is forwarded. This brings us to the second problem. Namely, the "sharp" acceleration profile of the *double S* trajectory excites resonance frequencies of the stator and gives rise to vibration and oscillations. These cannot be handled appropriately by the controller because it does not account for these effects. However, the peaking can be overcome, if the smoother polynomial trajectory is applied.

This fact is illustrated by Figure 5.3, where controller tracking error (left) and control input (right) are shown for $\mathcal{C}_0$ performing trajectory D. Obviously, there is no peaking due to the smooth acceleration profile and the specification is met. Observe the waviness of both, the control input and the tracking error signal, indicating the presence of external disturbances, discussed in section 3.1.5.

Although the performance of $\mathcal{C}_0$ seems quite promising the inability of tracking *double S* trajectories within the specified tracking error bounds is unacceptable. Moreover, it was experienced that despite the implementation of an anti windup mechanism, namely, the back calculation method of [6], the controller is very sensitive to even short period saturations of the control input rendering the closed loop system unstable.

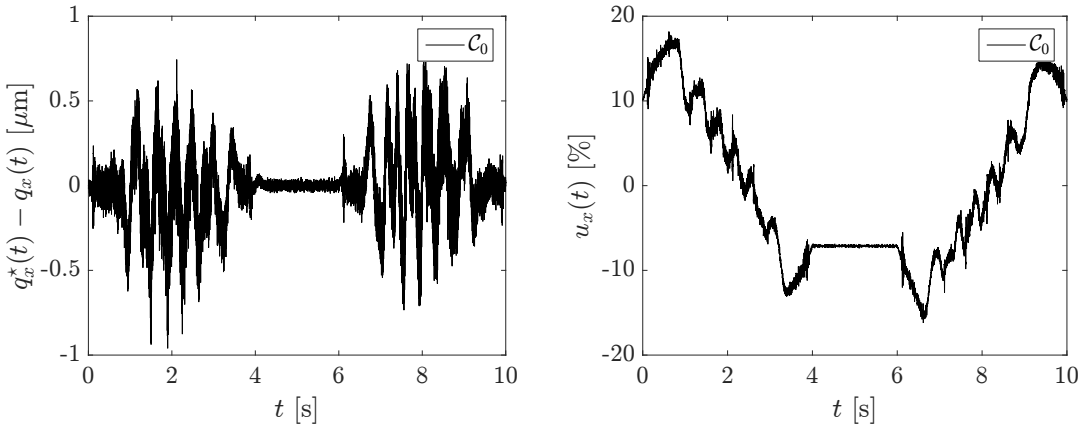

FIGURE 5.3: Tracking error (left) and control effort (right) for controller $\mathcal{C}_0$ and trajectory D.

All these facts motivated the work for the proposed control scheme.

5.3 Evaluation of the proposed control scheme

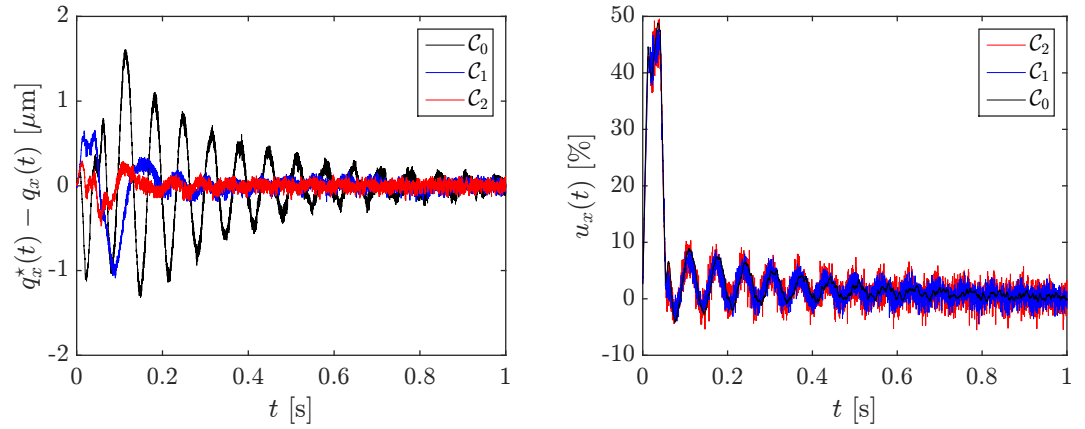

FIGURE 5.4: Close up of tracking errors (left) and control inputs (right) for controllers $\mathcal{C}_0$, $\mathcal{C}_1$, $\mathcal{C}_2$ on axes q_x and trajectory A.

Figures 5.4 and 5.5 present the measurement results for controllers $\mathcal{C}_0$, $\mathcal{C}_1$ and $\mathcal{C}_2$, performing trajectory A (see Tables 5.1 and 5.2). In order to get an intuition for the parasitic coupling between individual axes, in Figure 5.5 the tracking errors and control efforts are shown for the moving axes q_x and for the non-moving axes, i.e. q_y and q_ϕ, also. The respective performance indexes are provided by Table 5.3. When observing first the top row of Figure 5.5 and its zoomed representation in Figure 5.4, it is clearly visible that controllers $\mathcal{C}_1$ and $\mathcal{C}_2$ outperform controller $\mathcal{C}_0$. Indeed, due to the consideration of the elasticity of the stator within feedforward and feedback design, controllers $\mathcal{C}_1$ and $\mathcal{C}_2$ can nearly completely suppress the oscillations in the tracking error. This leads to a massive reduction of absolute peak values of the tracking error amplitude from initially $1.6\,\mu\mathrm{m}$ for $\mathcal{C}_0$, over $1.1\,\mu\mathrm{m}$ for $\mathcal{C}_1$, down to less than $500\,\mathrm{nm}$ for $\mathcal{C}_2$. The improvement

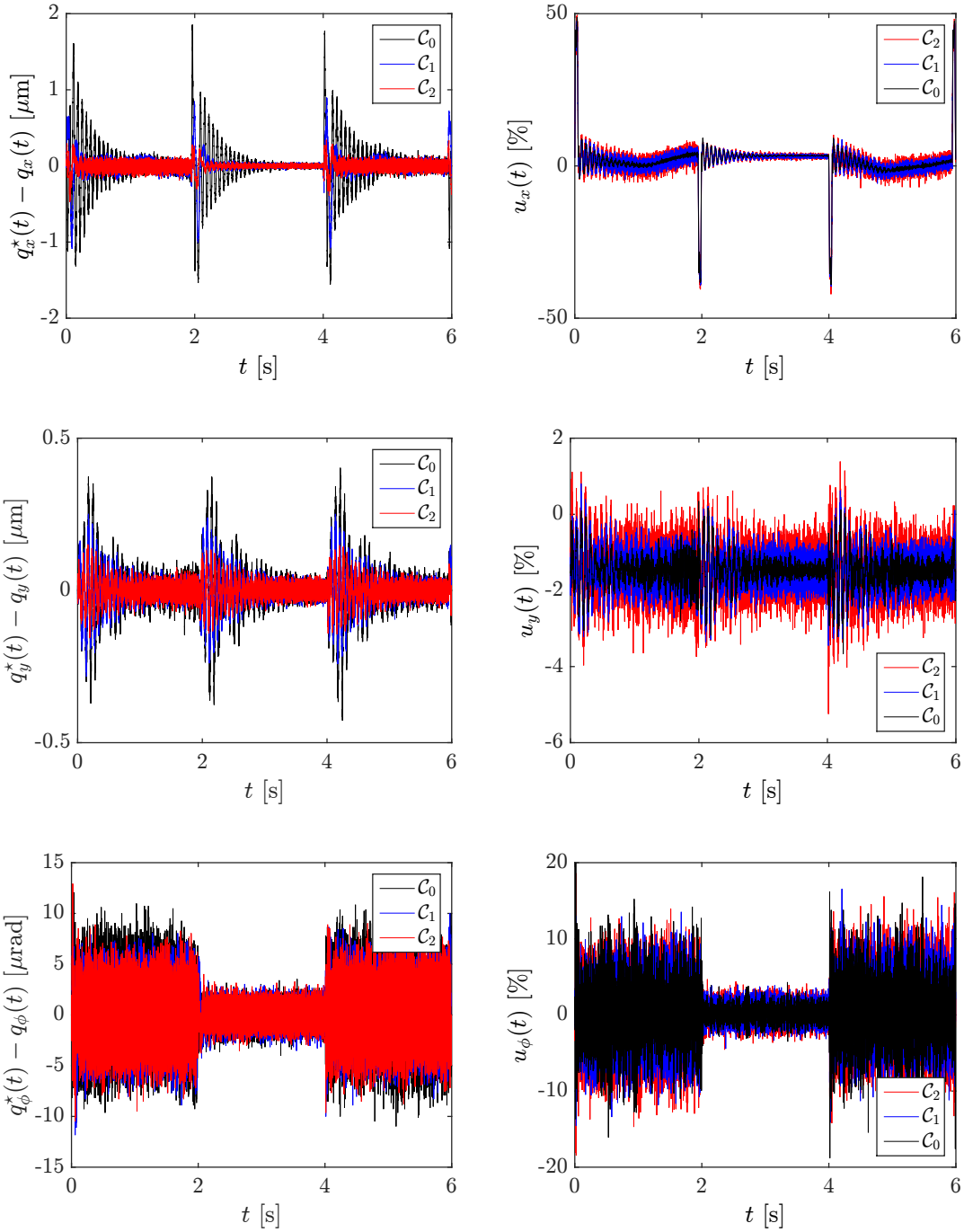

FIGURE 5.5: Tracking errors (left) and control inputs (right) for controllers $\mathcal{C}_0, \mathcal{C}_1, \mathcal{C}_2$ on axes q_x, q_y, q_ϕ (top to bottom) and trajectory A.

axis	performance index	$\mathcal{C}_0$	$\mathcal{C}_1$	$\mathcal{C}_2$
q_x	RMSE [mm]	3.1197×10^{-4}	1.6046×10^{-4}	6.2251×10^{-5}
	ISI	282.0529	268.4826	272.3659
q_y	RMSE [mm]	8.6574×10^{-5}	5.8664×10^{-5}	3.5015×10^{-5}
	ISI	14.1965	14.4539	15.2768
q_ϕ	RMSE [mrad]	2.896×10^{-3}	2.2786×10^{-3}	2.2671×10^{-3}
	ISI	79.7721	54.2307	70.1675

TABLE 5.3: Comparison of performance indexes for controllers $\mathcal{C}_0, \mathcal{C}_1, \mathcal{C}_2$ and trajectory A.

in performance is also visible in the RMSE values of the respective controllers summarized in Table 5.3. Controller $\mathcal{C}_2$ thus performs superior with an RMSE of $62.25\,\mathrm{nm}$. It meets the specification on the tracking error bound with a headroom of $500\,\mathrm{nm}$ which is excellent for these trajectories. Furthermore, through controllers $\mathcal{C}_1$ and $\mathcal{C}_2$ the settling time is more than halved, i.e. from initially $1\,\mathrm{s}$ for $\mathcal{C}_0$ to roughly $0.4\,\mathrm{s}$ for the other two controllers.

It is interesting to notice that the effect of the feedforward controller is directly visible from the signal $u_x(t)$ of the considered controllers (see right plot in Figure 5.4). In fact, when comparing the control inputs of $\mathcal{C}_0$ with the other two controllers it can be observed that there is a slight phase shift, with $\mathcal{C}_1$ and $\mathcal{C}_2$ being slightly ahead of $\mathcal{C}_0$. Notice that the oscillating behavior of $\mathcal{C}_0$, trying to compensate for the vibration, stems from a disturbance estimate of the observer. In the case of the remaining controllers, it mainly results from the feedforward controller and the solution of the internal dynamics. It is exactly this contribution of the feedforward controller that makes the difference and leads to an enormous improvement of tracking error performance. Please note that the peaks of the position errors of controllers $\mathcal{C}_1$ and $\mathcal{C}_2$ on $t \in [0, 0.2]$ are due to the mismatch between the feedforward controller and the high frequency unmodeled plant dynamics.

Apparently, the augmentation approach works as expected and supports the nominal controller, i.e. $\mathcal{C}_1$, with its superior disturbance rejection capabilities. However, this comes to the expense of a higher control effort and higher noise levels. This fact is expressed by the ISI value which shows this clear tendency. Namely, for almost all experiments (see Tables 5.3–5.6) $\mathcal{C}_2$ exhibits the highest control effort. Though, this is not surprising because $\mathcal{C}_2$ has the best disturbance rejection and this must somehow appear in the control effort. In view of the tracking error performance, however, the extra control effort is tolerable.

The tracking errors for the q_y and q_ϕ axis depicted in Figure 5.5 imply that there exists parasitic coupling between axes. However, this coupling has been experienced moderate, not interfering with the time domain specification on tracking errors. Typically, for the considered trajectories peak values are mostly far below $500\,\mathrm{nm}$. From Figure 5.5 it is evident, that controllers $\mathcal{C}_1$ and $\mathcal{C}_2$ have the ability to drastically reduce coupling effects in the q_y axis as compared to $\mathcal{C}_0$. This holds also for trajectories B–D as is verified by Tables 5.3–5.6.

On the other hand, the performance in regulating q_ϕ to zero is for all three controllers almost identical. And this, regardless of the trajectories considered in this experiment.

This observation is also supported by the performance indexes provided by Tables 5.3–5.6.

Since the couplings play a minor role, for the sake of brevity we omit the visual presentation of measurement results for q_y and q_ϕ and focus on the tracking errors of the moving axes only. Despite this fact, for the sake of completeness the performance indexes are presented for all axes in Tables 5.3–5.6. Moreover, for the reminder of this text we focus on the proposed schemes, namely, controllers $\mathcal{C}_1$ and $\mathcal{C}_2$

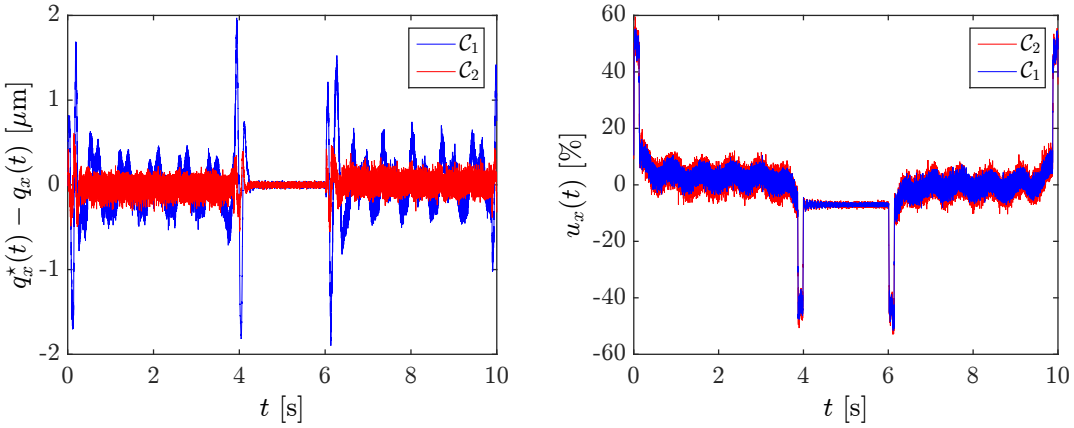

FIGURE 5.6: Tracking error (left) and control input (right) for controllers $\mathcal{C}_1, \mathcal{C}_2$ on axis q_x and trajectory B.

axis	performance index	$\mathcal{C}_0$	$\mathcal{C}_1$	$\mathcal{C}_2$
q_x	RMSE [mm]	3.2803×10^{-4}	3.4443×10^{-4}	9.5515×10^{-5}
	ISI	1238.8974	1464.3642	1281.4423
q_y	RMSE [mm]	7.9065×10^{-5}	3.8078×10^{-5}	3.8623×10^{-5}
	ISI	24.1104	24.5224	28.8721
q_ϕ	RMSE [mrad]	3.0154×10^{-3}	2.0663×10^{-3}	2.2335×10^{-3}
	ISI	81.5725	63.2649	83.7169

TABLE 5.4: Comparison of performance indexes for controllers $\mathcal{C}_0, \mathcal{C}_1, \mathcal{C}_2$ and trajectory B.

Let us next observe the measurement results of controllers $\mathcal{C}_1$ and $\mathcal{C}_2$ for trajectory B, illustrated in Figure 5.6. Trajectory B constitutes the long range version of trajectory A and is therefore more difficult to handle. This is due to the following reasons. First, long range implies that the amount of external disturbances is greater than for trajectory A. And second, for performing the tracking task in a specified transition time of 4 seconds, this means that compared to case A the velocity must be tripled. This in fact, implies that the frequency of position dependent and periodic disturbances increases which is obviously more demanding for the controller. These difficulties are evident when the tracking error performance of the nominal controller $\mathcal{C}_1$ is considered (cf. Figure 5.6). With peak values in the range of approximately $\pm 2\,\mu\text{m}$ it does not fulfill the tracking error specification. However, the $\mathcal{L}_1$ augmentation recovers a feasible amount

of the nominal performance as expected. With peak values in the error amplitude of $600\,\mathrm{nm}$ it almost reaches the same values as in the case of trajectory A. It thus meets the desired specifications. Again, the waviness of the control signal indicates the presence of external periodic disturbances that are handled very well by $\mathcal{C}_2$. With an RMSE value of $95.52\,\mathrm{nm}$ controller $\mathcal{C}_2$ performs best and as discussed previously it shows the highest control effort (see Table 5.4).

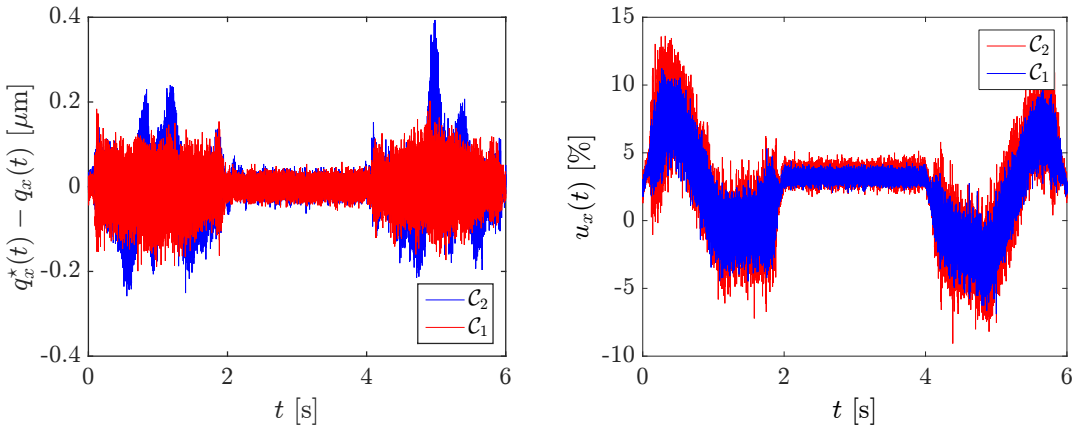

FIGURE 5.7: Tracking error (left) and control input (right) for controllers $\mathcal{C}_1, \mathcal{C}_2$ on axis q_x and trajectory C.

axis	performance index	$\mathcal{C}_0$	$\mathcal{C}_1$	$\mathcal{C}_2$
q_x	RMSE [mm]	5.3673×10^{-5}	6.1418×10^{-5}	3.9038×10^{-5}
	ISI	81.4335	81.2397	100.9913
q_y	RMSE [mm]	3.5752×10^{-5}	1.956×10^{-5}	2.3816×10^{-5}
	ISI	14.1255	14.7508	17.7708
q_ϕ	RMSE [mrad]	3.0663×10^{-3}	2.2578×10^{-3}	2.2655×10^{-3}
	ISI	135.0763	67.8526	92.4012

TABLE 5.5: Comparison of performance indexes for controllers $\mathcal{C}_0, \mathcal{C}_1, \mathcal{C}_2$ and trajectory C.

Although not shown visually, it is evident from Table 5.4 that coupling effects with respect to q_y are reduced with $\mathcal{C}_1$ and $\mathcal{C}_2$ as compared to controller $\mathcal{C}_0$.
Indeed, the RMSE value of $\mathcal{C}_0$ is halved by $\mathcal{C}_1$ and $\mathcal{C}_2$. Essentially, the latter two controllers show similar RMSE values with slightly better values for the nominal controller $\mathcal{C}_1$.

Trajectories C and D constitute the smoother (polynomial) counterparts of trajectories A and B. For a fair comparison the transition time is the same as in cases A and B. Exploiting these trajectories heavily reduces peaking in the acceleration and deceleration phases (see Figures 5.7 and 5.8). For the short trajectory C, the peak amplitudes of the tracking error yield values below $200\,\mathrm{nm}$ for $\mathcal{C}_2$ and less then $400\,\mathrm{nm}$ for $\mathcal{C}_1$ which is a further improvement with respect to trajectory A. This is also supported by the RMSE

axis	performance index	$\mathcal{C}_0$	$\mathcal{C}_1$	$\mathcal{C}_2$
q_x	RMSE [mm]	1.9091×10^{-4}	3.4835×10^{-4}	9.3107×10^{-5}
	ISI	849.2844	850.8693	1097.8471
q_y	RMSE [mm]	1.3685×10^{-4}	5.2035×10^{-5}	6.2465×10^{-5}
	ISI	49.5312	23.3557	43.7269
q_ϕ	RMSE [mrad]	3.1422×10^{-3}	2.2725×10^{-3}	2.262×10^{-3}
	ISI	163.5758	90.1709	122.6512

TABLE 5.6: Comparison of performance indexes for controllers $\mathcal{C}_0, \mathcal{C}_1, \mathcal{C}_2$ and trajectory D.

values from Table 5.5 which are far below the RMSE values of 5.3. The same is true for the coupling between axes.

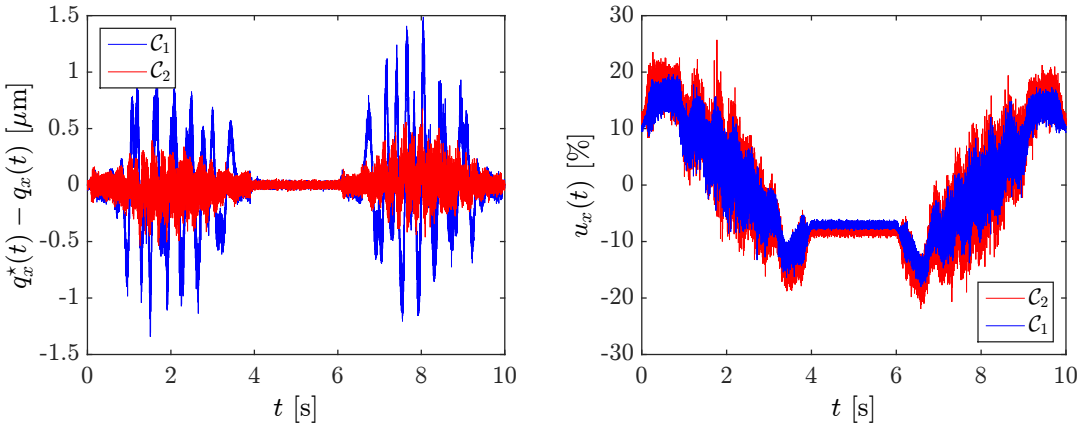

FIGURE 5.8: Tracking error (left) and control input (right) for controllers $\mathcal{C}_1, \mathcal{C}_2$ on axis q_x and trajectory D.

Also for the long range motion peaking is reduced. However, by virtue of the fact that the polynomial trajectory has a velocity hump instead of a constant velocity phase, the smoother acceleration profile requires a higher velocity for accomplishing the tracking task in the same amount of time (cf. velocities of trajectories B and D in Table 5.1). Therefore, position dependent, periodic disturbances appear at higher and even changing frequencies which renders the compensation of those disturbances even more challenging. This eventually results in an RMSE value of $348.35\,\mathrm{nm}$ for $\mathcal{C}_1$ which compared to a value of $344.43\,\mathrm{nm}$ is slightly worse then for trajectory B. On the other hand, controller $\mathcal{C}_2$ shows a slightly better performance with an RMSE value of $93.12\,\mathrm{nm}$ versus $95.52\,\mathrm{nm}$ for trajectory B. From that observation it can be concluded that a good reference trajectory should have a suitable amount of smoothness and should ideally exhibit a constant velocity phase.

Additionally, with regard to Tables 5.4 and 5.6 we recognize that the performance indexes for rating the control effort in the moving axes (q_x) are throughout better for trajectory D than for trajectory B. However, the RMSE values for the q_y axis are worse

for trajectory D than for trajectory B which indicates a larger amount of coupling between the translational axes. This issue is also attributed to the velocity hump and a higher amplitude in velocity.

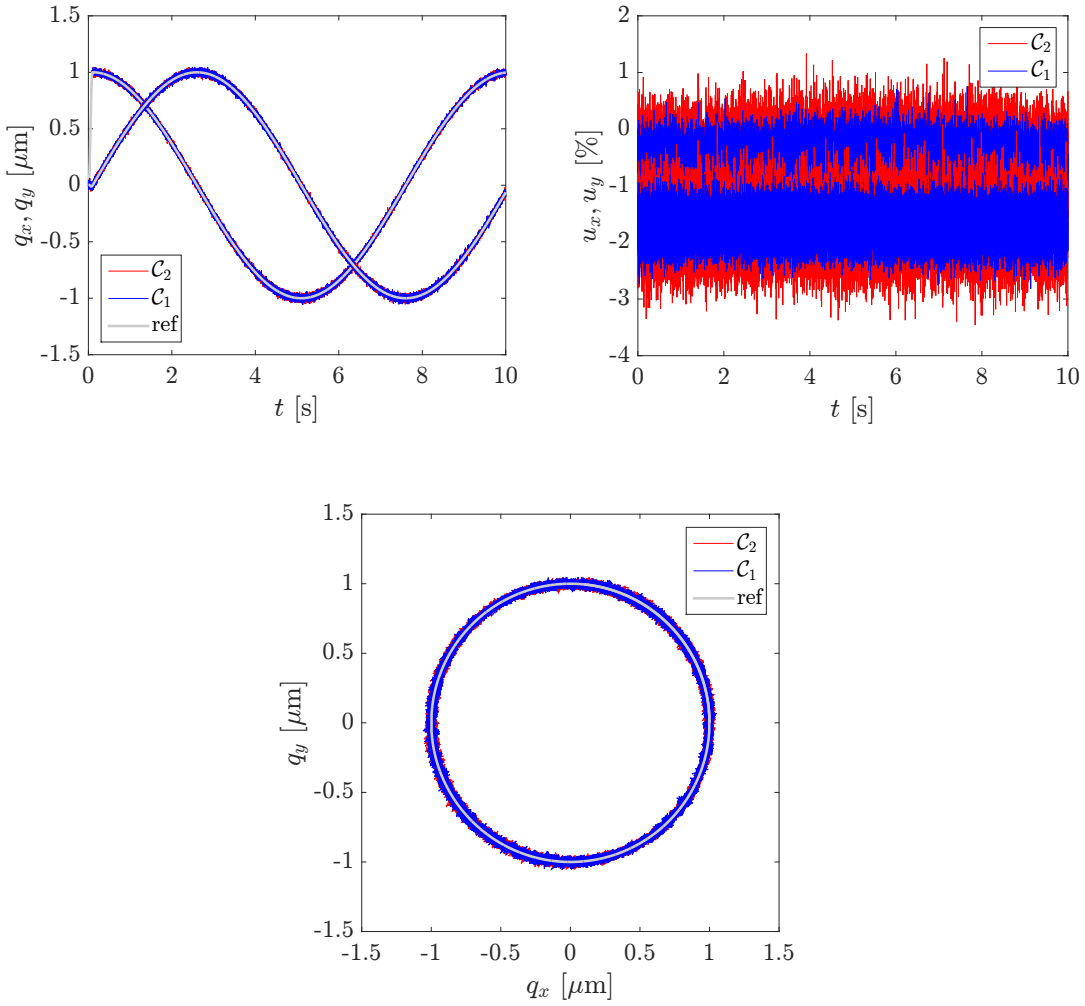

FIGURE 5.9: Reference signals, controlled variables (top left) and control inputs (top right) for controllers $\mathcal{C}_1$, $\mathcal{C}_2$ and trajectory E with dedicated q_x, q_y–plot (bottom).

Finally, Figure 5.9 presents the measurement results of $\mathcal{C}_1$ and $\mathcal{C}_2$ performing a circular path, i.e. trajectory E. Both controllers track the sinusoidal references very well and exhibit a similar performance with RMSE_C values of $21.37\,\text{nm}$ for $\mathcal{C}_1$ and $21.31\,\text{nm}$ for $\mathcal{C}_2$. Please note that the noise amplitude of the tracking errors has a value of approximately $50\,\text{nm}$ which is not shown here. It is remarkable that, although the control inputs seem very noisy and no distinct sinusoidal relationship is visible, the references are tracked very well.

5.4 Proposed Control Scheme in the Presence of Uncertainty

5.4.1 Parametric Uncertainty

In order to validate the functionality of the proposed control scheme in the presence of parametric uncertainties, the following experiment was conducted. For the purpose of virtually applying parametric uncertainties, we designed the nominal controller and the $\mathcal{L}_1$ augmentation on the nominal plant model whose parameters inside the A and B matrices were altered by a fixed percentage. This controller was than applied to the real process and the response was measured. On a random basis, we conducted this experiment for trajectory C. For the sake of simplicity, all parameters inside A and B were altered simultaneously, where a fixed percentage of each individual parameter inside these matrices was added or subtracted to the parameter itself. This was done for $\pm 10\,\% \ldots \pm 50\,\%$.

By virtue of the fact that there were only little changes in tracking errors for these percentages, for the sake of brevity, only the measurement for $\pm 50\,\%$ is provided in Figure 5.10. Obviously, both controllers react extremely robust to the parametric uncertainties and fulfill the tracking error specification for trajectory C. It is remarkable that, while there is a visible difference between the tracking error responses of the nominal controller $\mathcal{C}_1$ and the cases of $+50\%$ and -50% uncertainty, there is almost no noticeable difference for the $\mathcal{L}_1$ augmentation. It can thus be concluded that the $\mathcal{L}_1$ controller recovers the nominal performance as expected. However, we should not be illusioned by the superior performance of $\mathcal{C}_2$. Indeed, from a robust stability point of view, it is clear that $\mathcal{C}_1$ will react more robust against parametric uncertainties then $\mathcal{C}_2$. This is evident from the frequency response characteristics, i.e. the phase and gain margins, of the respective controllers (see Figure 4.11) and constitutes the natural robustness/performance trade-off that holds for all feedback controlled systems. With this design, however, a satisfactory trade-off has been found.

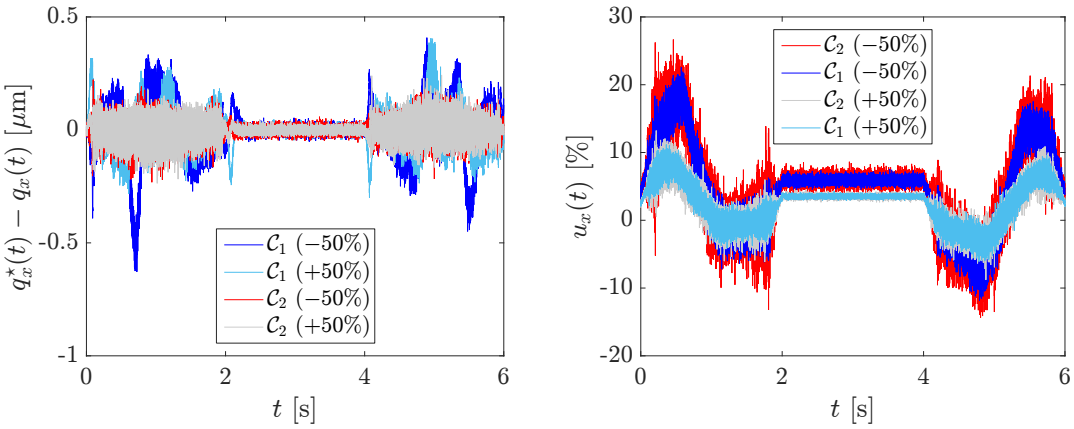

FIGURE 5.10: Tracking errors (left) and control inputs (right) for controllers $\mathcal{C}_1$ and $\mathcal{C}_2$ for $\pm 50\,\%$ additive parametric uncertainty on parameters inside the A and B matrices of the generic axis model.

5.4.2 Unexpected Uncertainty

Finally, in the course of practical validation of the proposed scheme, we consider the robustness of the controller with respect to unexpected changes such as an unexpected

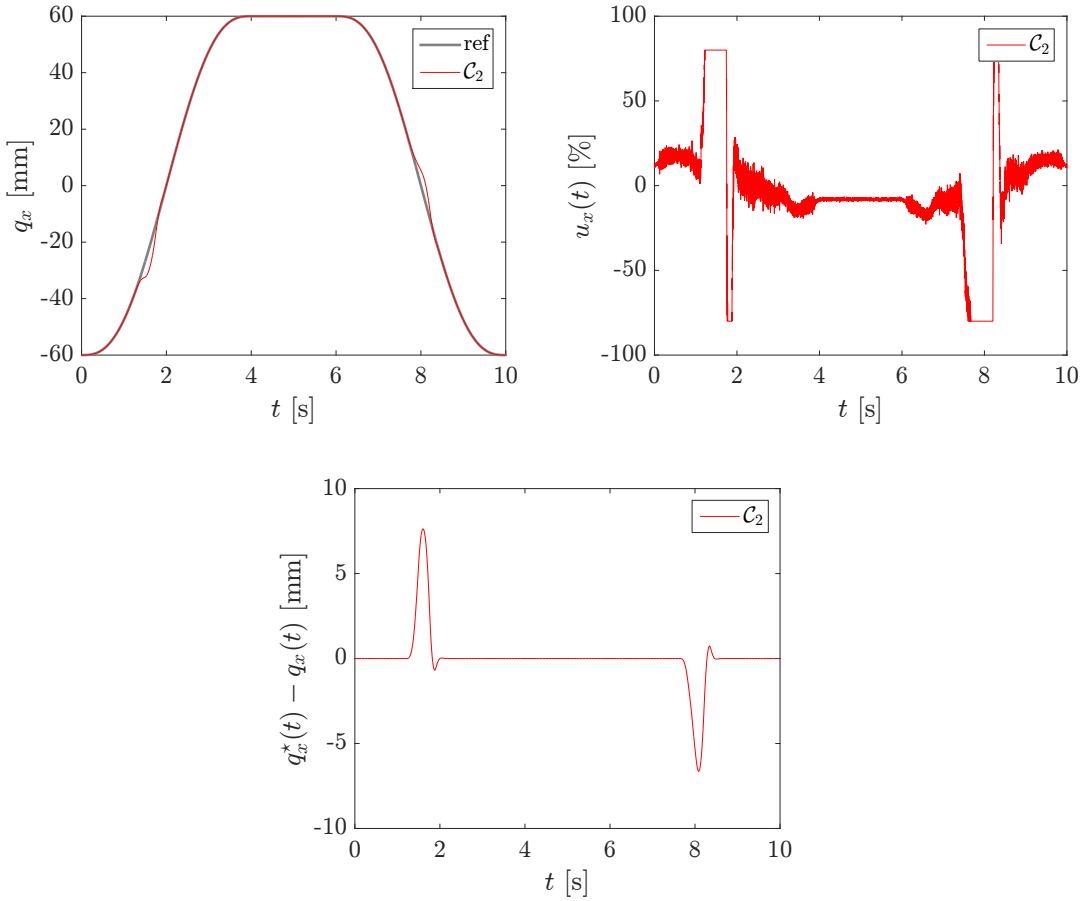

FIGURE 5.11: Experimental validation of PCH-approach.

blocking of the mover or the appearance of external forces that cause the control input to saturate. For a save operation and a prevention of possible damages of the positioning stage, the controller must be capable of robustly recovering from those disturbances. For investigating this issue, the controller was blocked manually during tracking of trajectory D. The results of this experiment are illustrated in Figure 5.11. Blocking the mover on the time intervals $t \in [1, 2]$ s and roughly $t \in [7, 9]$ s, apparently leads to a saturation of the control input as shown in the top right plot of Figure 5.11. Due to the proposed anti windup modifications including PCH, windup of the overall controller is prevented. Moreover, it has been observed throughout the experiments that the controller was able to completely recover and pickup normal operation shortly after the blocking was removed. The proposed scheme thus performs as expected.

Please note that during this experiment controller $\mathcal{C}_0$ went unstable shortly after the first blocking was removed. As compared to this, the proposed scheme performs extremely robust.

5.5 Evaluation of Achievements

Eventually, from the discussions above we can conclude the following. Firstly, the incorporation of stator elasticities within the stage of nominal feedforward and feedback controller design has paid off. This is especially visible for the *double S* trajectories A

and B. Here, controller $\mathcal{C}_2$ achieves a massive improvement over $\mathcal{C}_0$. In particular, for trajectories A and B, the RMSE shows an improvement of about $80\,\%$ and $70\,\%$, respectively (see Tables 5.3 and 5.4). The improvement for the smoother trajectories C and D is less with about $27\,\%$ and $51\,\%$, but still considerable. Hence, in terms of tracking error, controller $\mathcal{C}_2$ performs best. This behavior is not surprising and may be attributed to the high loop gain in the low frequency range which, roughly speaking, is provided by three (approximate) integrators. That is, two from the augmented baseline controller $\mathcal{C}_1$ and one from the $\mathcal{L}_1$ controller itself. Since the $\mathcal{L}_1$ controller is LTI, also other LTI architectures may obtain similar performance (see Sections 4.2.2 and 4.3.5).

The enhanced disturbance rejection capability, though, comes at the expense of control effort. In the worst case, the control energy of $\mathcal{C}_2$ deteriorates by about $29\,\%$ with respect to that of $\mathcal{C}_0$ (see Table 5.6). This is an inherent problem of the fast adaptation loop that can only be addressed by proper filter design. However, the improvements in tracking errors, even in the presence of a considerable amount of parametric uncertainty, justify the higher control efforts.

Finally, Figure 5.12 illustrates the achievements of this work. It compares the tracking performance of the motion controller $\mathcal{C}_3$ that is presently in operation with the advanced design proposed in this work.

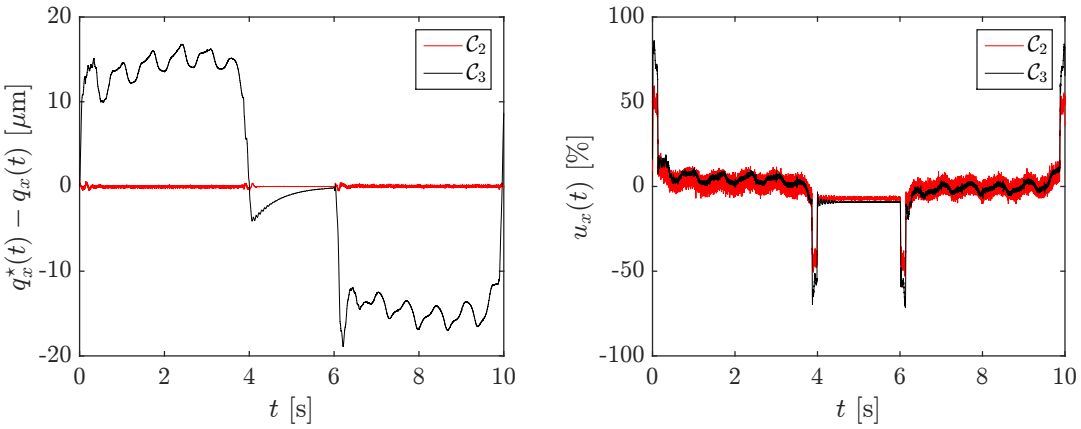

FIGURE 5.12: Tracking error (left) and control effort (right) for controllers $\mathcal{C}_2$, $\mathcal{C}_3$ and trajectory B.

Chapter 6

Conclusion

6.1 Conclusions

This dissertation investigates modeling and robust adaptive tracking control of a planar precision positioning system.

Driven by economic needs, the developed motion control concept is based on a combination of a model-based nominal controller and an $\mathcal{L}_1$ adaptive augmentation.

The starting point of the model-based control design is the development of a detailed model. At this stage we derive and identify models for the mathematical description of sensors, actuators, permanent magnet arrays, mover/stator interaction and external disturbances. A comparison of the overall model with experimental data shows an excellent agreement. The model captures all the relevant dynamics and thus serves well for the design and assessment of controllers.

Based on that model, we next investigate the stage of nominal control design. The nominal controller essentially comprises a feedforward and an output feedback controller. Core of the output feedback controller is a composite state and disturbance observer based on *disturbance accommodating control*, exploiting internal model principle ideas. The nominal part of the proposed architecture thus addresses the aspired goals of trajectory tracking, the capability of a priori parameterization and basic disturbance rejection. For obtaining good stability margins and a sufficient suppression of structural vibration, tuning of the controller is performed in both, the time, and frequency domain, based on systematic LQR/LQG design methods.

For pursuing the goal of parameter adaptation, $\mathcal{L}_1$ adaptive tracking schemes for the cases of full-state and output feedback are derived. The initial motives for the choice of $\mathcal{L}_1$ adaptive control were the promising properties of decoupling of the adaption from the control loop, a priori computable transient and steady state performance bounds and an intuitive performance/robustness trade-off via the choice of an appropriate low-pass filter. Moreover, the philosophy of posing a feasible control goal, while respecting the available bandwidth of the control channel is appealing in view of unmodeled dynamics.

Thereby, the respective $\mathcal{L}_1$ adaptive controllers are designed for the augmentation of the nominal control loop. So, any deviation from the nominal behavior may be identified and compensated for by the adaptive controller. The latter thus serves for recovering nominal performance even in the presence of parametric uncertainties.

Unfortunately, with regard to our application, not all expectations with respect to $\mathcal{L}_1$ adaptive control could be met. Specifically, it was found that the filter design, even though it appears simple in the first moment, is anything but trivial. Indeed, for the state feedback case, it is impossible to find a filter that both, fulfills the $\mathcal{L}_1$ norm stability condition and respects the bandwidth of the virtual actuator dynamics. After some

simulations and engineering intuition, finally, a filter could be designed such that the closed loop adaptive system was stable and delivered the expected performance.

Due to the conservatism of the $\mathcal{L}_1$ norm, sufficient stability condition, we are not able to derive bounds on tolerable intervals of parametric uncertainty for the motion stage system. In view of the theoretical effort this is an unsatisfactory result.

In the case of the presented $\mathcal{L}_1$ adaptive output feedback controller with piecewise constant adaptation law, we circumvented this problem by exploiting the LTI nature of the scheme. Using classical loop shaping ideas, the filter is designed in the frequency domain, for meeting minimum requirements concerning the amplification of measurement noise and for obtaining adequate stability margins. Thereby, the limiting factor for the choice of filter bandwidth and hence, the achievable performance, is essentially determined by the high frequency dynamics encountered at the plant.

The effect of the proposed $\mathcal{L}_1$ controller on the disturbance rejection properties of the overall closed loop system may also very well be observed in the frequency domain. This shows that the $\mathcal{L}_1$ augmented loop in comparison to the nominal design achieves significantly higher loop gains up to about the frequency of aspired bandwidth. This corresponds to a vital improvement of disturbance rejection quality and consequently leads to a significant increase in tracking performance. The compromise one has to make is as always, performance versus robustness and performance versus control effort.

Analysis of the $\mathcal{L}_1$ output feedback scheme reveals that, in our case, it basically represents an approximation of a PID type of controller with additional roll-off filters. Due to that approximative nature it is experienced that when applied as a standalone tracking controller, even in the nominal case, the $\mathcal{L}_1$ controller suffers from steady state tracking errors. However, in view of high performance motion control applications this is unacceptable.

To avoid these effects, there are e.g. the following possibilities. First, the use of the $\mathcal{L}_1$ controller together with a controller possessing integral action, as presented here. Or second, the implementation of the ideal LTI equivalent controller derived from the ideal closed loop system. However, the latter method may pose problems with respect to the modifiability of the control architecture.

Because of the close connection of $\mathcal{L}_1$ adaptive control to disturbance observer-based approaches, it is very likely that the extension of the nominal controller by an additional integrator would have brought similar results. However, in this case the choice of controller design parameters is not clear, since it is not guided by the design approach of $\mathcal{L}_1$ adaptive control.

For the case considered in this work, $\mathcal{L}_1$ adaptive output feedback control may be seen from two perspectives. In particular, it may be seen either as an implementable control architecture or also as a design method for the computation of equivalent linear controllers.

For the transition of the developed theoretical approach into motion control practice further modifications considering actuator saturation are examined and implemented.

Finally, the developed control architecture is tested experimentally on the PPS1405 platform using typical reference trajectories. Here, the developed concept shows outstanding positioning performance. Due to the consideration of stator flexibilities within the nominal controller, the overall control scheme achieves significant improvements. Compared to existing control schemes the proposed approach achieves an improvement of RMSE of up to $80\,\%$. Furthermore, in comparison to former controllers, the proposed approach yields better suppression of parasitic couplings on non-moving axes. In all experiments the $\mathcal{L}_1$ augmented controller shows a tracking error of

less than $500\,\mathrm{nm}$, whereby the desired positioning accuracy of less than $1\,\mu\mathrm{m}$ is easily met.

Moreover, the proposed approach is evaluated experimentally for its suitability to suppress parametric uncertainty. This too shows remarkable results. In fact, for a parametric uncertainty of all parameters of $\pm 50\%$ there is no significant difference of the tracking error with respect to the nominal behavior. Eventually, also the evaluation of the pseudo-control hedging approach has been successful and shows a robust behavior of the developed scheme in the presence of actuator saturation.

6.2 Recommendations

The achievable positioning accuracy of the considered positioning system is essentially limited by the following aspects:

- resolution of measurement system
- flexibility of stator
- high frequency dynamics

These points represent important tuning facilities for the improvement of the positioning system.

With a noise amplitude of $50\,\mathrm{nm}$ of the position measurement signal and a tracking error below $200\,\mathrm{nm}$ during the constant velocity phase, the developed controller is already close to the limit of what is achievable. An increase in the sensor resolution would therefore be necessary for gaining further improvements regarding positioning accuracy.

Because of the colocated sensor/actuator pair, the flexibility of the stator poses no immediate problem for the stability of the closed loop system. However, reaction forces of the mover have a detrimental impact on the time domain behavior of the tracking error. For a reduction of these effects it is recommended to revise the construction of the stator. The simplest way of doing this is to increase the mass, stiffness and damping of the stator. Other possibilities include the exploitation of additional sensors and actuators attached to the stator for an active damping of the stator or a direct compensation of reaction forces. In recent years, also balance- or counter-masses have been used. By opposing the movement of the mover they accommodate for reaction forces.

The greatest impact on the potential bandwidth of the controller and therefore on the achievable performance emanates from the high frequency dynamics observed in our experiments. In order to improve the performance of the positioning stage it is necessary, by means of constructional methods, to shift these dynamics up into a higher frequency band. Therefore, it is recommended to identify the source of these dynamics in future work.

Finally, if higher positioning accuracy is desired the effects of parasitic coupling between axis should be taken more and more into consideration which necessitates the exploitation of advanced MIMO control design methods.

Appendix A

Electromagnetic Field Theory

A.1 Maxwell's Equations

The theoretical foundation of our modern understanding of electromagnetism is governed by a set of four elegant equations, collectively known as Maxwell's equations. Named after Scottish physicist James Clerk Maxwell, these equations provide a unified description of the whole range of electromagnetic field phenomena and expose the intimate connection between electricity and magnetism [115].

Inspired by the previous work of Micheal Faraday, André-Marie Ampère and others, Maxwell was the first to formulate a rigorous mathematical model for electricity and magnetism unifying the observations and theories of his predecessors. Owing to the fact that vector calculus was not readily developed before the late 19th century, originally his model was governed by a set of 20 coupled differential equations with 20 variables [115]. Based on his work published during the period of 1861-1864, he concluded that light must be made up of electromagnetic waves. The experimental evidence for that was given by Heinrich Hertz in 1888 [115].

Maxwell's equations in its well-known condensed form, given by

$$\nabla \times \vec{E} = -\frac{\partial \vec{B}}{\partial t} \tag{A.1}$$

$$\nabla \cdot \vec{D} = \rho \tag{A.2}$$

$$\nabla \times \vec{H} = \vec{J} + \frac{\partial \vec{D}}{\partial t} \tag{A.3}$$

$$\nabla \cdot \vec{B} = 0, \tag{A.4}$$

are due to Oliver Heaviside (1885), an ingenious self-made mathematician and independent popularizer of vector calculus [101, 115]. These equations define the divergence $(\nabla\cdot)$ and curl $(\nabla\times)$ of the electric and magnetic field quantities and thus, according to the fundamental theorem B.2.1 of vector calculus, uniquely define the respective fields. Therein $\vec{E}$, $\vec{D}$, $\vec{H}$ and $\vec{B}$ are field quantities. They denote respectively, the electric field strength, the electric flux density and likewise the magnetic field strength as well as the magnetic flux density. $\vec{J}$ and ρ are source terms representing the free current density and the free charge density, while $\partial\vec{D}/\partial t$ is the displacement current density embodying Maxwell's concept of displacement current accounting for the motion of bound charge [44].

The importance of these equations follows from the fact that they embody the whole range of electromagnetic field appearances in a compact manner and expose the symmetry between electric and magnetic fields [115].

Please note that Maxwell's equations alone do not provide a complete theory [44, 57]. Indeed, the four vector variables of the fields $\vec{E}$, $\vec{D}$, $\vec{H}$, $\vec{B}$, each possessing three components in space, represent a system of equations with 12 unknown field components. However, Maxwell's equations alone provide only six independent scalar equations stemming from the two vector equations (A.1) and (A.3). Although (A.2) and (A.4) provide two further scalar equations it can be shown [44] by imposing the continuity of charge equation

$$\nabla \cdot \vec{J} + \frac{\partial \rho}{\partial t} = 0 \tag{A.5}$$

that the divergence equations may be obtained from the two curl equations. They are thus dependent. The continuity equation embodies the law of conservation of electric charge that states that electric charge cannot be created or destroyed.

To complete the theory, Maxwell's equations must be augmented by so-called constitutive relations [44, 57] that relate the respective field quantities to the material in which they are present. These relations are given by

$$\vec{D} = \epsilon_0 \vec{E} + \vec{P} \tag{A.6}$$

$$\vec{B} = \mu_0(\vec{H} + \vec{M}), \tag{A.7}$$

where $\vec{P}$ is the polarization, $\vec{M}$ is the magnetization, and $\mu_0 = 4\pi \cdot 10^{-7}$ Tm/A and $\epsilon_0 = 8.854 \cdot 10^{-12}$ F/m are the permeability and permittivity of vacuum. It is well known that in stationary, linear, homogeneous and isotropic media the constitutive relations reduce to [44]

$$\vec{D} = \epsilon \vec{E} \tag{A.8}$$

$$\vec{B} = \mu \vec{H}, \tag{A.9}$$

where μ and ϵ are the permeability and permittivity of the media. These two vector equations represent six additional scalar equations. Thus, in total we obtain a system of 12 equations for solving 12 unknowns. Hence, the theory is complete. Please note further that Ohm's law in differential form given by

$$\vec{J} = \sigma \vec{E} \tag{A.10}$$

constitutes an additional constitutive relation, where σ represents the conductivity.

For the physical interpretation of Maxwell's equations it is convenient to convert them into integral form. This may be accomplished using the fundamental integral theorems

of Gauss (B.2.3) and Stokes (B.2.4) (see Appendix B) giving

$$\oint_C \vec{E}\, d\vec{l} = -\int_S \frac{\partial \vec{B}}{\partial t}\, d\vec{S} \tag{A.11}$$

$$\oint_S \vec{D}\, d\vec{S} = \int_V \rho\, dV \tag{A.12}$$

$$\oint_C \vec{H}\, d\vec{l} = \int_S \left(\vec{J} + \frac{\partial \vec{D}}{\partial t} \right) d\vec{S} \tag{A.13}$$

$$\oint_S \vec{B}\, d\vec{S} = 0. \tag{A.14}$$

Now, let us shed some light on the physical interpretation of these equations. To this end, consider first the definition of electric and magnetic flux as per

$$\Phi_D = \int_S \vec{D}\, d\vec{S} \tag{A.15}$$

$$\Phi_B = \int_S \vec{B}\, d\vec{S}. \tag{A.16}$$

According to the mathematical definition given above, intuitively speaking, the flux is the net number of field vectors (of the respective vector field) passing through an open surface S. Due to the scalar product between the vector field and the surface element $d\vec{S}$ (see Appendix B) only the vector component that is normal (perpendicular) to the surface element contributes to the total flux.

Faraday's Law of Electromagnetic Induction

The first integral equation (A.11) is a generalization of Faraday's law of electromagnetic induction. It constitutes the fundamental principle for the operation of coils, motors and generators. Loosely speaking, it states that a changing magnetic field creates an electric field and can thus give rise to currents and voltages, e.g. in a wire loop exposed to a changing magnetic field.

According to [44], the partial time derivative inside the integral might be replaced by a total time derivative outside the integral. Taking further the definition of magnetic flux (A.16) into account, equation (A.11) may finally be rewritten as

$$u_{emf} = \oint_C \vec{E}\, d\vec{l} = -\frac{d\Phi_B}{dt}. \tag{A.17}$$

So, in particular Faraday's law of electromagnetic induction states that in a closed circuit with an open surface S bounded by a closed contour C, e.g. a wire loop, an electromotive force (EMF), a voltage u_{emf}, is induced. It is equal to the negative rate of change of the magnetic flux.

The negative sign on the right hand side of equation (A.17) implies that the induced EMF will oppose its origin which formalizes Lenz' law [25, 44, 57, 109]. We use Faraday's law extensively for the derivation of the driving coil model (see Section 3.1.2).

Gauss's Law

The second equation (A.12) is also known as Gauss's law, relating electrical sources inside a volume to the field they produce. More specifically, it equates the total charge

inside a volume V spanned by a closed surface S to the total outward electrical flux passing through the entire surface. It is noteworthy that electric particles or charges appear as monopoles. That is, they can be isolated into either positive or negative charges.

Ampère's Circuit Law

Equation (A.13) is a generalization of Ampère's circuit law and equates the line integral of the magnetic field strength $\vec{H}$ along a closed path C to both, the current

$$I = \int_S \vec{J}\, d\vec{S} \tag{A.18}$$

plus the time-rate of change of the total electric flux ϕ_D through the surface S, enclosed by C. The latter term embodies Maxwell's concept of displacement current that must be accounted for as a direct consequence of enforcing the continuity equation [57]. Ampères law consequently constitutes the magnetic analogue to Faraday's law. That is, currents as well as changing electric fields create magnetic fields versus changing magnetic fields produce/induce electric fields and currents.

Gauss' Law for Magnetism

Due to the duality of the electric and magnetic fields it is most likely that Gauss's law for the electric field has a dual counterpart for the magnetic field. Indeed, that is Gauss' law for magnetism. However, in contrast to the existence of electric monopoles, i.e. isolated electric charges, in the electric field, magnetic particles are usually observed as so-called dipoles carrying both, a magnetic north pole and a magnetic south pole. Now, equation (A.14) states that the total outward magnetic flux through an arbitrary closed surface S is always zero. This implies that there are no magnetic sources or sinks and the magnetic flux lines follow closed paths emanating from a magnetic north pole and terminating at a magnetic south pole. Also it implies that magnetic north and south poles might not be isolated, i.e. magnetic monopoles do not exist. Classically [24], this is illustrated by an experiment, where a bar magnet is cut into segments down to atomic dimensions. It shows that each of the infinitesimal small magnets would still have a north and a south pole instead of isolated north and south poles. Note that, some scientists believe in a more strict duality/symmetry of the Maxwell equations predicting the fact that magnetic monopoles must exist [115]. However, the evidence for the existence of magnetic monopoles could not be supplied yet. Hence, Gauss' law for magnetism is sometimes also referred to as *nonexistence of magnetic monopoles* [57].

Field Conditions

Please note that for a particular problem at hand, Maxwell's equations can mostly be simplified by imposing special field conditions in view of the problem. In particular we distinguish between the

- static and
- quasi-static

field conditions [44, 57] for the electric and the magnetic field. In the static theory apparently all time derivatives vanish. Although at first sight this seems quite restrictive, surprisingly this theory applies to a wide variety of problems including steady currents, and stationary charge distributions. Especially for the modeling and analysis of permanent magnet structures it is very useful [44].

On the other hand, in the quasi-static field theory Maxwell's equations are used as in (A.1) - (A.4) with the only difference that the displacement current density $\partial\vec{D}/\partial t$ is neglected. This approximation is valid for low frequencies in the sense that the time-rate of change of the field is much more slowly than time required for the field to propagate through a considered region. As the field propagates at the speed of light it can be concluded that also this theory applies to a wide range of practically important applications such as electrical circuit analysis, electromechanical devices with moving conductors/magnets as well as eddy current analysis [44].

Forces and Torques

For the analysis of electromechanical systems it is important to understand how electrical charged matter interacts with external magnetic fields. In fact, this interaction may be expressed in terms of a force

$$\vec{F} = Q(\vec{v} \times \vec{B}), \tag{A.19}$$

known as Lorentz force. It is this particular force a charged particle Q experiences when moving through an external magnetic field $\vec{B}$ with a velocity $\vec{v}$ [44, 109]. Due to the fact that an electric current I flowing through a wire is actually nothing other then charged particles moving along that wire, the above equation may be generalized to the case of currents giving

$$\vec{F} = I(\vec{l} \times \vec{B}). \tag{A.20}$$

This relation holds for the classical arrangement of a straight current carrying wire exposed to an external magnetic field (see [25]), where the action of force is on the wire. Therein, $\vec{l}$ indicates the direction of current flow, while its magnitude represents the effective length of the wire inside the magnetic field. Hence, the Lorentz force is proportional to the effective length and the amount of current flowing through the wire. Apparently, the vector product implies that the generated force acts perpendicular to the magnetic field as well as perpendicular to the direction of current flow. According to the definition of the vector product, the magnitude of the Lorentz force is given by

$$|\vec{F}| = F = I|\vec{l} \times \vec{B}| = I|\vec{l}||\vec{B}| \sin\varphi = IlB \sin\varphi, \tag{A.21}$$

where $\varphi = \angle(\vec{l}, \vec{B})$ implies the maximal force for $\vec{l} \perp \vec{B}$, i.e. $\varphi = \pi/2$.

If we are interested in computing the Lorentz force for wires or coils with more complex geometries we can calculate the force for an infinitesimal length of wire, that is

$$d\vec{F} = I(d\vec{l} \times \vec{B}). \tag{A.22}$$

If we then perform an integration in the direction of current flow, over the length C of the wire or coil we find that

$$\vec{F} = I \int_C d\vec{l} \times \vec{B} \tag{A.23}$$

gives the total force for the corresponding arrangement [44]. Now, knowing $\vec{F}$, the torque follows from $\vec{T} = \vec{r} \times \vec{F}$ as

$$\vec{T} = I \int_C \vec{r} \times (d\vec{l} \times \vec{B}). \tag{A.24}$$

Consequently, the Lorentz force enables a means of electromechanical coupling, allowing the acceleration and hence, a displacement of a certain mechanical structure by a proper arrangement of coils and magnets with respect to this structure. It thus constitutes the fundamental actuation principle of electric machines.

As mentioned earlier, the Lorentz force is proportional to the current I, so the same is valid for the acceleration it produces, e.g. for the acceleration of a mechanical structure. Due to the fact that a coil can be considered as a storage element, storing magnetic energy, the current flowing through the coil cannot jump instantaneously. This means that the mechanical structure cannot be accelerated arbitrarily fast. Instead, the achievable acceleration depends on the dynamic response of I, while this is governed by a differential equation and essentially depends on the respective time constant of the coil. The latter is determined by the ratio of the self induction and the winding resistance. Moreover, the dynamical behavior of the current inside the coil can also be influenced by such effects like mutual induction and motion induction also known as back-EMF. So let us shortly elaborate on these effects.

Self and Mutual Inductance

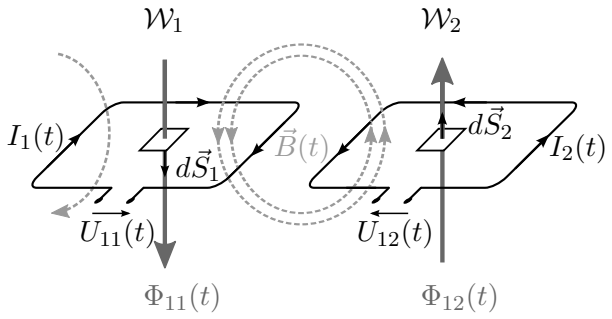

FIGURE A.1: self and mutual induction of two wire loops $\mathcal{W}_1$ and $\mathcal{W}_2$

The concept of self and mutual inductance is best explained considering two simple wire loops $\mathcal{W}_1$ and $\mathcal{W}_2$ as illustrated in Figure A.1. For the time being let us consider that the wire loop $\mathcal{W}_1$ is completely isolated from $\mathcal{W}_2$. In other words, let us first ignore the loop $\mathcal{W}_2$ entirely.

When a time-varying current $I_1(t)$ flows through $\mathcal{W}_1$ a time-varying magnetic field $\vec{B}(t)$ with time varying flux $\Phi_{11}(t)$ is produced. Due to the fact that the flux is changing over time, according to Faraday's law of induction (see equation (A.17)), the voltage

$$U_{11}(t) = -\frac{d\Phi_{11}(I_1(t))}{dt} \tag{A.25}$$

is induced in $\mathcal{W}_1$. This voltage can be measured at the terminals of $\mathcal{W}_1$. When the B-field propagates through linear media it is well-known [57, 109] that the magnetic flux is proportional to the current that produced it, that is

$$\Phi_{11}(t) = L_1\, I_1(t). \tag{A.26}$$

Hence, the induced voltage is eventually given by

$$U_{11}(t) = -\frac{d\Phi_{11}(I_1(t))}{dt} = -\frac{\partial\Phi_{11}(I_1)}{\partial I_1}\,\frac{dI_1(t)}{dt} = -L_1\,\frac{dI_1(t)}{dt}, \tag{A.27}$$

where the factor L_1 is called the self inductance of the wire loop $\mathcal{W}_1$. The term self inductance stems from the fact that it is caused by the change of its own magnetic field rather than an external one [44, 57, 109]. It depends on the geometry of the coil and the permeability of the media in which the field is propagated [109].

The results from a single wire loop can be extended to coils with more then one winding by introducing the concept of flux linkage. The flux linkage that we shall denote by Ψ, represents the total flux linking every individual winding of the coil. For instance for a coil with a single winding such as $\mathcal{W}_1$, $\Psi = \Phi_{11} = \Phi_B$, whereas for a coil with N tightly wound turns in a good approximation the relation $\Psi = N\Phi_B$ holds [25, 44].

Note that the flux linkage embodies the whole range of electromagnetic induction appearances occurring in a coil. To demonstrate this, let us now consider both wire loops $\mathcal{W}_1$ and $\mathcal{W}_2$ and their electromagnetic coupling.

To this end, suppose that $\mathcal{W}_1$ is supplied by $I_1(t)$, while $\mathcal{W}_2$ carries no current. Then one can observe from Figure A.1 that in $\mathcal{W}_1$ the time varying current $I_1(t)$ generates a clockwise circulating B-field with flux $\Phi_{11}(t)$, just as in the isolated case. However, besides the self induction of $U_{11}(t)$ in $\mathcal{W}_1$, parts of the B-filed permeate the second wire loop giving rise to a flux $\Phi_{12}(t)$. Its time rate of change thus induces an EMF (voltage) $U_{12}(t)$, also referred to as transformer EMF, in $\mathcal{W}_2$.

Since $I_1(t)$ and $\Phi_{12}(t)$ are connected in a linear relationship also [44, 57, 109], i.e.

$$\Phi_{12}(t) = M_{12}\, I_1(t), \tag{A.28}$$

the induced EMF is finally given by

$$U_{12}(t) = -\frac{d\Phi_{12}(I_1(t))}{dt} = -\frac{\partial\Phi_{12}(I_1)}{\partial I_1}\,\frac{dI_1(t)}{dt} = -M_{12}\,\frac{dI_1(t)}{dt}.$$

In analogy

$$U_{21}(t) = -\frac{d\Phi_{21}(I_2(t))}{dt} = -\frac{\partial\Phi_{21}(I_2)}{\partial I_2}\,\frac{dI_2(t)}{dt} = -M_{21}\,\frac{dI_2(t)}{dt}$$

represents the induced voltage for the inverse situation, where $\mathcal{W}_2$ is active, carrying a current $I_2(t)$, while $\mathcal{W}_1$ stays passive, i.e. is not supplied by any current.

The factors M_{12} and M_{21} are called mutual inductances. Their indices resemble their cause and effect, respectively. For instance M_{12} is the mutual inductance caused by circuit one affecting a second one and vice versa. It can be shown [57, 109] that

$$M_{12} = M_{21} = M, \tag{A.29}$$

where M can be further expressed in terms of the self inductances of the first and the second wire loop by [57]

$$M = k\sqrt{L_1 L_2}, \quad -1 \leq k \leq 1, \tag{A.30}$$

where k is referred to as coupling coefficient.

If we now assume that both, the circuits $\mathcal{W}_1$ and $\mathcal{W}_2$, carry the currents $I_1(t)$ and $I_2(t)$, respectively, than the total effects of electromagnetic induction, in the first circuit, are resembled by the sum

$$U_1(t) = U_{11}(t) + U_{21}(t) = -\frac{d}{dt}\left(\Phi_{11}(t) + \Phi_{21}(t)\right) = -\frac{d\Psi_1(t)}{dt} \tag{A.31}$$

of self and mutual induction effects. Notice that the induced voltage $U_{21}(t)$ is caused by $I_2(t)$ of the second circuit, affecting the first one, which is consistent with the convention of indices stated above.

As illustrated by the last equation, the induction effects as a whole are captured by the flux linkage $\Psi_1(t)$, linking the circuits $\mathcal{W}_1$ and $\mathcal{W}_2$. In order to extend this result to coils with multiple windings instead of simple wire loops one has simply to substitute $\Phi_{11}(t)$ and $\Phi_{21}(t)$ by the respective flux linkages $\Psi_{11}(t)$ and $\Psi_{21}(t)$ of the coils.

Back-Electromotive Force

In the preceding section we focused on the effect of transformer EMF, where it was evident that the flux linkage is a function of currents of the considered circuits. Thus in general for n electromagnetically coupled circuits

$$\Psi = \Psi(I_1(t), I_2(t), \ldots, I_n(t)). \tag{A.32}$$

However, under certain circumstances Ψ can also depend on additional variables. This is especially true if an external magnetic field moves relative to a coil or vice versa. Then Ψ no longer depends on currents only but also on the position of a moving ferromagnetic member [44].

This is exactly what we will encounter in the context of the planar motion stage. In fact, the magnetic field of the permanent magnet arrays along the translational motion axes is not constant. Moreover, it moves relative to the driving coils that are fixed to the stator. Assuming such a motion in the direction of q_x implies that during motion the flux linkage changes over time. According to Faraday's law this leads to a voltage

$$U_b(t) = -\frac{d\Psi(q_x(t))}{dt} = -\frac{\partial\Psi(q_x)}{\partial q_x}\,\frac{dq_x(t)}{dt} \tag{A.33}$$

that is induced in the coils to which the relative motion is performed. In the literature this voltage is referred to as back-EMF (voltage) [25] or motion EMF. Obviously, the amplitude of $U_b(t)$ scales with the velocity of the moving magnets by a factor of $\partial\Psi(q_x)/\partial q_x$.

However, in terms of modeling and analysis it is sometimes useful/convenient to express the factor $\partial\Psi(q_x)/\partial q_x$ in terms of the magnetic flux density. To this end, we consider the following example also representative for the back-EMF induced due to translational motion of a linear or planar actuator.

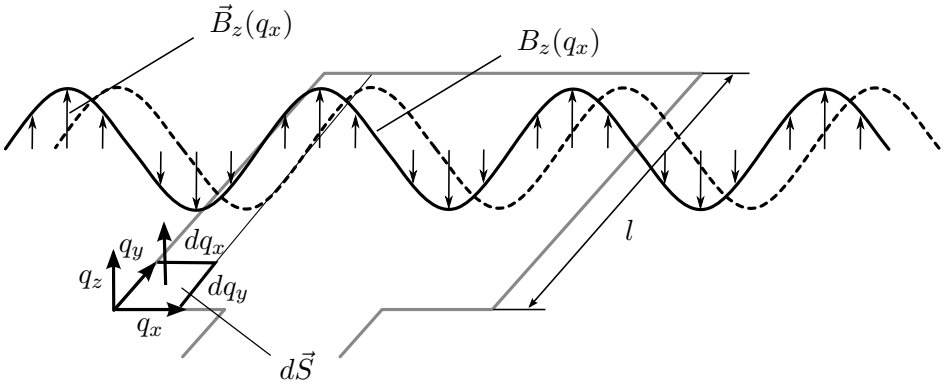

FIGURE A.2: Stationary wire loop within a moving permanent magnetic field as an abstraction of the $\mathcal{X}_{11}$ servomotor.

Example A.1.1. *Consider the arrangement given in Figure A.2. It illustrates a thin, stationary wire loop located in the (q_x, q_y)-plane. Suppose that a permanent magnet array is situated directly above the wire loop at a constant vertical hight of $q_z = q_{z,0}$. Let l be the length of the permanent magnet. Moreover, since we are concerned with translational motions along q_x, for the sake of simplicity, we assume that the magnetic field provided by the magnets is simply given by*

$$\vec{B}(q_x, q_y, q_z) = \vec{B}_z(q_x) = B_z(q_x)\,\vec{e}_z. \tag{A.34}$$

Therein, $B_z(q_x)$ denotes the vertical vector component showing a distinct dependence on q_x as indicated by Figure A.2. Furthermore, $\vec{e}_z$ is the unit vector for the vertical axis.

Compute the induced back-EMF voltage in the wire loop, when the magnets move relative to the wire loop along q_x. Thereby, assume that during motion a constant air gap $q_{z,0}$ and a constant position $q_{y,0}$ is maintained.

To this end, consider a differential (small) displacement dq_x of the permanent magnets relative to the conductor loop in a differential time instant dt. This results in a time rate of change of the flux linkage and consequently leads to the induction of a back-EMF voltage as given in (A.33)*. Substituting the definition of flux in* (A.16) *into* (A.33)*, noting that $\Psi = \Phi$, the partial derivative of Ψ can be rewritten into*

$$\frac{\partial \Psi(q_x)}{\partial q_x} = \frac{\partial}{\partial q_x} \int_S \vec{B}_z(q_x)\, d\vec{S}.$$

Let $\vec{e}_z$ be the normal to the differential surface element $dS = dq_x dq_y$ such that $d\vec{S} = dq_x dq_y \vec{e}_z$. Then, evaluating the surface integral over the effective wire length l inside the magnetic field and the relative position q_x of the magnets yields

$$\frac{\partial \Psi(q_x)}{\partial q_x} = \frac{\partial}{\partial q_x} \int_0^l \int_0^{q_x} \vec{B}(\bar{q}_x)\, d\bar{q}_x dq_y \vec{e}_z = \frac{\partial}{\partial q_x} \int_0^{q_x} \int_0^l B_z(\bar{q}_x)\, \vec{e}_z \vec{e}_z dq_y d\bar{q}_x = B_z(q_x)\, l.$$

The induced back-EMF voltage is thus finally given by

$$U_b(t) = -B_z(q_x)\, l\, \dot{q}_x(t) = -K(q_x)\, \dot{q}_x(t).$$

In particular, the last equation is equivalent to the classical result of a conductive bar moving through a uniform B-field [25, 44]. However, due to the fact that we intentionally avoided

the assumption of uniformity of the B-field, the induced voltage is no longer dependent on the velocity $\dot{q}_x$ of the moving member only, but also on q_x. Consequently, $K(q_x)$ is rather a back-EMF function than a back-EMF constant. ▲

Example A.1.1 shows that the back-EMF voltage induced in a single-turn conductor loop inside a moving non-uniform external magnetic field reads

$$U_b(t) = -B_z(q_x)\, l\, \dot{q}_x(t) = -K(q_x)\, \dot{q}_x(t), \tag{A.35}$$

where the product of $B_z(q_x)$ and l defines a back-EMF function $K(q_x)$. Apparently, parameter l is the effective wire length inside the magnetic field. It is determined by the geometry of the conductor/coil. For simple arrangements l may be computed analytically by a line integral along the circuit tracks. For a tightly wound N-turn coil the total voltage induced would sum up to

$$U_b(t) = -N\, l\, B_z(q_x)\, \dot{q}_x(t). \tag{A.36}$$

As exposed in the last two sections, as a function of circuit currents and position coordinates, the flux linkage Ψ is the key parameter to electromechanical coupling [44]. Indeed, it captures the entity of induction phenomena either they originate from a change of circuit current and/or a movement of a ferromagnetic member altering the field [44].

Remark A.1.1. Besides the generation of the flux linkage as a result of the mechanical displacement of the magnets, there is also a flux linkage $\Psi = LI$ due to the current I through the circuit. However, for this example we consider that the inductance is small and set $L = 0$.

This completes the review on electromagnetic field theory.

Appendix B

Vector Field Calculus

The following represents a compilation of references [25, 44, 57, 109].

B.1 The Vector Differential Operator

For the computation of differentials of scalar or vector fields in Cartesian coordinates, we introduce the vector differential operator given by

$$\nabla = \frac{\partial}{\partial q_x}\vec{e}_x + \frac{\partial}{\partial q_y}\vec{e}_y + \frac{\partial}{\partial q_z}\vec{e}_z. \tag{B.1}$$

This operator is sometimes referred to as *del*- [44] or *nabla*-operator [57]. Applying the *nabla*-operator to scalar or vector fields leads to the gradient, divergence and curl of the corresponding field given in the following definition:

Definition B.1.1 (gradient, divergence and curl[57])**.** *Let ϕ and $\vec{F}$ be arbitrary scalar and vector fields, respectively. Then the gradient, divergence and curl of a scalar or vector field are defined by:*

$$\operatorname{grad}\phi = \nabla\phi \tag{B.2}$$

$$\operatorname{div}\vec{F} = \nabla\cdot\vec{F} \tag{B.3}$$

$$\operatorname{curl}\vec{F} = \nabla\times\vec{F} \tag{B.4}$$

▼

In particular the gradient of ϕ then reads

$$\nabla\phi = \frac{\partial\phi}{\partial q_x}\vec{e}_x + \frac{\partial\phi}{\partial q_y}\vec{e}_y + \frac{\partial\phi}{\partial q_z}\vec{e}_z \tag{B.5}$$

and obviously yields a vector. This vector intuitively gives the slope in any point P for which ϕ is defined. It is perpendicular to the level set of ϕ and points in the direction of steepest increase.

According to definition B.1.1 the divergence of a vector field $\vec{F}$ is computed as per

$$\nabla\cdot\vec{F} = \frac{\partial F_x}{\partial q_x} + \frac{\partial F_y}{\partial q_y} + \frac{\partial F_z}{\partial q_z} \tag{B.6}$$

and apparently yields a scalar field whose value at a certain point is a measure of the rate at which the field diverges from that point [57]. Thus, roughly speaking, the divergence gives evidence about the existence of sources and sinks with respect to a differential volume element. Consider for instance a volume element V located in a region

Ω in the three dimensional space. Let $\vec{F}$ be a vector field that is defined on Ω. If there is an excess of the net number of field vectors (flux) leaving the volume element, then the vector field expands from that point and by convention the divergence of $\vec{F}$ will be greater than zero. We then say that the vector field $\vec{F}$ possesses a source in Ω. Similarly, if the flux enters V this means that the vector field contracts to that point. Consequently the divergence is less than zero and we call this point a sink in Ω.

Finally, the curl of $\vec{F}$ is computed by

$$\nabla \times \vec{F} = \begin{vmatrix} \vec{e}_x & \vec{e}_y & \vec{e}_z \\ \frac{\partial}{\partial q_x} & \frac{\partial}{\partial q_y} & \frac{\partial}{\partial q_z} \\ F_x & F_y & F_z \end{vmatrix} \tag{B.7}$$

and again results in a vector field that loosely speaking determines to which extent the vector field swirls around a certain point.

Please note that the *nabla*-operator must be applied to both, the individual components of the scalar or vector field as well as the basis vectors. In fact this is trivial in Cartesian coordinates because the basis vectors are independent of the coordinates. So their derivatives vanish. However, this is not the case for cylindrical or spherical coordinates, where the unit vectors explicitly depend on the coordinates themselves.

Moreover, applying the *nabla*-operator twice to scalar or vector valued functions leads to

$$\nabla^2 \phi = \nabla \cdot \nabla \phi = \frac{\partial^2 \phi}{\partial q_x^2} + \frac{\partial^2 \phi}{\partial q_y^2} + \frac{\partial^2 \phi}{\partial q_z^2} \tag{B.8}$$

and

$$\nabla^2 \vec{F} = (\nabla^2 F_x)\, \vec{e}_x + (\nabla^2 F_y)\, \vec{e}_y + (\nabla^2 F_z)\, \vec{e}_z, \tag{B.9}$$

respectively. Thereby, ∇^2 is the so-called Laplacian operator defined by

$$\nabla^2 = \frac{\partial^2}{dq_x^2} + \frac{\partial^2}{dq_y^2} + \frac{\partial^2}{dq_z^2}. \tag{B.10}$$

B.2 Theorems and Identities

Next, we state some important theorems and identities for the analysis of scalar and vector fields. We begin with Helmholtz' theorem which indicates when a vector field is uniquely defined:

Theorem B.2.1 (Helmholtz' Theorem[44, 57])**.** *A sufficiently smooth vector field $\vec{F}$ is uniquely defined (within an additive constant) by specifying its divergence and its curl with both vanishing at infinity.* ■

The conclusions that may be drawn from this theorem are so important that it is also known as fundamental theorem of vector calculus. Now, knowing that a vector field is completely defined by its curl and divergence, let us classify some types of vector fields. To this end, consider the following definitions:

Definition B.2.1. *A vector field $\vec{F}$ is said to be solenoidal (nonsolenoidal) if the divergence of the vector field is zero (nonzero).* ▼

Definition B.2.2. *A vector field $\vec{F}$ is said to be irrotational (rotational) if the curl of the vector field is zero (nonzero).* ▼

Therefore, considering a combination of all these types of fields, we find that in total four types of vector fields can be classified [57]. In particular, we distinguish the classes of

- nonsolenoidal, rotational vector fields
- nonsolenoidal, irrotational vector fields
- solenodial, rotational vector fields
- solenodial, irrotational vector fields.

Consider the identities given next:

Theorem B.2.2 (Identities [57])**.** *Let ϕ be a scalar field and $\vec{F}$ a vector field, all assumed to be sufficiently smooth such that all the partial derivatives in the identities are existent and continuous. Then the following identities hold:*

$$\nabla \cdot (\nabla \times \vec{F}) = 0 \tag{B.11}$$

$$\nabla \times (\pm \nabla \phi) = 0 \tag{B.12}$$

■

In words, the first identity states that the divergence of an arbitrary rotational field is always zero (solenoidal), while the second identity says that the curl of the gradient of a scalar field is always zero (irrotational) also.

With the use of these identities, from Helmholtz' theorem we can draw the following fundamental conclusions:

Corollary B.2.1 (Scalar potential [44])**.** *An irrotational vector field $\vec{F}$ can be written as the gradient of a scalar potential, that is,*

$$\nabla \times \vec{F} = 0 \quad \Rightarrow \quad \vec{F} = \pm \nabla \phi \tag{B.13}$$

□

Indeed, if we apply the curl operator to $\vec{F} = \pm \nabla \phi$ we get

$$\nabla \times \vec{F} = \nabla \times (\pm \nabla \phi). \tag{B.14}$$

Due to identity (B.12) the right hand side becomes zero which is consistent with the curl of the irrotational vector field. Note that the choice of the scalar valued function ϕ is not unique. A constant might be added without affecting $\vec{F}$. Note further, that mathematically the sign of the gradient of the scalar potential is not important. However, due to historical conventions/reasons, in electromagnetic field theory, usually the gradient of the vector potential is chosen negative.

Regarding solenoidal vector fields a similar conclusion can be drawn:

Corollary B.2.2 (Vector potential [44])**.** *A solenoidal vector field $\vec{F}$ can be written as the curl of a vector field $\vec{A}$, a so-called vector potential, that is*

$$\nabla \cdot \vec{F} = 0 \quad \Rightarrow \quad \vec{F} = \nabla \times \vec{A}. \tag{B.15}$$

□

Applying the divergence operator to $\vec{F} = \nabla \times \vec{A}$ one obtains

$$\nabla \cdot \vec{F} = \nabla \cdot (\nabla \times \vec{A}). \tag{B.16}$$

Apparently, in view of identity (B.11) the right hand side becomes zero which analogously is consistent with the divergence of the solenoidal field. Note that also the choice of vector potential $\vec{A}$ is not unique. Identity (B.12) suggests that the gradient of an arbitrary scalar valued function might be added to $\vec{A}$ without affecting the field $\vec{F}$.

Due to corollaries B.2.1 and B.2.2 the following can be concluded:

Corollary B.2.3 ([44]). *In general, an arbitrary vector field $\vec{F}$ may be expressed as a sum of two parts, one that is irrotational, and another that is solenoidal, that is*

$$\vec{F} = -\nabla\phi + \nabla \times \vec{A}. \tag{B.17}$$

□

The latter is also known as Helmholtz decomposition. To understand the last statement, let us consider the divergence and curl of (B.17). Hence,

$$\nabla \cdot \vec{F} = \underbrace{\nabla \cdot (-\nabla\phi)}_{\text{some scalar } f} + \underbrace{\nabla \cdot (\nabla \times \vec{A})}_{\text{0 due to (B.11)}} = f \tag{B.18}$$

$$\nabla \times \vec{F} = \underbrace{\nabla \times (-\nabla\phi)}_{\text{0 due to (B.12)}} + \underbrace{\nabla \times (\nabla \times \vec{A})}_{\text{some vector } \vec{K}} = \vec{K}. \tag{B.19}$$

The nonzero scalar f and nonzero vector $\vec{K}$ resemble unique descriptions of the divergence and curl of the vector field $\vec{F}$. Thus, according to Helmholtz' theorem together they uniquely define the whole vector field $\vec{F}$. Moreover, as stated by the theorem, an arbitrary constant c might be added to $\vec{F}$ without affecting the divergence and curl.

B.2.1 Integral Identities

The following two integral theorems are fundamental to vector field calculus. In electromagnetic field theory they are especially useful when, for instance, we are interested in converting Maxwell's equations from differential into integral form. These theorems are Gauss's and Stokes' theorem stated next:

Theorem B.2.3 (Gauss's Theorem). *Let $\vec{F}$ denote an arbitrary vector field. Then the integral of the divergence of $\vec{F}$ over a volume V may be reduced to a surface integral of $\vec{F}$ over the surface S enclosing V. That is*

$$\int_V \nabla \cdot \vec{F}\, dV = \oint_S \vec{F}\, d\vec{S}. \tag{B.20}$$

■

Theorem B.2.4 (Stokes' Theorem). *Let $\vec{F}$ denote an arbitrary vector field. Then the line integral of $\vec{F}$ along a closed contour C is equal to the surface integral of the curl of the vector field with respect to an open surface S that is bounded by C, i.e.*

$$\oint_C \vec{F}\, d\vec{l} = \int_S (\nabla \times \vec{F})\, d\vec{S}. \tag{B.21}$$

■

In theorems B.2.3 and B.2.4 the vector $d\vec{S} = dS\vec{n}$ is the so-called surface element vector. It has a magnitude of a differential (small) surface element dS and a direction specified by the unit vector $\vec{n}$ that is normal to the surface element.

Appendix C

Parameter Values of Identified Motion Stage Model

C.1 Parameters of the coupled two-phase coil model

$$R = \text{diag}(2.0864, 2.3351, 2.0864, 2.3351, 3.1795, 3.6357, 3.1795, 3.6357)\ \Omega$$

$$\tilde{L}_{x_1} = \tilde{L}_{x_2} = \begin{pmatrix} 227.44 & 9.0381 \\ 9.0381 & 208.05 \end{pmatrix} \times 10^{-6}\ \text{H}$$

$$\tilde{L}_{y_1} = \tilde{L}_{y_2} = \begin{pmatrix} 257.36 & 16.28 \\ 16.28 & 268.94 \end{pmatrix} \times 10^{-6}\ \text{H}$$

$$K_{x_1}(q_x) = K_{x_2}(q_x) = \begin{pmatrix} K_{mx} \sin(\frac{2\pi}{T_m} q_x + \varphi_x) \\ K_{mx} \cos(\frac{2\pi}{T_m} q_x + \varphi_x) \end{pmatrix}$$

$$K_{mx} = 1.6218\ \text{N/A},\ \varphi_x = -2.2343$$

$$K_{y_1}(q_y) = K_{y_2}(q_x) = \begin{pmatrix} K_{my} \sin(\frac{2\pi}{T_m} q_y + \varphi_y) \\ K_{my} \cos(\frac{2\pi}{T_m} q_y + \varphi_y) \end{pmatrix}$$

$$K_{my} = 1.5931\ \text{N/A},\ \varphi_y = 2.1748$$

$$T_m = 21.4\ \text{mm}$$

TABLE C.1: Parameter values for the coupled two-phase coil model.

C.2 Parameters of the DCA model

$$T_s = 1/2e5\ \text{s}$$

$$N = 8$$

$$K_p = \text{diag}(0.025, 0.025, 0.025, 0.025, 0.02, 0.02, 0.02, 0.02)$$

$$K_i = \text{diag}(200, 200, 200, 200, 360, 360, 360, 360)$$

$$K_T = \text{diag}(171.89, 162.84, 171.89, 162.84, 164.44, 163.66, 164.44, 163.66)$$

TABLE C.2: DCA current controller parameters

Table C.3 represents the look-up-table for the implementation of function $f_s(i^\star)$. Therein, $i^\star_{(\cdot)}$ denotes the reference current input to either of the DCA's and $i^s_{x_{ij}}$ such as $i^s_{y_{ij}}$ represent the stationary values of the respective output currents.

Assuming a similar characteristic for the systems $\mathcal{X}_{2j}$ and $\mathcal{Y}_{2j}$ and applying linear regression (see equation (3.16)), yields the following parameters for the stationary

$i^{\star}_{(\cdot)}$ [A]	$i^{s}_{x_{11}}$ [A]	$i^{s}_{x_{12}}$ [A]	$i^{s}_{y_{11}}$ [A]	$i^{s}_{y_{12}}$ [A]
-3	-3.155	-3.17	-3.105	-3.145
-2.5	-2.75	-2.73	-2.695	-2.725
-2	-2.215	-2.193	-2.14	-2.195
-1.5	-1.655	-1.68	-1.59	-1.677
-1	-1.115	-1.14	-1.05	-1.135
-0.5	-0.55	-0.57	-0.53	-0.58
0.5	0.55	0.542	0.51	0.54
1	1.075	1.065	1.03	1.075
1.5	1.626	1.616	1.6	1.63
2	2.2	2.19	2.21	2.19
2.5	2.72	2.72	2.78	2.72
3	3.14	3.14	3.32	3.11

TABLE C.3: Look-up-table for stationary input-output characteristics of the DCA-coil-systems $\mathcal{X}_{1j}$ and $\mathcal{Y}_{1j}$.

input-output characteristics for all DCA-coil-systems, i.e.

$$p_1 = 1.0769, \quad p_0^{\mathrm{T}} = -3.9792 \begin{pmatrix} 1 & 1 & 1 & 1 & 1 & 1 & 1 & 1 \end{pmatrix} \times 10^{-3} \tag{C.1}$$

C.3 Parameters of the generic axis models

$$A = \begin{pmatrix} 0.0000 & 1.0000 & 0.0000 & 0.0000 \\ 0.0000 & -0.4013 & 9630.2 & 4.9989 \\ 0.0000 & 0.0000 & 0.0000 & 1.0000 \\ 0.0000 & 0.0271 & -9630.2 & -4.9989 \end{pmatrix}$$

$$B = \begin{pmatrix} 0.0000 \\ 232.6975 \\ 0.0000 \\ -15.6897 \end{pmatrix}$$

$$C = \begin{pmatrix} 1 & 0 & 0 & 0 \end{pmatrix}$$

$$\Sigma_2(s) = \frac{7.5846\text{e}09(s+128.2)}{(s+1781)(s+132.7)(s^2+567s+4.116\text{e}06)}$$

TABLE C.4: Numerical parameter values for the q_x axis model with input current in [A] and output position in [mm].

$$A = \begin{pmatrix} 0.0000 & 1.0000 & 0.0000 & 0.0000 \\ 0.0000 & -0.3952 & 6638.9708 & 3.6502 \\ 0.0000 & 0.0000 & 0.0000 & 1.0000 \\ 0.0000 & 0.02665 & -6638.9708 & -3.6502 \end{pmatrix}$$

$$B = \begin{pmatrix} 0.0000 \\ 232.1693 \\ 0.0000 \\ -15.6540 \end{pmatrix}$$

$$C = \begin{pmatrix} 1 & 0 & 0 & 0 \end{pmatrix}$$

$$\Sigma_2(s) = \frac{9.6082\text{e}09(s+75.76)}{(s+2727)(s+78.53)(s^2+442.2s+3.399\text{e}06)}$$

TABLE C.5: Numerical parameter values for the q_y axis model with input current in [A] and output position in [mm].

$$A = \begin{pmatrix} 0.0000 & 1.0000 \\ 0.0000 & 0.0000 \end{pmatrix}$$

$$B = \begin{pmatrix} 0.0000 \\ 3556.46189 \end{pmatrix}$$

$$C = \begin{pmatrix} 1 & 0 \end{pmatrix}$$

$$\Sigma_2(s) = \frac{0.00039389(s^2+0.004904s+1.509\text{e}17)}{(s^2+1863s+4.844\text{e}06)(s^2+1701s+1.227\text{e}07)}$$

TABLE C.6: Numerical parameter values for the q_ϕ axis model with input current in [A] and output position in [mrad].

Bibliography

[1] Gilles Akoun and J-P Yonnet. "3D analytical calculation of the forces exerted between two cuboidal magnets". In: *IEEE Transactions on magnetics* 20.5 (1984), pp. 1962–1964.

[2] A. Amthor et al. "Asymmetric motion profile planning for nanopositioning and nanomeasuring machines". In: *Proceedings of the Institution of Mechanical Engineers, Part I: Journal of Systems and Control Engineering* 224.1 (2010), pp. 79–92.

[3] Brian DO Anderson et al. "Failures of adaptive control theory and their resolution". In: *Communications in Information & Systems* 5.1 (2005), pp. 1–20.

[4] Brian Armstrong-Hélouvry, Pierre Dupont, and Carlos Canudas De Wit. "A survey of models, analysis tools and compensation methods for the control of machines with friction". In: *Automatica* 30.7 (1994), pp. 1083–1138.

[5] Karl J. Åström and Björn Wittenmark. *Adaptive control*. Addison-Wesley Longman Publishing Co., Inc., 1994.

[6] Karl J. Åström and Björn Wittenmark. *Computer-controlled systems: theory and design*. Courier Corporation, 2013.

[7] Julius S. Bendat and Allan G. Piersol. *Random data: analysis and measurement procedures*. Vol. 729. John Wiley & Sons, 2011.

[8] Luigi Biagiotti and Claudio Melchiorri. *Trajectory planning for automatic machines and robots*. Springer Science & Business Media, 2008.

[9] T. Bierling. "Comparative Analysis of Adaptive Control Techniques for Improved Robust Performance". PhD thesis. Technische Universität München, 2014.

[10] Robert H. Bishop. *The Mechatronics Handbook, -2 Volume Set*. CRC Press, 2002.

[11] P. Bolognesi et al. "Electromagnetic actuators featuring multiple degrees of freedom: a survey". In: *International Conference on Electrical Machines (ICEM 2004), Cracow, Poland*. 2004.

[12] Marc-Anthony Brunsch. "Zeitdiskrete, störbeobachterbasierte Trajektorienfolgeregelung eines planar Präzisionspositioniersystems". MA thesis. Technische Universität Ilmenau, 2015.

[13] Hans Butler. "Position Control in Lithographic Equipment [Applications of Control]". In: *IEEE Control System Magazin* 31.5 (2011), pp. 28–47.

[14] Christopher I Byrnes and Alberto Isidori. "A frequency domain philosophy for nonlinear systems, with applications to stabilization and to adaptive control". In: *The 23rd IEEE Conference on Decision and Control, 1984.* 1984, pp. 1569–1573.

[15] Stefan F. Campbell and John T. Kaneshige. "A nonlinear dynamic inversion L1 adaptive controller for a Generic Transport Model". In: *American Control Conference*. 2010, pp. 862–867.

[16] Chengyu Cao and Naira Hovakimyan. "Design and analysis of a novel L1 adaptive controller, Part I: Control signal and asymptotic stability". In: *American Control Conference*. 2006, pp. 3397–3402.

[17] Chengyu Cao and Naira Hovakimyan. "Effect of Non-zero Initialization Error on the Performance Bounds in L1 Adaptive Control Architecture". In: *Proceedings of AIAA Guidance, Navigation & Control Conference*. 2007.

[18] Chengyu Cao and Naira Hovakimyan. "Guaranteed transient performance with L1 adaptive controller for systems with unknown time-varying parameters and bounded disturbances: Part I". In: *American Control Conference*. 2007, pp. 3925–3930.

[19] Chengyu Cao and Naira Hovakimyan. "L1 adaptive output feedback controller for non strictly positive real Multi-input Multi-output systems in the presence of unknown nonlinearities". In: *2009 American Control Conference*. 2009, pp. 5138–5143.

[20] Chengyu Cao and Naira Hovakimyan. "L1 adaptive output-feedback controller for non-strictly-positive-real reference systems: missile longitudinal autopilot design". In: *Journal of guidance, control, and dynamics* 32.3 (2009), pp. 717–726.

[21] Chengyu Cao and Naira Hovakimyan. "L1 adaptive output feedback controller for non-strictly positive real reference systems with applications to aerospace examples". In: *AIAA Guidance, Navigation, and Control Conference and Exhibit*. 2008.

[22] Jiayong Cao et al. "A novel synchronous permanent magnet planar motor and its model for control applications". In: *IEEE Transactions on Magnetics* 41.6 (2005), pp. 2156–2163.

[23] Wen-Hua Chen et al. "Disturbance-observer-based control and related methods–An overview". In: *IEEE Transactions on Industrial Electronics* 63.2 (2016), pp. 1083–1095.

[24] David Keun Cheng et al. *Field and wave electromagnetics*. Pearson Education India, 1989.

[25] J. Chiasson. *Modeling and high performance control of electric machines*. John Wiley & Sons, 2005.

[26] T.T. Chung et al. "Development of a nano-positioning planar motion stage". In: *2nd International Conference on Mechanical and Electronics Engineering (ICMEE)*. Vol. 1. 2010, pp. 122–126.

[27] Garrett M. Clayton et al. "A review of feedforward control approaches in nanopositioning for high-speed SPM". In: *Journal of dynamic systems, measurement, and control* 131.6 (2009), p. 061101.

[28] Michael B. Cohn et al. "Microassembly technologies for MEMS". In: *Micromachining and Microfabrication*. International Society for Optics and Photonics. 1998, pp. 2–16.

[29] E. Davison. "The robust control of a servomechanism problem for linear time-invariant multivariable systems". In: *IEEE Trans. Automat. Contr.* 21.1 (1976), pp. 25–34.

[30] Paul De Monte and Boris Lohmann. "Position trajectory tracking of a quadrotor helicopter based on L1 adaptive control". In: *European Control Conference*. 2013, pp. 3346–3353.

[31] D. De Roover and O.H. Bosgra. "Dualization of the internal model principle in compensator and observer theory with application to repetitive and learning control". In: *Proceedings of the 1997 American Control Conference* (1997).

[32] S. Dejima et al. "Dynamic modeling, controller design and experimental validation of a planar motion stage for precision positioning". In: *Precision engineering* 29.3 (2005), pp. 263–271.

[33] S. Devasia, Degang Chen, and B. Paden. "Nonlinear inversion-based output tracking". In: *IEEE Transactions on Automatic Control* 41.7 (1996), pp. 930–942.

[34] Santosh Devasia, Evangelos Eleftheriou, and S. O. Reza Moheimani. "A Survey of Control Issues in Nanopositioning". In: *IEEE Transactions on Control Systems Technology* 15.5 (2007), pp. 802–823.

[35] S. Dian, Y. Arai, and W. Gao. "Dynamic compensation of modeling uncertainties and disturbances of a precision planar motion stage based on sliding mode observer". In: *International Journal of Advanced Manufacturing Technology* 46.9 (2010), pp. 899–912.

[36] S. Diop and M. Fliess. "Nonlinear observability, identifiability, and persistent trajectories". In: *Proceedings of the 30th IEEE Conference on Decision and Control, 1991*. Vol. 1. 1991, pp. 714–719.

[37] Peter Dittrich and Daniel Radeck. "3-DOF planar induction motor". In: *2006 IEEE International Conference on Electro/Information Technology*. 2006, pp. 81–86.

[38] John C. Doyle and Gunter Stein. "Multivariable feedback design: Concepts for a classical/modern synthesis". In: (1981).

[39] A.J. Fleming and K.K. Leang. *Design, Modeling and Control of Nanopositioning Systems*. Advances in Industrial Control. Springer International Publishing, 2014.

[40] Michel Fliess et al. "Flatness and defect of non-linear systems: introductory theory and examples". In: *International Journal of Control* 61.6 (1995), pp. 1327–1361.

[41] T.I. Fossen. *Guidance and control of ocean vehicles*. John Wiley & Sons, 1994.

[42] B. A. Francis and W. M. Wonham. "The Internal Model Principle for Linear Multivariable Regulators". In: *Applied Mathematics & Optimization* 2.4 (Dec. 1975), pp. 380–380.

[43] B.A. Francis and W.M. Wonham. "The internal model principle of control theory". In: *Automatica* 12.5 (1976), pp. 457–465.

[44] E.P. Furlani. *Permanent magnet and electromechanical devices: materials, analysis, and applications*. Academic Press, 2001.

[45] W. Gao et al. "A surface motor-driven planar motion stage integrated with an XY surface encoder for precision positioning". In: *Precision Engineering* 28.3 (2004), pp. 329–337.

[46] Robert Gauvin et al. "Microfabrication of complex porous tissue engineering scaffolds using 3D projection stereolithography". In: *Biomaterials* 33.15 (2012), pp. 3824–3834.

[47] Travis E Gibson, Anuradha M Annaswamy, and Eugene Lavretsky. "On adaptive control with closed-loop reference models: transients, oscillations, and peaking". In: *IEEE Access* 1 (2013), pp. 703–717.

[48] Travis E Gibson et al. "Adaptive output feedback based on closed-loop reference models". In: *arXiv preprint arXiv:1410.1944* (2014).

[49] Dr. Johannes Heidenhein GmbH. *Linear Encoders for Numerically Controlled Machine Tools*. 2005. URL: `http://www.auto-met.com/heidenhain/08PDF/NC%20Linear.pdf`.

[50] Numerik Jena GmbH. *LIK 2D-Incremental 2D linear encoder*. 2015. URL: http://www.downloads-numerikjena.de/sheets/DS_LIK_2D_eng.pdf.

[51] Graham Clifford Goodwin, Stefan F. Graebe, and Mario E. Salgado. *Control system design*. Vol. 240. Prentice Hall New Jersey, 2001.

[52] Knut Graichen, Veit Hagenmayer, and Michael Zeitz. "A new approach to inversion-based feedforward control design for nonlinear systems". In: *Automatica* 41.12 (2005), pp. 2033–2041.

[53] Knut Graichen and Michael Zeitz. "Feedforward control design for finite-time transition problems of nonlinear systems with input and output constraints". In: *IEEE Transactions on Automatic Control* 53.5 (2008), pp. 1273–1278.

[54] Brian Griffin, John Burken, and Enric Xargay. "L1 adaptive control augmentation system with application to the x-29 lateral/directional dynamics: A multi-input multi-output approach". In: *Guidance, Navigation, and Control and Co-located Conferences. American Institute of Aeronautics and Astronautics*. 2010.

[55] Veit Hagenmeyer and Michael Zeitz. "Übersicht-Flachheitsbasierter Entwurf von linearen und nichtlinearen Vorsteuerungen". In: *Automatisierungstechnik* 52.1 (2004), pp. 5–14.

[56] K. Halbach. "Design of permanent multipole magnets with oriented rare earth cobalt material". In: *Nuclear Instruments and Methods* 169.1 (1980), 1–10.

[57] MR Hamers. *Actuation principles of permanent magnet synchronous planar motors: a literature survey*. Tech. rep. Tech. Rep. CBT 534-05-2717 DCT 2005.149, Philips Applied Technologies, Eindhoven, 2005.

[58] Michael R. Hannan. "On the Observed Robustness of Disturbance-Observers; A Technical Explanation and Simulation Validation". In: *2008 40th Southeastern Symposium on System Theory (SSST)*. IEEE. 2008, pp. 25–30.

[59] Robert Haschke, Erik Weitnauer, and Helge Ritter. "On-line planning of time-optimal, jerk-limited trajectories". In: *2008 IEEE/RSJ International Conference on Intelligent Robots and Systems*. IEEE. 2008, pp. 3248–3253.

[60] Robbert van Herpen et al. "Exploiting additional actuators and sensors for nano-positioning robust motion control". In: *Mechatronics* 24.6 (2014), pp. 619–631.

[61] Joao P Hespanha. *Linear systems theory*. Princeton university press, 2009.

[62] Klaske van Heusden and Guy A Dumont. "Analysis of L1 adaptive output feedback control; equivalent LTI controllers". In: *IFAC Proceedings Volumes* 45.16 (2012), pp. 1472–1477.

[63] Peter Hippe. *Windup in control: its effects and their prevention*. Springer Science & Business Media, 2006.

[64] Øystein Hov Holhjem. "L1 Adaptive Control of the Inner Control Loops of an F-16 Aircraft". MA thesis. Norwegian Institute of Science and Technology, 2012.

[65] Isaac M Horowitz. *Synthesis of feedback systems*. Academic Press, New York, 1963.

[66] Yi Hou et al. "Active disturbance rejection control for web tension regulation". In: *40th IEEE Conference on Decision and Control*. Vol. 5. 2001, pp. 4974–4979.

[67] N. Hovakimyan. *L1 adaptive control*. URL: http://naira.mechse.illinois.edu/clarifications-on-l1-adaptive-control/.

[68] N. Hovakimyan and C. Cao. *L1 adaptive control theory: guaranteed robustness with fast adaptation*. Siam, 2010.

[69] N. Hovakimyan et al. "L1 adaptive control for safety-critical systems". In: *IEEE Control Systems Magazine* 1066.033X/11 (2011).

[70] Yi Huang et al. "Flight control design using extended state observer and non-smooth feedback". In: *40th IEEE Conference on Decision and Control*. Vol. 1. 2001, pp. 223–228.

[71] Petros A Ioannou and Jing Sun. *Robust adaptive control*. Prentice hall New Jersey, 1996.

[72] Alberto Isidori. *Nonlinear control systems*. Springer Science & Business Media, 2013.

[73] Saeid Jafari, Petros A Ioannou, and Lael Rudd. "What is L1 adaptive control". In: *AIAA Guidance, Navigation, and Control (GNC) Conference*. 2013, p. 4513.

[74] C.D. Johnson. "A new approach to adaptive control". In: *Control and Dynamic Systems V27: Advances in Theory and Applications* 27 (1988), p. 1.

[75] C.D. Johnson. "Adaptive controller design using disturbance-accommodation techniques". In: *International Journal of Control* 42.1 (1985), pp. 193–210.

[76] C.D. Johnson. "Disturbance-accommodating control; an overview". In: *American Control Conference, 1986*. IEEE. 1986, pp. 526–536.

[77] C.D. Johnson. *Effective techniques for the identification and accommodation of disturbances*. Tech. rep. 1989.

[78] CD Johnson. "Real-time disturbance-observers; origin and evolution of the idea part 1: The early years". In: *40th Southeastern Symposium on System Theory (SSST)*. 2008, pp. 88–91.

[79] Eric N Johnson. "Limited authority adaptive flight control". PhD thesis. Georgia Institute of Technology, 2000.

[80] Eric N Johnson and Anthony J Calise. "Pseudo-control hedging: a new method for adaptive control". In: *Advances in navigation guidance and control technology workshop*. Alabama, USA Alabama, USA. 2000, pp. 1–2.

[81] M.U. Khan et al. "A long stroke electromagnetic XY positioning stage for micro applications". In: *IEEE/ASME Transactions on Mechatronics* (2011), pp. 1–10.

[82] Muneeb Ullah Khan. "Contribution to the design and fabrication of an integrated micro-positioning system". PhD thesis. Compiègne, 2014.

[83] Evgeny Kharisov. "L1 adaptive output-feedback control architectures". PhD thesis. University of Illinois at Urbana-Champaign, 2014.

[84] Evgeny Kharisov and Naira Hovakimyan. "Generalization of L1 adaptive control architecture for switching estimation laws". In: *American Control Conference*. 2012, pp. 1907–1912.

[85] Evgeny Kharisov, Naira Hovakimyan, and Karl J. Åström. "Comparison of several adaptive controllers according to their robustness metrics". In: *AIAA Paper No. AIAA-2010-8047* (2010).

[86] Evgeny Kharisov et al. "Limiting behavior of L1 adaptive controllers". In: *AIAA Guidance, Navigation and Control Conference*. 2011.

[87] Won-jong Kim and David L. Trumper. "High-precision magnetic levitation stage for photolithography". In: *Precision Engineering* 22.2 (1998), pp. 66–77.

[88] Masaaki Kumagai and Ralph L. Hollis. "Development and control of a three DOF planar induction motor". In: *2012 IEEE International Conference on Robotics and Automation (ICRA)*. IEEE. 2012, pp. 3757–3762.

[89] Paul Lambrechts, Matthijs Boerlage, and Maarten Steinbuch. "Trajectory planning and feedforward design for electromechanical motion systems". In: *Control Engineering Practice* 13.2 (2005), pp. 145–157.

[90] Eugene Lavretsky. "Adaptive output feedback design using asymptotic properties of LQG/LTR controllers". In: *IEEE Transactions on Automatic Control* 57.6 (2012), pp. 1587–1591.

[91] Eugene Lavretsky and Travis E Gibson. "Projection operator in adaptive systems". In: *arXiv e–Prints* (2011).

[92] Eugene Lavretsky and Kevin A. Wise. *Robust and Adaptive Control with Aerospace Applications*. Springer, 2013, pp. 317–353.

[93] M. Ludloff. "Systemidentifikation im geschlossenen Regelkreis an einem Präzisions-Positioniersystem". MA thesis. Technische Universität Ilmenau, 2016.

[94] Jie Luo and Chengyu Cao. "L1 adaptive output feedback controller for a class of nonlinear systems". In: *2011 50th IEEE Conference on Decision and Control and European Control Conference*. IEEE. 2011, pp. 5425–5430.

[95] A. Luviano-Juarez, J. Cortes-Romero, and H. Sira-Ramirez. "Synchronization of chaotic oscillators by means of Generalized Proportional Integral observers". In: *International Journal of Bifurcation and Chaos* 20.05 (2010), pp. 1509–1517.

[96] Divine Maalouf, Ahmed Chemori, Vincent Creuze, et al. "A new extension of the L1 adaptive controller to drastically reduce the tracking time lags". In: *IFAC Symposium on Nonlinear Control Systems*. 2013, pp. 001–006.

[97] Institut für Mikroelektronik-und Mechatronik-Systeme gGmbH. "Elektrodynamischer planar x-y-ϕ-Dierektantrieb sowie dessen Regelung". Pat. DE 100 54 376 A 1 (Institut für Mikroelektronik- und Mechatronik-Systeme gGmbH, Ilmenau). June 2001.

[98] Robert Miklosovic, Aaron Radke, and Zhiqiang Gao. "Discrete implementation and generalization of the extended state observer". In: *American Control Conference*. 2006, pp. 2209–2214.

[99] Sandipan Mishra, Joshua Coaplen, and Masavoshi Tomizuka. "Precision positioning of wafer scanners segmented iterative learning control for nonrepetitive disturbances [applications of control]". In: *IEEE control systems* 27.4 (2007), pp. 20–25.

[100] Mark Müller. "Adaptive Trajektorienfolgeregelung eines Nanopositioniersystems mittels Ausgangsrückführung". MA thesis. Technische Universität Ilmenau, 2016.

[101] Paul J Nahin. "Among the giants: Oliver Heaviside: Genius and curmudgeon". In: *IEEE spectrum* 20.7 (1983), pp. 63–69.

[102] Kumpati S Narendra and Anuradha M Annaswamy. *Stable adaptive systems*. Courier Corporation, 2012.

[103] Robert C O'Handley. *Modern Magnetic Materials Principles and Applications*. Wiley, 2000.

[104] Tom Oomen. "System identification for robust and inferential control: with applications to ILC and precision motion systems". PhD thesis. Technische Universiteit Eindhoven, 2010.

[105] Tom Oomen et al. "Connecting system identification and robust control for next-generation motion control of a wafer stage". In: *IEEE Transactions on Control Systems Technology* 22.1 (2014), pp. 102–118.

[106] Roméo Ortega and Elena Panteley. "Adaptation is Unnecessary in L1-" Adaptive" Control". In: *arXiv preprint arXiv:1409.2389* (2014).

[107] Markus Pappert. "Robuste L1-adaptive Regelung eines planaren Nanopositioniersystems unter Modellunsicherheiten und Störungen". MA thesis. Technische Universität Ilmenau, 2013.

[108] Anders Pettersson et al. "Analysis of linear l1 adaptive control architectures for aerospace applications". In: *51st IEEE Conference on Decision and Control*. IEEE. 2012, pp. 1136–1141.

[109] E. Philippow. *Grundlagen der Elektrotechnik, 10*. Verlag Technik, Berlin, 2000.

[110] Rik Pintelon and Johan Schoukens. *System identification: a frequency domain approach*. John Wiley & Sons, 2012.

[111] J-B Pomet and Laurent Praly. "Adaptive nonlinear regulation: Estimation from the Lyapunov equation". In: *IEEE Transaction on Automatic Control* 37.6 (1992), pp. 729–740.

[112] Arthur E Quaid and Ralph L Hollis. "3-DOF closed-loop control for planar linear motors". In: *Proceedings of 1998 IEEE International Conference on Robotics and Automation*. Vol. 3. IEEE. 1998, pp. 2488–2493.

[113] Aaron Radke and Zhiqiang Gao. "A survey of state and disturbance observers for practitioners". In: *American Control Conference*. 2006, pp. 5183–5188.

[114] Adrian Mathias Rankers. "Machine dynamics in mechatronic systems: an engineering approach". PhD thesis. 1997.

[115] James C Rautio. "The Long Road to Maxwell's Equations". In: *IEEE Spectrum* 51.12 (2014), pp. 36–56.

[116] Aristides AG Requicha. "Nanorobots, NEMS, and nanoassembly". In: *Proceedings of the IEEE* 91.11 (2003), pp. 1922–1933.

[117] C. Röhrig. "Optimal commutation law for three-phase surface-mounted permanent magnet linear synchronous motors". In: *45th IEEE Conference on Decision and Control*. 2006, pp. 3996–4001.

[118] Christof Rohrig. "Current waveform optimization for force ripple compensation of linear synchronous motors". In: *Proceedings of the 42nd IEEE Conference on Decision and Control*. Vol. 6. IEEE. 2003, pp. 5891–5896.

[119] Charles E Rohrs et al. "Robustness of adaptive control algorithms in the presence of unmodeled dynamics". In: *IEEE Conference on Decision and Control*. Vol. 21. 1982, pp. 3–11.

[120] Dirk de Roover. "Motion control of a wafer stage: a design approach for speeding up IC production". PhD thesis. 1997.

[121] S.D. Ruben and T.C. Tsao. "Optimal commutation laws by real-time optimization for multiple motor driven systems". In: *American Control Conference*. 2010, pp. 1942–1947.

[122] B. A. Sawyer. "Magnetic Positioning Device". Pat. 3,376,578. 1968.

[123] C. Schäffel. "Untersuchungen zur Gestaltung integrierter Mehrkoordinatenantriebe". PhD thesis. Technische Universität Ilmenau, 1996.

[124] Robert Seifried. *Dynamics of underactuated multibody systems*. Springer, 2014.

[125] Vijay Shilpiekandula et al. "Load positioning in the presence of base vibrations". In: *2012 American Control Conference (ACC)*. IEEE. 2012, pp. 6282–6287.

[126] L. Silverman. "Inversion of multivariable linear systems". In: *IEEE Trans. Automat. Contr.* 14.3 (1969), 270–276.

[127] H. Sira-Ramirez, A. Luviano-Juarez, and J. Cortes-Romero. "A disturbance rejection-flatness based linear output feedback control approach for tracking tasks on a Chua's circuit". In: *50th IEEE Conference on Decision and Control and European Control Conference*. 2011, pp. 3496–3501.

[128] H Sira-Ramirez, M Ramirez-Neria, and A Rodriguez-Angeles. "On the linear control of nonlinear mechanical systems". In: *49th IEEE Conference on Decision and Control*. 2010, pp. 1999–2004.

[129] Hebertt Sira-Ramirez and Sunil K Agrawal. *Differentially flat systems*. Vol. 17. CRC Press, 2004.

[130] Hebertt Sira-Ramírez et al. "On the control of the permanent magnet synchronous motor: an active disturbance rejection control approach". In: *IEEE Transactions on Control Systems Technology* 22.5 (2014), pp. 2056–2063.

[131] J.J.E. Slotine and W. Li. "On the adaptive control of robot manipulators". In: *The International Journal of Robotics Research* 6.3 (1987), pp. 49–59.

[132] Günter Stein and Michael Athans. "The LQG/LTR procedure for multivariable feedback control design". In: *IEEE Transactions on Automatic Control* 32.2 (1987), pp. 105–114.

[133] Maarten Steinbuch and ML Norg. "Advanced motion control: An industrial perspective". In: *European Journal of Control* 4.4 (1998), pp. 278–293.

[134] SE Talole and SB Phadke. "Extended State Observer based control of flexible joint system". In: *IEEE International Symposium on Industrial Electronics (ISIE)*. 2008, pp. 2514–2519.

[135] KK Tan et al. "Development of an integrated and open-architecture precision motion control system". In: *Control Engineering Practice* 10.7 (2002), pp. 757–772.

[136] Kok Kiong Tan, Tong Heng Lee, and Sunan Huang. *Precision motion control: design and implementation*. Springer Science & Business Media, 2007.

[137] *Tetra GmbH Ilmenau PPS-Positioniertechnologie*. `http://www.tetra-ilmenau.de/automation/produkte/pps-positioniertechnologie.html`. Accessed: 20.09.2016.

[138] Y. Tomita, Y. Koyanagawa, and F. Satoh. "A surface motor-driven precise positioning system". In: *Precision engineering* 16.3 (1994), pp. 184–191.

[139] K. Treichel et al. "Modelling and identification of a high-precision planar positioning system". In: *55th International Scientific Colloquium (IWK), Ilmenau*. 2010.

[140] Kai Treichel, Johann Reger, and Remon Al Azrak. "On flatness based L 1 adaptive trajectory tracking control". In: *2014 IEEE Conference on Control Applications (CCA)*. IEEE. 2014, pp. 1158–1165.

[141] Kai Treichel et al. "Modeling of a planar motion stage for precision positioning". In: *18th International Conference on Methods and Models in Automation and Robotics (MMAR)*. IEEE. 2013, pp. 51–56.

[142] Kai Treichel et al. "Robust output feedback trajectory tracking control of an electrodynamic planar motion stage for precision positioning". In: *18th International Conference on Methods and Models in Automation and Robotics (MMAR)*. IEEE. 2013, pp. 57–62.

[143] J. Vanness. "Two new extensions to L1 adaptive control theory". MA thesis. University of Illinois, 2012.

[144] Justin Vanness, Evgeny Kharisov, and Naira Hovakimyan. "L1 adaptive control with proportional adaptation law". In: *2012 American Control Conference (ACC)*. IEEE. 2012, pp. 1919–1924.

[145] Jiang Wang et al. "L1 adaptive controller for a missile longitudinal autopilot design". In: *AIAA Guidance, Navigation and Control Conference*. 2008, pp. 18–21.

[146] M. Weck. *Werkzeugmaschinen Fertigungssysteme 3: Mechatronische Systeme: Vorschubantriebe und Prozessdiagnose*. VDI-Buch. Springer Berlin Heidelberg, 2013.

[147] Enric Xargay, Naira Hovakimyan, and Chengyu Cao. "Benchmark problems of adaptive control revisited by L1 adaptive control". In: *Mediterranean Conference on Control and Automation*. 2009, pp. 31–36.

[148] Bong-Jun Yang. "Adaptive output feedback control of flexible systems". PhD thesis. Georgia Institute of Technology, 2004.

[149] T. Żabiński and L. Trybus. "Tuning P-PI and PI-PI controllers for electrical servos". In: *Bulletin of the Polish Academy of Sciences: Technical Sciences* 58.1 (2010), pp. 51–58.

[150] Q. Zou and S. Devasia. "Preview-based stable-inversion for output tracking". In: *Proceedings of the 1999 American Control Conference* ().

[151] S. Zschäck, A. Amthor, and C. Ament. "Decentralized high precision motion control for nanopositioning and nanomeasuring machines". In: *IECON 2011-37th Annual Conference on IEEE Industrial Electronics Society*. 2011, pp. 546–551.

[152] Stephan Zschäck. "Mehrgrößenregelung von Nanopositionier-und Nanomessmaschinen mit großen Bewegungsbereichen". PhD thesis. Technische Universität Ilmenau, 2016.

List of Figures

List of Tables